ANL–01/04

ARGONNE NATIONAL LABORATORY
9700 South Cass Avenue
Argonne, Illinois 60439

DEVELOPMENT OF ADVANCED FIBROUS MONOLITHS

FINAL REPORT FOR PROJECT OF 1998–2000

Contributors:

K. C. Goretta
D. Singh
T. A. Cruse
W. A. Ellingson
J. J. Picciolo
B. J. Polzin
J. L. Routbort
T. W. Spohnholtz
F. W. Zok[1]
J. C. McNulty[1]
M. He[1]
W. M. Kriven[2]
S. J. Lee[2]
D. K. Kim[2]
G. Hilmas[3]
A. J. Mercer[3]
M. R. Begley[4]
A. R. de Arellano-López[5]

Energy Technology Division

February 2001

Work supported by U.S. Defense Advanced Research Projects Agency through an Interagency Agreement with the U.S. Department of Energy

[1]University of California, Santa Barbara, CA
[2]University of Illinois, Urbana–Champaign, IL
[3]University of Missouri, Rolla, MO
[4]University of Connecticut, Storrs, CT
[5]University of Seville, Seville, Spain

TABLE OF CONTENTS

LIST OF FIGURES

LIST OF TABLES

DEVELOPMENT OF ADVANCED FIBROUS MONOLITHS

FINAL REPORT FOR PROJECT OF 1998–2000

Abstract

Efforts to develop fibrous ceramic monoliths for primarily structural applications are described. Fibrous monoliths (FMs) are relatively insensitive to flaws and can exhibit graceful failure and large work-of-fracture values. They can be inexpensively produced in a wide variety of forms by conventional ceramic processing methods such as extrusion. The FM project that is the subject of this report involved investigations to (1) develop FMs that can be pressureless sintered rather than hot pressed, (2) develop technologies to continuously extrude FM filaments and inexpensively fabricate FM components, (3) evaluate the performance of commercial and new, prototype FMs, (4) develop micromechanical models to guide the design of new FMs and predict their properties, and (5) forge collaborations with industry to produce useful parts.

1 Introduction

Ceramic fibrous monoliths (FMs) were first developed as low-cost ceramic composites that offered many of the advantages of continuous-fiber ceramic composites. Commercially available ceramic fibers exhibit very high strengths, but are expensive, and are generally damaged during component processing. The damage during processing reduces their strengths substantially. FMs, which possess a fibrous microstructure similar to that of composites that contain commercial fibers, develop their fibrous structures during processing. Continuous cells, which constitute the fibrous portion of an FM, are formed by techniques such as dip-coating (c.f., W. S. Coblenz, U.S. Patent 4,772,524, Sept. 20, 1988) or extrusion (c.f., D. Popovic' et al., U. S. Patent 5,645,781, July 8, 1997). These techniques are inexpensive and can be adapted to virtually any ceramic or metallic form that can be formed from powders. Simple or complex parts can be fabricated from the basic FM cell feedstock. The advantages of low-cost constituents, simplicity of manufacture, and versatility of composition and form make FMs uniquely promising materials for many applications.

This project focused on developing technology to substantially reduce the cost of producing FMs and to better understand and predict the mechanical properties of FMs. Cost-reduction efforts made use of pressureless sintering in place of hot-pressing to consolidate FMs. Micromechanical modeling efforts, which required gathering a large body of test data, focused on in-plane response to load and presence of thermoelastic stresses. Unidirectional and cross-ply laminates were examined. The models that were developed complement those from the University of Michigan for FM response to flexure (c.f., e.g., D. Kovar et al., J. Am. Ceram. Soc. 80 (1997) 2471). Optimal design protocols have been identified and properties of FMs can now be predicted with confidence.

This report covers details of the fabrication of new, oxide-based FMs, synthesis and sintering information for various oxide monoliths and particulate composites; mechanical-property and microstructural characterization of the new FMs, commercial FMs based on Si_3N_4 cells, and a BN cell-boundary phase; and modeling of the mechanical response of Si_3N_4/BN FMs. The Si_3N_4/BN FMs, other samples, and invaluable information and assistance were provided by Advanced Ceramics Research (ACR) of Tucson, AZ.

This project was funded by the Defense Advanced Research Projects Agency (DARPA), though an Interagency Agreement with the U.S. Department of Energy (DOE). The primary contract was granted to Argonne National Laboratory (ANL). Subcontracts were issued to Prof. G. Hilmas of the University of Missouri at Rolla (UMR) for extrusion development, Prof. W. M. Kriven of the University of Illinois at Urbana-Champaign (UIUC) for study of new, stronger materials, and Prof. F. W.

Zok of the University of California at Santa Barbara (UCSB) for mechanical testing and modeling. Results were shared with and input was received from ACR and Dr. L. P. Zawada of Wright-Patterson Air Force Base (WPAFB). WPAFB has been responsible for high-temperature testing and nondestructive examination (NDE) of Si_3N_4/BN FMs.

2 Manufacture of Oxide Fibrous Monoliths

Discussions with ACR and Dr. W. S. Coblenz of DARPA indicated that hot-pressing has been the most expensive step in fabricating FMs. Pressureless sintering has the potential to decrease the cost of FM components by up to one order of magnitude. Oxides are more amenable to sintering than are, for example, carbides or nitrides. Oxides are also relatively stable in most engineering environments. We decided, therefore, to fabricate oxide FMs by a process of extrusion, layup, and sintering. To further reduce costs and aid manufacturing, we also investigated solid freeform fabrication (SFF) as a technique to produce oxide FMs.

In Si_3N_4/BN FMs, the BN cell boundary is responsible for the high toughness values and insensitivity to flaws that have been achieved. The BN phase consists of highly textured, platelike grains that bond poorly to each other or to Si_3N_4. Examination of oxide literature indicated that it will be difficult to identify and incorporate into FM architecture an oxide phase with properties similar to those of BN. Instead, we focused on the use of a cell boundary with controlled porosity. Several reports over the past few years have indicated that such a phase can, much like BN, impart an ability to resist crack propagation (c.f., e.g., C. G. Levi et al., J. Am. Ceram. Soc. 81 (1998) 2077).

We first produced FMs based on dense $ZrSiO_4$ cells and porous $ZrSiO_4$ cell boundaries. These FMs failed gracefully in flexure and provided validation of the new approach to fabricating FMs. They were, however, not as strong as Si_3N_4/BN FMs, and remained bound to a rule of mixtures for strength. That is, the strength of the $ZrSiO_4$ FMs was lower than that of monolithic $ZrSiO_4$ by a factor approximately equal to the volume fraction of cell boundary. We, therefore, followed two paths to produce stronger oxide FMs: incorporation of favorable residual stresses and higher-strength oxides.

2.1 $ZrSiO_4$-Based Fibrous Monoliths

$ZrSiO_4$-based FMs were produced by three methods. At ANL, we developed a new coextrusion method that involved use of a dual-feed extrusion die that could be fed by screws from two independent hoppers to produce filaments. At UMR,

filaments were produced by extrusion of a duplex feed rod. Also at ANL, SFF was used to form simple parts directly.

2.1.1 $ZrSiO_4$ Powder Studies

To fabricate $ZrSiO_4$ FMs, it was necessary to learn how to sinter $ZrSiO_4$ to various densities and how to process a monolithic FM that consisted of a dense cell and a porous cell boundary. The work could be divided into three main tasks: (1) characterize the powder and study the sintering and thermomechanical responses of the constituents; (2) fabricate FMs by coextrusion; and (3) characterize resulting structures and properties.

$ZrSiO_4$ proved easy to produce in a wide range of final densities; its theoretical density is 4.6 g/cm^3. Two commercial sources of $ZrSiO_4$ powder were exploited, Alfa Aesar (Ward Hill, MA) and Remet (Utica, NY). Alfa powder, which exhibited an initial average particle size of ≈1 μm, was used for the cell. Remet powder, which exhibited an initial average particle size of ≈10 μm, was used for the cell boundary.

To improve sintering of the Alfa powder, it was ball-milled in isopropyl alcohol with ZrO_2 milling media for 72 h, dried, and screened though a 100-mesh sieve. The resultant average particle size was 0.5–0.7 μm. The Remet powder was not milled.

In all of the sintering studies, bars made from Alfa $ZrSiO_4$ exhibited higher densities than those made from Remet. Sintering in air at 1550°C produced Alfa bars that were ≥95% dense and Remet bars that were ≈70% dense. This difference in density affected the strength of sintered specimens. In four-point flexure tests conducted at room temperature (inner and outer load spans of 20 and 40 mm, respectively), the fracture strengths of dense Alfa and porous Remet $ZrSiO_4$ bars were 254 ± 33 and 55 ± 2.6 MPa, respectively. This inherent difference in fracture strength should allow fabrication of successful FMs.

All $ZrSiO_4$ bars exhibited a coefficient of thermal expansion (α or CTE) of ≈5.15 x 10^{-6} $°C^{-1}$, regardless of density or starting powder. Representative data are shown in Fig. 1. The result that α was approximately independent of density proved to be true for all oxides examined. Hence, the procedures required to produce an all-$ZrSiO_4$ FM were greatly simplified. To fabricate a monolithic structure, shrinkages during firing had to be matched, but no significant stresses were expected to be generated during cooling.

To examine the likelihood of fabricating robust FMs, $ZrSiO_4$ layers were tape cast and laminates were produced. For a given firing schedule, Alfa $ZrSiO_4$ exhibited substantially more shrinkage than did Remet. For a dual-phase

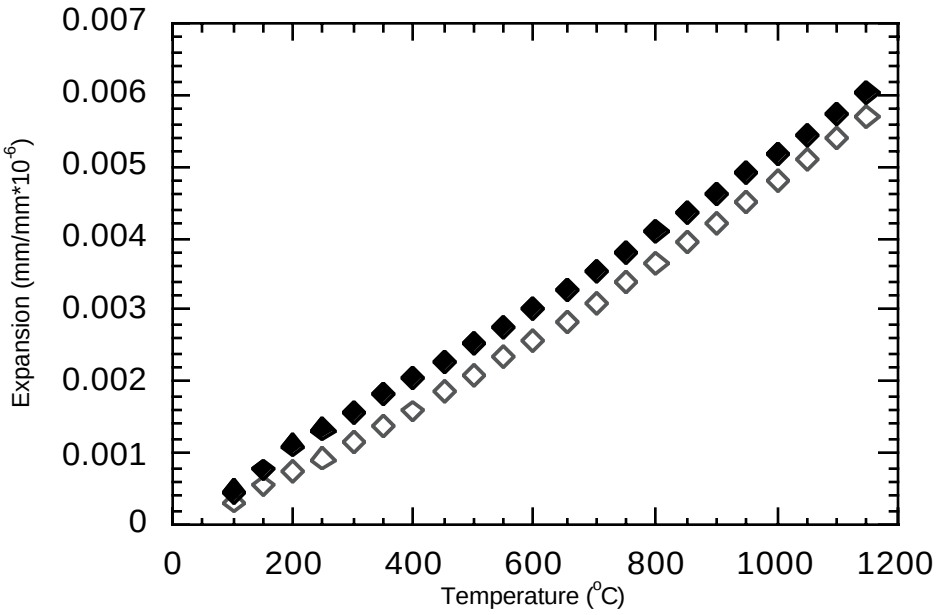

Fig. 1. Thermal-expansion data for $ZrSiO_4$ in air, with 300°C/h heating; filled diamonds = 95%-dense, and open diamonds = 70%-dense specimens.

microstructure, a higher fraction of organic additives was required in the Alfa mix to balance shrinkages. Layered materials were produced by casting one material on top of the other and then cold-pressing several of these layers. Cofiring produced multilayers with little warping or cracking (Fig. 2) and approximated what we intended to produce by FM technology.

To control sintering of the Remet $ZrSiO_4$, it proved to be necessary to tailor particle size to a greater extent than could be accomplished by, for example, sieving. In particular, we determined that sintering could be selectively reduced by removing fractions of the fines that were present in the as-received powder. Sedimentation in 800 mL of deionized water that contained 20 drops of Darvan C dispersant removed various fractions of the fines. Depending on sedimentation procedures, the average size of the Remet $ZrSiO_4$ powder could be controlled between ≈10 and ≈30 μm.

Effects of tailoring the Remet particle size were readily observed in the strength and microstructure of sintered bars. The strength of bars sintered at 1550°C for 3 h ranged from ≈25 to 60 MPa. Microstructures of representative sets of bars are shown in Fig. 3.

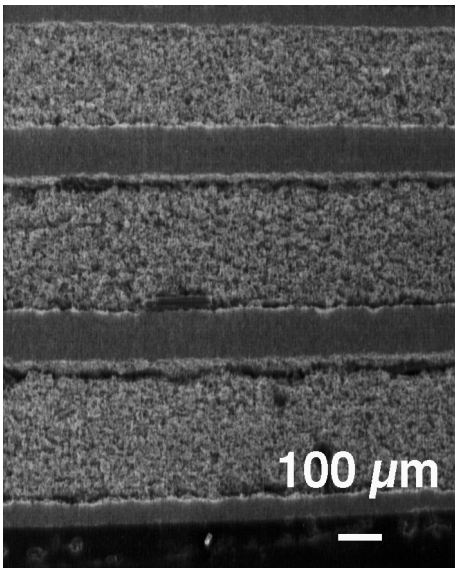

Fig. 2.
Scanning electron microscopy (SEM) photomicrograph of $ZrSiO_4$ multilayer, which comprised alternating dense and porous layers.

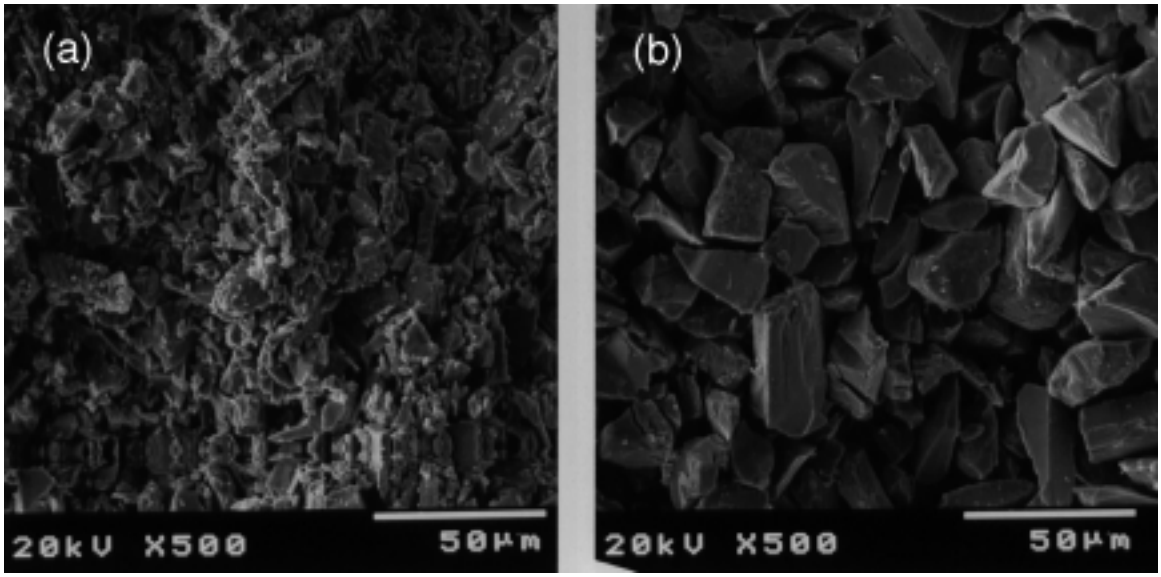

Fig. 3. Fracture surfaces of sintered bars made from (a) partially settled and (b) fully settled Remet $ZrSiO_4$.

2.1.2 Coextruded $ZrSiO_4$ Fibrous Monoliths

We decided to fabricate FM filaments by a sequential method. In the key first step, we coextruded duplex monofilaments that consisted of a core of Alfa $ZrSiO_4$ and a sheath of Remet $ZrSiO_4$. Twin extrusion screws were fed into a single die, inside of which the sheath was formed around the core (Figs. 4 and 5). In the second step, filament was cut and bundled and then ram-extruded to produce filaments suitable for FM manufacture (Fig. 6).

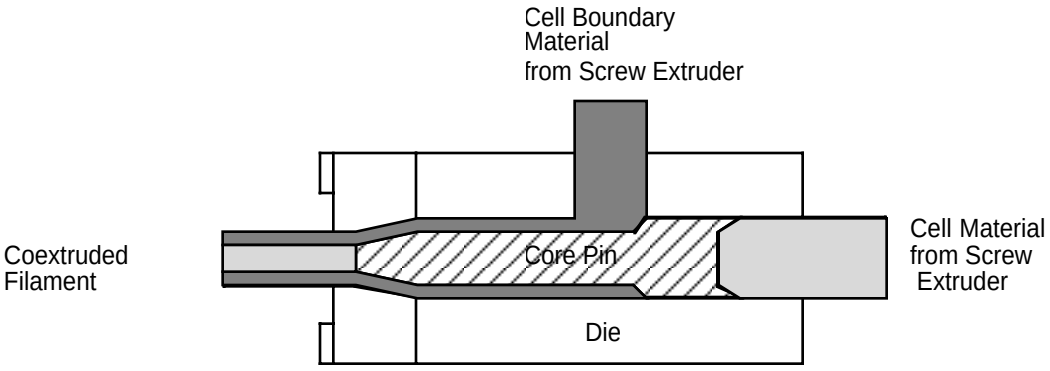

Fig. 4. Cross-sectional view of coextrusion die showing pattern of material flow.

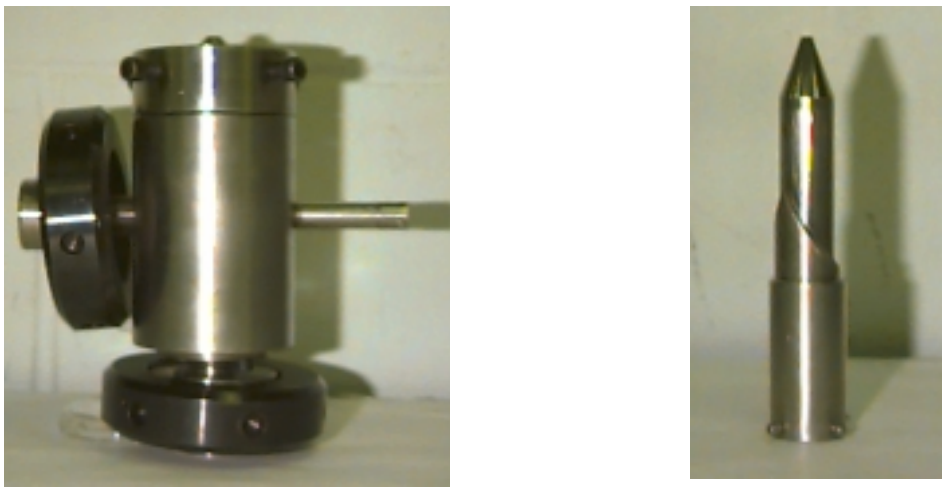

(a) (b)

Fig. 5. Photographs of (a) coextrusion die and (b) core pin of die.

The coextrusion approach has several significant advantages over conventional ram extrusion. The hoppers can be fed individually and continuously, so virtually any length of any filament can be formed. The extrusion screws can be controlled independently, which allows for successful processing, despite a significant extent of mismatch between the rheologies of the core and sheath. Should one desire to change diameters, only inexpensive and easy-to-install pins or orifices need be replaced; in ram-extrusion processes, new sets of core or sheath dies must be manufactured for each change in filament dimension. The pins and orifices can be readily made into various cross-sectional shapes; thus, the process is not restricted to cylindrical configurations. No provisions are required to avoid sticking to dies and therefore plastic-mass formulations can be simplified.

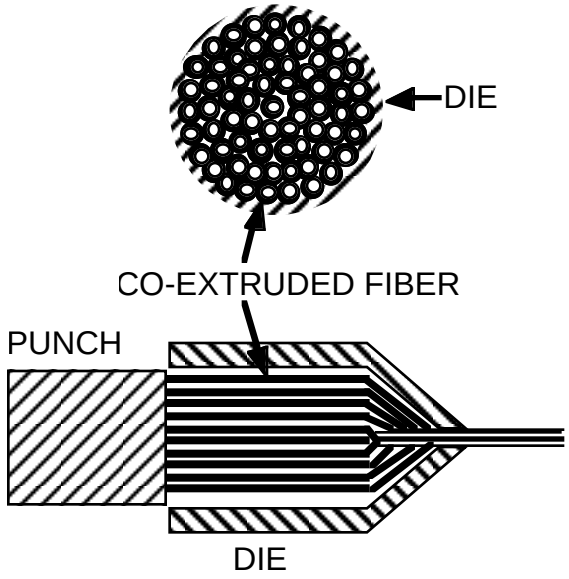

Fig. 6. Schematic diagram showing bundle of coextruded filaments and subsequent ram extrusion to form final filaments for FM fabrication.

The first step in plastic processing was to batch the necessary composition and vibratory-mill the mixture overnight. The formulation settled upon after some experimentation was based on one that is used at ANL for electronic ceramics (c.f., H. J. Leu et al., Supercond. Sci. Technol. 2 (1989) 311-313). It consisted of an azeotropic vehicle, binder, plasticizer, and dispersant (Table 1). The Rohm & Haas (Philadelphia, PA) binder is a thermosetting acrylic polymer. The Monsanto (Fayetteville, NC) plasticizer is a butyl benzyl phthalate. Menhaden fish oil is a standard dispersant used in ceramic processing.

Table 1. Composition (g) of plastic mixes used to extrude Alfa and Remet $ZrSiO_4$ filaments

Constituent	Alfa $ZrSiO_4$	Remet $ZrSiO_4$
78 wt.% xylene/22 wt.% butanol	20	15
Monsanto S-160 plasticizer	10	10
Menhaden fish oil in xylene/butanol	10	10
$ZrSiO_4$ powder	200	200
Rohm & Haas AT-51 binder	21	21
Carbon powder	0	0.25

After the mixes were vibratory-milled overnight, they were de-aired, tape cast to a thickness of ≈0.5 mm, dried, and stripped. The tapes were allowed to sit overnight and were then mixed in a Brabender (South Hackensack, NJ) high-shear mixer. Mixing was used to adjust viscosity to the necessary levels for coextrusion. Extrusion occurred at a temperature ≤30°C. The extruded filaments were dried for several days. They were then cut into 10-cm sections and bundled. The filament bundles were placed in a ram extrusion die and extruded.

To produce specimens for sintering studies and studies of microstructure and mechanical properties, the resultant filaments were cut into ≈50-mm sections and pressed in a bar die at a pressure of ≈100 MPa. The resultant bars were then heat treated. Binder burnout was accomplished in flowing O_2. Each bar was heated to 140°C at 50°C/h and held for 0.1 h. After the hold, each bar was heated to 500°C at 5°C/h, held for 3 h, and then cooled to room temperature at 50°C/h. The bars were sintered at 1550°C for 3 h to complete the processing of prototype $ZrSiO_4$ FMs.

The FM bars experienced ≈23 vol.% shrinkage between initial pressing and the fired state. The properties of these bars will be discussed in Section 4.1. SEM was conducted on several fracture surfaces and polished cross sections to determine the effectiveness of the processing. Representative SEM photomicrographs of a fired FM bar are shown in Fig. 7.

The FM bars were ≈60 vol.% cell and 40 vol.% cell boundary. This differs significantly from the ≈80–85 vol.% cell and ≈15–20 vol.% cell boundary that is generally observed for Si_3N_4/BN FMs. The rather large fraction of cell boundary could be attributed, at least in part, to the large size of the Remet $ZrSiO_4$ powder. The average cell size of the $ZrSiO_4$ FMs was ≈150 μm.

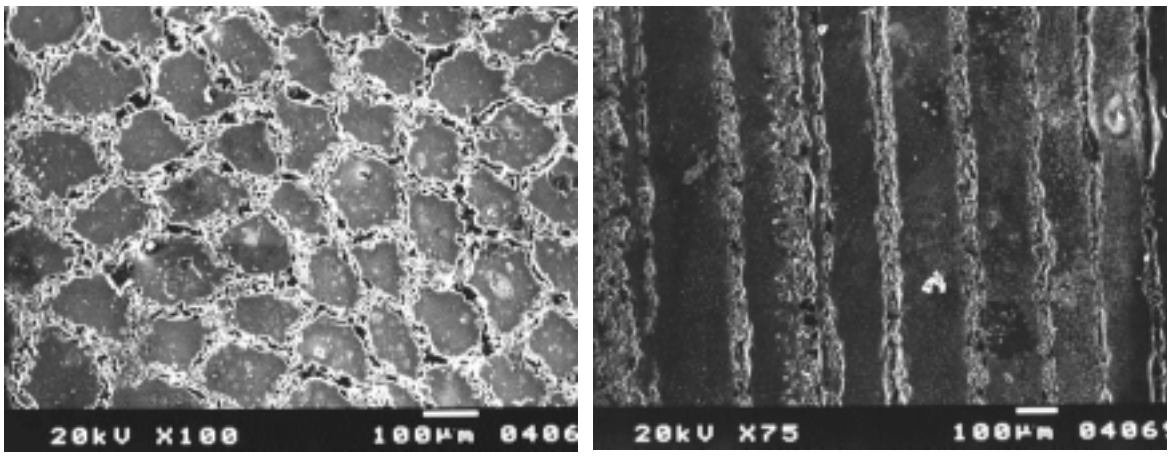

(a) (b)

Fig. 7. SEM photomicrographs of (a) transverse and (b) longitudinal cross sections of $ZrSiO_4$ FM bars.

The longitudinal cross section in Fig. 7 revealed good alignment of the individual filaments and relatively smooth interfaces. Shear instabilities during extrusion appear to have been minimal. Given the 30–35% porosity in the cell boundary, the expectation would be for substantial energy dissipation during fracture in flexure.

2.1.3 Ram-Extruded $ZrSiO_4$ Fibrous Monoliths

The plastic mixtures developed at ANL have advantages and disadvantages. They are entirely organic and are not applicable to all types of ceramic powders. Work at UMR focused on development of alternative routes to FM production, including use of aqueous-based mixtures. To help with the effort, Alfa and Remet $ZrSiO_4$ powders were supplied by ANL.

Organic Systems

In the first stage of the work, rheological studies of the organic systems that contained the $ZrSiO_4$ powders and thermoplastic resins were initiated. Batch 1 was produced from 50 vol.% $ZrSiO_4$, 20 vol.% each ethylene ethyl acrylate (DuPont Elvax® 550, Wilmington, DE) and ethylene vinyl acetate (Union Carbide DPDA 6141 N, Danbury, CT), and 10 vol.% heavy mineral oil (Aldrich Chemical, Milwaukee, WI). Batch 2 was produced from 40 vol.% fine $ZrSiO_4$, 28 vol.% each ethylene ethyl acrylate and ethylene vinyl acetate, and 4 vol.% heavy mineral oil. The final volume of each batch was ≈42 cm^3.

Each batch was blended in the Brabender high-shear mixer that was heated to 135°C. The powder and plasticizer were added slowly and allowed to mix 5 min at 25 rpm and 150°C after all of the constituents were added. After the first mixing was complete, the batch was removed from the Brabender, and then remixed. Two sets of rheology data were acquired. The first set was taken by varying the speed of the blade stepwise by 5-rpm increments. The temperature was allowed to equilibrate for the new rpm level, and then the torque reading and temperature were noted. The second set was taken by noting the torque for each rpm level (again, stepwise by 5-rpm) at a constant temperature of 150°C. Data on the 50%-fine $ZrSiO_4$, which are representative of our measurements, are presented in Table 2. After the measurements were recorded, the batches were removed from the mixer and stored for subsequent extrusion.

When working with an extrusion process, it is important to characterize the flow behavior of the system. The system must behave as a Newtonian or shear-thinning fluid to be viable. The flow characteristics of the blended powders can be analyzed by plotting torque vs. rpm because the rotational speed of the blade and the torque are directly proportional to the shear rate and viscosity, respectively.

Table 2. Two sets of rheology data for Batch 1 $ZrSiO_4$

First data set[a]			Second data set[b]	
rpm	T (°C)	torque	rpm	torque (150°C)
15	144	14.2	15	13.1
20	145	15.7	20	14.8
25	147	16.9	25	15.9
30	149	18.1	30	16.6
35	150	18.7	35	18.5
40	152	19.4	40	18.7
45	154	19.7	45	19.4
50	156	20.2	50	20.0
55	158	20.3	55	20.7
60	160	20.3	60	21.3
65	162	20.5	65	22.4

[a]Obtained by varying speed of blade stepwise by 5-rpm increments; allowing temperature to equilibrate for new rpm; then reading torque and temperature.
[b]Obtained by noting torque for each rmp level (by 5-rpm increments) at constant temperature of 150°C.

The shear stress τ can be related to the shear rate γ through the power-law equation $\tau = K\gamma^n$. Plotting log τ vs. log γ produces a straight line; the power-law exponent n is determined from the slope. The values of n for the two batches studied were $n_{(50\%)} = 0.35$ and $n_{(40\%)} = 0.33$ (Fig. 8), which denotes shear-thinning behavior. Therefore, these systems should be extrudable.

During ram extrusion of a duplex FM filament, two shells surround a core. As shown in Fig. 9, three pieces must be pressed into appropriate dies. Various compositions were used for the cores and shells, but detailed rheological data were not taken for all systems; in general, only torque readings at 150°C and 60 rpm for the first and second batchings were recorded. All batches were formulated to have a final volume of 42 cm^3 to avoid false torque readings from the thermal expansion of the polymers.

After some experimentation to achieve the optimal organic formulation, the core batches were produced by blending appropriate weights of fine Alfa $ZrSiO_4$ powder, DuPont ethylene ethyl acrylate (EEA) binder, Rohm & Haas Paraloid B-67 resin (B-67), and heavy mineral oil (HMO). The shell batches were made from coarse Remet $ZrSiO_4$ and contained Carbowax methoxypolyethylene glycol (MPEG) 550 (provided by Union Carbide) instead of the HMO.

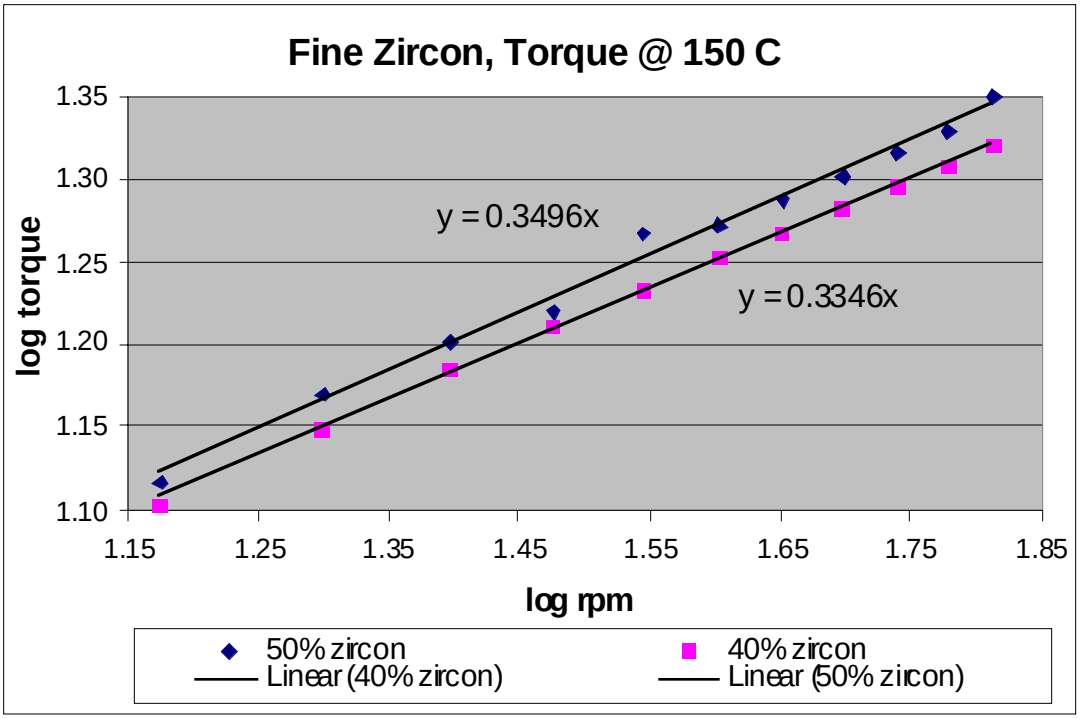

Fig. 8. Torque-vs.-rpm data for two $ZrSiO_4$ batches.

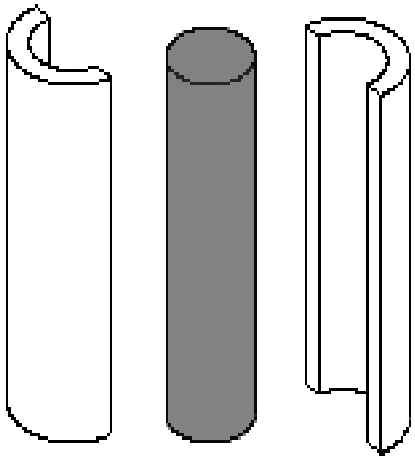

Fig. 9. Schematic diagram showing the split outer jacket of interphase material before pressing onto the core material.

For both core and shell, the mixer was heated to 135°C and the binders were added and allowed to mix for ≈5 min. The powder and plasticizer were added slowly over a span of ≈10 min and allowed to mix ≈10 min at 35 rpm and ≈150°C after all of the components were added. After the first mixing was complete, a torque reading was taken at 60 rpm and 150°C; the batch was then removed from the Brabender and rebatched. Rebatching involved adding portions of the batch back into the mixer and allowing them to mix for another 5 min at 35 rpm and 150°C. The second torque reading (also at 60 rpm, 150°C) was taken after this rebatching step was complete. For the shell batches, the MPEG-550 was not added until after the second torque reading was taken because the MPEG-550 tends to be an external plasticizer, which causes the batch to slip in the mixer and can lead to a false torque reading.

Batches of the following compositions (by weight) were produced:

Core of fine Alfa $ZrSiO_4$:

54% $ZrSiO_4$	32.4% EEA	3.6% B-67	10% HMO
45% $ZrSiO_4$	35% EEA	10% B-67	10% HMO
50% $ZrSiO_4$	25% EEA	15% B-67	10% HMO
54% $ZrSiO_4$	36% EEA		10% HMO
44.6% $ZrSiO_4$	44.6% EEA	9.9% B-67	0.9% HMO
54.2% $ZrSiO_4$	34.5% EEA	9.9% B-67	1.4% HMO.

Shell of coarse Remet $ZrSiO_4$:

50.2% $ZrSiO_4$	46.5% EEA		3.2% MPEG
50.2% $ZrSiO_4$	41.7% EEA	4.8% B-67	3.2% MPEG
43.7% $ZrSiO_4$	43.7% EEA	9.7% B-67	3.0% MPEG
46.3% $ZrSiO_4$	41.6% EEA	9.2% B-67	2.9% MPEG
51.3% $ZrSiO_4$	37.3% EEA	4.7% B-67	6.7% MPEG
55% $ZrSiO_4$	33.9% EEA	4.0% B-67	7.1% MPEG
55% $ZrSiO_4$	37% EEA	3.2% B-67	4.8% MPEG.

The 55% $ZrSiO_4$/35% EEA/10% HMO composition was adopted as the standard for producing cores. The standard composition eventually adopted for the shells was 55% $ZrSiO_4$/33.9% EEA/4% B-67/7.1% MPEG-550. We found that significant additions of MPEG-550 improved shell production. The optimal MPEG level reduced die-wall friction during extrusion, which decreased the possibility of the shell and core materials mixing during extrusion. The volume of B-67 in the shells was adjusted to contain at least 10% of the total volume of thermoplastics.

This adjustment increased the difference between the shell and core compositions and was designed to decrease the propensity for mixing between the shell and core during the extrusion process.

Core batching rapidly evolved to a consistent process. Shell batching initially suffered from bubbling and sticking to the die during shell pressing. These problems were eventually overcome. At first, we believed that the powder was not completely dried after dying them with food coloring, but further drying of the powders did not alleviate the shell bubbling. Another possible concern, the water content in the MPEG-550 supply, proved not to be a problem. To alleviate the sticking problem, a clean room was used, the formulation of the batch was slightly altered to incorporate additional MPEG, and a procedure was developed for preparing the dies before pressing.

An ongoing concern was the humidity level and how it affected the dies. A procedure was developed for preparing and storing the dies. They were placed overnight in a furnace heated to 170°C. After cooling, the dies were transferred to a small vacuum desiccator that contained a desiccant. The desiccator was then taken to the clean room. Before pressing, the dies were removed from the desiccator, wiped with ethanol or acetone to ensure cleanliness, and allowed to air dry. After the alcohol dried, the dies were wiped with Buehler (Lake Bluff, IL) Release Agent. After pressing operations were complete, the dies were cleaned and stored under light vacuum in the desiccator.

All initial ram extrusions were through a spinnerette of final orifice 1.75 mm. First-pass extrusion quickly became a repeatable process. Second-pass extrusion was also successful, but the rebundling practice had to be perfected to keep the cross sections consistent throughout the feedrod and subsequent second-pass filament. An optical photomicrograph of the 1.75 mm-to-1.75 mm second-pass filament is shown in Fig. 10. The cross section was smooth and uniform.

Thermogravimetric analysis of a filament was conducted in air with a ramp rate of 5°C/min. The weight-loss-vs.-temperature data indicated that binder began to burn at ≈150-200°C. Calculations of the concentration of binder in the system compared to weight-loss data revealed that the binder-burnout process was complete by ≈525°C.

FM fabrication involved layup of filaments, warm-pressing, and heat treatment. The procedures followed were similar to those for the $ZrSiO_4$ produced at ANL, except for the binder-burnout sequence. The filaments were cut into pieces of desired length and arranged in a plate die. All test pieces were produced by unidirectional stacking of one layer of filament on top of another. After the filaments were arranged in the die, they were heated in a curing oven to 150°C and

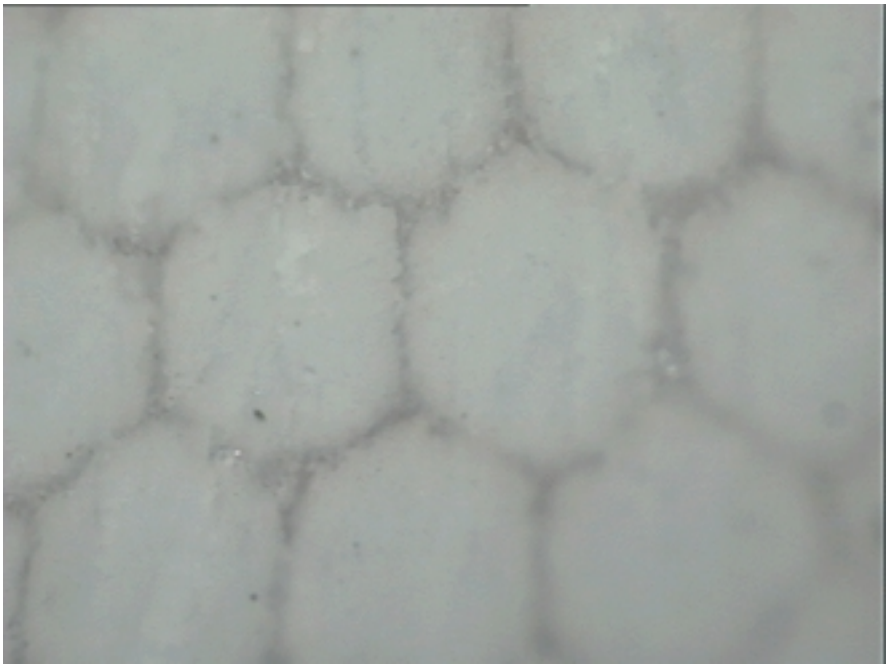

Fig. 10. Optical photomicrograph (≈5X magnification) of extrusion end.

then pressed in a Carver laboratory press at 15 MPa. A procedure was also developed for pressing test billets in a Wabash press (the press used for fabricating shells). The filaments were arranged in the die and placed in the Wabash press. The platens were closed so they just barely clamped the die. The system was heated to 135°C and the pressure was increased to 3 tons after the desired temperature was reached. The temperature was then reduced to ambient while the load was maintained.

The organic binders were removed from the ram-extruded specimens in a 4-torr vacuum. Dry N_2 was trickled through the burnout chamber, which was heated on the following schedule: heat to 150°C at 60°C/h and hold for 2 h; heat to 200°C at 6°C/h and hold for 6 h; heat to 390°C at 6°C/h and hold for 24 h; heat to 500°C at 18°C/h and hold for 0.1 h; heat to 600°C at 60°C/h and hold for 2 h; and cool to room temperature at 120°C/h.

The resultant specimens were sintered in air at 1550°C for 3 h. The heating rate was 60°C/h and the cooling rate was 180°C/h. We produced ≈82.5 vol.% cell/17.5 vol.% cell-boundary specimens from ram-extruded filaments (Fig. 11). The final die orifice was 1.75 mm for both the first- and second-pass coextrusions. The cellular phase for the ram-extruded filament was ≈95% dense; the cell-boundary material remained coarse and porous.

(a)

(b)

(c)

Fig. 11. Optical photomicrographs of (a) typical green billet, (b) typical billet after binder burnout, and (c) typical billet after sintering.

Concerns about the macrostructure of sintered filaments arose after studying SEM photomicrographs of prototype FMs. Cross-sectional examination revealed that the filaments were fairly regular in shape, but that voids were also present (Fig. 12a). Voids (areas in which the shell material eroded away and the cores of two filaments connected) were shown to be a greater problem in examination of longitudinal cross sections (Fig. 12b). To correct this problem, filaments were produced with 80 vol.% core / 20 vol.% shell and 70 vol.% core / 30 vol.% shell ratios,

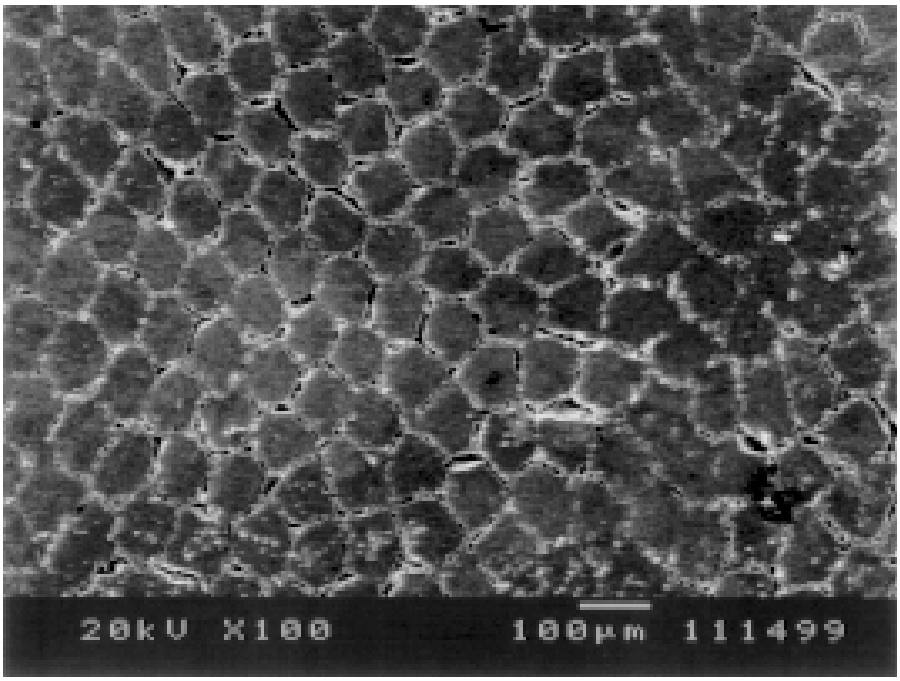

(a)

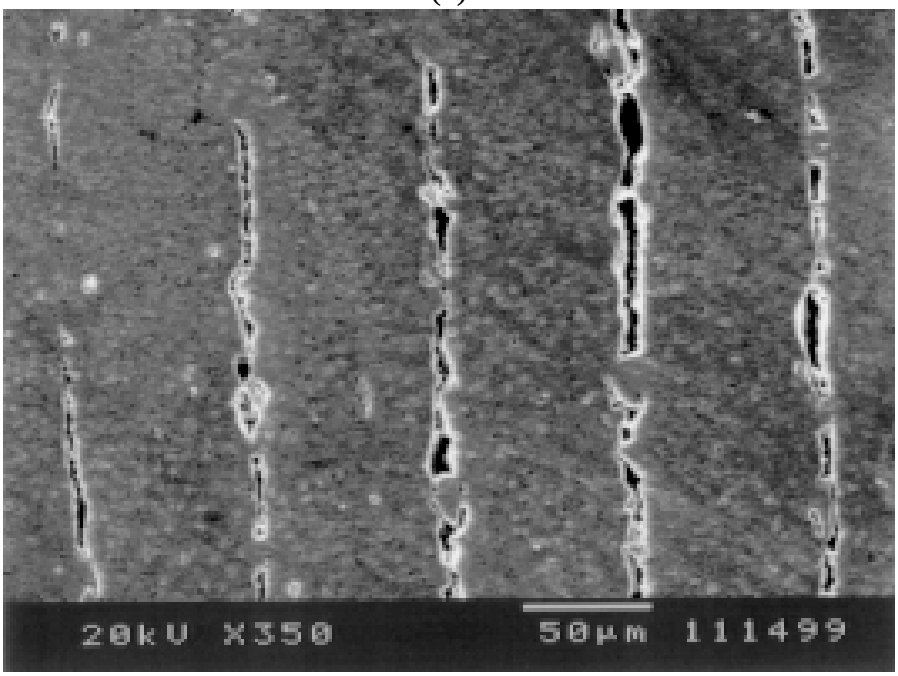

(b)

Fig. 12. SEM photomicrograph of (a) transverse cross section and (b) longitudinal cross section of an 82.5% core/17.5% shell FM test piece.

as opposed to the 82.5 vol.% core / 17.5 vol.% shell filaments initially used. Increasing the shell-to-core ratio eliminated the voids (see Fig. 13, in which an FM produced from 70 vol.% core / 30 vol. % shell coextruded $ZrSiO_4$ filament is shown).

Use of powders of finer size should also minimize void formation in future FMs. The Remet $ZrSiO_4$ used for the current shells is ≈15–20 μm in size, which is coarser than we expect to use in new oxide FMs.

The mechanical properties of the ram-extruded $ZrSiO_4$ FMs will be discussed in Section 4.1.

Aqueous Systems

Aqueous systems offer several advantages to commercialization of FM products, including cost and environmental impact. A literature review identified several promising binders that are soluble in water. Among them were Polyox® polyethylene oxide powder and Carbowax® polyethylene glycol 3350 flake (Union Carbide, Danbury, CT); Duramax™ B-1051 and B-1052 emulsions (Rohm & Haas, Philadelphia, PA); polyvinyl alcohol (PVA) (Air Products, Allentown, PA); and Aquazol 200 and 500 water-soluble binders (Polymer Chemistry Innovations, Inc., Tucson, AZ). Carbowax® polyethylene glycol (PEG) 400 liquid (Union Carbide) and AMP-95 (a pH-control agent from the Angus Chemical subsidiary of Dow Chemical, Midland, MI) were needed to complete the Duramax recipe. Aquazol is a 2-ethyl-2-oxazoline polymer that is highly soluble in polar solvents and is being used in the ceramics industry as a greenware binder because of its clean burnout. Batches that were made are listed in Table 3.

The solids loading was typically ≈55% for all batches. The Rohm & Haas recipe that follows served as the starting point for aqueous-based binder formulations.

Oxide:	55 vol.% Alfa $ZrSiO_4$
Solvent:	22.6 vol.% deionized water
Binders:	11.9 vol.% Duramax™ B-1051 and 6.4 vol.% Duramax™ B-1052
Plasticizer:	0.8 vol.% PEG-400
pH control:	3.3 vol.% AMP-95.

Polyvinyl alcohol binders were also studied extensively. Initial efforts focused on determining the maximum PVA solids loading. For the preliminary tests, with stirring in water at 95°C, we achieved an ≈40 wt.% concentration of PVA solids. The consistency of this binder batch was similar to that of molasses.

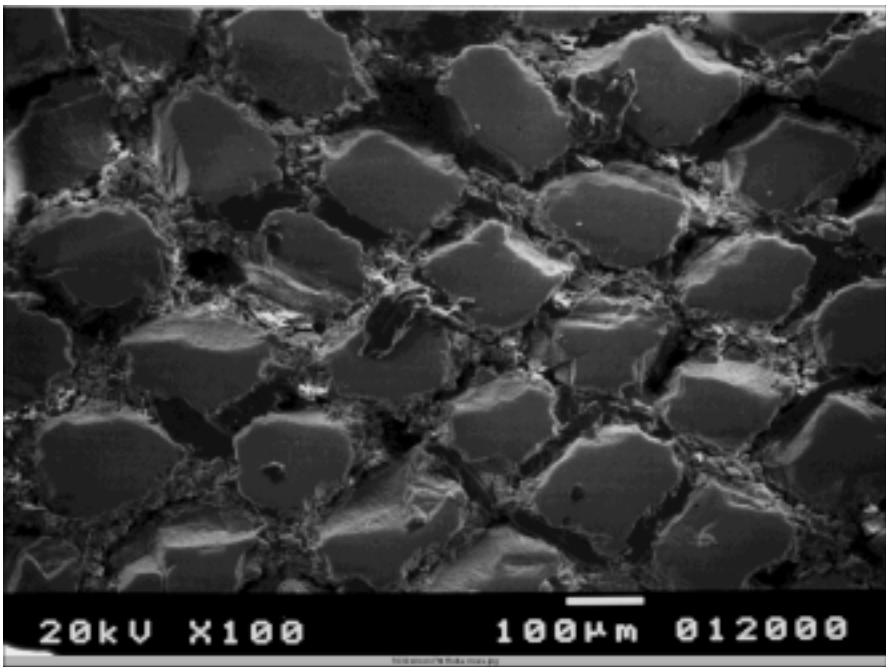

Fig. 13. Transverse cross section of $ZrSiO_4$ FM.

Table 3. Aqueous binder test matrix for oxide core with coarse $ZrSiO_4$ shell

Binder	Plasticizer	Other
Aquazol 200	PEG-400	—
Aquazol 500	PEG-400	—
Duramax B-1051	PEG-400	AMP-95
Duramax B-1052	PEG-400	AMP-95
Duramax B-1051 and B-1052	PEG-400	AMP-95
Polyvinyl alcohol	PEG-400	biocide
Duramax and polyvinyl alcohol	PEG-400	AMP-95

A typical extrusion formulation was

55% fine zircon powder
42% PVA solution
3% ethylene glycol (plasticizer)
(At ≈90°C, add water or solid PVOH to adjust torque as needed).

The torque reading for this batch was adjusted to ≈2.4 x 10^4 MG by using distilled water and polyethylene glycol as the plasticizer.

Fine zircon batches have also been produced from Aquazol® 200 granules as the binder and PEG-400 as the plasticizer:

55% fine $ZrSiO_4$
40% Aquazol-200
5% polyethylene glycol (400 MW)

50% fine $ZrSiO_4$
35% Aquazol-200
15% PEG-400

55% fine $ZrSiO_4$
32.5% Aquazol-200
12.5% PEG-400.

These recipes were mixed at ≈105°C, and PEG-400 was used to adjust the torque to an appropriate level (240 x 10^2 MG). The batches appeared to mix well, but were tacky to the touch. Cores could be compacted successfully, but the tackiness of the composition prevented the cores from being ejected readily from the die. Despite this tackiness, the composition has been shown to be extrudable without application of a shell and is therefore a candidate for a coextrusion system.

In summary, several recipes have produced well-mixed aqueous batches, but uniform cores and shells have proved to be difficult to press. Care must be taken to prevent the batches from drying out before pressing, so it is best to press the core immediately after removing the batch from the mixer. We believe that the systems that have been studied can be perfected, but, owing to insufficient time and resources, we have been unable to do so.

2.1.4 Fibrous Monoliths by Solid Freeform Fabrication

Although SFF offers perhaps unrivaled advantages for production of FMs, it is a complex technology that requires substantial development before it can compete with the more-mature extrusion approaches. Work in the ANL program focused on SFF itself and laser machining. These two technologies are, in concert, capable of producing near-net-shape forms of virtually any degree of complexity. In the SFF work, we collaborated extensively with ACR. In the laser-machining work, we collaborated with the Illinois Institute of Technology (IIT).

Solid Freeform Fabrication

The SFF work was conducted with a Stratasys 3D Modeler (Eden Prairie, MN). Several modifications of the base unit were necessary. The existing liquefier in the unit consisted of a cylinder with a wrap-around resistance heater. It was reverse-engineered at ANL so that we could manufacture, on site, the liquefier units with various throat diameters. The initial default diameter was 1.8 mm. The Stratasys unit was first modified with the installation of an ACR-designed high-pressure head (Fig. 14).

In FMs, with a duplex structure of outer material applied over a central core, it is imperative that the SFF methods hold the ratio of the outer shell thickness to the central core diameter constant during extrusion. We initially experienced difficulty in extruding FM materials while holding the outer shell in place. The shell was generally stripped during initial extrusion, but remained intact later during extrusion.

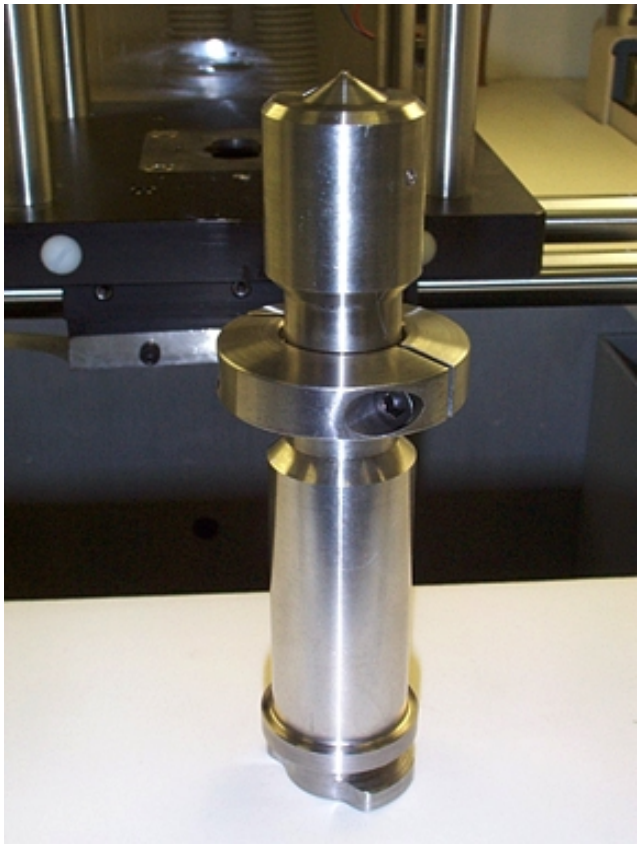

Fig. 14. Photograph of high-pressure liquefier section of new SFF delivery system.

To compensate for the lack of shell retention, analysis of the internal structure of the ACR heater assembly and nozzle suggested that the taper inside the current heater nozzle was too blunt, and thus a high shear load was being placed on the shell material. We, therefore, designed and had fabricated a new nozzle with a much shallower taper. The extruder nozzle design was revised to include an internal ≈77° cone, which gradually reduced the feedstock diameter from a nominal 16.4-mm outer diameter (input) to a 2.3-mm outer diameter (output).

This revision in nozzle design provided three benefits: (a) reduced shear forces on the outer shell and stripping/tearing of the outer shell from the central core feedstock during the extrusion process by allowing more uniform flow of material through the liquefier; (b) extrusion of FM filament with a more uniform cell geometry; and (c) reduced force needed to push materials through the tip. The last benefit is important, because it may provide a means to avoid the need to use a 1.0-turn-per-2.5 mm pitch instead of the current 0.5 pitch per 2.5 mm.

To verify the dimensions of the nozzle, we obtained high-energy X-ray projection images of the as-built nozzle (Fig. 15). By using digital image processing, we determined that the angle as built was 76°, close to the requested 77°.

In the initial SFF work, $ZrSiO_4$-based green filaments were produced for feedstock for SFF of monofilament FMs. Two feedstock diameters were investigated: a 3-mm continuous filament for use in the low-pressure 3D Modeler (LP-3D), and a 16.4-mm billet, 5–12.5 cm long, to be used as feedstock in the high-pressure 3D Modeler (HP-3D).

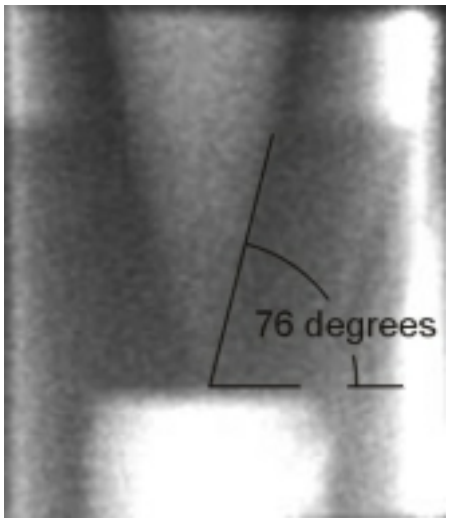

Fig. 15.
Digital X-ray image of as-built new nozzle design.

Feedstock billets consisting of multiple $ZrSiO_4/ZrSiO_4$ FM monofilaments were manually formed by cold isostatic pressing to the dimensions of the extrusion chamber in the high-pressure Stratasys HP-3D. These billets were then extruded. Rough, green bars were made with the machine by use of a manual tool path (Fig. 16). The rough edges could be easily removed. This bar was generated at a modeling envelope temperature of 40°C; the liquefier head was heated to 60°C.

Individual rows adhered to each other and there was no separation. These materials appeared to be amenable to SFF processing.

To further develop the SFF capability for fabricating FM components, we also worked with Si_3N_4/BN feed rods that were provided by ACR. This work supported ACR's efforts to develop SFF and sinterable compositions and helped our effort because we were able to work with sufficient quantities of high-quality feedstock. Flexure bars were fabricated from the Si_3N_4/BN FM feed rod with the high-pressure head in the Stratasys 3D Modeler. These feed rods were ≈16 cm in diameter and 11 cm long. The BN layer was ≈0.635 mm thick (Fig. 17).

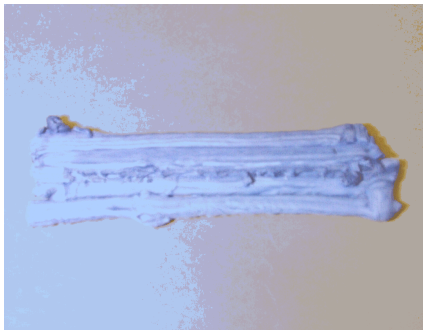

Fig. 16.
Initial as-produced green bar of FM single-core material made by SFF.

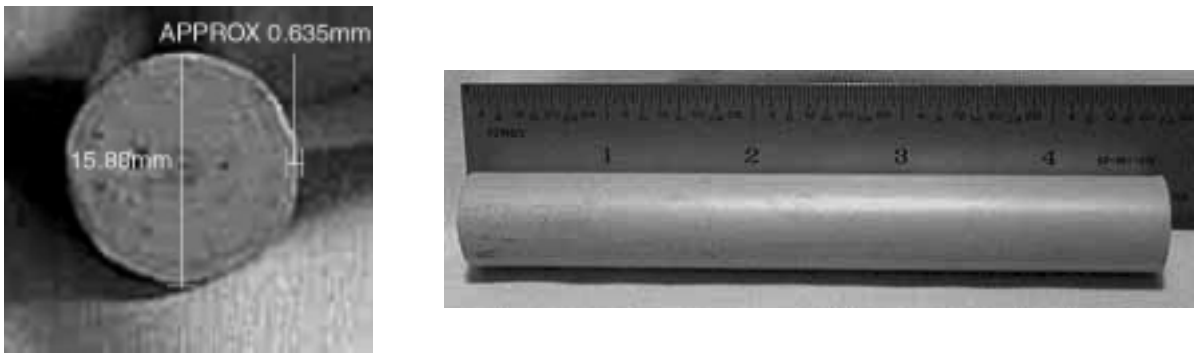

(a) (b)

Fig. 17. Photographs of an ACR-supplied Si_3N_4/BN feed rod.

The dimensions of the green Si_3N_4/BN flexure bars were ≈38 x 12.7 x 9.5 mm. Each bar consisted of a four-layer lay-up of 0/±45°/0 (Fig. 18). A nozzle diameter of 2.2 mm was used to fabricate these bars. The liquefier temperature was 130°C and the modeling envelope was kept at 70°C. The bars appeared to be dense and reasonably uniform (Fig. 19).

One of the primary concerns was how to keep a consistent interface between the Si_3N_4 and BN layers. Another, related issue with extrusion in the Stratasys was thickness of the BN layer, or more generally, of the shell layer. To address these issues, we produced a redesigned nozzle tip that incorporates the same principles as the recently redesigned head. The older tip featured a straight bore to the bottom, where it was drilled out to the desired tip dimension. The new tips feature a gradual taper from the top to the bottom of the tip (Fig. 20). This improvement should lead to a more consistent coating of the core.

After the nozzle tip was tapered, additional Si_3N_4/BN bars were made with feedstock from ACR. Three of five bars from each of three formulations were isostatically pressed before sintering. The process incorporated a 1.5-h preheat of the bars at 80°C immediately before placement in the cold isostatic press. The bars were then pressed at a pressure of ≈414 MPa.

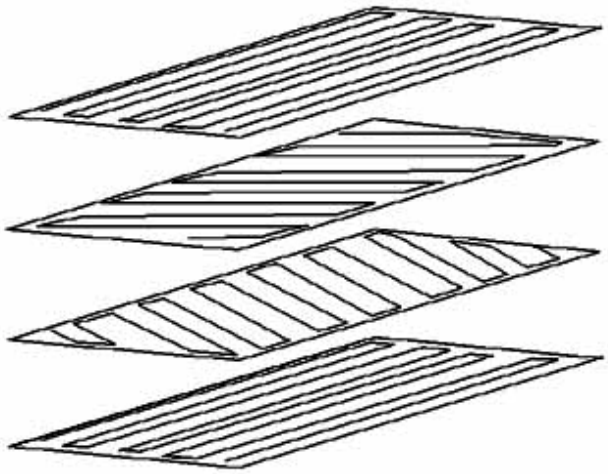

Fig. 18. Schematic diagram of the lay-up for Si_3N_4/BN bars.

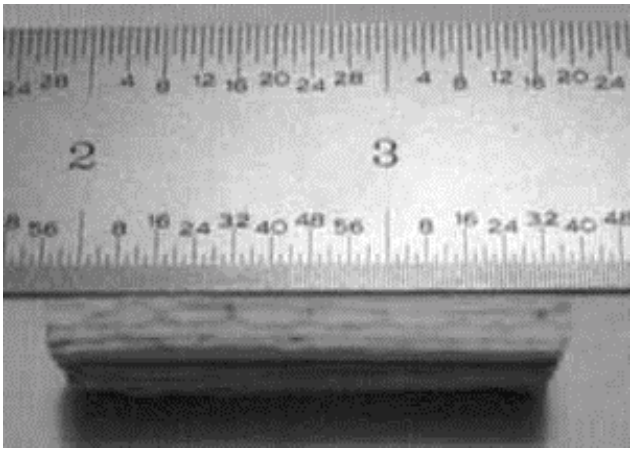

Fig. 19. Side-view photograph of Si_3N_4/BN four-layer bar.

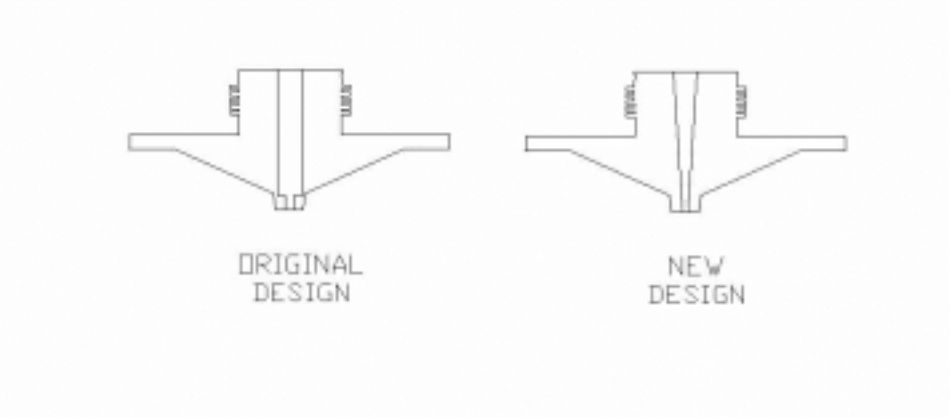

Fig. 20. Schematic diagrams of the original and new high-pressure feed tips.

Five standard-flexural-strength bars were made from each formulation. The flexure bars were made as eight-layer laminates, with a ±45° tool path. All bars were made with a 0.635-mm nozzle tip. The materials were extruded at a liquefier temperature of 100°C and a cabin temperature of 80°C. The pressure required in the high-pressure feed system to extrude the Si_3N_4/BN materials at these temperatures varied with formulation. These differences were caused by the addition of a lubricant-like additive to two of the blends, and by differences in concentration and composition of the sintering aids.

The flexure bars measured ≈4 x 4 x 35 mm in the green state (Fig. 21). ACR was responsible for heat treatment and subsequent characterization.

Fig. 21. Photograph of Si_3N_4/BN flexure bar as produced by SFF.

Although the green bars appeared to be uniform, SEM examination revealed irregularities. There was evidence of smearing of the individual cells or filaments, and the cells were not completely uniform. Each of the coextruded filaments appeared to have been compressed. This nonuniformity was thought to be induced by the SFF tool path. It was intended that some overlap occur during fabrication toeliminate voids within the part. The combination of the extent of compression and the extent of overlap may have led to the smearing and distortion. The overall microstructure of the bar could be improved substantially by use of less overlap, but with nearly the same amount of filament compression to yield a low void concentration.

The software used in the Stratasys Modeler was QUICKSLICE Version 6.1, which runs with the Windows NT operating system. A software package written by ACR to control the ACR high-pressure head was also purchased. An issue with Stratasys Quickslice 6.1, in conjunction with the modified machine, was production of complex forms that require, for example, a support structure to hold an overhang in place. The Quickslice 6.1 program was originally developed for use with a dual-head machine, which simultaneously deposits the build material and a support structure. This type of machine features two feeds, one for depositing the primary structural material and the other for depositing a water-soluble support material.

The Stratasys machine language was rewritten to recognize the existence of only one head. Solving this problem allowed a support structure created by the Quickslice 6.1 program to be fabricated with the part; thus, complex parts could be made.

As part of our SFF development work, experiments were conducted to determine whether SFF could be used to form complex, three-dimensional parts from FM materials. Si_3N_4/BN FM material produced by ACR was used first. The SFF work was performed without aid of a support material, because our unit did not have a second head for the support-generating capability. We knew before the test that this deficiency would yield less-than-optimal results.

Because turbine blades are one application in which FM materials are of interest, and because we owned a suitable CADS file, we chose to run our tests with this part. The machine parameters used were liquefier head temperature of 100°C and modeling envelope at 65°C. A 0.635-mm diameter tip was used for the material extrusion. The material was extruded with a force of ≈1500 kg. Upon visual inspection of the part (Fig. 22), it was observed that there were areas in which the cell boundary of the filament was not consistent. The edges of the blade itself were rough. This roughness was primarily caused by the fact we made the blade without using a support structure. In addition, motion-control software was rewritten to improve part uniformity.

The work with Si_3N_4/BN feedstock convinced us that SFF was a viable means to produce FMs. We then returned to fabricating $ZrSiO_4$-based FMs. The primary efforts centered on developing proper fabrication techniques to allow formation of uniform $ZrSiO_4$/$ZrSiO_4$ filaments and subsequent manufacture of flexure bars.

$ZrSiO_4$ feed rods for the SFF were fabricated by rolling a tape-cast shell around a pre-formed cylindrical core. The resulting feed rods were ≈1.63 cm in diameter and ≈8.9 cm long. A 1.27-mm-diameter nozzle was used for the high-pressure SFF. The filament was extruded with a liquefier temperature of 40°C and a cabin temperature of 28°C. The bars were fabricated in five layers, with all filaments in a 0/90° orientation.

After heat treatment, the bars were ≈51 mm long, 4.5 mm thick, and 5.5 mm wide. A small amount of warping occurred. Changes in the SFF tool path could reduce the extent of warping.

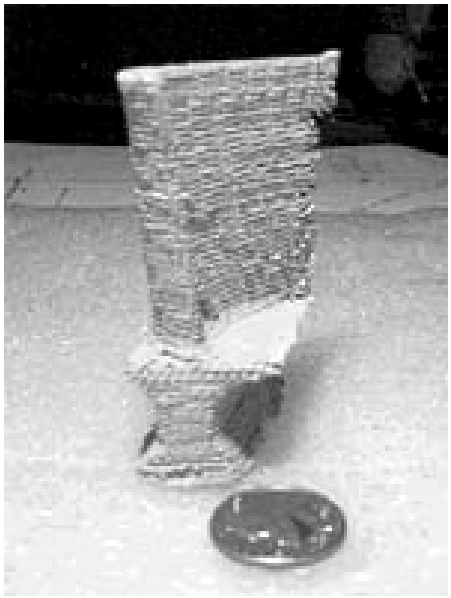

Fig. 22.
Si_3N_4/BN turbine blade made by SFF without a support structure.

Given the success in forming simple $ZrSiO_4$ bars, we undertook again the fabrication of a turbine blade. The major obstacle continued to be the forming of parts that contain overhanging edges, because the ANL Stratasys unit with the high-pressure attachment was outfitted with only a primary feed head. The blade was fabricated without significant problems, until the overhanging section of the base was reached. We also determined that the hand-rolled shell for the duplex feed rod did not provide sufficient uniformity. We, therefore, designed and had machined a new SFF die to fit the current feed rod better. The new die allowed the overall feed rod to maintain an ≈80/20 cell/cell-boundary ratio. A few parts were then fabricated from multifilament $ZrSiO_4$ feed rods.

The structure obtained from the $ZrSiO_4$ extrusion was imperfect. Significant cross-sectional distortions were observed. Solutions to this problem included tighter, more uniform packing of the individual filaments into the feed rod, and extrusion of the material at higher viscosity.

In the final stage of the SFF work, we initiated a study to determine what would be required to install a second head into the high-pressure Stratasys 3D Modeler. We had concluded that without this head, smooth uniform parts could not be reliably produced. The effort included six tasks: redesign of the carriage assembly, redesign of the carriage transport mechanism, design of the second head assembly, design of the second-head material feed system, interfacing with the control CPU, and modification of the process code that manipulates the two heads.

The 3D Modeler, as originally developed by Stratasys, featured a friction-driven, material feed system. ACR modified the material delivery system to allow extrusion of high-viscosity materials at high pressures. The proposed second head was a derivative of low-pressure Stratasys designs. Although, dual-head Modelers have been built by Stratasys, the work here represented the first time that a high-pressure head would be combined with a low-pressure head in the same SFF unit. This combination of high- and low-pressure extrusion capabilities was a unique requirement that arose from the need to extrude high-solids-loaded ceramics of the type being developed at ANL and ACR.

The design studies were completed and we concluded that the required modifications could be made. However, the second head was not built because of insufficient funds and time. Should the project be resumed, we believe that a dual-head Modeler could be assembled, and then dense, complex parts of well-controlled dimensions could be produced by SFF.

Laser Machining

Techniques were also examined to improve the as-built surface finish of SFF parts by follow on mechanical means. Three-axis milling was attempted on several

parts. Part fixtures presented an immediate challenge. It proved difficult to hold smaller parts firmly during the milling process. This difficulty drove us to focus on laser machining. Laser machining can be accomplished quickly and in situ. Much of the laser machining work was completed in cooperation with Prof. J. A. Todd of the IIT in Chicago, Illinois.

Because SFF FM materials were not available for the initial studies, we first studied the machining of SFF-produced components made of ≈30 vol.% hydroxyapatite and 70 vol.% polymer binder. In preliminary studies, a 700-W continuous-wave CO_2 laser was focused by using an eight-facet polygonal scanner and a five-axis motion-control system (Fig. 23). All machining used the TEM_{00} mode of the laser, with the electric vector oriented perpendicular to the direction of beam travel. The linear beam speed of the laser was estimated to be ≈200 cm/s.

The as-laser-machined surfaces were observed to be significantly smoother after the machining operation. No carbon residue was observed on the surface of the samples after machining. These initial studies demonstrated that ceramic parts produced by SFF could be effectively laser machined. However, to better control surface quality and depth of cut, it was necessary to optimize the linear beam speed, feed rate, and power levels. We anticipated that use of a pulsing beam instead of a continuous beam would lead to better results.

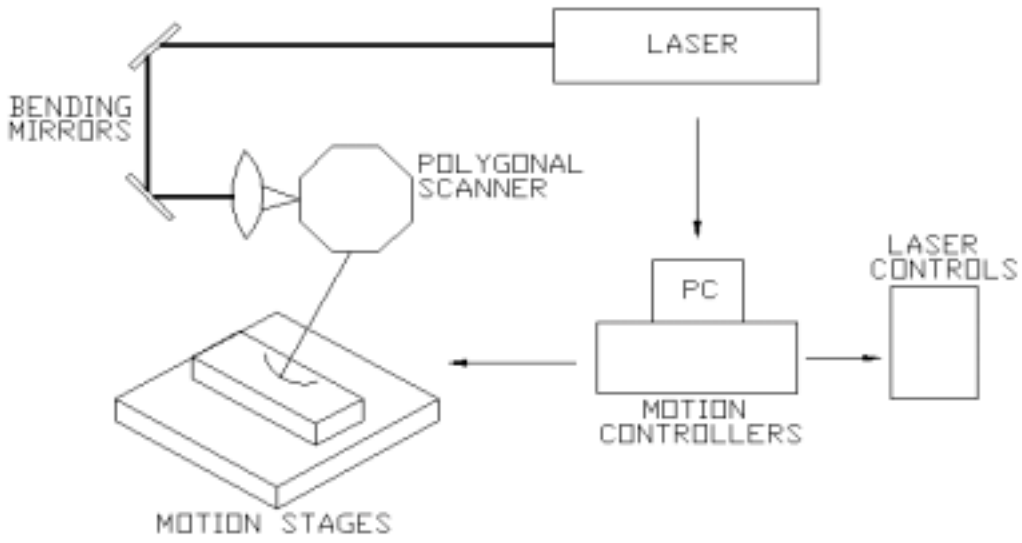

Fig. 23. Schematic diagram of the laser system used for machining studies.

With the continuous CO_2-laser system, two through-cuts were made on a green Si_3N_4/BN FM flexure bar ≈5.5 mm thick and ≈6.5 mm wide that was produced by SFF. The cuts were accomplished in four passes of the laser beam at a power of ≈700 W. The bar was positioned perpendicular to the beam path, with the focal plane of the beam being focused on the top surface. Each pass was made at a linear beam speed of 10 cm/s, with a downward focus adjustment of 0.5 mm per pass to keep the focal plane on the surface of the bar as the depth of the cut increased. Unlike the situation of cutting tricalcium phosphate bioceramics, for Si_3N_4/BN FMs, the laser beam was operated in a pulse mode, with an output of 10 pulses/mm of travel. This was done to lower the amount of debris incurred during the cutting process. Figure 24 shows a photograph of the laser-machined SFF-produced Si_3N_4/BN bar.

The first cut led to a face nearly perpendicular to the surface, with the presence of small amounts of strongly adherent debris (Fig. 25a). To lower the extent of debris, during the second cut, an air stream at ≈69 kPa was passed over the bar surface in the direction of cutting. This minimized debris formation and significantly reduced adhesion of the debris that formed (Fig. 25b).

This initial work suggested that a high-power CO_2 laser moving at high linear-beam speeds could be used to machine green Si_3N_4/BN FMs. With low-pressure air aimed at the bar in the cut direction, debris caused by cutting could be effectively minimized. Further development called for use of a five-axis, numerically controlled system, integrated with the pulsing of the laser to allow production of more advanced shapes.

In the next studies, one perimeter cut was made on a green Si_3N_4/BN FM flexure bar fabricated by SFF, and a single face of a green Si_3N_4/BN FM turbine blade base, fabricated by SFF, was finished.

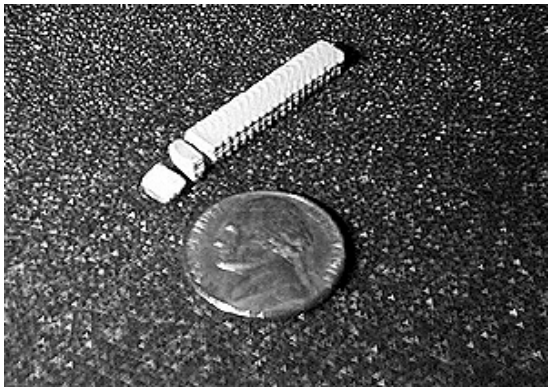

Fig. 24. Laser-machined SFF-produced Si_3N_4/BN flexure bar.

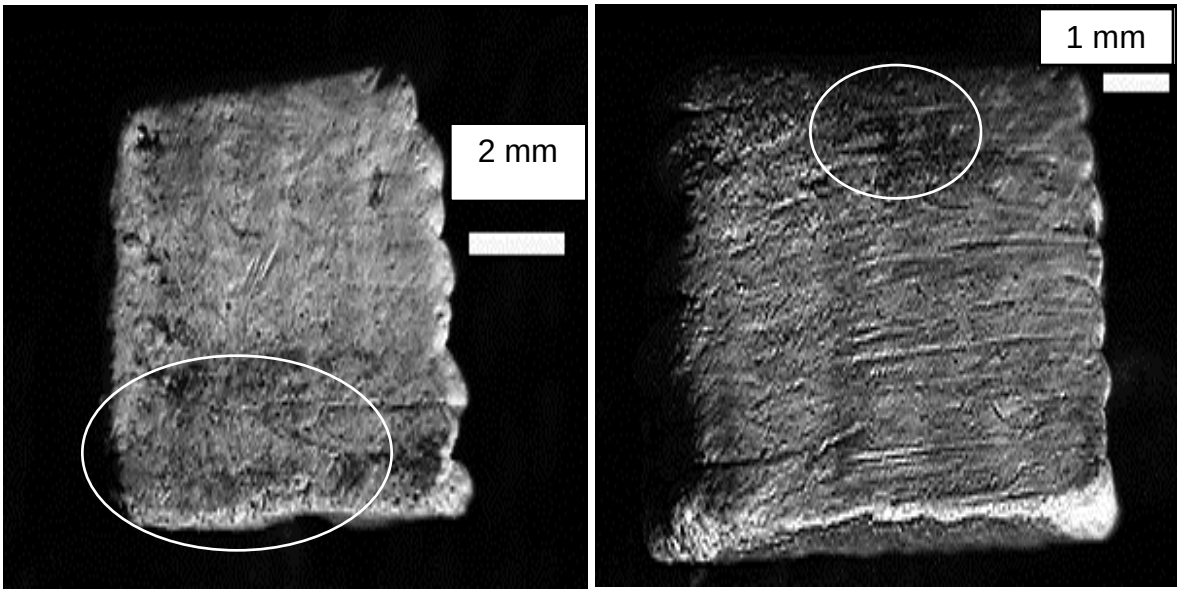

(a) (b)

Fig. 25. Photographs of laser-machined SFF-produced Si_3N_4/BN bar: (a) small, strongly adherent debris (circle) at bottom center of first cut face and (b) on second cut face, minimal formation of weakly adherent debris (circle).

The perimeter cut was accomplished in two consecutive passes of the laser beam at a beam power of ≈700 W. The work piece was positioned perpendicular to the beam path, with the focal plane of the beam on the top surface. Each pass was made at a linear-beam speed of 10 cm/s, with a down focus of 0.5 mm per pass to keep the focal plane on the surface of the work piece as the depth of the cut increased. The laser beam was in pulse mode with an output of 10 pulses/mm of linear travel.

For the surface finishing, the laser beam was scanned continuously with the aid of the eight-faceted polygonal scanner, with a beam velocity of 200 cm/s and a beam power of ≈700W. The focal plane was set at the top edge of the sample (Fig. 26). Significant improvements in surface finish were effected.

The laser-machining studies unequivocally established the efficacy of this approach to cutting or finishing surfaces. We recommend that future efforts extend characterization of the machined surfaces and determine the effects of the machining on, primarily, microstructure and mechanical properties.

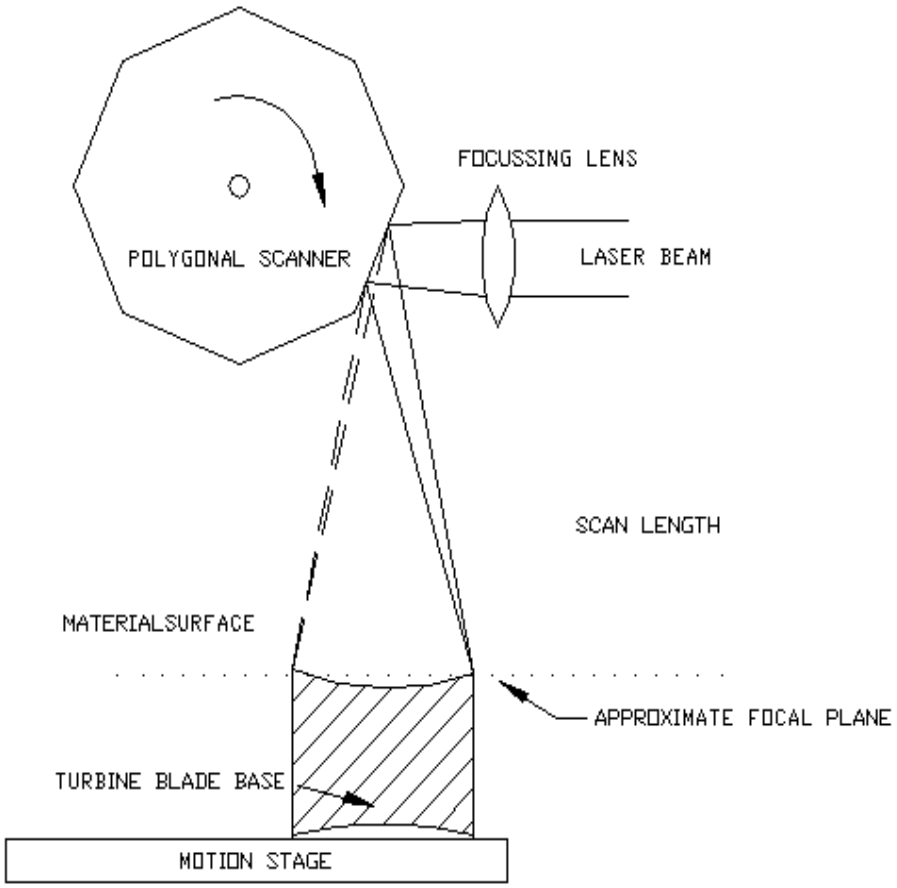

Fig. 26. Schematic illustration of how the polygonal scanner directs a high-velocity laser beam over the base of the turbine blade.

2.2 Strong and Tough Fibrous Monoliths

Proof of concept for the viability of oxide FMs was provided by the $ZrSiO_4/ZrSiO_4$ system. The mechanical properties of this system were, however, not exceptional. We identified three paths to follow in attempts to improve the mechanical performance of oxide FMs:

1. Fabricate FMs that contain cell boundaries or interphases that do not require the very large grain sizes of the $ZrSiO_4$ cell boundaries;

2. Fabricate FMs with cells that are inherently stronger, especially at elevated temperature, than $ZrSiO_4$;

3. Fabricate FMs that contain residual stresses that are distributed so as to maximize flaw tolerance.

To follow the first two paths, work was initiated at UIUC under Prof. W. M. Kriven. A summary of the UIUC accomplishments is provided in this section.

2.2.1 Development of New, High-Toughness Oxide Composites

Yttrium Aluminum Garnet as a Cell Material

$Y_3Al_5O_{12}$ (YAG) is a good high-temperature material with good creep resistance. However, pure YAG has exhibited a low strength of ≈102 MPa after sintering at 1800°C for 3 h (c.f., K. Keller et al., Ceram. Eng. Sci. Proc. 11 [7-8] (1990) 1122). Al_2O_3-YAG composite systems were, therefore, developed for use in high-temperature oxide FMs.

YAG-Al_2O_3 eutectic composites with strengths to 373 MPa have been produced (c.f., T. Mah et al., Ceram. Eng. Proc. 11 [9-10] (1990) 1617). However, the process for making the eutectic composites is complicated, and so an attempt was made to increase the strength of YAG by adding particulate Al_2O_3.

Amorphous YAG was synthesized by a proprietary solution-polymerization method and calcined at 800°C for 1 h. Samples were then cold isostatically pressed at ≈420 MPa and sintered under various conditions. Density, shrinkage, and three-point bend strengths are summarized in Table 4.

Table 4. Properties of YAG as a function of sintering temperature and time

Sintering schedule	Density (g/cm^3) and (% theoretical)	Sintering shrinkage (%)	Three-point bend strength (MPa)
1600°C / 5 h	2.80 (61.6)	5.32	79.7 ± 10.9
1600°C / 10 h	—	—	—
1650°C / 10 h	4.36 (95.92)	—	188.2 ± 13.9

The density of the YAG specimens increased from ≈62 to ≈96% of theoretical density after changing the sintering conditions from 1600°C for 5 h to 1650°C for 10 h.

The properties of specimens prepared from crystalline Alcoa A16-SG Al_2O_3 were also investigated as a function of sintering temperature and time (Table 5). Decreases in density and strength were attributed to increased grain size with increasing sintering temperature.

Table 5. Properties of Alcoa A16-SG Al_2O_3 as a function of sintering temperature and time

Sintering schedule	Density (g/cm^3) and (% theoretical)	Sintering shrinkage (%)	Three-point bend strength (MPa)
1600°C / 5 h	3.87 (97.6)	15.34	396 ± 37
1600°C / 10 h	3.87 (97.6)	15.74	344 ± 12
1650°C / 10 h	3.81 (95.9)	16.25	323 ± 21

We first fabricated specimens of 30 vol.% Al_2O_3/70 vol.% YAG. The average strength of this composite was 227 ± 27 MPa with sintering at 1600°C for 5 h. The value increased to 313 ± 14 MPa after sintering at 1650°C for 10 h. The latter value indicates an increase in strength of ≈66% when compared with that of pure YAG. SEM studies indicated that the average grain size of both the Al_2O_3 and the YAG was ≈1 μm.

For comparison, amorphous Al_2O_3 was prepared by the solution polymerization method and calcined at 800°C for 1 h. The strength of bars from amorphous Al_2O_3 was 10–30% higher than that of bars from crystalline Al_2O_3. Amorphous Al_2O_3 was thus used to fabricate Al_2O_3/YAG particulate composites.

Amorphous YAG and crystalline YAG powder were formed after calcination at 800 and 1300°C, respectively. Appropriate amounts of aluminum nitrate and yttrium nitrate were mixed in solution; this mixture formed the Al_2O_3/YAG composite during the calcination and sintering processes. For comparison, other composites were made by ball-milling crystalline A16SG Al_2O_3 and YAG powders (in amorphous or crystalline form) for 24 h. The Al_2O_3 content was either 30 or 50 vol.%.

All of the pellets were cold isostatically pressed at ≈390 MPa and then sintered under various conditions. Densities were measured by Archimedes' method. Sintering shrinkages were measured for the three orthogonal directions. Three-point bending tests were conducted on 3–5 samples per sintering condition.

The densities of the amorphous and crystalline YAG powders were 3.46 and 4.45 g/cm^3, respectively. During sintering, the amorphous powders exhibited approximately twice the shrinkage of the crystalline powders. The maximum strength observed was ≈244 MPa (bars from crystalline powder, sintered at 1650°C for 10 h).

The properties of the various composites are listed in Table 6. For a given set of sintering conditions, all of the 50 vol.% Al_2O_3 composites exhibited higher strengths than the 30 vol.% Al_2O_3 composites. All of the mechanically mixed composites made from the crystalline YAG bloated under sintering conditions of 1750 and 1800°C for 5 h. Mechanical-mixture composites of composition 50 vol.% A16SG/50 vol.% crystalline YAG exhibited higher strengths than the 50 vol.% Al_2O_3/50 vol.% YAG in-situ composites under sintering conditions of 1600°C for 5 h and 1650°C for 10 h. The strength of the 50 vol.% A16SG/50 vol.% crystalline YAG mechanical-mixture composites decreased dramatically with sintering at >1700°C, but the 50 vol.% Al_2O_3 /50 vol.% YAG in-situ composites retained high strengths with sintering at 1700, 1750, and 1800° for 5 h.

The 50 vol.% Al_2O_3/50 vol.% YAG in-situ composite sintered 5 h at 1700°C exhibited the highest average strength of 361 MPa. This strength is comparable to that of Al_2O_3/YAG eutectic composites grown from the melt. However, our processing procedure is simpler. The 50 vol.% Al_2O_3/50 vol.% YAG in-situ composite is, therefore, a candidate cell material for high-temperature FMs.

Table 6. Three-point bending strengths (MPa) of Al_2O_3/YAG composites under various sintering conditions; starting powders were amorphous (Am) or crystalline (Cry)

Composite	1600°C/5h	1650°C /10h	1700°C /5h	1750°C /5h	1800°C /5h
30% A16SG/ 70% Am YAG	217	–––	282	268	149
50% A16SG/ 50% Am YAG	314	291	–––	–––	–––
30% A16SG/ 70% Cry YAG	202	249	214	Bloated	Bloated
50% A16SG/ 50% Cry YAG	332	354	241	118 (Bloating)	Bloated
30% Al_2O_3/ 70% YAG in-situ	76	–––	271	254	178
50% Al_2O_3/ 50% YAG in-situ	202	330	361	336	240

Microstructures were examined by SEM and grain sizes were measured by the linear-intercept method. The grain size of the amorphous YAG was 9.5 μm after heat treatment at 1800°C for 5 h. The grain size of the crystalline YAG specimens was smaller than that of amorphous YAG specimens. The grain sizes of the Al_2O_3 and YAG in the composites were smaller than those of the single phases of Al_2O_3 and YAG because of their restrained growth in the composite. When compared with the Al_2O_3 grains, the YAG grains in the composites remained ≈3 μm, even after sintering at 1800°C for 5 h. The 50 vol.% Al_2O_3/50 vol.% YAG in-situ composites showed smaller Al_2O_3 and YAG grains when compared with those of the 50 vol.% A16SG/50 vol.% YAG mechanical-mixture composites. Figure 27 shows the microstructure of the 50 vol.% Al_2O_3/50 vol.% YAG in-situ composite that was heat treated at 1700°C for 5 h. The microstructure was dense, and the grain size of the Al_2O_3 and YAG phases was homogeneous.

In summary, specimens made from amorphous YAG powders and crystalline YAG powders experienced linear shrinkages that ranged from 13.3 to 23.1% and from 7.06 to 13.1%, respectively. Samples made from the crystalline YAG powder reached a maximum three-point bending strength of 244 MPa, with sintering at 1650°C for 10 h. The 50 vol.% Al_2O_3/50 vol.% YAG in–situ composites reached a maximum average three-point bending strength of 361 MPa after sintering at 1700°C for 5 h. Moreover, this type of composite sustained its strength with sintering at 1700, 1750, and 1800°C for 5 h. Grain-size measurements indicated restrained grain growth of the Al_2O_3 and YAG phases in the composites.

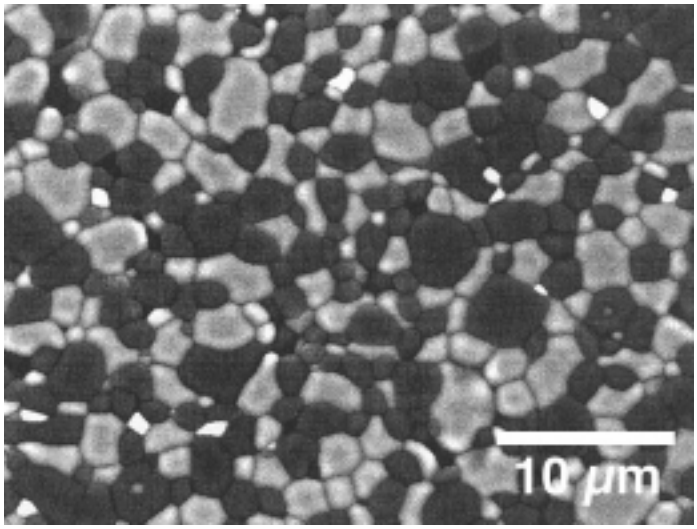

Fig. 27. SEM photomicrograph of 50 vol.% Al_2O_3/50 vol.% YAG sintered at 1700° for 5 h (darker phase is Al_2O_3 and lighter phase is YAG).

Leucite Composite as Cell-Boundary Material

Use of leucite ($KAlSi_2O_6$) in FMs was examined in work that was performed at UIUC. Leucite exhibits tetragonal symmetry, with space group $I4_{1/a}$ at room temperature. It undergoes a phase transformation to a cubic phase of space group Ia3d at 620–690°C. A total 5.27% volume contraction, plus thermal contraction, should accumulate in the leucite phase on cooling through the transformation and then to room temperature. The linear thermal expansion coefficient of the low-temperature tetragonal phase is ≈20–25 x 10^{-6} K^{-1}, whereas the linear thermal expansion coefficient of the cubic phase is ≈11.7–12.8 x 10^{-6} K^{-1}. The high thermal expansion coefficient of leucite has stimulated its use in toughening of ceramic composites via a crack-deflection mechanism.

The goals of the FM work were to make a particulate composite of Al_2O_3 and leucite and to investigate the effects of leucite on the resultant mechanical and microstructural properties of the composite. The aim was to assess the effectiveness of an Al_2O_3-leucite composite as a cell-boundary phase in oxide FMs.

Leucite powder was synthesized by a proprietary solution-polymerization method. Potassium nitrate, aluminum nitrate, and Ludox AS-40 were used as source materials. Alcoa A-16SG was used as the Al_2O_3 powder. Mixtures of 5, 10, 20, 30, 50, 70, 80, and 90 vol.%, calcined, amorphous leucite plus Al_2O_3 were prepared by ball milling for 24 h. Resultant powders were formed into bars by pressing and then sintering at 1600°C for 3 h under a leucite atmosphere.

Flexural strength was measured in four-point-bending tests. The specimen size was ≈1.5 x 2 x 25 mm. The supporting span was 20 mm and the loading span was 10 mm. Fracture toughness (K_{IC}) was measured by an indentation method. Thermal expansion was also measured. The microstructures of the composites were examined by X-ray diffraction and SEM.

The X-ray diffraction results suggested that stable Al_2O_3-leucite composites of several compositions could be produced. SEM indicated no formation of a third phase.

The results of the four-point-bending and indentation tests are summarized in Table 7. The flexural strengths of composites decreased with addition of up to 50 vol.% of leucite. However, composites that contained 70 and 80 vol.% of leucite exhibited higher strengths than the composites with 50 vol.% leucite. The composite composed of 90 vol.% leucite exhibited low strength because of the presence of relatively large pores. The bending strength of pure leucite was 78.5 ± 20.5 MPa. The 10-vol.% leucite composite exhibited the highest K_{IC} value.

Table 7. F*lexural strength and fracture toughness as a function of leucite content*

Leucite (vol.%)	Flexural Strength (MPa)	K_{IC} (MPa-$m^{0.5}$)
0	416 ± 23	3.3 ± 0.3
5	328 ± 44	2.4 ± 0.3
10	296 ± 46	4.0 ± 0.6
20	229 ± 35	2.2 ± 0.5
30	175 ± 19	2.0 ± 0.2
50	42 ± 6.6	-
70	170 ± 20	-
80	157 ± 19	-
90	82 ± 15	-
100	79 ± 21	-

The average α value of pure Al_2O_3 was ≈8 x 10^{-6} K^{-1}. The α value of a 90 vol.% Al_2O_3/10 vol.% leucite composite was ≈10 x 10^{-6} K^{-1}. The increased expansion and higher toughness with leucite additions implied that Al_2O_3/leucite may be of use in FM structures.

$AlPO_4$ as a Cell-Boundary Material

Work has focused on use of $AlPO_4$ as a candidate interphase material because of its low reactivity and sinterability. For example, after 10 h at 1600°C, it remained porous. To assess the efficacy of $AlPO_4$ as a cell boundary, mullite/$AlPO_4$ laminates were made by tape casting. Slurries contained ≈25 vol.% powder, 58 vol.% methyl ethyl ketone/ethanol solvent, 6 vol.% polyvinyl butyrol binder, 5 vol.% polythylene glycol and 6 vol.% dibutyl phthalate plasticizers, and 1 vol.% phosphate ester dispersant. The powders and solvent were ball-milled for 48 h, and then the remaining constituents were added and the mixture was ball-milled for another 24 h. The slurries were then de-aired. Tape casting was conducted with a first doctor blade opening of 600 μm and a second opening of 300 μm. The casting rate was 1 cm/s. Figure 28 shows an SEM photomicrograph of a laminated composite that was composed of five layers of mullite and one layer of $AlPO_4$. The interfaces between the two phases were well bonded.

To investigate the effects of mullite layer thickness on the strength of the laminate, the ratio of mullite layers to $AlPO_4$ layers was 1, 3, 5, or 7. All of the laminates exhibited crack deflection and noncatastrophic failure (Figs. 29 and 30). The strengths in three-point bending were 21, 45, 31, and 39 MPa for the 1-, 3-, 5-, and 7-mullite-layer laminates, respectively.

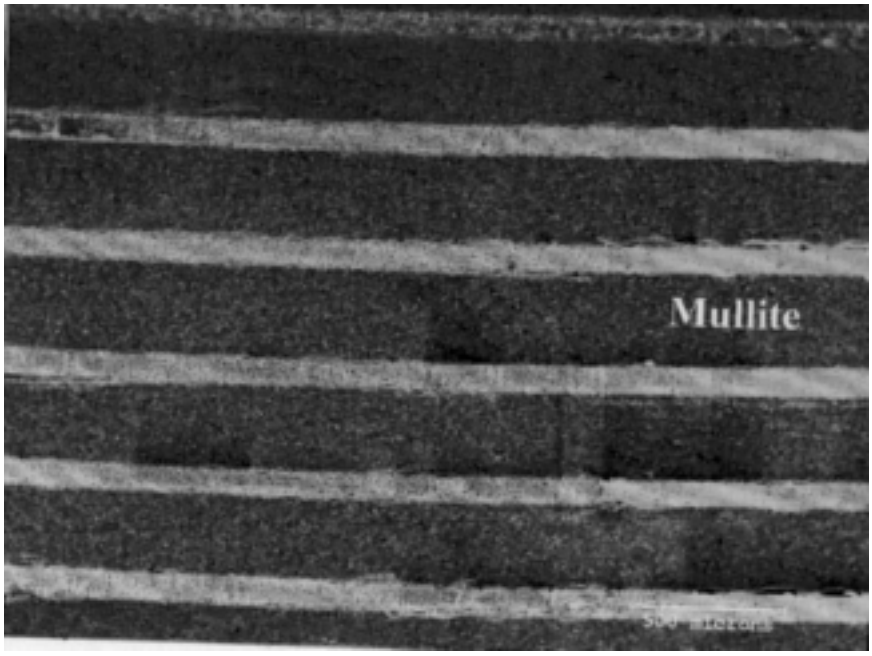

Fig. 28. SEM photomicrograph of a mullite/$AlPO_4$ laminate.

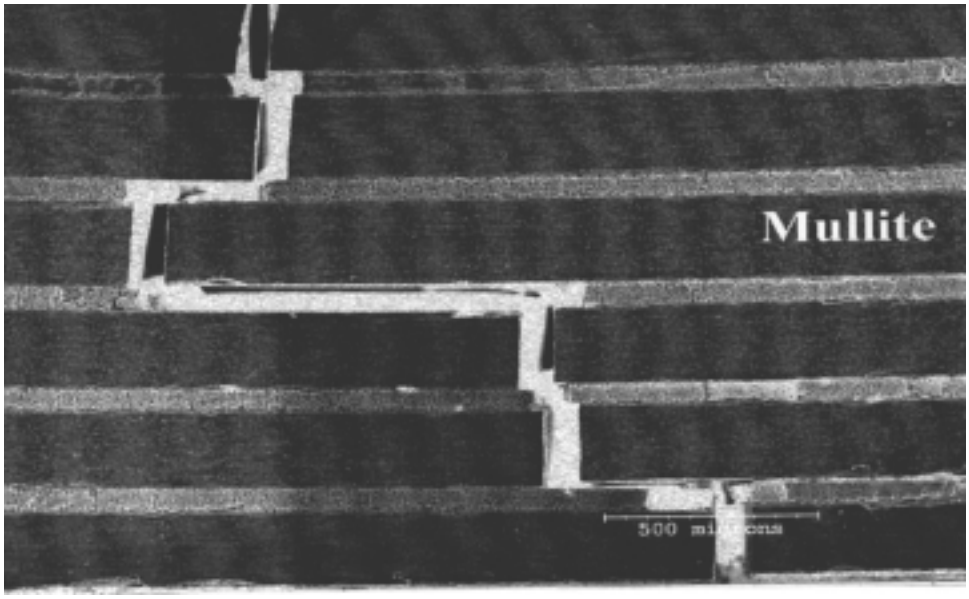

Fig. 29. SEM photomicrograph of crack path in 5-to-1 mullite/$AlPO_4$ laminate.

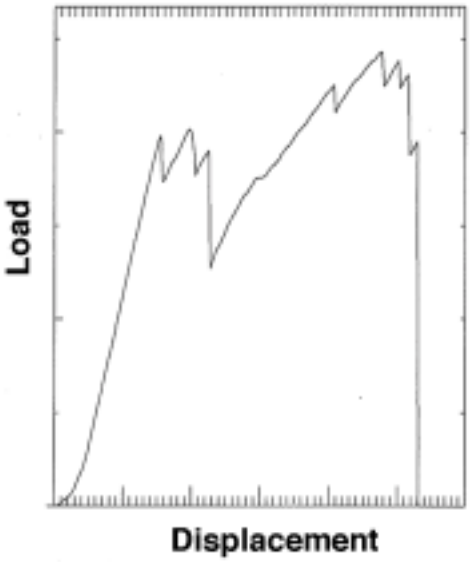

Fig. 30.
Representative three-point-flexure data (arbitrary units) for 5-to-1 mullite/$AlPO_4$ laminate; graceful failure is evident.

Addition of mullite to the $AlPO_4$ phase did not increase crack deflection, but 30 vol.% mullite within the $AlPO_4$ layer did increase strength to 77 MPa.

2.2.2 Fibrous Monoliths that Contain Novel Cell Boundaries

Mullite/$AlPO_4$ Fibrous Monoliths

Based on the multilayer results, we decided to fabricate FMs from mullite and $AlPO_4$ without addition of another powder to the $AlPO_4$. The FM was made with EVA binder by ram extrusion. In the FMs, the $AlPO_4$ phase remained porous and bonded to the mullite (Fig. 31). The FMs exhibited clear evidence of crack deflection and graceful failure (Fig. 32).

Fibrous Monoliths that Contain Platelet Al_2O_3

A new mechanism for debonding at a weak interphase in an all-oxide composite was developed. It involved the use of Al_2O_3 platelets that were 10–15 µm or 5–10 µm in diameter by ≈1 µm thick (Fig. 33). The platelets constrained sintering, leading to permanent porosity. Laminated composites with both mullite and Al_2O_3 matrices were fabricated first, and subsequently, Al_2O_3 FMs in a triple layer arrangement of core/interphase/matrix. In the laminated systems, intimate mixing of strong-vs.-tough microstructures was tailored by the matrix-to-interphase thickness ratio. Load-vs.-deflection curves clearly demonstrated characteristics of graceful failure and notable improvement in the work of fracture (WOF). SEM observations of crack paths confirm the viability of platelets in permanently porous debondable interphases at elevated temperatures in air.

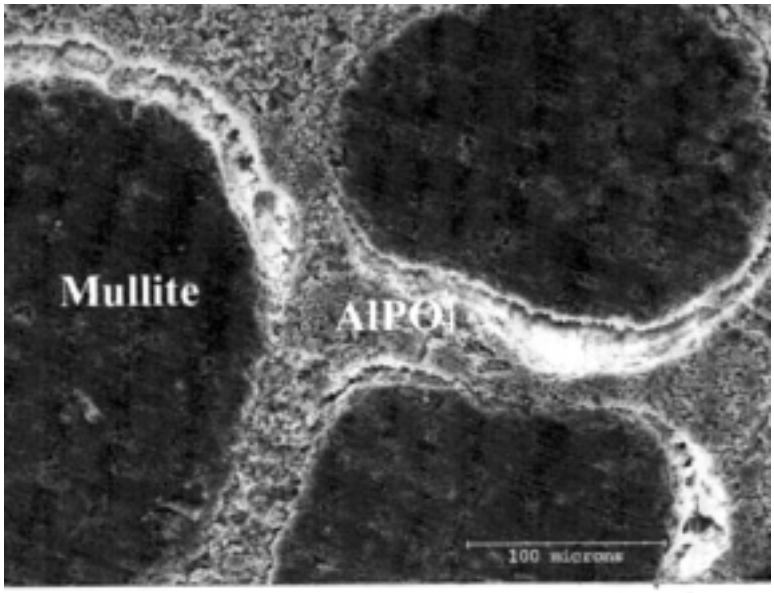

Fig. 31. SEM photomicrograph of mullite/$AlPO_4$ FM.

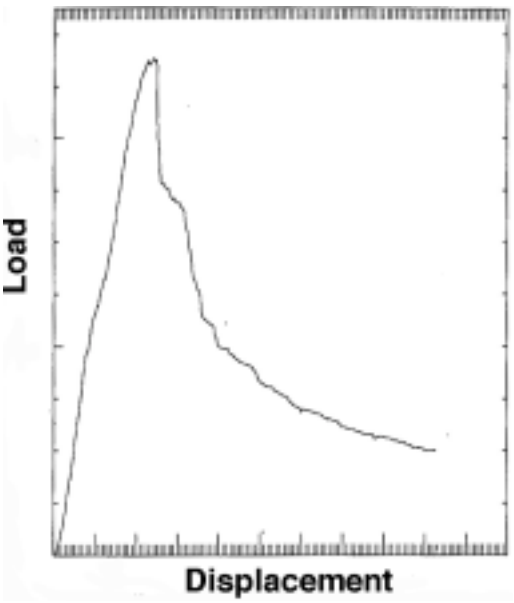

Fig. 32.
Representative stress/strain curve (arbitrary units) for mullite/$AlPO_4$ FM.

A suitable mixture of Al_2O_3 platelets and ceramic powder should be sufficiently weak and porous to be able to deflect a crack along the interphase (Fig. 34). This crack-deflection mechanism should be essentially independent of temperature. It can function, for example, at up to ≈1700°C in Al_2O_3-rich mullite or nearly 2000°C in a suitable matrix such as YAG or nickel aluminate.

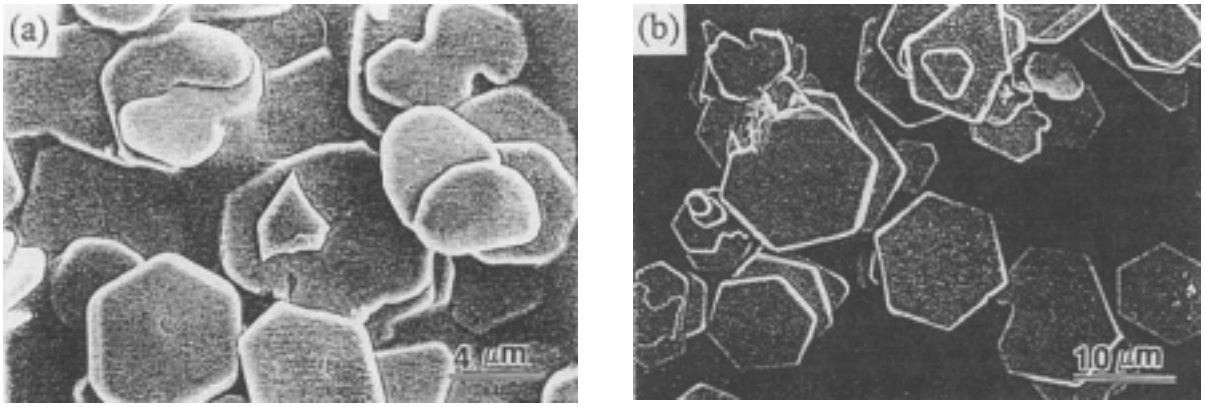

Fig. 33. SEM photomicrographs of (a) 5–10 and (b) 10–15 μm Al_2O_3 platelets.

In this work, bars were fabricated, and three-point flexural testing at room temperatures was performed. The apparent WOF was obtained by dividing the area under the load displacement curve by the cross-sectional area of the sample. The microstructures of the platelet powders, surfaces of the sintered samples, and various fracture surfaces were observed by SEM.

The Al_2O_3 platelets were randomly oriented and clearly showed an unsintered, porous microstructure. However, the interfacial region between the mullite matrix and the platelet phase was relatively dense. After fracture testing, crack deflection along the porous region at the center of the interphase was observed. Results indicated that flexural strength increased with the mullite content of the interphase. This was attributed to a denser, albeit still porous microstructure formed during sintering. However, the strength of the laminate that contained no mullite powder in the interphase was rather low.

It was noticed that the WOF at room temperature decreased for specimens with >5-vol.% additions of mullite (despite thicker interphases, and hence more likelihood crack deflection along the interphase). This implied that at room temperature, interphases with >5 vol.% mullite were not sufficiently weak for crack deflection to occur. In the 3-vol.%-interphase mullite specimen, crack deflection occurred along the weak Al_2O_3 platelet interphase, despite the fact that interphase layers were relatively thin (Fig. 35). These observations implied that the crack deflection is probably more strongly dependent on the microstructure of the porous interphase than on the thickness of the interphase. In general, as the matrix thickness increased, strength and WOF values increased (representative data shown in Fig. 36).

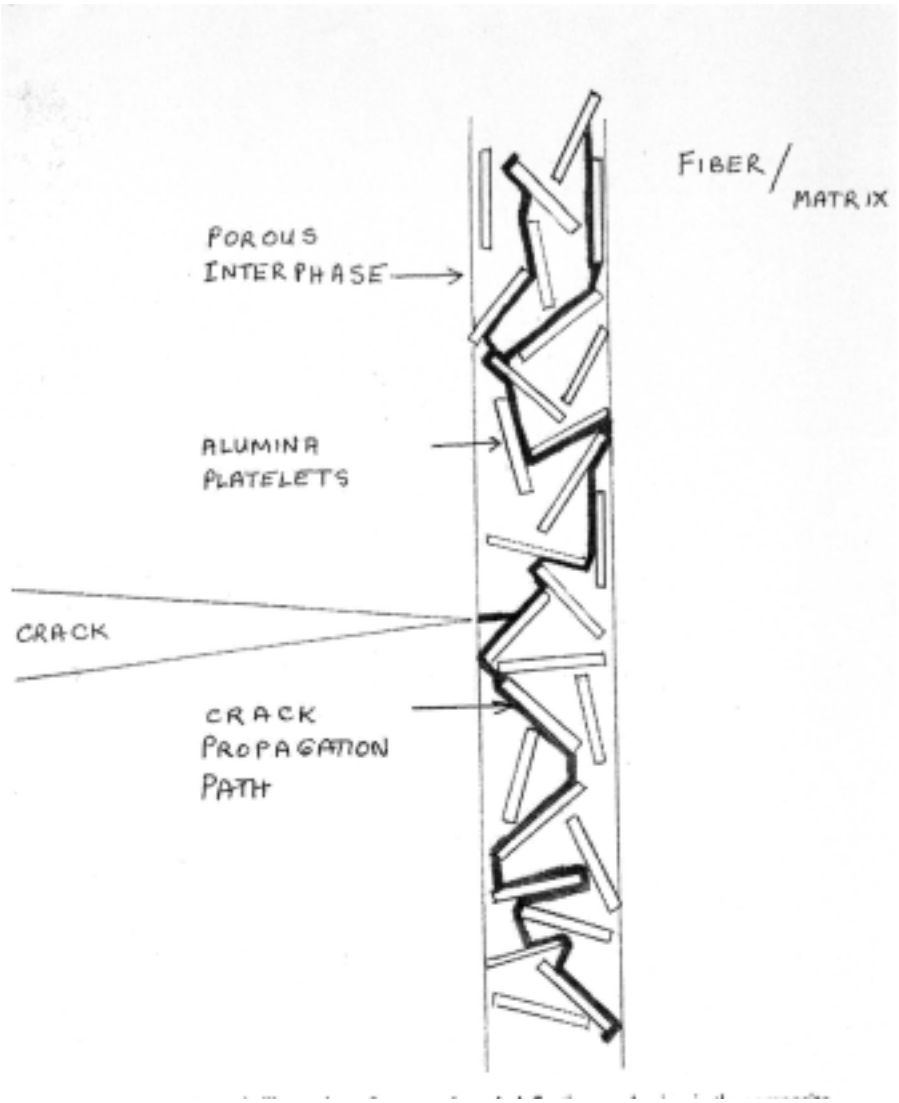

Fig. 34. Schematic illustration of crack deflection in a composite that contains a weak interphase composed primarily of Al_2O_3 platelets.

To make a tough, flaw-tolerant FM, the results from the laminate study were applied to the fibrous design. An Al_2O_3 matrix and 5–10 μm Al_2O_3 platelets were selected. A typical microstructure of the as-sintered FM is shown in Fig. 37. The discontinuous Al_2O_3-platelet boundaries are clearly revealed.

The strength and WOF values were increased slightly, compared with those of the alumina-matrix laminates. In contrast to the fracture curves of the laminates, the FMs retained significant load-bearing capacity after the initial step-wise load drops (Fig. 38). Fractured specimens exhibited nonbrittle fracture surfaces with fibrous structures. Pulled-out Al_2O_3 cores were observed.

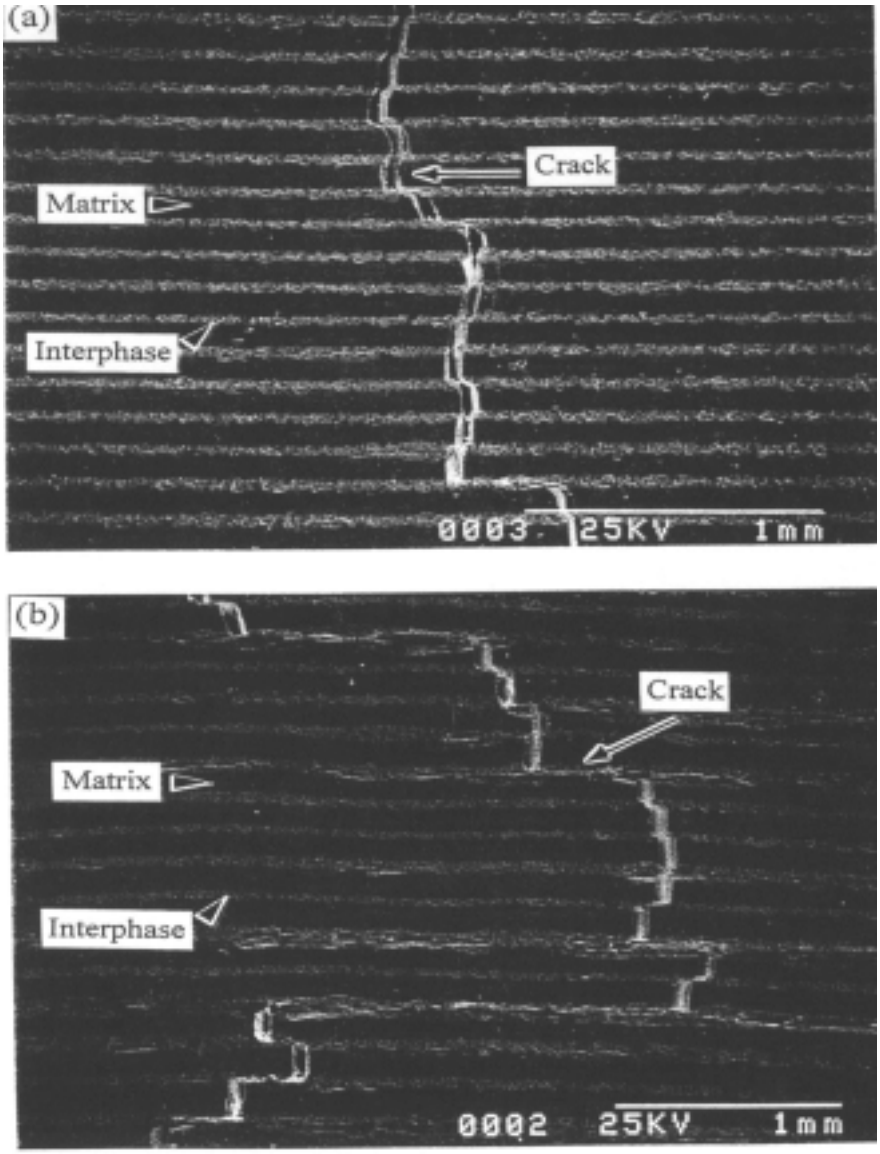

Fig. 35. SEM photomicrographs of laminates with (a) 5 and (b) 3 vol.% mullite; crack deflection is much more pronounced in the latter.

In summary, an effective mechanism for interphase debonding in an all-oxide composite system was exploited. It was based on engineering a suitably weak interphase through the use of relatively unsinterable Al_2O_3 platelets. The strength of the interphase could be adjusted by minor additions of matrix powders on the order of 1–3 vol.%. Both laminated composites of mullite and Al_2O_3 and Al_2O_3 FMs consisting of a triple layer core / interphase / matrix arrangement were fabricated. Preliminary mechanical data and SEM observations indicated that this structure is viable for high-temperature applications in which oxidation resistance is needed.

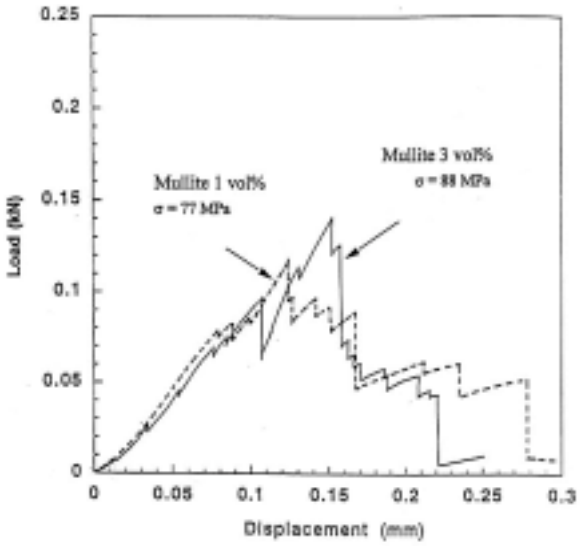

Fig. 36.
Load-deflection of mullite-matrix laminates for two mullite loadings in interphase; 10–15 μm Al_2O_3 platelets and ≈5:1 thickness ratio for mullite:interphase.

2.3 Strong, Flaw-Tolerant Fibrous Monoliths

The FMs discussed in Sections 2.1 and 2.2 share a common trait. For all of them, strength is approximately a rule of mixtures, in which the volume fraction of cell phase establishes the strength of the FM. To increase FM strengths, we examined the use of favorable residual stresses introduced during cooling from the sintering temperature. Two configurations were envisioned:

1. A new architecture, which most closely emulates that of current FMs, was to consist of a weak matrix (essentially the continuous cell-boundary phase of current FMs), in which would be embedded duplex filaments. The sheath of each filament would be in compression and the core, in tension. These FMs should exhibit higher strengths because of higher-strength cells.

2. A new architecture, which modifies recently developed multilayers, was to consist of strong cells under a tensile residual stress and a continuous cell boundary under a large compressive residual stress. Work at, for example, UCSB under Prof. F. F. Lange has demonstrated that compressively stressed layers can arrest propagating cracks and suitably designed multilayers in flexure can exhibit fracture strengths that are independent of surface flaws (c.f., M. Rao et al., Science 286 (1999) 102). Adapting this concept to FMs should allow fabrication of parts that are strong and highly flaw tolerant to stresses within the plane of the part, not perpendicular to the plane. This stress state is the most common in service.

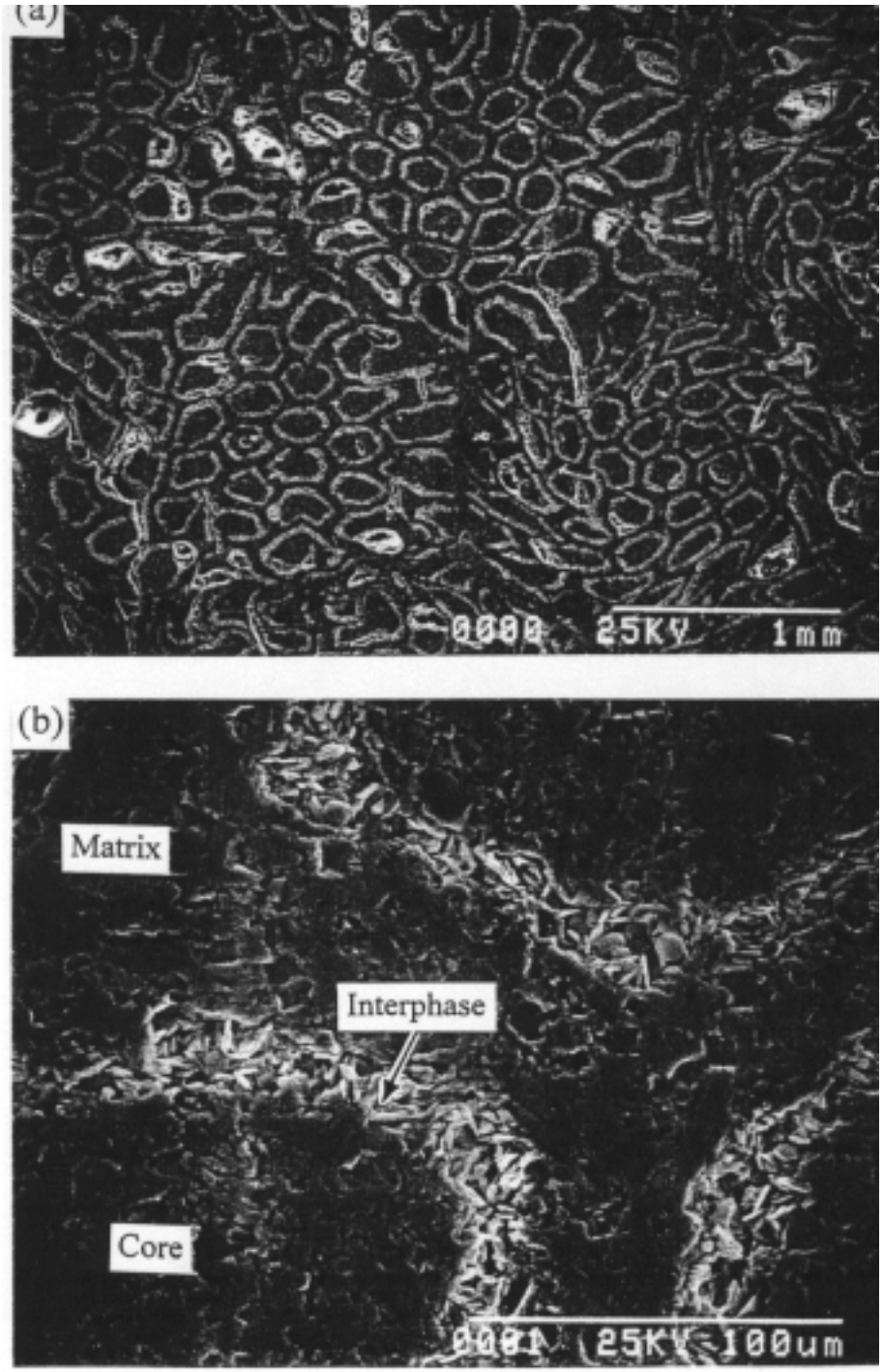

Fig. 37. SEM photomicrographs of an as-sintered Al_2O_3 FM: (a) short transverse cross section and (b) higher-magnification view of (a).

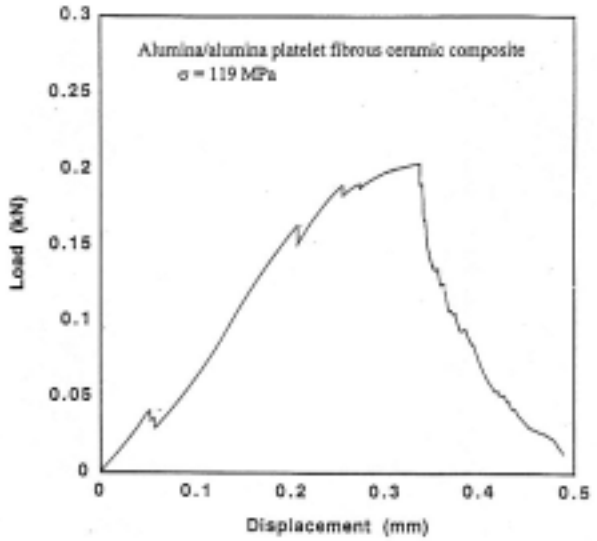

Fig. 38. Typical load/displacement data for Al_2O_3/Al_2O_3 platelet FM.

Work at ANL established that mullite, Al_2O_3, and Y_2O_3-stabilized ZrO_2 (YSZ; the YSZ contained 3 mole% Y_2O_3) particulate composites with dense, fine-grained, uniform microstructures can be made. Work at UCSB under Prof. Lange demonstrated that the residual stresses required for crack arrest could be created in mullite/Al_2O_3 composites. We therefore adopted two approaches to developing these new FMs. At ANL, three-component FMs that incorporated a weak matrix were fabricated from mullite/Al_2O_3 (MTA) and YSZ/mullite (ZTM). YSZ/Al_2O_3 (ZTA) composites were also studied. At UMR, working in collaboration with UCSB, two-component, mullite/Al_2O_3 FMs that incorporated a strong, compressively stressed cell boundary were attempted.

Results from these efforts are summarized below. Although significant progress was made, because these projects were begun relatively late in the program, we did not achieve our goal of producing FMs with enhanced strength.

2.3.1 YSZ/Al_2O_3–YSZ/Mullite Composites

Work to produce ZTA-ZTM-MTA composite systems required basic sintering studies; design of appropriate forms, based on calculations of thermally induced residual stresses; production of new filaments; and fabrication and characterization of prototype FMs. Progress was made in each of these tasks.

Sintering of ZTA, ZTM, and MTA

Sintering studies focused on compositions of ZTA with concentrations of up to 50 vol.% YSZ, ZTM with concentrations of up to 50 vol.% YSZ, and MTA with compositions of up to 80 vol.% mullite. Figure 39 graphically summarizes the

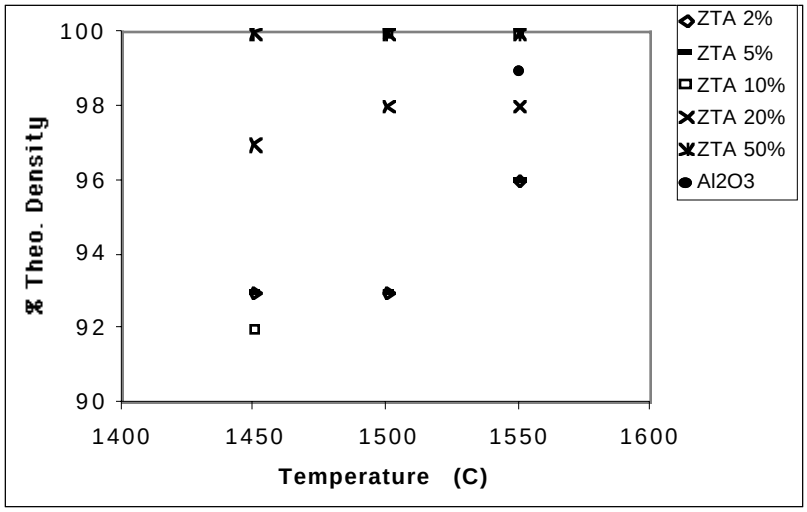

Fig. 39. Density based on rule of mixtures vs. sintering temperature for sintering time of 3 h for various ZTA composites (vol.% of YSZ in Al_2O_3).

effects of sintering temperature on the various compositions of ZTA for sintering for 3 h in air. At least 10 vol.% YSZ was needed to produce near fully dense materials and to begin to pin grain growth in the Al_2O_3 (Fig. 40).

ZTM compositions of 5, 10, and 20 vol.% YSZ were initially sintered at various temperatures for 3 h (Fig. 41); 50 vol.%/50 vol.% composites were prepared later. Sintering in air at 1550°C for 3 h produced fully dense specimens. The microstructure of all of the specimens consisted of fine grains with a uniform distribution of the YSZ (Fig. 42). No reaction between the two phases was observed.

MTA composites with up to 50 vol.% mullite that were sintered for 3 h achieved full density at 1600°C. For the composite that contained 80 vol.% mullite, full density was not achieved even at 1650°C, although the density was considerably higher than that of pure mullite (Fig. 43). Attempts to sinter MTA (80 vol. % mullite) at 1600°C showed no increase in density for up to 15 h at temperature. At least 10 vol.% mullite was needed to significantly reduce grain growth in the Al_2O_3. The larger concentrations of mullite (50 and 80 vol.%) produced very fine microstructures that were not significantly affected by sintering time at 1600°C. Sintering of the MTA 50 vol.% mullite at 1550°C for 12 h produced fully dense specimens with no apparent effect on the microstructure (Fig. 44).

The sintering studies clearly revealed that the composites that contained YSZ were the most tractable. MTA composites that contained large concentrations of mullite proved to be difficult to sinter without inducing significant grain growth.

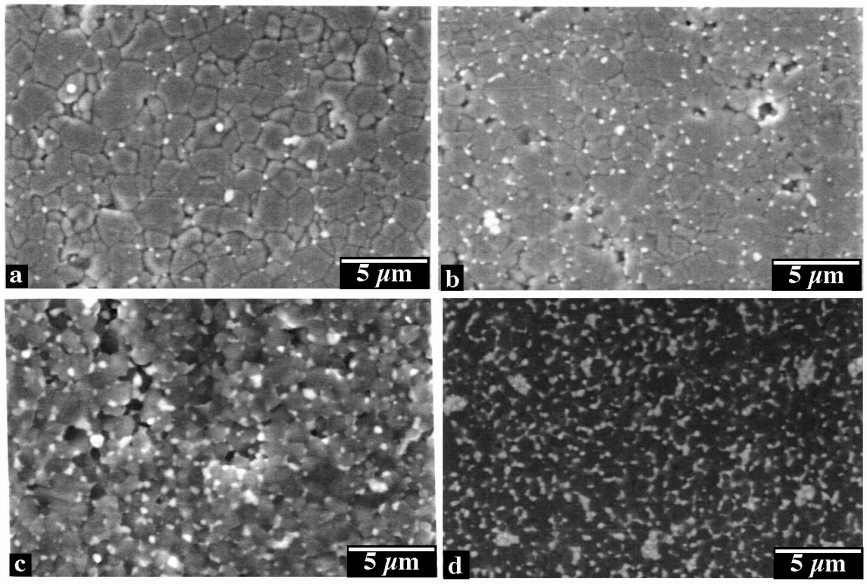

Fig. 40. SEM photomicrographs of (a) ZTA (2% TZ3Y), (b) ZTA (5% TZ3Y), (c) ZTA (10% TZ3Y), and (d) ZTA (20% TZ3Y) sintered at 1550°C for 3 h.

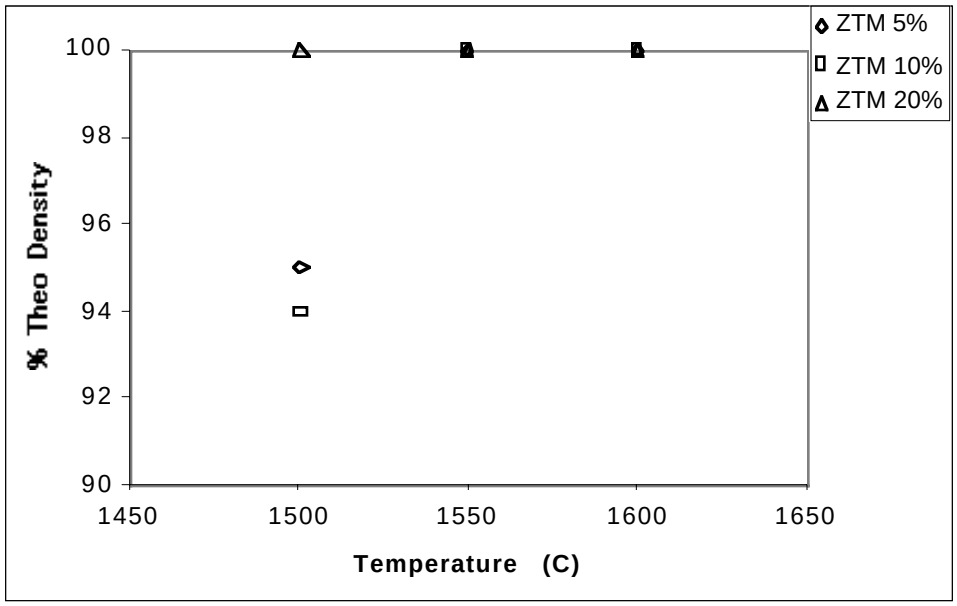

Fig. 41. Density based on rule of mixtures vs. sintering temperature for sintering time of 3 h for various ZTM composites (vol.% of YSZ in mullite).

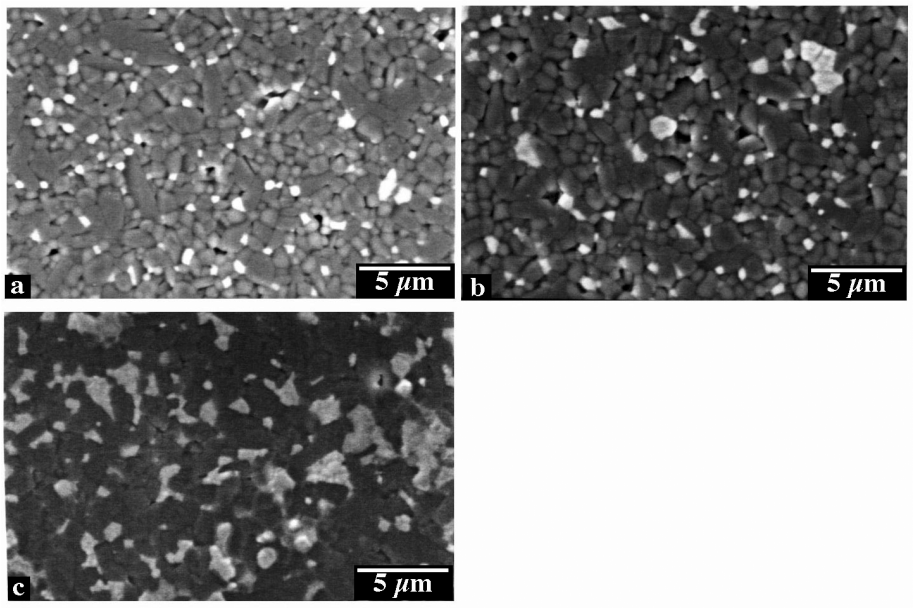

Fig. 42. SEM photomicrographs of (a) ZTM (5 vol.% TZ3Y), (b) ZTM (10 vol.% TZ3Y), and (c) ZTM (20 vol.% TZ3Y) sintered at 1550°C for 3 h.

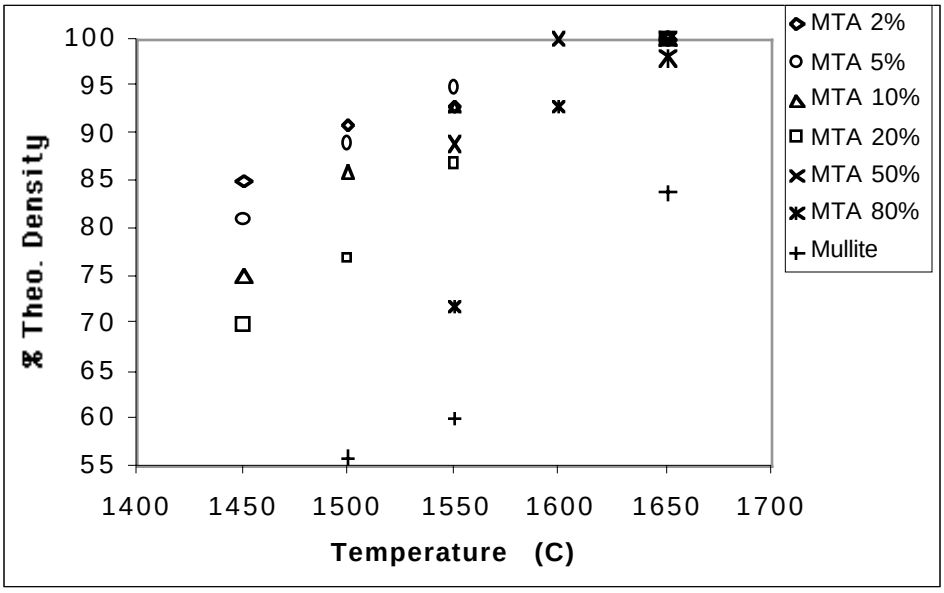

Fig. 43. Density based on rule of mixtures vs. sintering temperature for a sintering time of 3 h for various MTA composites (vol.% of mullite in Al_2O_3).

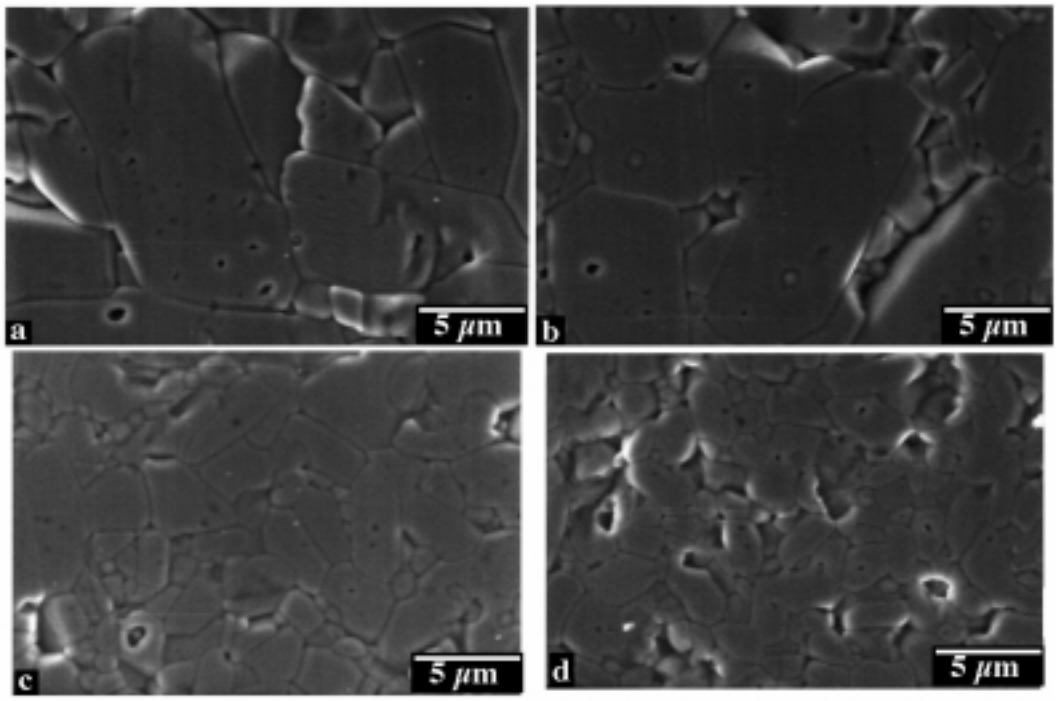

Fig. 44. SEM photomicrographs showing that sintering time did not affect grain size for (a) MTA (50 vol.% mullite) sintered for 3 h, (b) MTA (50 vol.% mullite) sintered for 12 h, (c) MTA (80 vol.% mullite) sintered for 3 h, and (d) MTA (80 vol.% mullite) sintered for 12 h.

Thermal Residual Stresses in Duplex Filaments

FMs are assembled from round, coextruded filaments. Commercial FMs are hot-pressed; thus, they present a flattened hexagonal cross section. The oxide FMs produced in this study are sintered rather than hot-pressed. Sintering reduces the distortion, and the cell cross section can be approximated reasonably well by a circle.

Residual stresses that arise from differences in thermal expansion between constituents have been calculated for cylindrical composites (c.f., e.g., C.-H. Hsueh and P. F. Becher, J. Am. Ceram. Soc. 71 (1988) C428). It is assumed that, if present, the porous matrix has little influence on residual stresses and, therefore, that the stresses arise from differential contraction between the cell core and sheath with cooling. The temperature difference (ΔT) is assumed to be ≈1200°C. The data required to estimate residual stresses are shown in Table 8 (Ceramic Source, Vol. 6., Am. Ceram. Soc., Westerville, OH (1990)).

The configuration for the residual-stress calculations was a coaxial cylinder (Fig. 45). Values for the axial stress at the surface of the duplex cell ($\sigma_{z,2}$), the tangential stress at the surface of the sheath ($\sigma_{t,1}$), and the tangential stress at the outer sheath surface ($\sigma_{t,2}$) can be calculated from

Table 8. Coefficient of thermal expansion (α), Young's modulus (E), and Poisson's ratio (ν) for FM constituents

Oxide	α (°C^{-1})	E (GPa)	ν
Mullite	5.9 x 10^{-6}	145	0.25
Al_2O_3	9.2 x 10^{-6}	380	0.26
YSZ	11.6 x 10^{-6}	205	0.23

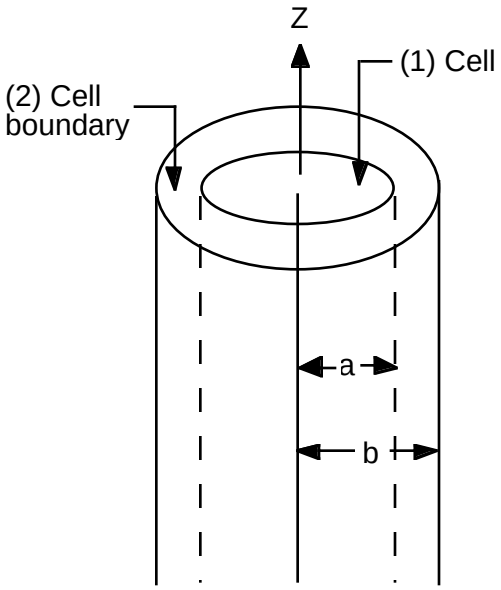

Fig. 45. Schematic diagram of composite cylinder.

$$P = \left(\frac{\beta_2 + \beta_3}{\beta_1 \beta_3 - 2\beta_2^2} \right) (\alpha_2 - \alpha_1) \Delta T \quad , \tag{2.1}$$

$$\sigma_{t,1} = -\frac{1 + V_1}{V_2} P \quad , \tag{2.2}$$

$$\sigma_{t,2} = -\frac{2V_1}{V_2} P \quad , \tag{2.3}$$

$$\beta_1 = \frac{1-\upsilon_1}{E_1} + \frac{\upsilon_2}{E_2} + \frac{1+V_2}{V_1 E_2} \quad , \tag{2.4}$$

$$\beta_2 = \frac{\upsilon_1}{E_1} + \frac{V_1 \upsilon_2}{V_2 E_2} \quad , \tag{2.5}$$

$$\beta_3 = \frac{1}{E_1} + \frac{V_1}{V_2 E_2} \quad , \tag{2.6}$$

$$\sigma_{z,2} = -\frac{V_1}{V_2}\left(\frac{\beta_1}{\beta_2}\frac{\beta_2+\beta_3}{\beta_1\beta_3 - 2\beta_2^2} - \frac{1}{\beta_2}\right)(\alpha_2 - \alpha_1)\Delta T \quad , \tag{2.7}$$

where V is the volume fraction, the subscript 1 refers to the core and the subscript 2 refers to the sheath, and the other terms are defined in Table 8.

Residual-stress values were calculated for three volume fractions of core/sheath, with the core being 50 vol.% mullite/50 vol.% YSZ and the sheath being 50 vol.% mullite/50 vol.% Al_2O_3 (Table 9). Equal volume fractions were selected with both the core and sheath because they tend to sinter well and be relatively resistant to creep. The residual stresses were a strong function of the core/sheath volume fraction. The compressive stresses were very large. Volume fractions of sheath of ≈20%, which can be readily attained in FMs, should be able to generate stresses sufficiently large to arrest cracks.

Table 9. Calculated residual stresses in duplex FM cell; negative values are compressive

Core/sheath ratio	$\sigma_{z,2}$ (GPa)	$\sigma_{t,1}$ (GPa)	$\sigma_{t,2}$ (GPa)
90/10	–6.7	–7.1	–2.0
80/20	–1.7	–1.9	0.5
70/30	–0.8	–1.0	1.8

Production of Duplex MTA/ZTM Filaments

Powders were obtained from commercial sources: KM101 mullite, from Kyoritsu Ceramic Materials Co. (Nagoya, Japan); RC-HP-DBM Al_2O_3, from Malakoff Industries (Malakoff, TX); and TZ-3Y Y_2O_3-stabilized ZrO_2 (YSZ), from Tosoh

Ceramics (Bound Brook, NJ). The average particle sizes were 0.8 μm for the mullite, 0.5 μm for the Al_2O_3, and 0.3 μm for the YSZ.

To test the possibility of making FMs from the particulate composites, we first cofired several tape-cast multilayers. The formulation used was a diluted version of that used for extrusion (shown in Table 10). We found that virtually all of the combinations that were used could be cofired without cracking (Fig. 46).

Table 10. Composition of plastic mixes used for coextrusion of duplex celdl in mullite-based FMs

Constituent	Mullite/YSZ (g)	Mullite/ Al_2O_3 (g)
Ceramic powders	200	200
Rohm & Haas AT-51 binder	78	78
78 wt.% xylene/22 wt.% butanol	12	12
Monsanto S-160 plasticizer	14	14
ICI Americas Solsperse 9000	10	10
Carbon powder	-	1

Several of these multilayers were fractured in flexure. Figure 47 shows a fracture surface of one of them. Crack initiation sites were present within each ZTA layer. That is, a single crack did not propagate through the specimen. This finding qualitatively confirms the UCSB claim of a composite structure that exhibits a threshold failure stress.

The multilayer studies confirmed all of our expectations and fully justified a move to work with extruded filaments and FMs. MTA was selected for the sheath of the cell phase. If we are to produce a matrix phase that isolates the individual dual-phase cells, a layer must be applied to the MTA. We first examined dip-coating as a possible technology.

A batch of the selected MTA was prepared for ram extrusion to form experimental filaments. These filaments were cut and dipped into a mullite slurry that was produced from the same organics that are used to produce the extrusion plastic mass (Table 10). Each filament was dipped several times; some were allowed to dry before being re-dipped. After the filaments were dry, they underwent binder burnout, followed by sintering in air at 1550°C for 3 h. Specimens were then cut, polished, and thermally etched for SEM examination. Often, some of the coating spalled off during cutting. The thickest coatings were produced when the filament

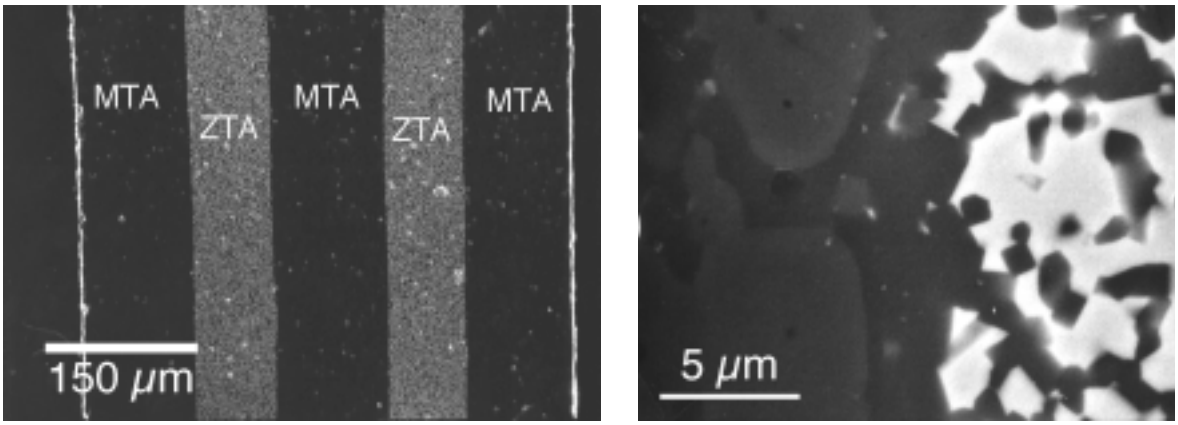

(a) (b)

Fig. 46. SEM photomicrographs of MTA/ZTA multilayer: (a) low-magnification view and (b) higher magnification view, indicating that interfaces were sharp and free of defects.

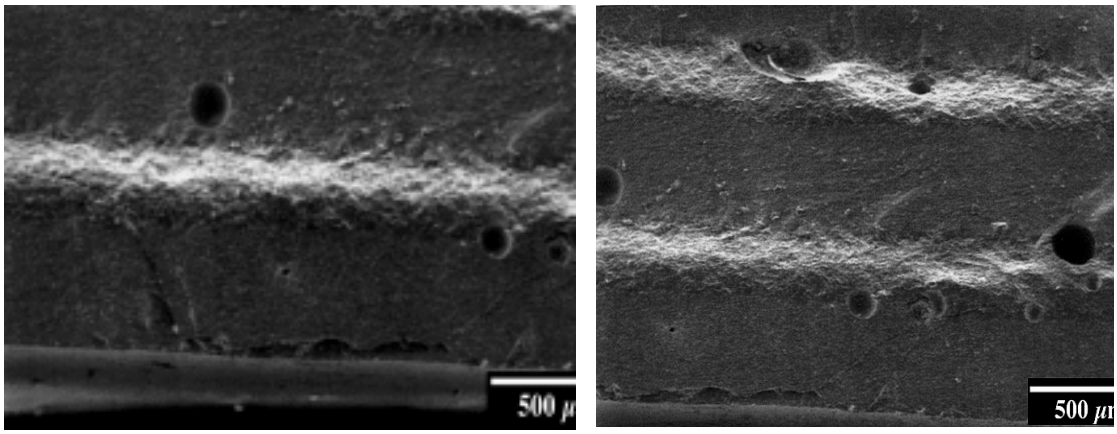

(a) (b)

Fig. 47. SEM photomicrographs of fracture surface of multilayer tape consisting of 4 ZTA/2 MTA/4 ZTA/2 MTA/4 ZTA layers. Multiple fracture initiation sites are evident; compressive surface is at top of each image.

was dried between each dipping (Figs. 48 and 49). It appeared that placing a coating on a coextruded filament should not be a problem and by adjusting the consistency of the mullite slurry, the coating thickness could be controlled reliably.

The extruded MTA filaments proved to be usable, but tended to dry and crack relatively soon after extrusion. Increasing the concentrations of binder and plasticizer did not improve the dryness significantly.

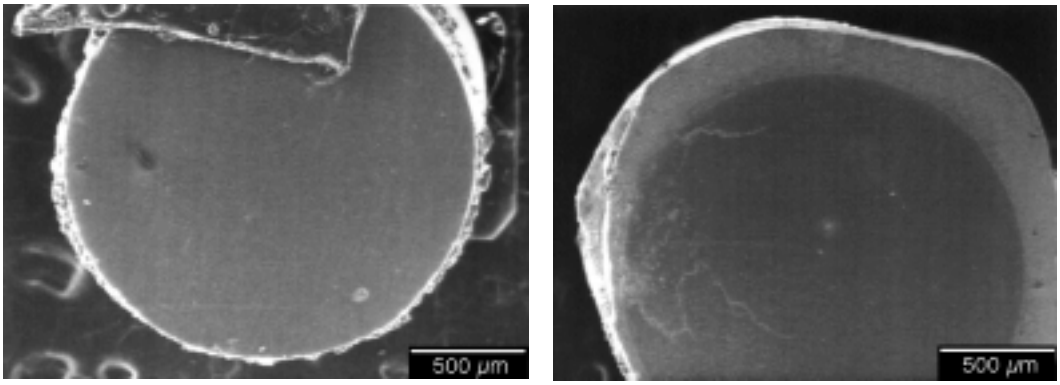

(a) (b)

Fig. 48. SEM photomicrographs of transverse cross section of heat-treated MTA filaments dipped five times into a mullite slurry (a) without drying between each dipping and (b) with drying.

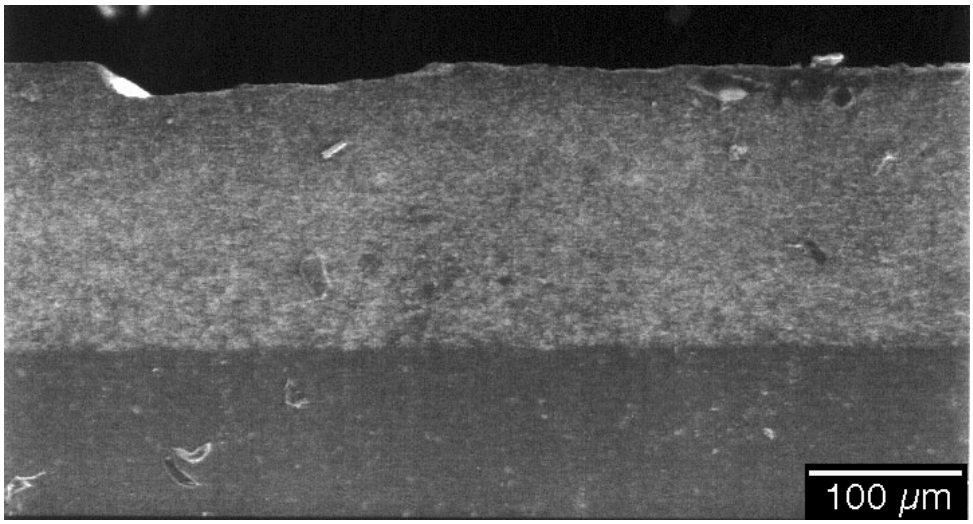

Fig. 49. SEM photomicrograph of longitudinal cross section of coated MTA filament from Fig. 48b.

If dip coating a matrix for the FM proves to be effective, we believe that the process can be made to be nearly continuous. We have available an apparatus that was designed and built in-house for coating ceramic fiber tows (Fig. 50); it can be easily adapted to coating FM filaments.

FM Fabrication

For the first formulation for extrusion of duplex filaments, powders were mixed with organics (Table 10) and vibratory-milled for 24 h. The resultant mixtures were de-aired, tape-cast to a thickness of ≈0.6 mm, and partially dried for

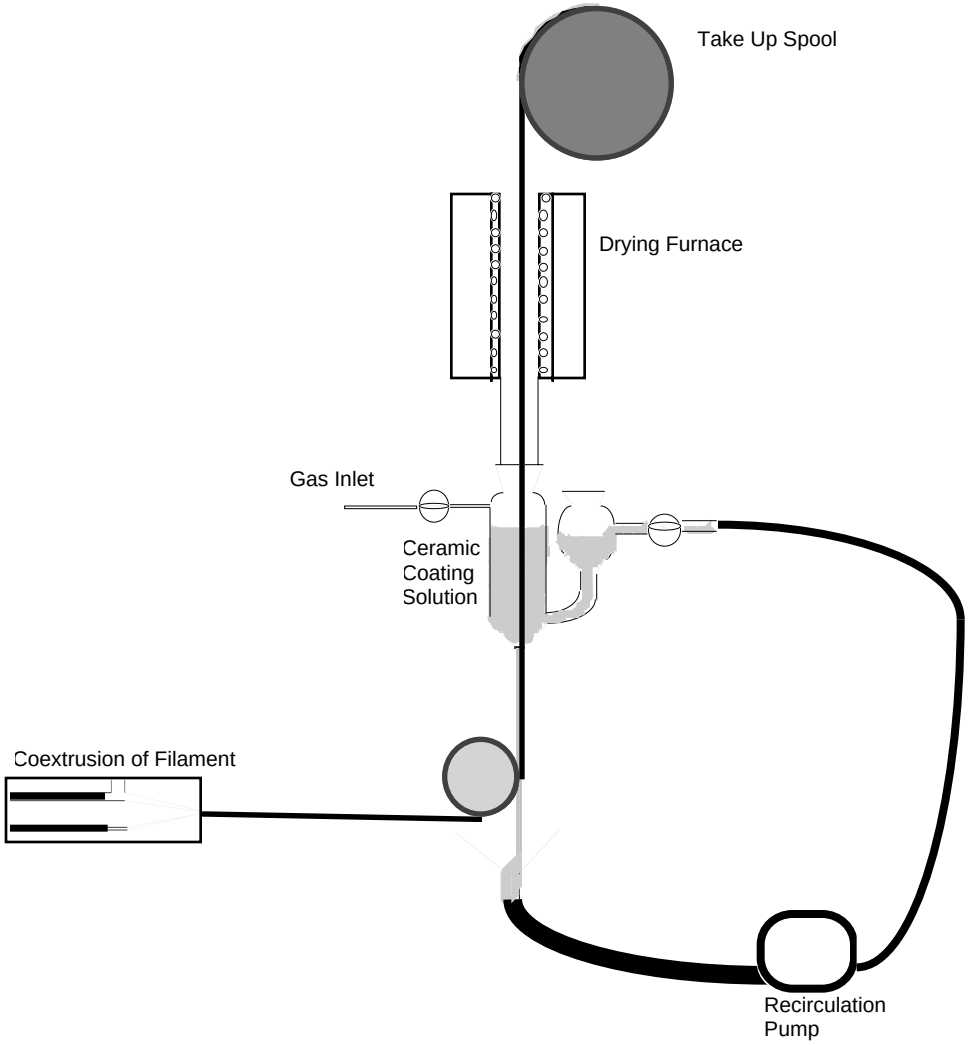

Fig. 50. Schematic diagram of apparatus for coating green FM filaments.

2 h. The tapes were then stripped, compacted, and mixed in a Brabender high-shear mixer to ensure homogeneity. Each plastic mass was then fed into a separate extruder hopper and forced into a coextrusion die to produce an initial duplex filament.

To form a three-component FM, the matrix was created by dip-coating filaments with a mullite slurry. The mullite powder was preheated in air at 1400°C for ≈6 h to reduce its surface area slightly and retard sintering. The slurry composition was similar to that used for extrusion, but the solvent and binder concentrations were increased because lower viscosity and added shrinkage during firing were required. Coated filaments were suspended and partially dried overnight in a xylene/butanol-containing atmosphere.

Dried filaments, either coated or uncoated, were sectioned, stacked, and pressed into bars, which were then heat treated in air. Therefore, two- and three-component prototype FMs were formed. After binder burnout, the bars were sintered in air at ≈1600°C for 3 h. The FM filaments were not bundled and extruded a second time, as has been our practice. Thus, the average final cell size was ≈2 mm, as opposed to the 100–150 μm cells that are generally observed.

The fired FMs were too irregularly shaped to allow reliable mechanical testing. A few were fractured by impact so their surfaces could be examined.

Only a few rudimentary FMs were processed. Most contained an MTA filament, not the sought-after MTA-sheath / ZTM-core filament (Fig. 51).

Optical microscopy and SEM revealed an area around the MTA that appeared to be denser than the remaining mullite phase, but not as dense as the MTA central core (Fig. 52). Chemical analysis of this area indicated that its composition was the same as that of the mullite further from the MTA; no Al_2O_3 was present. The bonding between the MTA and mullite appeared to be only partial. It may become necessary to use somewhat larger particles of mullite for the cell-boundary phase to better reduce densification of the matrix and promote crack deflection.

In all of the simple mullite-based FMs that were processed, the mullite matrix and the MTA cells were substantially cracked (Fig. 53). It is likely that the porous mullite could not provide sufficient constraint to prevent the cell from cracking

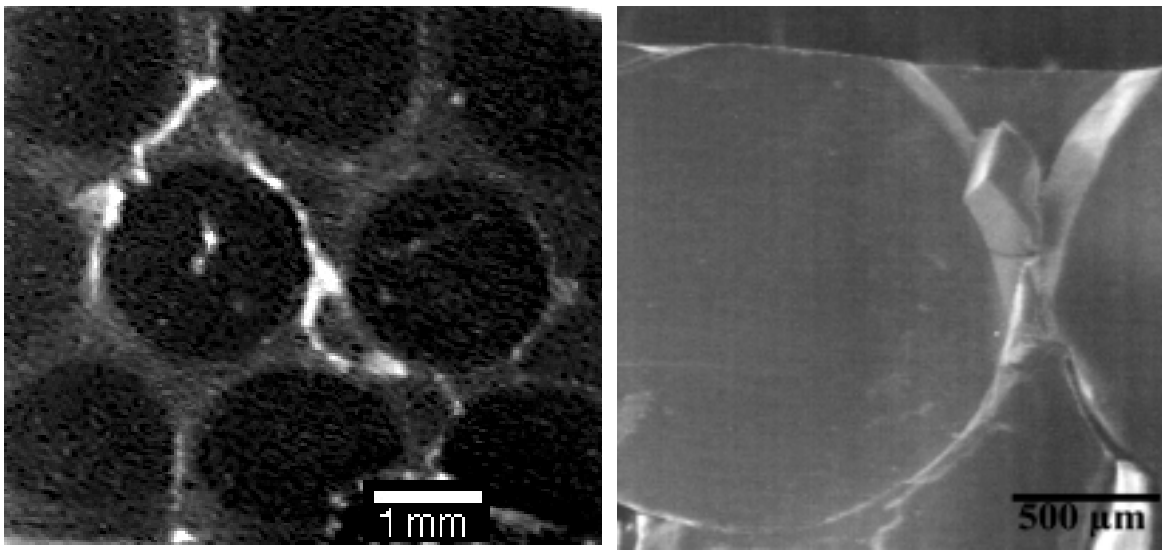

(a) (b)

Fig. 51. SEM photomicrograph of sections of FM bars; mullite between MTA filaments is thicker in (a) than in (b).

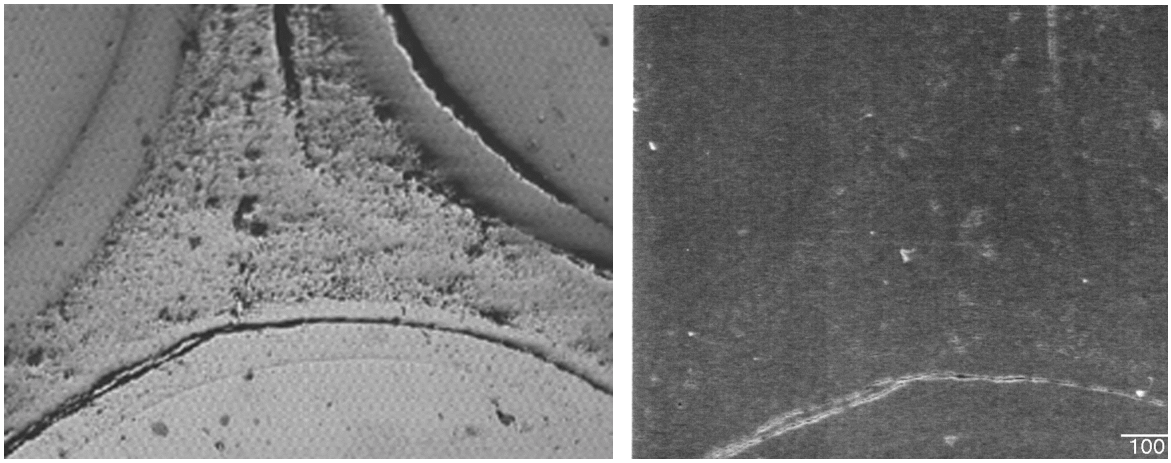

(a) (b)

Fig. 52. Optical (a) and SEM (b) photomicrographs of mullite-based FM; enhanced densification of mullite near MTA cores is evident.

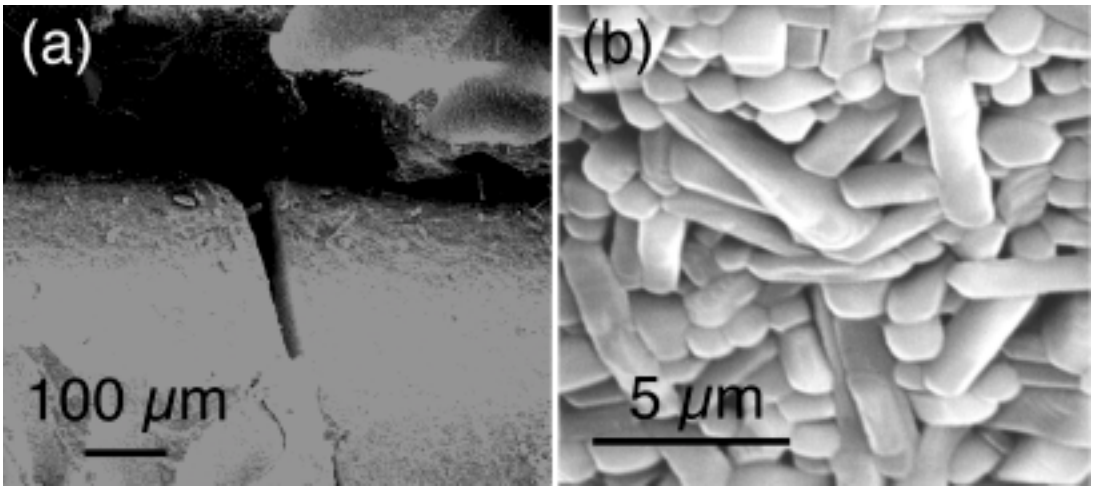

Fig. 53. SEM photomicrographs of FM that contains porous mullite matrix: (a) cracks induced by heat treatment and (b) mullite matrix.

because of the large stresses generated during cooling. It appeared that the thermal expansions of the constituents of the duplex cell would have to be better matched so the maximum residual stresses would be lower, or that the matrix phase would have to be eliminated. However, substantially more work is required before an informed assessment can be made.

Preliminary work on the ZTM/MTA systems was also conducted at UMR. The results were in qualitative agreement with those from ANL. FMs based on mullite, with Al_2O_3 or YSZ added to control sintering and thermally induced residual stresses, can be processed successfully. They offer promise of attaining

higher strengths than those obtained by simple oxide FMs. However, work is required to perfect the extrusion compositions and to determine the configurations that will lead to the best overall mechanical properties. Time and resources were exhausted before we could undertake steps to address these challenges.

2.3.2 Al_2O_3/Mullite Composites

In late 2000, Prof. F. F. Lange of UCSB and Prof. G. Hilmas of UMR agreed to collaborate on a study of an Al_2O_3 cellular and 70 vol.% Al_2O_3/30 vol.% mullite cell-boundary FM system. This effort applied Prof. Lange's work on a threshold-stress phenomenon in laminar ceramics to FMs. Mr. Mark Snyder (Ph.D. candidate at UCSB) provided the necessary supplies of Al_2O_3 and 70% Al_2O_3/30% mullite powders for fabrication of coextruded filament.

The binder formulations for the $ZrSiO_4$ system were applied to the new oxides. The core recipe (55% Al_2O_3, 35% EEA, 10% HMO) blended well during the batching process. In addition, a controlled geometry core has been successfully pressed. The shell recipe (55% MTA, 34% EEA, 4% B-67, 7% MPEG-550) also blended well during batching and when shells were pressed. At this point, the project was terminated because of time and funding constraints.

3 Synthesis and Sintering Studies

Oxide FMs that can be sintered require high-quality powders of fine particle size. In addition, it is essential to determine compatibilities and extents to which various powders can be cofired.

In the FM programs, we evaluated processing of several structural oxides for cells and cell boundaries. Most powders were obtained commercially, but some were synthesized by simple sol-gel methods or, at UIUC, by a proprietary solution-polymerization method.

Much of the work on two-phase mixtures and cell boundaries was covered previously in this report. Additional results on synthesis and sintering of several candidate cell materials will be summarized here.

3.1 Synthesis of Oxide Powders

At ANL, mullite ($3Al_2O_3 \cdot 2SiO_2$) and cordierite ($2MgO \cdot 2Al_2O_3 \cdot 5SiO_2$) were synthesized by a simple sol-gel method. At UIUC, mullite, Al_2O_3, and YAG were synthesized by a solution process based on polyvinyl alcohol (PVA).

3.1.1 Sol-Gel Synthesis

Mullite

Mullite was produced by a colloidal sol-gel approach. Colloidal SiO_2 with average particle size of ≈0.02 μm (Alfa Aesar, Ward Hill, MA) was used to prepare a sol, and boehmite (γ-AlOOH, Alcoa Hi-Q 10, Pittsburgh, PA) was used to prepare an Al_2O_3 sol. The sols were mixed together and HNO_3 was added to produce a pH of 3. The sol was gelled by heating in air at 80°C for 24 h. The gel was ground and calcined in air at 1000°C for 2 h. The calcined material was ball-milled for 24 h in isopropyl alcohol. The resultant material was dried and sieved, and the powder was then fired in air for various times (0–12 h) at 1550°C and for 3 h at various temperatures (1500–1650°C).

We found that phase-pure mullite could be formed by firing at all temperatures. However, the sol-gel-derived powder did not prove any easier to sinter than a commercial powder (KM101) from Kyoritsu (Nagoya, Japan). We therefore used the commercial mullite for most of our studies.

Cordierite

Cordierite sinters at a lower temperature than any of the other oxides with which we worked. Cordierite was successfully produced by two methods: directly from oxide powders and by a sol-gel technique based on the use of colloidal SiO_2, boehmite, and magnesium nitrate. Formation of cordierite was confirmed by X–ray diffraction. Differential thermal analysis (DTA) studies revealed that the cordierite formed at a lower temperature when produced by the sol–gel method, i.e., at ≈1200°C vs. 1270°C, when made from oxides (Fig. 54).

In addition to forming at a lower temperature, when fired in air at 1350°C, sol-gel-derived cordierite was >95% dense, whereas the oxide cordierite was only 65% dense.

3.1.2 PVA Solution-Polymerization Synthesis

The PVA process developed at UIUC can be applied to virtually any oxide. In general, PVA is made commercially by hydrolysis of polyvinyl acetate (Fig. 55). The properties of a PVA depend on its degree of polymerization, degree of hydrolysis, and distribution of the degree of hydrolysis.

The solubility of PVA in water depends on the degree of hydrolysis and polymerization. The OH^- groups impair solubility because of strong hydrogen bonding between intramolecular and intermolecular OH^- groups. This bonding can

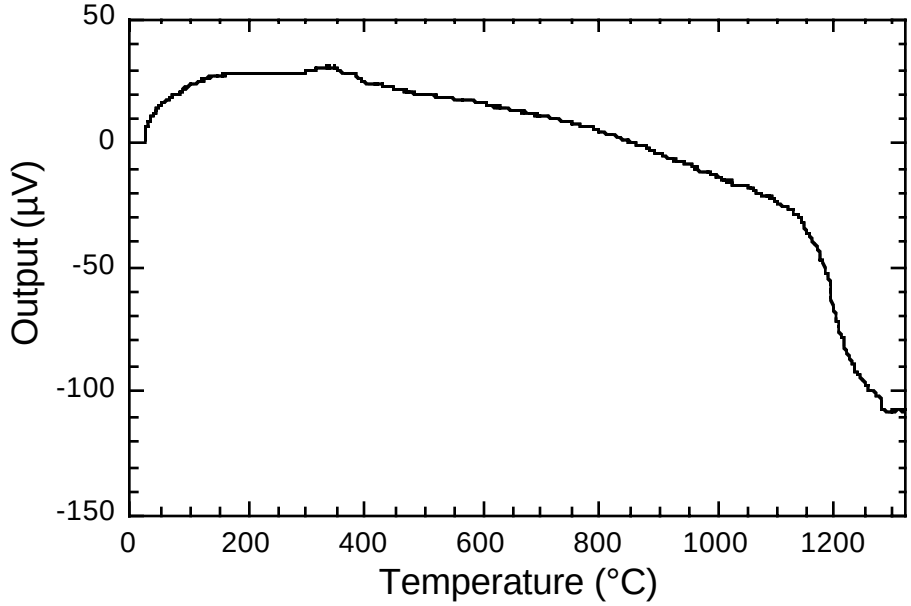

Fig. 54. DTA plot for sol-gel cordierite precursors heated in air at 5°C/min.

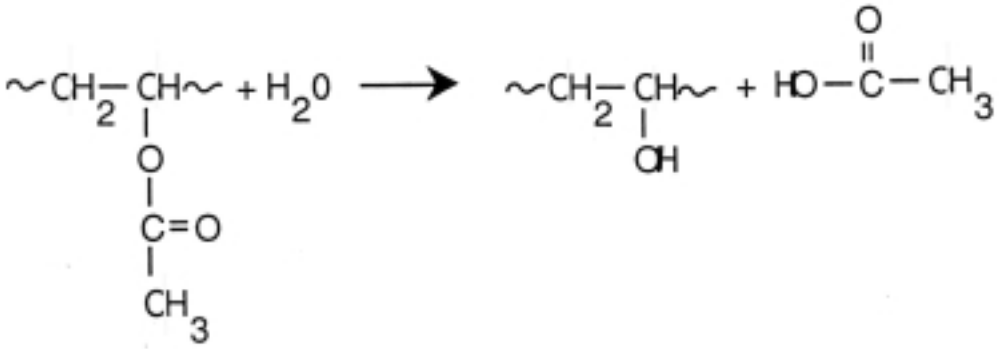

Fig. 55. Synthesis reaction of PVA by hydrolysis.

be reduced if residual acetate groups are present. Water acts, in effect, as a terminator to the polymerization of PVA. In a PVA solution, the OH^- functional ends serve as a strong stearic entrapment agent (Fig. 56).

In the PVA solution-polymerization process (Fig. 57), nitrate salts were the source for all of the cations, except Si, which came from colloidal SiO_2 (Ludox SK, Du Pont, Wilmington, DE). For each oxide, the salts were dissolved in deionized water and the pH was adjusted with HNO_3, if needed. A 5 wt.% PVA in water solution was then added. The proportions of the cation sources were adjusted so there were 4, 8, or 12 times more positive charges from the cations than negative changes from the OH^- function ends of the PVA.

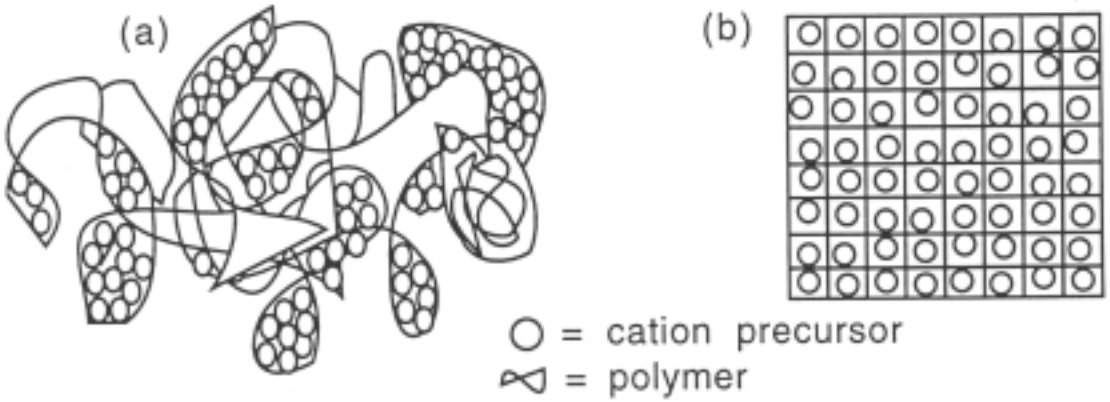

Fig. 56. Schematic diagram of cationic entrapment with (a) small concentration of polymer and (b) optimal concentration of polymer.

Each solution was heated on a hot plate while being stirred. A gel-type precursor was formed, and then dried for ≈12 h in an oven set at >100°C. The resultant precursors were then ground and calcined. Each oxide required its own heat-treatment schedule. Results for some of the oxides were as follows.

Mullite: calcination at 800°C and crystallization at 1300°C;
specific surface area ≈157 m^2/g.

Al_2O_3: calcination at 800°C and crystallization at 1100°C;
specific surface area ≈83 m^2/g.

$ZrSiO_4$: calcination at 800°C and crystallization at 1100°C;
specific surface area ≈81 m^2/g.

Each of the powders that was produced by the PVA process exhibited very large surface areas. As expected, each powder proved to be relatively easy to sinter.

3.2 Sintering of Oxides

The initial studies of various oxides for possible use in FMs included examination of compatibilities and densification. For possible use in cells, we focused on mullite, Al_2O_3, $ZrSiO_4$, YSZ, YAG, and cordierite.

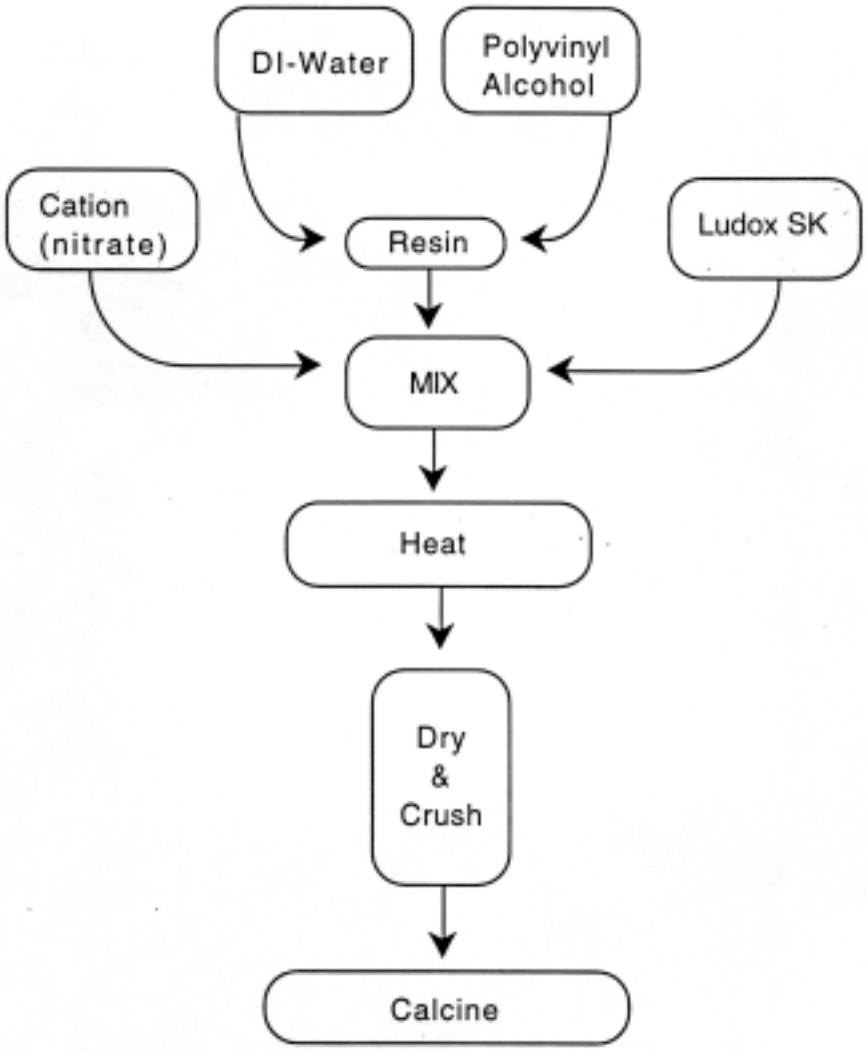

Fig. 57. Flowchart for PVA synthesis of oxides.

3.2.1 Compatibility Studies

It can be difficult to determine from phase-diagram literature only the likely interactions between oxide species. Kinetic aspects can be important, and thus direct experimentation is required. We therefore conducted a round-robin study of reaction couples between the six above-mentioned oxides listed.

Not surprisingly, cordierite, which has the lowest melting temperature, proved to be the most reactive; none of the other oxides resisted strong compound formation with it. Al_2O_3 proved to be virtually stable with respect to mullite, YSZ, and YAG. Mullite was also relatively stable with respect to Al_2O_3 and YSZ. Although YAG proved to be rather unreactive, it was also difficult to sinter, and so the bulk of our efforts were focused on other oxides.

3.2.2 Sintering Studies

The six candidate oxides cleaved readily into two groups, those that could be easily sintered to high density (Al_2O_3, $ZrSiO_4$, YSZ, and cordierite) and those that could not (mullite and YAG). A few sintering aids were tested for mullite and YAG.

Oxides that can be easily sintered

YSZ and cordierite could be sintered to ≥95% density at temperatures ≤1350°C. We judged these temperatures to be too low to allow high-temperature use of FMs made primarily from these two oxides, and so work shifted to the higher-temperature oxides.

With very slight MgO doping for grain-size control, Al_2O_3 could be sintered at ≈1500–1550°C to high density with limited grain growth. Commercial Al_2O_3 powders with ≈0.25% MgO was obtained from a few suppliers. We settled on using Grade RC-HP DBM from Mallakoff Industries. Its average particle size was ≈0.5-0.7 µm. With firing for 3 h in air at 1550°C, compact densities approached 98.5%. Firing in oxygen produced ≈100% dense pieces. SEM indicated that the average grain size of the air-fired Al_2O_3 was <2 µm (Fig. 58a).

We attempted to reduce the sintering temperature by adding sintering aids; Li_2CO_3, HBO_3, MnO, CuO, and TiO_2 were tried. In each case, they either provided little benefit to densification, or induced unwanted grain growth. Malakoff Al_2O_3 became a standard oxide from which to produce the FMs.

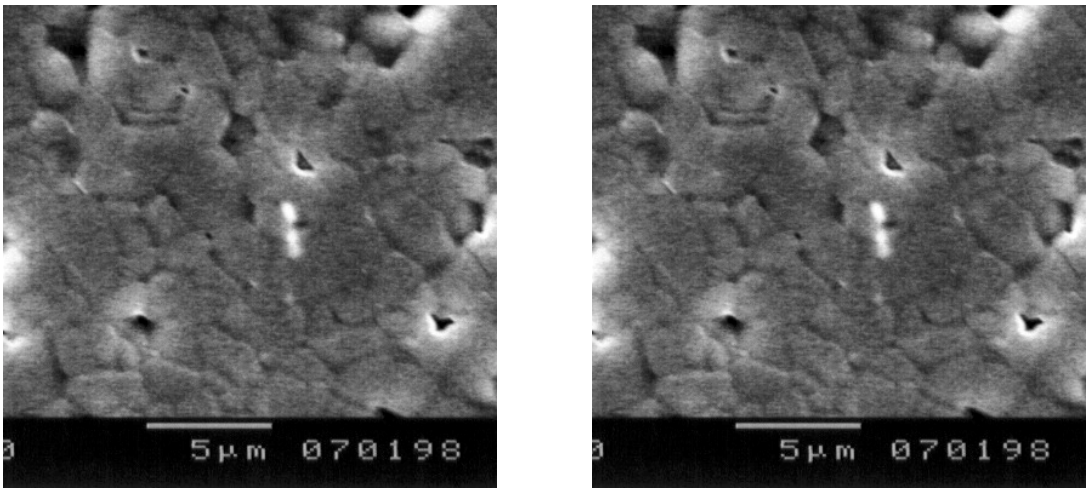

(a) (b)

Fig. 58. SEM photomicrographs of polished and thermally etched cross sections of pellets of (a) Al_2O_3 and (b) $ZrSiO_4$.

Compacts from commercial $ZrSiO_4$ (Alpha Aesar, Ward Hill, MA) were sintered for 3 h in air at 1550°C. The maximum density obtained was ≈95–96% (Fig. 58b). Efforts to improve density through the use of transient sintering aids, such as Li_2CO_3 and HBO_3, proved ineffective.

Oxides that are difficult to sinter

Mullite commanded most of the attention at ANL, whereas YAG was studied primarily at UIUC. The YAG work was summarized in Section 2.2.1.

For the ANL mullite work, mullite was synthesized as described or purchased from Kyoritsu. Results of sintering studies exhibited minimal differences based on origin of powder. Most of the studies focused on differences between sintering pure mullite and mullite + 1–15 wt.% Y_2O_3. The Y_2O_3 (Sigma Aldrich, Milwaukee, WI) particle size was ≈1 μm.

The powders were vibratory-milled and then uniaxially pressed in a 1.27-cm cylindrical die or in a larger bar die. The resultant specimens were then fired for various times (0–12 h) at 1550°C and for 3 h at various temperatures (1400–1650°C). Some specimens were then annealed at 1300°C for 24 h, cooled to 1200°C, and held for another 24 h, in an attempt to crystallize an amorphous grain-boundary phase.

All concentrations of Y_2O_3 induced significant improvement in densification. Y_2O_3 additions >5 wt.% significantly increased grain growth, whereas Y_2O_3 additions <5 wt.% did not densify quickly. Because our goal was to achieve rapid densification with minimal grain growth, 5 wt.% addition was selected.

We conducted time and temperature studies to determine optimal processing conditions for the 5 wt.% addition (Fig. 59). At 1550°C, most of the sintering occurred within the first 3 h for mullite + 5 wt.% Y_2O_3; for pure mullite, density continued to increase with increasing sintering time. The maximum density for mullite + 5 wt.% Y_2O_3 occurred at 1500°C, whereas with pure mullite, the density continued to increase with increasing sintering temperature. The decrease in density observed with mullite-5 wt.% Y_2O_3 with longer sintering times and higher sintering temperatures coincides with an increase in anisotropic grain growth and an increase in porosity (Fig. 60).

For many FMs, the constituents are tailored to have nearly equal α values. The average values of α from 25 to 1400°C were 5.9×10^{-6} °C^{-1} for mullite and 6.2×10^{-6} °C^{-1} for mullite + 5 wt.% Y_2O_3. The slight change in the thermal expansion of mullite with the addition of Y_2O_3 indicates that little internal stress should develop in cofired mullite structures.

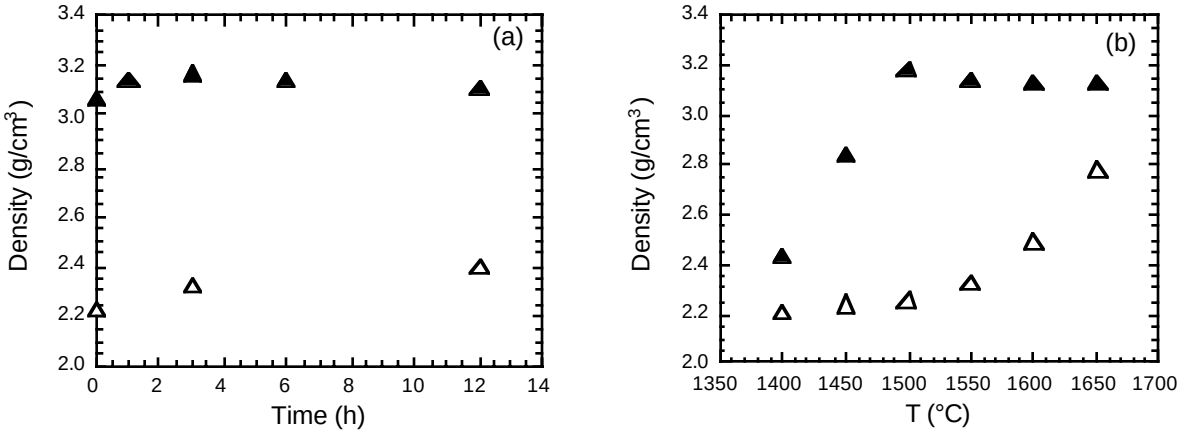

(a) (b)

Fig. 59. Effect of (a) sintering time at 1550°C and (b) temperature for 3-h sintering; mullite (open triangles) and mullite-5 wt.% Y_2O_3 (filled triangles).

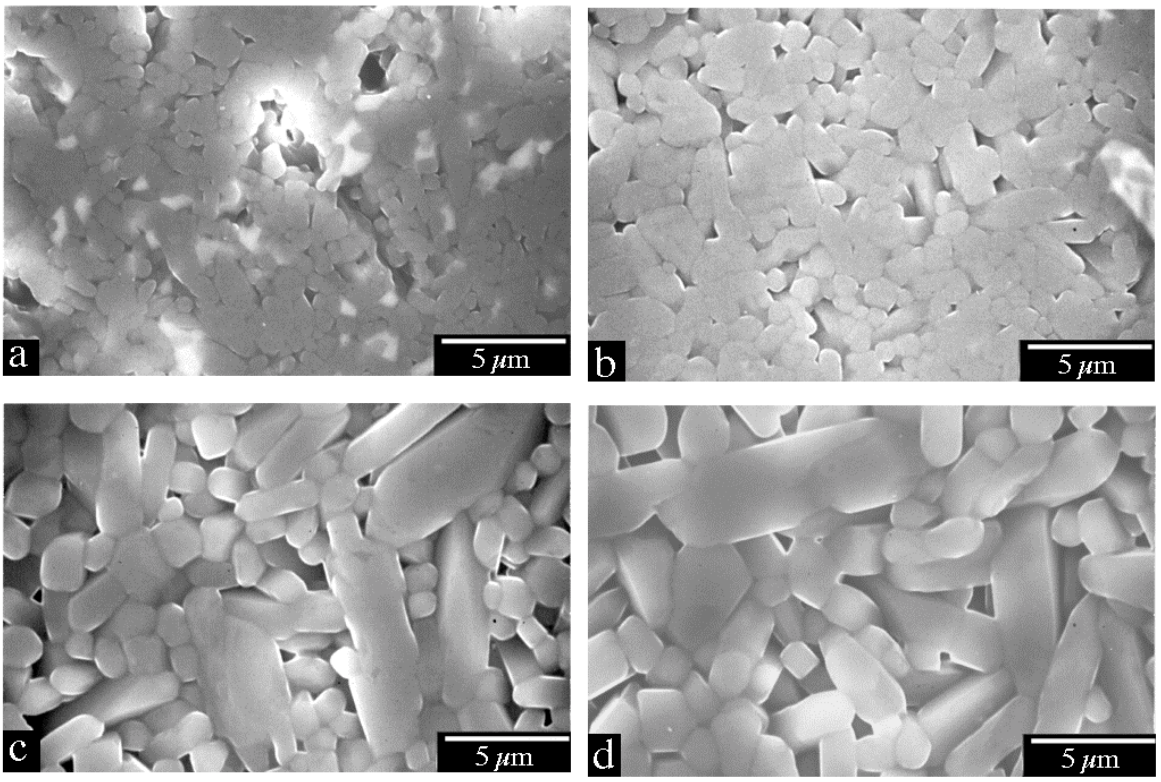

Fig. 60. SEM photomicrographs of mullite + 5 wt.% Y_2O_3 specimens sintered for 3 h at (a) 1450, (b) 1500, (c) 1550, and (d) 1600°C.

Further characterization of mullite + 5 wt.% Y_2O_3 was conducted to better understand the sintering response and properties of this material. Examination of phase diagrams indicated that the phases present in mullite + 5 wt.% Y_2O_3 at room temperature should be mullite, Al_2O_3, and $Y_2Si_2O_7$. X-ray diffraction of conventionally cooled specimens revealed only mullite. However, by annealing the material at 1300°C, the presence of β-$Y_2Si_2O_7$ was detected (Fig. 61).

SEM examination of the surface of a mullite + 5 wt.% Y_2O_3 specimen indicated the presence of a secondary phase, which energy dispersive analysis revealed to have a composition of ≈$YSi_2Al_2O_x$, which is similar to the composition of the liquid phase reported present at ≈1400°C.

TEM analysis of sintered specimens confirmed the presence of an amorphous phase along the grain boundaries of as-sintered specimens and crystalline $Y_2Si_2O_7$ at triple points in annealed specimens (Fig. 62). Transformation of the $Y_2Si_2O_7$ from amorphous to crystalline has been shown to significantly increase the strength of Si_3N_4, although no mechanism for the effect has been accepted. Crystallizing the $Y_2Si_2O_7$ phase in mullite may also produce an increase in strength.

Differential thermal analysis of the mullite + 5 wt.% Y_2O_3 revealed endotherms at ≈1175, 1375, and 1425°C. A reaction at 1375°C has been reported to be a phase transformation of the $Y_2Si_2O_7$. The reactions at 1375 and 1425°C are probably the result of formation of yttrium aluminosilicate liquid phase, as seems to be indicated by the phase diagram.

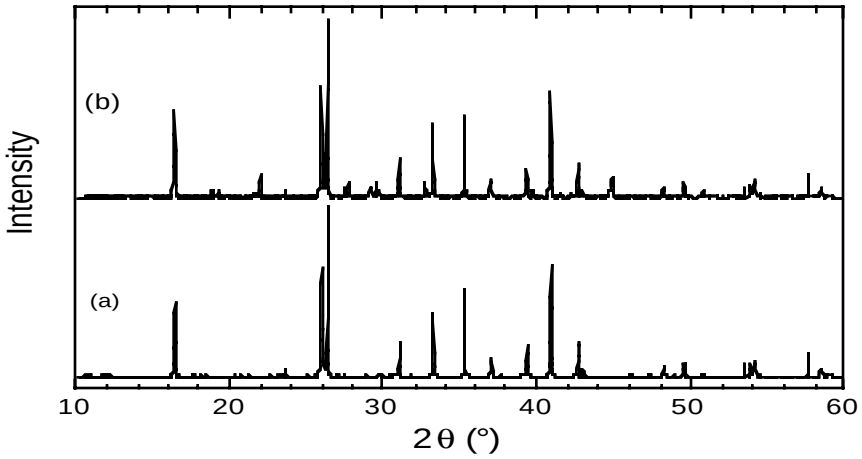

Fig. 61. X-ray diffraction of mullite + 5 wt.% Y_2O_3: (a) as sintered and (b) after annealing.

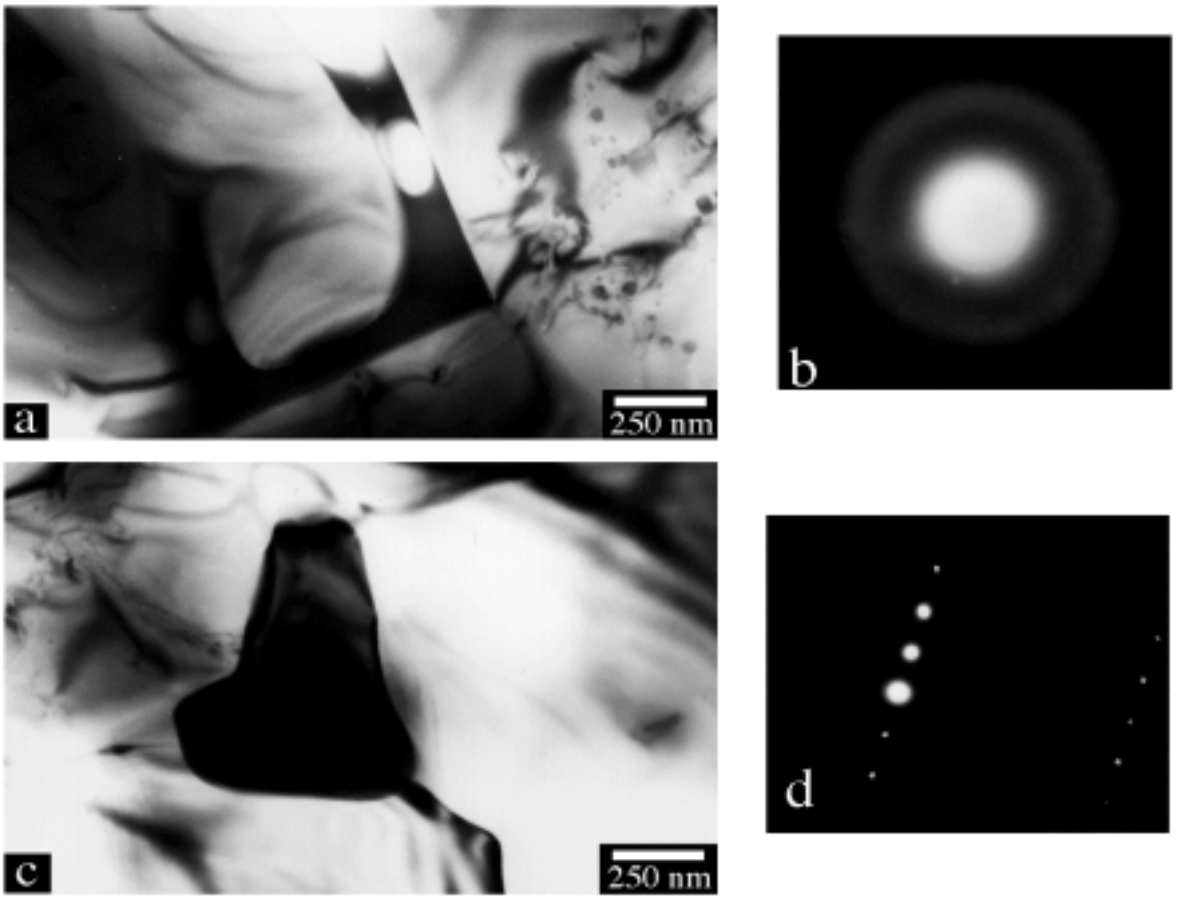

Fig. 62. TEM analysis of mullite + 5 wt.% Y_2O_3: (a) as sintered, (b) electron diffraction pattern of amorphous grain-boundary phase, (c) after annealing, and (d) electron diffraction pattern of crystalline $Y_2Si_2O_7$ phase at triple point.

We concluded that Y_2O_3 was effective at reducing the sintering time and temperature needed to achieve highly dense mullite. Addition of 5 wt.% Y_2O_3 did not significantly affect α. By proper annealing, a Y-rich amorphous grain-boundary phase could be at least partially crystallized.

4 Microstructure and Property Characterization

$ZrSiO_4$-based FMs were fabricated successfully. Their microstructures, room-temperature mechanical properties, and creep response were characterized. Mullite-based FMs were less successful, and only their microstructures and creep properties were characterized in detail.

Si_3N_4/BN FMs and Si_3N_4 and BN plates were obtained from ACR. These well-made materials were studied extensively, in large part to provide baseline data of use to the modeling effort discussed in Section 5. Basic studies of microstructure, elasticity, cell push-out, fracture, thermoelastic effects, and creep will be reported in this section. Additional, more-involved mechanical studies will be covered in Section 5.

4.1 Oxide Fibrous Monoliths

The basic microstructures of the $ZrSiO_4$ and mullite FMs were presented in Sections 2 and 3. Microstructures only as they relate directly to mechanical properties will be presented here.

4.1.1 $ZrSiO_4$-Based Fibrous Monoliths

Fracture

At ANL, fired $ZrSiO_4$ FMs were compared with monolithic dense Alpha Aesar and porous Remet bars. Fired FMs were cut to dimensions of ≈45 x 5 x 3 mm for four-point flexural testing. All monolithic bars were sintered at 1550°C for 3 h. The Alfa bars were ≈95% dense and the 1X Remet bars were ≈70% dense. The tensile surface of each bar was ground and polished to a 1-μm finish. The inner span of the testing fixture was 15 mm; its outer span was 40 mm. The samples were loaded into an Instron Model 4505 tester (Canton, MA).

The Alfa $ZrSiO_4$ bars exhibited fast fracture at maximum stresses of ≈200 MPa. The 1X Remet $ZrSiO_4$ bars also exhibited fast fracture, but the maximum stresses were only ≈30 MPa (Fig. 63). Unlike the Alfa and Remet 1X bars, the FM bars exhibited graceful failure (Fig. 64). Nonlinearity was observed before the maximum load was reached, and some load-bearing capability was retained to large displacements. The average maximum stress was 100-120 MPa.

SEM indicated that the unloading steps that were observed in the FM stress-vs.-displacement curves were caused by energy-dissipating events, such as delamination, crack deflection, and limited cell pullout (Fig. 65). Primary cracks followed a tortuous path though the FM, making several 90° deviations through the cell-boundary phase before continuing through the FM.

The $ZrSiO_4$ FMs exhibited significant energy dissipation during fracture and retained some load to large displacements. The WOF values were ≈0.5 kJ/m^2. However, they also exhibited ≈50% of the strength of monolithic dense $ZrSiO_4$ bars. Thus, FM strength roughly followed a rule of mixtures, with a further slight decrease in strength that was probably caused by flaws introduced by the coarse

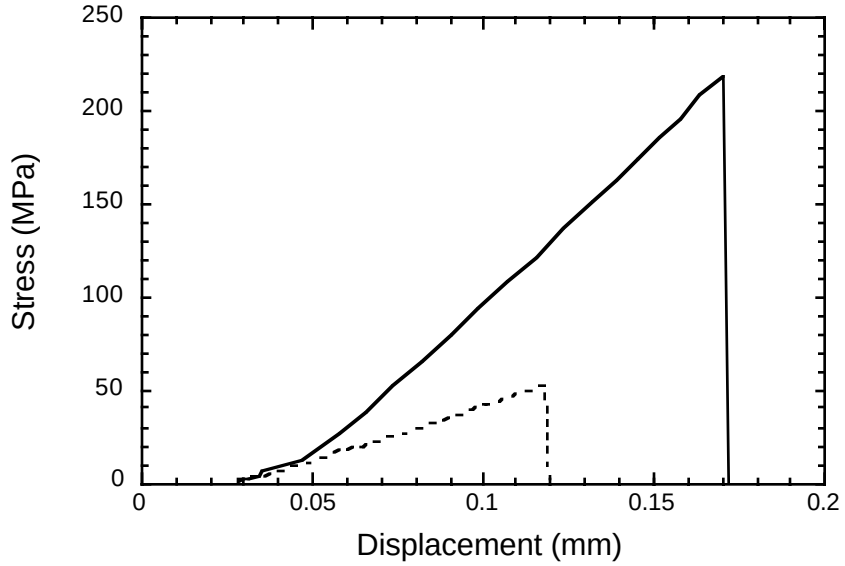

Fig. 63. Stress-vs.-displacement curves for representative Alfa $ZrSiO_4$ bars (solid line) and 1X Remet $ZrSiO_4$ bars (dashed line).

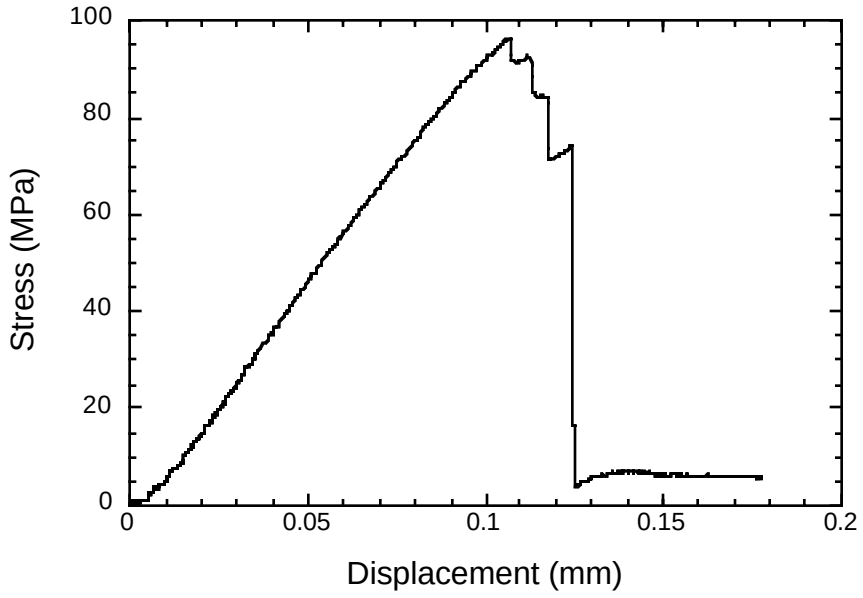

Fig. 64. Stress-vs.-displacement curve for representative $ZrSiO_4$ FM bar.

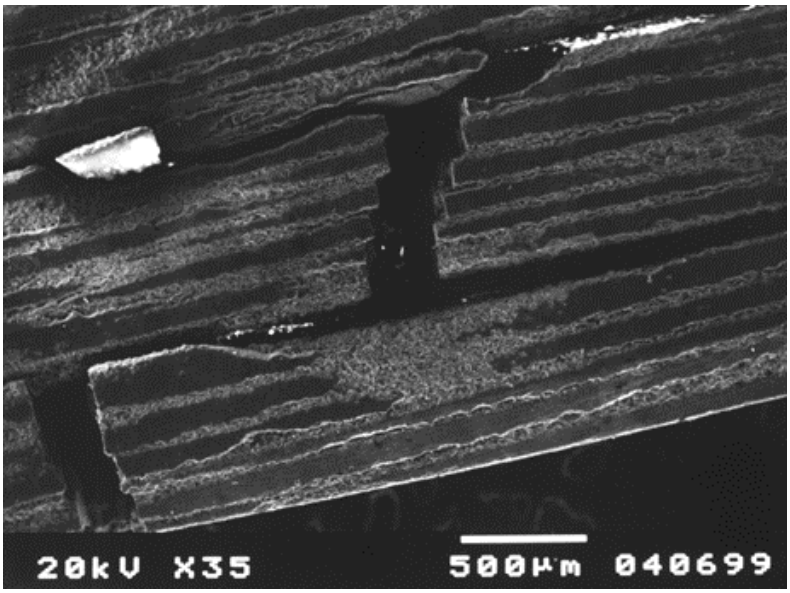

Fig. 65. SEM photomicrograph of crack through FM bar.

Remet $ZrSiO_4$. These results offer promise and clearly indicate a need for improvements in strength and toughness through, for example, the use of inherently stronger oxides, higher fractions of cell phase, and possible favorable residual-stress states.

The UMR approach was also used to produce $ZrSiO_4$ FMs for fracture testing. The results obtained were nearly identical with those from the ANL FMs (Fig. 66). The equivalence of results strongly suggests that the observed limitations were determined by the powders and their volume fractions, not the extrusion procedures.

Creep

It has been shown that creep of uniaxial FMs also follows a rule of mixtures. Because no definitive studies of $ZrSiO_4$ creep have been reported, we studied creep of the cell phase, i.e., dense, fine-grained $ZrSiO_4$.

Alfa Aesar $ZrSiO_4$ powders were ball-milled with YSZ grinding media for 72 h in isopropyl alcohol, yielding an average particle size of ≈0.7 µm, with a surface area, as determined by BET analysis, of 11 m^2/g. Chemical analysis by inductively coupled plasma atomic emission spectroscopy (ICP-AES) revealed a moderate concentration of cation impurities (Table 11).

Specimens for creep testing were prepared by first cold-pressing dry powders in a cylindrical die. The resultant compacts were placed on ZrO_2 plates and sintered in air at 1550°C for 3-5 h. Final specimens were ≈5.25 mm tall, ≈3.5 mm in diameter,

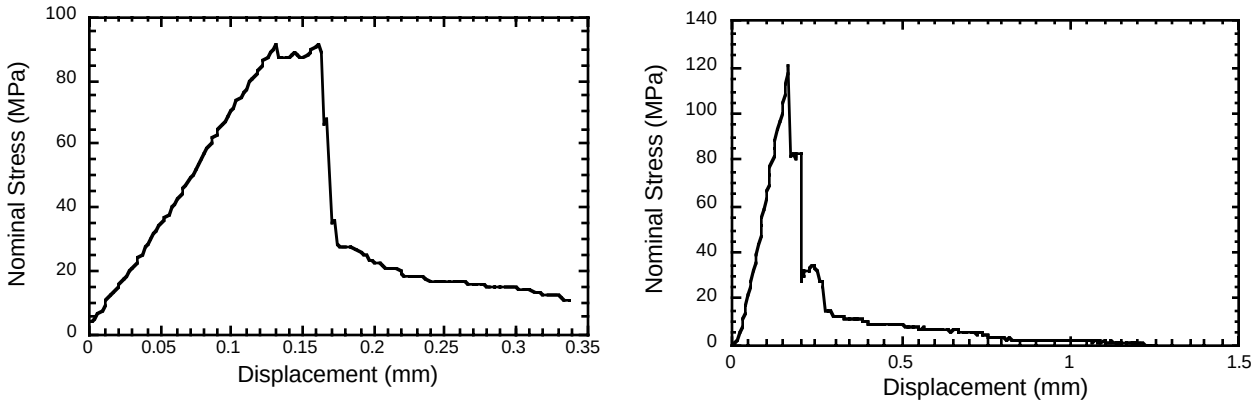

(a) (b)

Fig. 66. Stress vs. displacement for two UMR $ZrSiO_4$ FMs.

Table 11. ICP-AES analysis of cation impurities in $ZrSiO_4$; accuracy of ±20%

Element	Concentration (µg/g)
Al	700
Ba	35
Ca	370
Cu	26
Fe	350
Mg	31
Ti	450
Zn	24

and ≈99% dense. SEM indicated an equiaxed grain structure, with an average grain size of 1.2 ± 0.2 µm; the largest grains were ≈5 µm in average dimension. TEM of foils polished and ion-thinned by conventional means revealed the presence of an SiO_2-based glass at triple junctions and pockets between more than three grains. The grain boundaries appeared to be otherwise free of glass. SEM and TEM observations indicated that the $ZrSiO_4$ specimens contained ≈5% glass.

The $ZrSiO_4$ specimens were compressed in Ar between Al_2O_3 platens at constant crosshead velocity, i.e., at nearly constant strain rate (CSR), or under constant load (CL). The temperature range was 1197-1400°C and the approximate stress range was 1-100 MPa. No appreciable reaction occurred between the specimens and the Al_2O_3 platens.

For stresses of ≈1-120 MPa, steady-state creep occurred by diffusional flow. For stresses >3 MPa, data (Figs. 67 and 68) indicated that the steady-state strain rate $\dot{\varepsilon}$ could be expressed as

$$\dot{\varepsilon} = A\,\sigma^{1.1 \pm 0.1} \exp -[(470 \pm 40\ \text{kJ/mole})/RT],$$

where A is a constant; σ, the steady-state stress; R, the gas constant; and T, the absolute temperature. At 1400°C and 1 MPa, an increase in the value of n was observed. Electron microscopy revealed no deformation-induced change in the microstructures of any of the specimens, a funding that is consistent with creep by diffusion-controlled grain-boundary sliding. Comparison with literature data indicated that volume diffusion of oxygen controlled the creep rate.

The literature contains several reports on the creep of highly phase-pure mullite. Results of representative studies were compared with the $ZrSiO_4$ data taken at 20 MPa by extrapolating the $ZrSiO_4$ data to 100 MPa. For highly crystalline specimens at ≈1200-1400°C, mullite was approximately one order of magnitude more creep resistant than the $ZrSiO_4$ used in this study (Fig. 69). If, however, highly pure bulk $ZrSiO_4$ material can be fabricated, perhaps its diffusional creep resistance can be improved substantially because diffusion rates may be lowered. For commercial-grade materials, mullite is likely to be the superior FM cell material. These high-temperature studies, therefore, reinforce our conclusions from other FM work.

4.1.2 Mullite-Based Fibrous Monoliths

Creep

Specimens of pure mullite, mullite + 5 wt.% Y_2O_3, and mullite + 9 wt.% Y_2O_3 were crept. Some of the mullite + 5 wt.% Y_2O_3 specimens were annealed at 1300°C to crystallize the glass phase along grain boundaries. Key results from the creep tests are shown in Fig. 70. Higher concentrations of Y_2O_3 led to faster creep rates. The creep rate was independent of whether the grain-boundary phase had been crystallized or not. At stresses >≈40 MPa, the pure mullite exhibited steady-state creep, but the Y_2O_3-containing specimens exhibited tertiary creep. Electron microscopy indicated that the specimens that contained an amorphous grain-boundary phase generally exhibited a single large creep crack. The specimens that

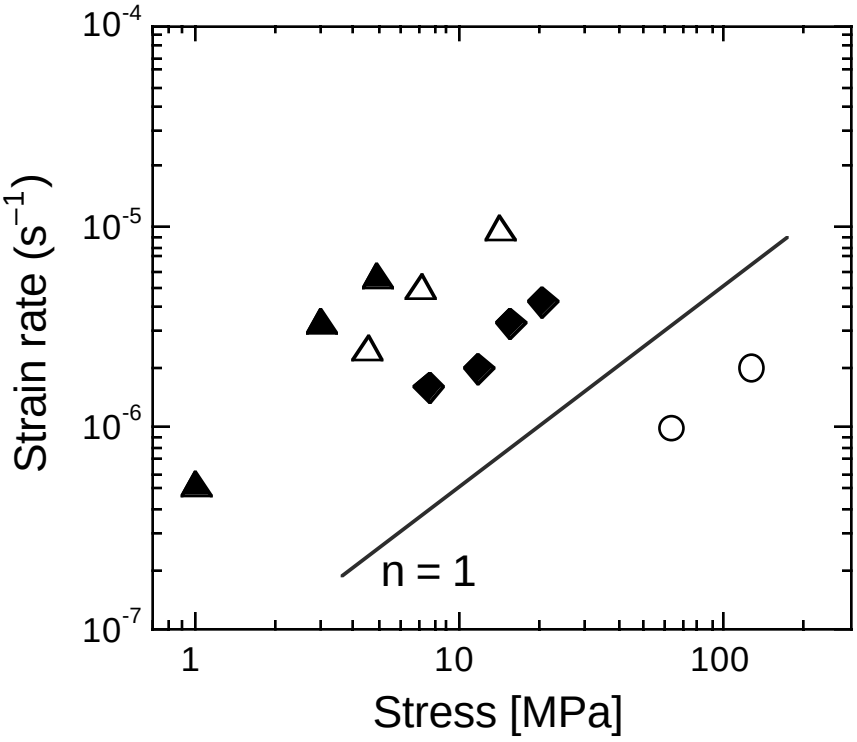

Fig. 67. Steady-state strain rate as a function of stress: open circles = 1197°C, CSR test; filled diamonds = 1300°C, CL test; open triangles = 1398°C, CSR test; filled triangles = 1400°C, CL test. Line drawn for n = 1.

contained a crystallized grain-boundary phase exhibited many smaller cavity-like cracks. The crystallization treatment appeared to have been partially effective, but did not produce complete crystallization (Fig. 71). The remaining Y_2O_3-rich material promoted rapid creep rates.

It is clear that for many high-temperature structural applications, pure mullite is a suitable candidate. Mullite that contains a sintering aid such as Y_2O_3 will not be able to achieve the same level of performance.

4.2 Si_3N_4/BN Fibrous Monoliths

Several hot-pressed plates for property studies were received from ACR: Si_3N_4, BN, unidirectionally reinforced Si_3N_4/BN FMs, and 0/90° and ±45° FMs. These materials were used for microstructural studies, and measurement of elastic, interfacial, fracture, thermal-expansion, residual-strain, and creep properties.

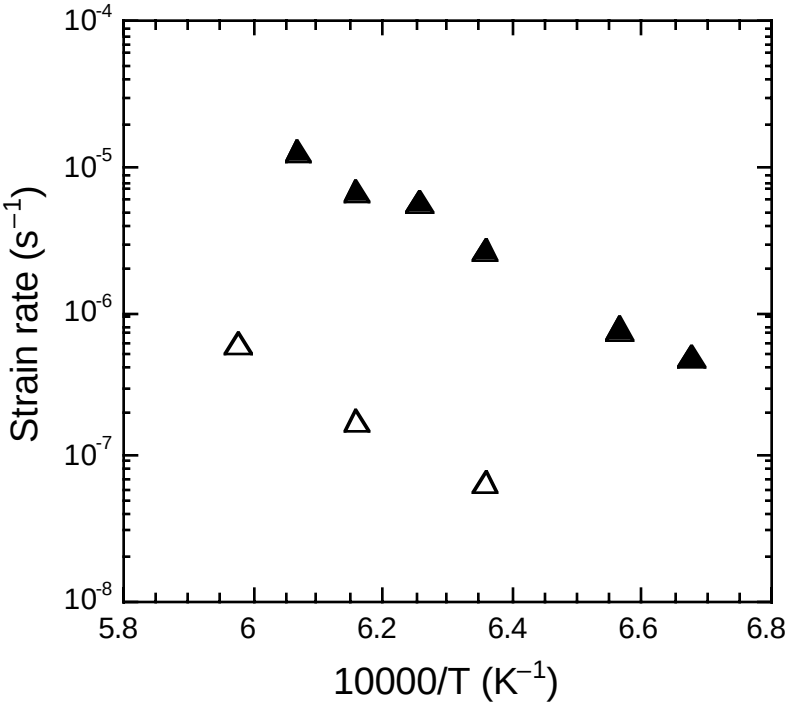

Fig. 68. Steady-state strain rate vs. reciprocal temperature in CL tests for stresses of 3 MPa (open triangles) and 20 MPa (filled triangles).

4.2.1 Microstructures of Si_3N_4/BN Fibrous Monoliths

Nondestructive evaluation (NDE) studies of FMs began at ANL in the fall of 1997. Work before the onset of this program was conducted in conjunction with WPAFB and was supported by other DOE programs. In these FM studies, WPAFB sent two types of specimen for examination: one with 125-µm cells and the other with 250-µm cells. Some of the specimens contained notches. For these first studies, the layup was mainly 45/0/45°. Monolithic Si_3N_4 specimens were also examined. In total, 25 specimens were examined.

Because of the BN cell boundary, it was not possible to immerse the specimens into water; thus, the use of conventional water-coupled ultrasonic methods was precluded. Furthermore, the main failure mechanism was thought to be a form of delamination because of the fabrication technique that was used. Therefore, we initially concentrated on two NDE methods in this work: (1) air-coupled ultrasonics for detection of delamination and (2) high-sensitivity thermal-imaging techniques. WPAFB used other NDE methods, including conventional X-ray film radiography, which probably will not be sensitive to delamination.

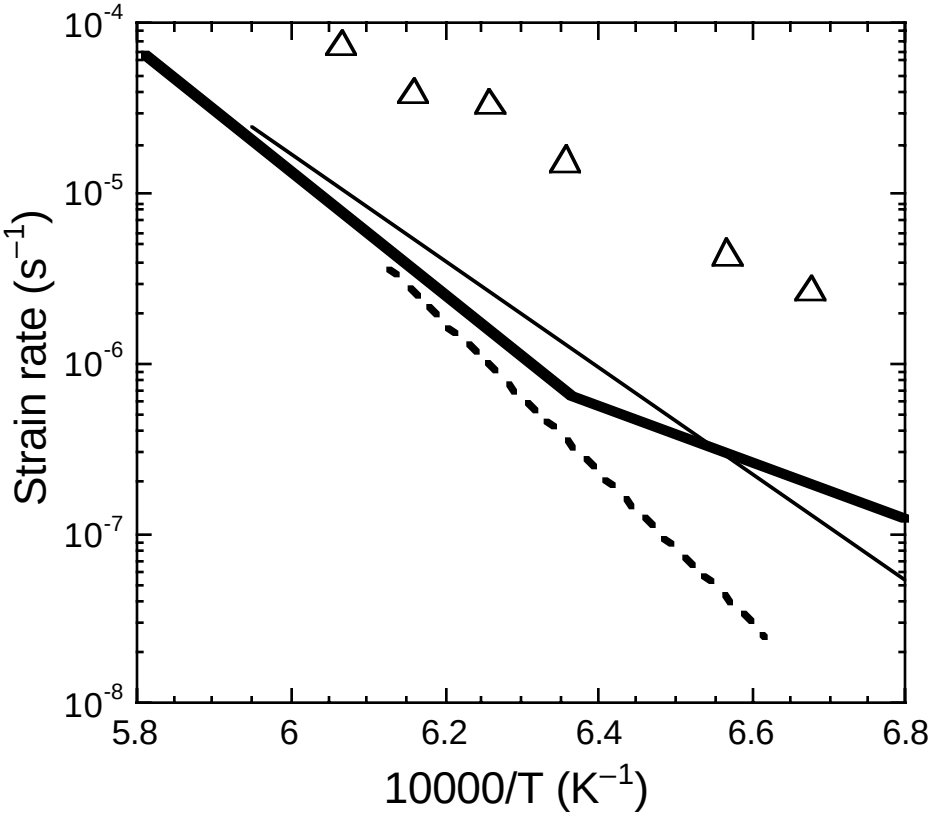

Fig. 69. Calculated creep rates at 100 MPa stress for $ZrSiO_4$ (triangles) and creep rates for mullite from Torrecillas et al. (Acta Mater. 45 (1997) 897), bold line; Hynes and Doremus (J. Am. Ceram. Soc. 74 (1991) 2469), fine line; and Tkalcec et al. *(J. Euro. Ceram. Soc. 18 (1998) 1089), dashed line.*

Data from NDE results suggest that the thermal-diffusivity value of monolithic Si_3N_4 is 1.13 x 10^{-5} m / s^2, whereas a quasi-isotropic FM weave geometry increases the thermal diffusivity to 1.33 x 10^{-5} m / s^2. BN thicknesses of 125–250 µm correspond to thermal diffusivities of 1.03–1.06 x 10^{-5} m / s^2. The sensitivity of thermal imaging is quite high to variations in fiber architecture. Damage from fast fracture has also been detected both by thermal imaging and air-coupled ultrasonic methods. We concluded that NDE can be used to map out density variations as a function of processing methods and techniques, detect and quantify delaminations, and determine cracking in the material caused by loads or thermal treatments.

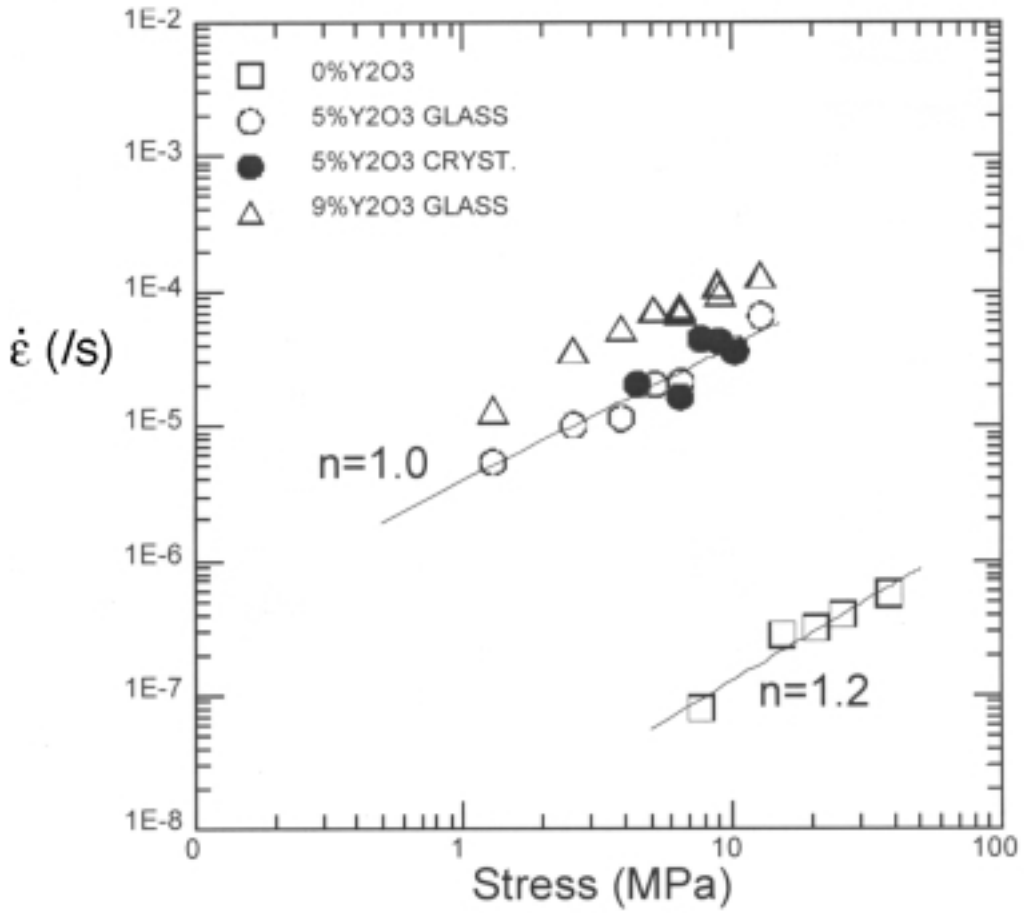

Fig. 70. Creep data at 1400°C for various mullite specimens.

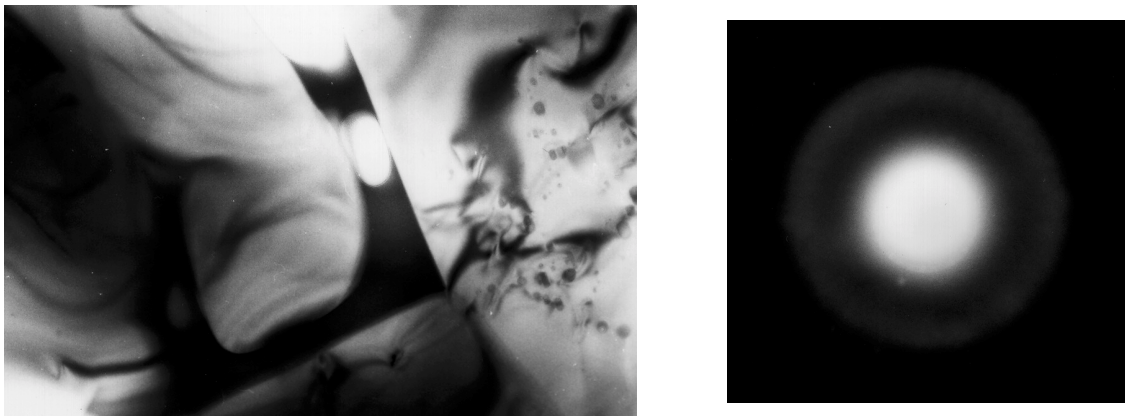

(a) (b)

Fig. 71. TEM photomicrograph showing (a) amorphous-plus-crystalline grain-boundary phase in mullite + 5% Y_2O_3 specimen and (b) electron diffraction pattern from amorphous region.

Notched specimens for fracture toughness testing were examined by complementary NDE techniques before and after mechanical testing. Most had a notch depth a to width w ratio of a/w = 0.3. NDE studies included: air-coupled through-transmission ultrasonic attenuation mappings (C-scans), water-coupled through-transmission C-scans, and high-sensitivity thermal imaging that incorporated closeup imaging with pixel sizes of ≈74 μm.

In the water-coupled ultrasonic study, we employed a configuration significantly different from that used by WPAFB. We employed a through-transmission configuration with 5-MHz focused transducers, as opposed to a reflection back plate and unfocused transducers. The acoustic attenuation image appeared to have better spatial resolution than the image produced when a reflector back plate was used.

An example of the type of data generated, Fig. 72 shows NDE data obtained by through-transmission water-coupled ultrasound (UT), through-thickness thermal diffusivity (≈75 μm spatial resolution), and through-transmission film X-ray imaging methods. Si_3N_4/BN FM specimen 97-57B, which had been fatigue loaded, was thought to have delaminations. The thermal image revealed the delaminations with the best definition, and the water-coupled UT also verified the presence of these features. The through-transmission X-ray image revealed damage, but not its extent.

Under the auspices of this program, we examined all of the plates provided to us by ACR (FMs shown in Fig. 73). In one aspect of this work, we used a 160-kVp microfocus X-ray system with a 15–20 μm spot size. The detector was an image intensifier/CCD array camera. We used 80-KV accelerating voltage and a detector pixel size of 75 μm. The data acquisition time was 2 s.

The Si_3N_4 and BN plates contained no serious flaws. Figure 74 shows the through-transmission X-ray image for Plate 1 (0/90° layup) and Plate 2 (±45° layup). Plate 1 exhibited slight, but detectable, density variations. The curved sides are the result of an artifact in data acquisition.

Thermal images were also obtaind. We used a 256 x 256 x 12-bit thermal imaging camera with the test setup configured for through transmission. Full-field image data were taken from four 78 x 78-mm regions with a pixel resolution of 348 μm. The thermal diffusivity of the material was determined by a method developed at ANL.

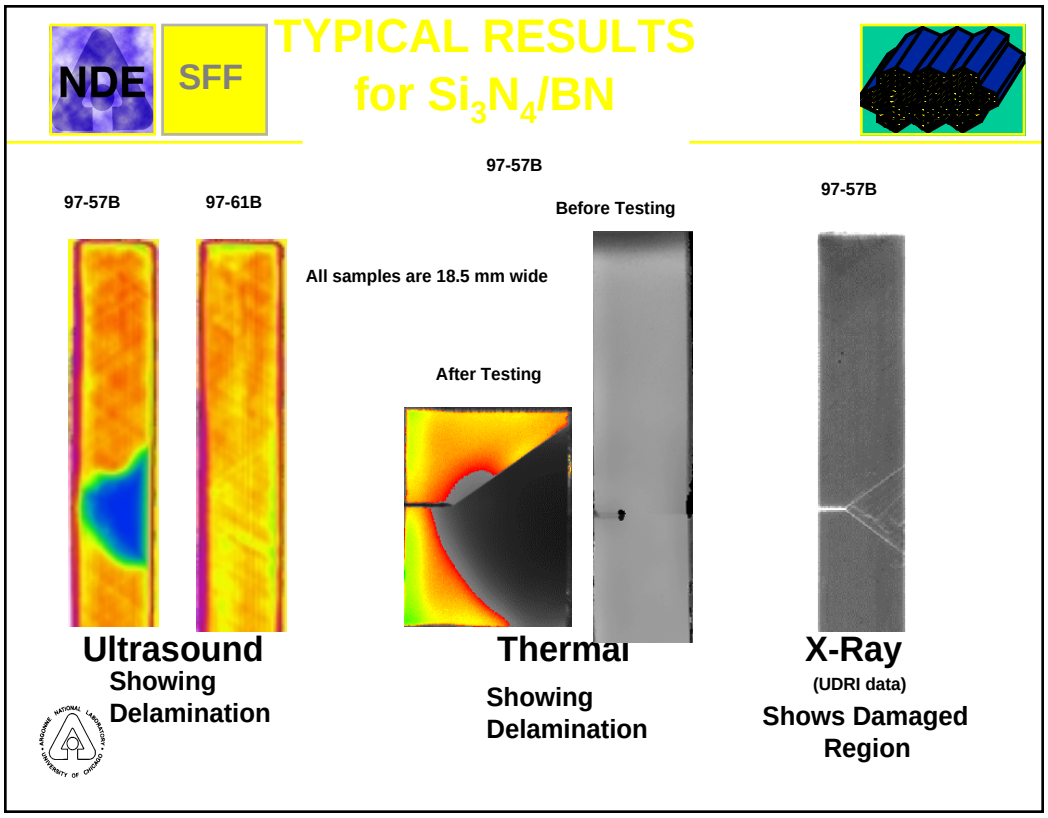

Fig. 72. NDE image data for FM specimen 97-57B: (a) through-transmission water-coupled UT data, (b) thermal-diffusivity image data, and (c) through-transmission X-ray image (from WPAFB).

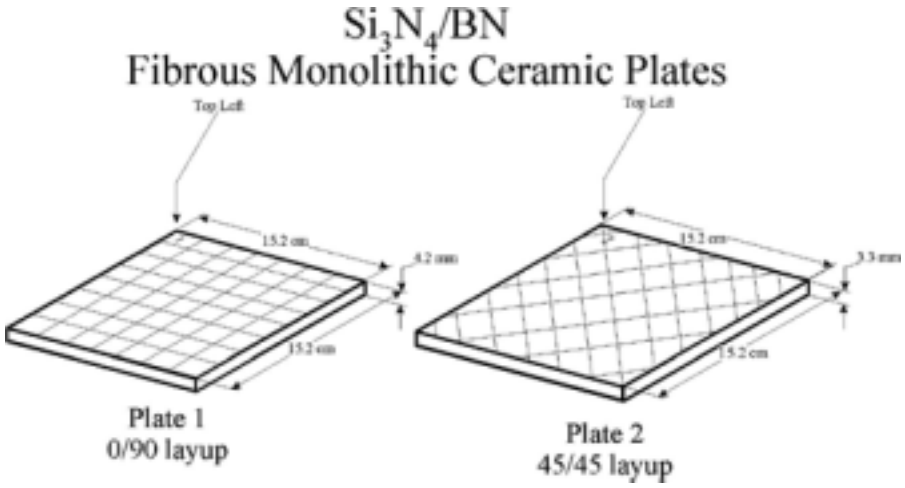

Fig. 73. Schematic diagrams of FM plates for NDE studies.

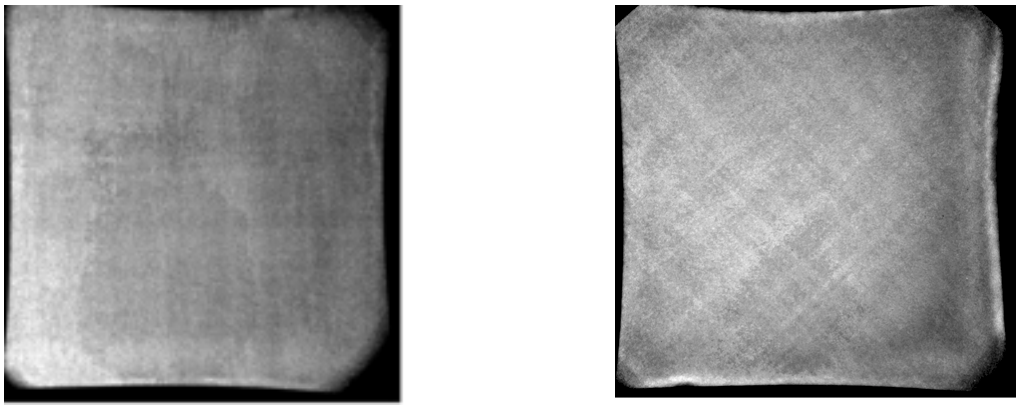

(a) (b)

Fig. 74. Through-transmission X-ray image for (a) 0/90° layup plate and (b) ±45° layup plate.

One significant delamination, in the upper right corner, was detected in Plate 1; several smaller regions of low diffusivity were also found toward the top-center of Plate 1 (Fig. 75). These irregularities did not appear in any other image and may have been an artifact of the data acquisition. The centers of both plates were free of appreciable defects.

A second set of Si_3N_4/BN FM plates from ACR was also examined by thermal imaging. The pixel resolution was 296 µm. No major flaws were found in either of these plates (Fig. 76). The dark regions seen in the right side of the images are due to the mounting of plates in the experimental setup. The thermal-diffusivity values of these two plates were 9.13 x 10^{-6} cm^2/s for an SFF-processed 0/90° plate and 7.87 x 10^{-6} cm^2/s for a uniaxial plate. These values compare to the thermal-diffusivity values of 6.32 x 10^{-6} cm^2/s for the previous 0/90° plate and 7.13 x 10^{-6} cm^2/s for the ±45° plate.

4.2.2 Elastic Moduli of Si_3N_4/BN Fibrous Monoliths

Fundamental baseline data are clearly needed to support the modeling efforts. Elastic moduli are essential, but they proved to require substantial ingenuity to obtain. Values for dense Si_3N_4 are available in the literature; we obtained 242.5 GPa. Values reported for BN have yet to gain complete acceptance and those for our various Si_3N_4 BN FMs had not yet been measured.

Several techniques and collaborations with many institutions were implemented to measure the elastic moduli of BN and the FMs. Hot-pressed BN plate specimens were produced by FM techniques at ACR. The plates incorporated

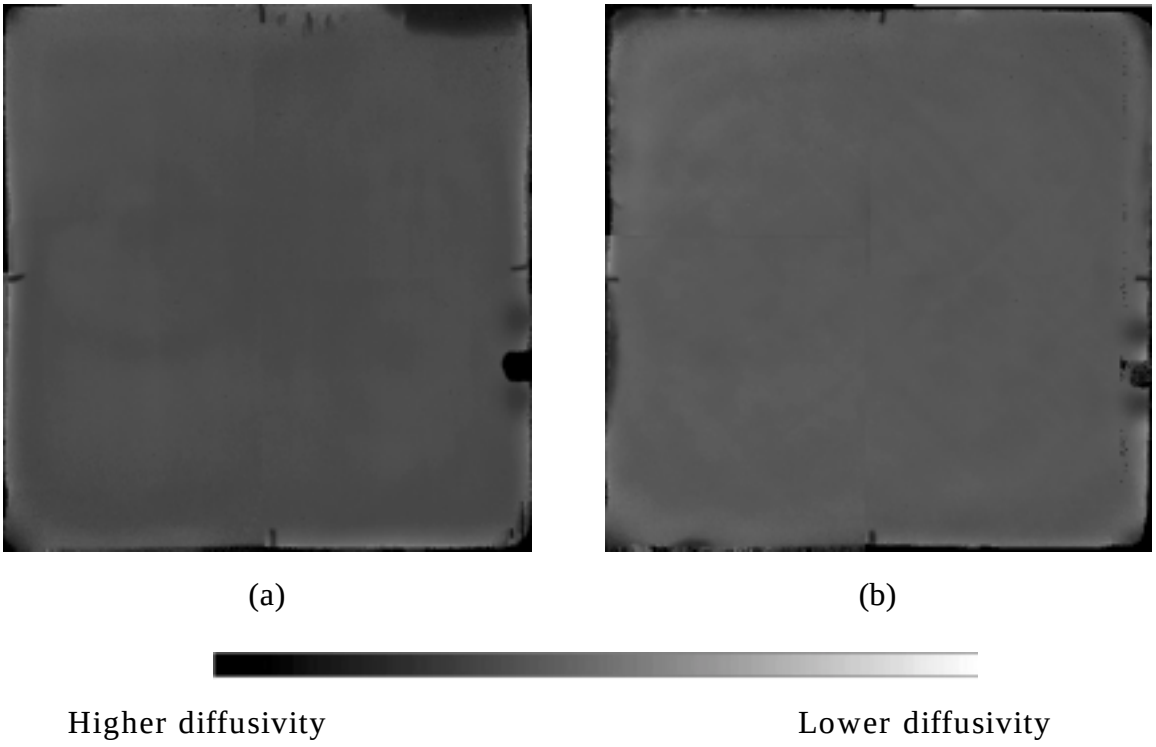

Fig. 75. Thermal diffusivity maps of (a) Plate 1 (0/90°) and (b) Plate 2 (±45°).

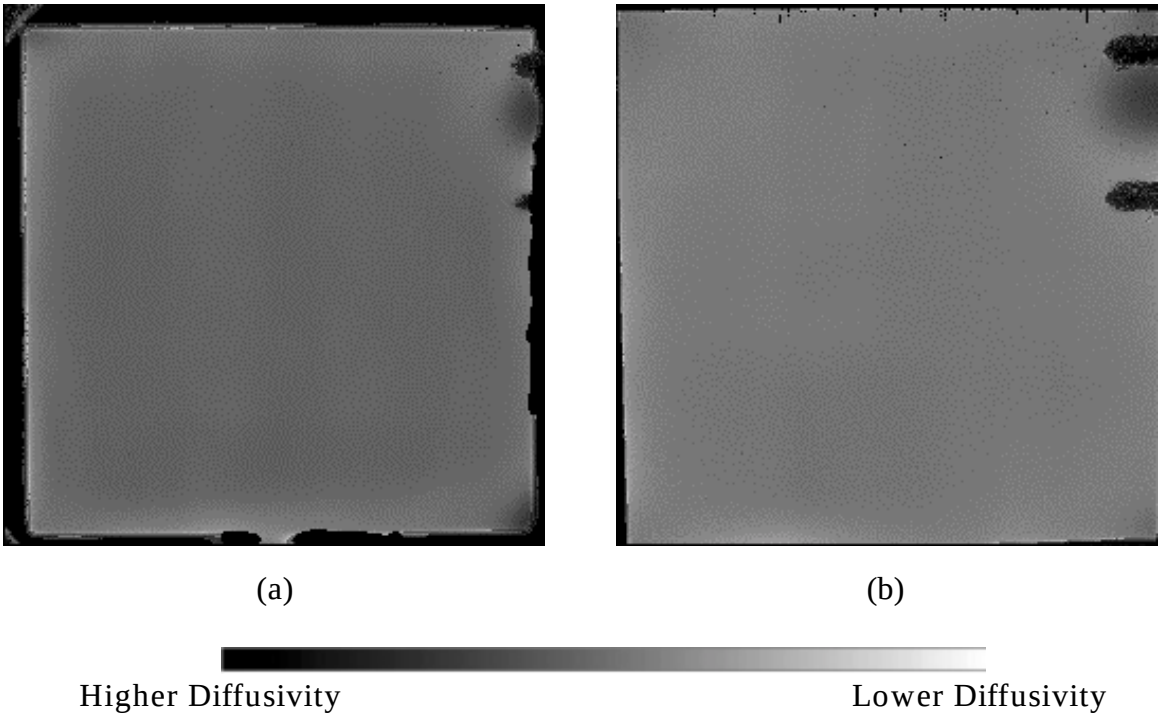

Fig. 76. Thermal-diffusivity images for two FM plates: (a) uniaxial and (b) 0/90°.

Al_2O_3 and Y_2O_3 sintering aids, which are found in the BN cell-boundary phase of FMs. They enter the BN by diffusion from the Si_3N_4 cells. The Si_3N_4/BN FMs were also supplied by ACR.

At ANL, a laser vibrometer was used to measure the elastic modulus (E) of BN. The laser vibrometer, which incorporated a low-power He-Ne laser (wavelength 0.63 μm), was part of a project funded by NASA, but the equipment and technology were used on this project (Fig. 77). Measurements were taken on flexure bars (Fig 78).

To determine the through-thickness elastic modulus, an ultrasonic-mode conversion technique was used at ANL. In this technique, both shear and longitudinal wave velocities were measured. From these velocities, both elastic modulus and Poisson's ratio could be determined. A breakdown of the sample distribution from a single plate specimen is shown in (Fig. 79).

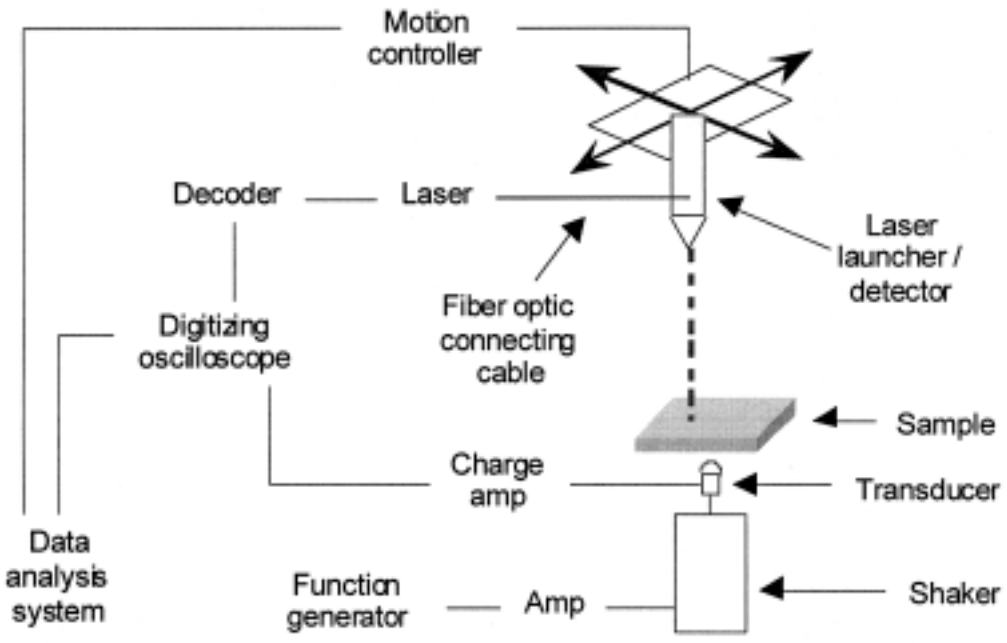

Fig. 77. Laser vibrometer schematic diagram.

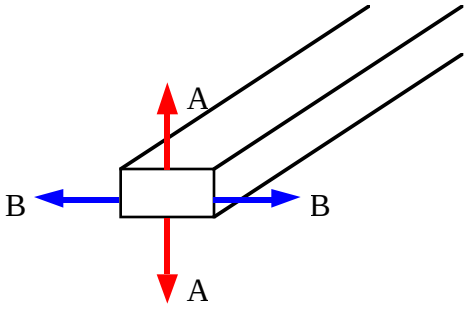

Fig. 78. Schematic diagram of flexure specimen, showing orientations used for elastic modulus determinations.

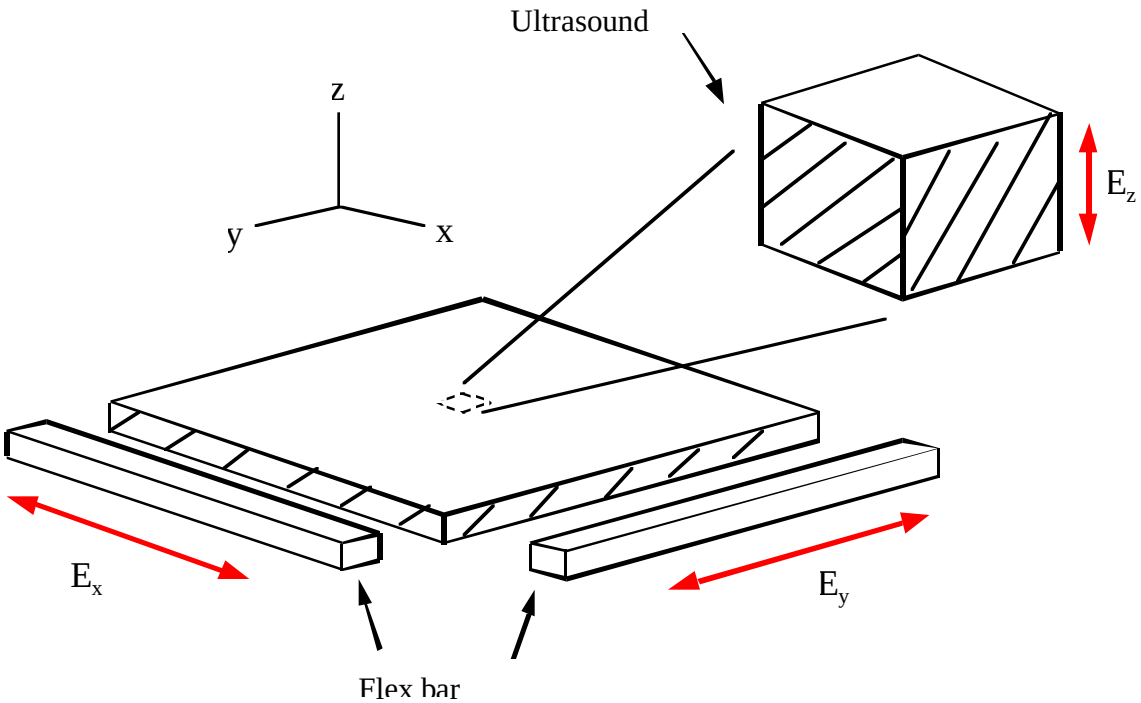

Fig. 79. Diagram showing three-axis specimens for elastic-modulus measurements.

At ANL, values of E for BN were also obtained directly from stress-strain curves. Specimens were fitted with strain gauges and loaded into an Instron Model 4505 tester. The loading rate was 0.5 mm/min. Applied stress and strain were recorded. A typical profile for the through-thickness value of E is shown in Fig. 80. From this figure, E was calculated to be 6.9 and 6.6 GPa. These values are significantly lower than the value of 20.7 GPa measured for in-plane loading.

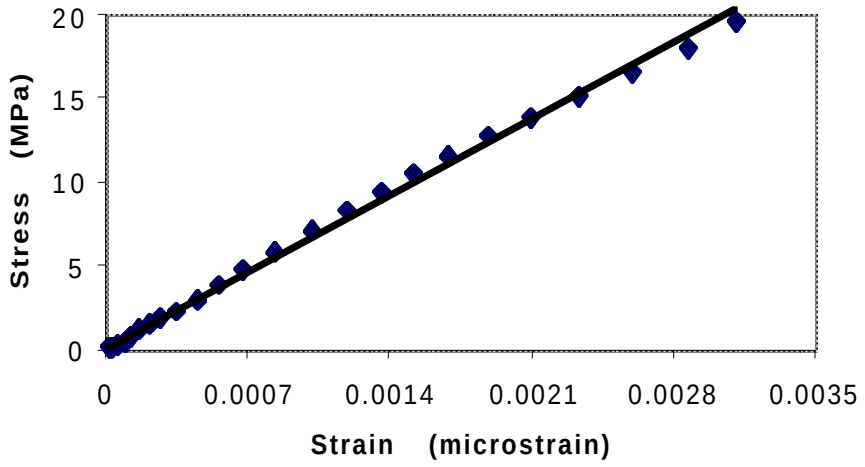

Fig. 80. Stress-strain profile of BN specimen obtained in compression loading parallel to hot-pressing direction.

BN specimens were also sent to Southern Research Institute (SRI), Prof. Murli Manghnani at the University of Hawaii, and Prof. Raj Singh at the University of Cincinnati (UC) for independent testing. Two separate methodologies were applied, an ultrasonic-mode conversion technique and an ultrasonic modal technique.

BN and Si_3N_4/BN FM specimens were also sent to Prof. Boris Smirnov of the A. F. Ioffe Physico-Technical Institute in St. Petersburg, Russia. E was determined at room temperature with a resonance technique by electrostatic excitation of longitudinal vibrations of rod-shaped specimens. The value of E was calculated from the measured fundamental frequency f and the equation $E = 4d\ l^2\ f^2\ n^{-2}$, where l is the length of the sample, d is bulk density, and n is the number of the excited harmonic (in this case, n = 1). For E as a function of temperature, E(T), acoustical measurements were conducted on 2.5 x 2.4 x 24.5-mm^3 bars cut from a larger plate. The bars were attached to knife-edge holders at the midpoint (i.e., at the displacement node of a standing ultrasonic wave) for excitation of longitudinal vibrations; the first harmonic was at a frequency of ≈200 kHz. The measurements were carried out in a chamber filled with He.

The results for the BN are summarized in Table 12. Through-thickness values were approximately independent of measurement technique, but the in-plane values exhibited a fixed trend. The statically obtained value was 20.7 GPa, whereas all vibrational measurements yielded values of ≈37 GPa. The lower value of E in the through-thickness direction is related to the layered crystal structure of BN and the strong texture imparted by the hot-pressing (Fig. 81).

Table 12. Measured values of E for BN

Measurement	E (GPa)
In-plane (ANL, static)	20.7
In-plane (ANL, vibrational)	37.1
In-plane (UC, vibrational)	37.8
In-plane (Ioffe, vibrational)	36.1
Through-thickness (ANL, static)	6.75
Through-thickness (SRI, vibrational)	5.6

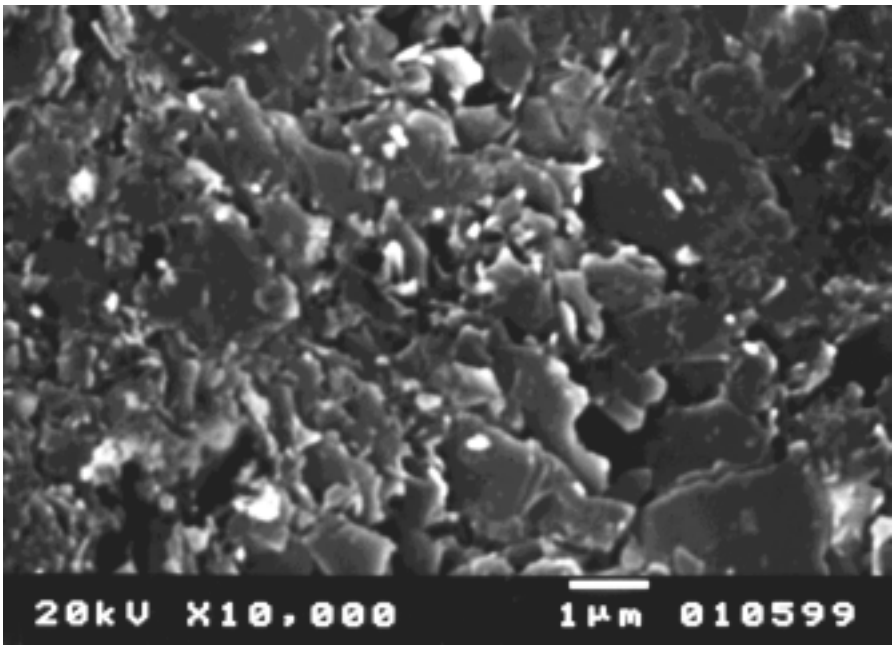

Fig. 81. SEM photomicrograph of BN surface, revealing highly textured, platelike grains.

Variations in microstructure accounted for only a small amount of the difference between the vibrational and statically determined values. For example, many samples were measured at ANL and UC, and the value of E was found to be 37.1 ± 0.2 GPa and 37.8 ± 0.2 GPa, respectively.

To determine if the elastic modulus of BN is significantly dependent on measurement dynamics, it was remeasured at ANL at various resonant frequencies. We found that E increased slightly with decreasing frequency, so clearly frequency cannot account for the difference observed in the in-plane value of E.

Given that the static measurements were direct, and that they were supported by at least three other measurements (c.f., e.g., J. H. Edgar, in Properties of Group III Nitrides, ed. J. H. Edgar (INSPEC, London, 1994) pp. 7-21), the values of 20.7 and 6.75 GPa were used for the modeling studies. The fact that all of the vibrational studies yielded different but consistent results is a matter for further study.

Several comparisons were also made of the values of E for various FMs. In these studies, the effects of microstructure were likely to be more pronounced. Several results are shown in Table 13. The observed variations can, in all likelihood, be attributed to processing and microstructural differences.

In collaboration with Prof. Smirnov, we also obtained E(T) data for Si_3N_4/BN FMs and their two constituents. The data are clearly of interest to applications of these FMs. Various resonance techniques were used, but only moderate temperatures could be reached. Results are presented in Table 14. Given the inherent experimental difficulties, the data are quite consistent and within expectations for structural ceramics.

No explanation is offered for why the BN appears to become stiffer at moderate temperatures. The FMs are slightly stiffer in the longitudinal direction than would be predicted by a simple rule of mixtures. Alloying between the Si_3N_4 constituents and the BN is a possible cause.

Table 13. Values of E for various Si_3N_4/BN FMs

Sample type	Fabrication method	E (GPa) Vibrational	E (GPa) Static
0/90°	Hand layup	189 ± 3	158 ± 34
0/90°	Hand layup	235.4	-
0/90°	SFF	213.8 ± 55	-
±45°	SFF	112 ± 1	92 ± 15
0°	Hand layup	208 ± 3	216 ± 2
0°	Hand layup	295.0	-
0°	SFF	85.8 ± 27	-
90°	Hand layup	128.0	-

Table 14. Elastic-modulus data for Si_3N_4/BN FMs, Si_3N_4, and BN

Sample type	E (GPa)	% change	
		400°C	600°C
Si_3N_4	311.1	-1.2	-2.3
BN	36.1	-0.0	+4.3
Si_3N_4/BN, 0°	295.0	-0.4	—
Si_3N_4/BN, 0/90°	235.4	-0.4	—
Si_3N_4/BN, 90°	128.0	-1.1	—

4.2.3 Push-out of Si_3N_4 Cells

Based on theoretical modeling and experimental work on fracture resistance of Si_3N_4/BN FMs being conducted at UCSB, it is clear that interfacial sliding stress plays an important role in controlling the fracture resistance of FMs. Professor Zok and his colleagues have shown that crack bridging stresses can be directly correlated to parameters that include interfacial sliding stress, cell pull-out lengths, cell volume fraction, and cell dimensions. Thus, characterization of interfacial sliding stresses can be a quick and easy method to gain information about the overall fracture resistance of FMs. Therefore, interfacial fracture resistance of Si_3N_4/BN was determined by cell push-out tests (Fig. 82).

Push-out tests were conducted by first locating individual cells under a tungsten carbide indenter with a circular flat tip ≈100 μm in diameter and fixed to the top plate of the testing system. After positioning, cells were loaded at a constant displacement rate of 0.05 mm/min, while the load-displacement behavior was continuously monitored. Typically, 15-20 cells were pushed out to obtain a representative value for the interfacial properties.

It was clear that the sliding of the cells occurred at the interface between the Si_3N_4 and BN (Figs. 83 and 84). In a typical load-displacement plot, there was a linear increase in load, followed by a sharp drop, probably corresponding to a debonding phenomenon at the interface. Subsequently, the load again increased and gradually dropped, indicating frictional sliding and push-out of the cell (Fig. 85). The debond load and the peak load values ($P_{d,s}$) during push-out were used to determine the debonding and frictional sliding stresses $\tau_{d,s}$:

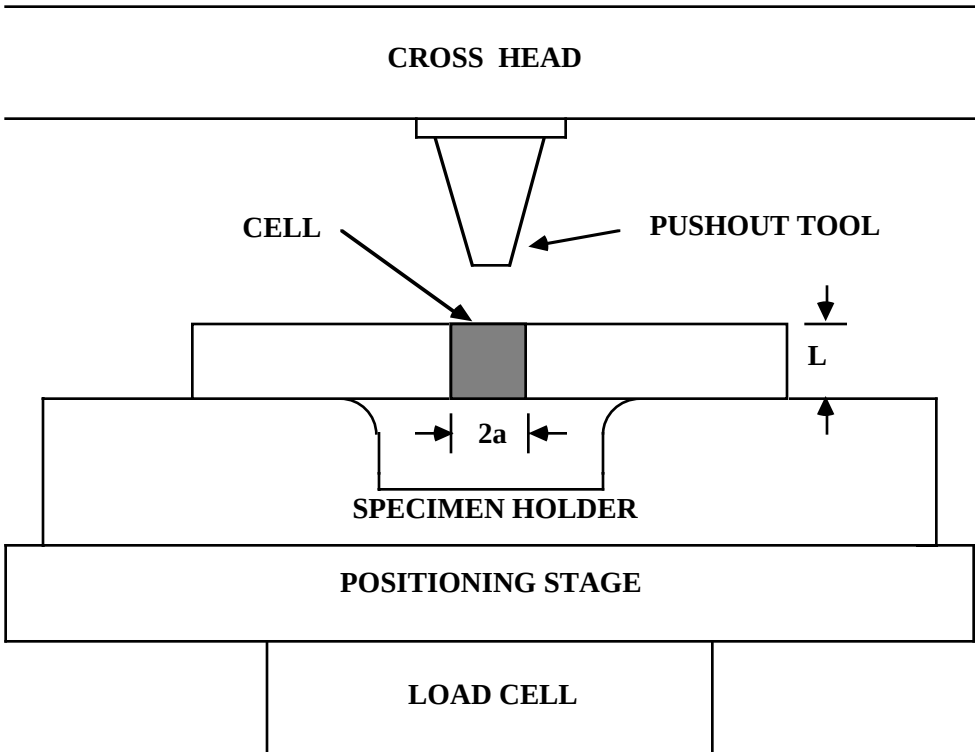

Fig. 82. Schematic diagram of experimental setup used for cell push-out test.

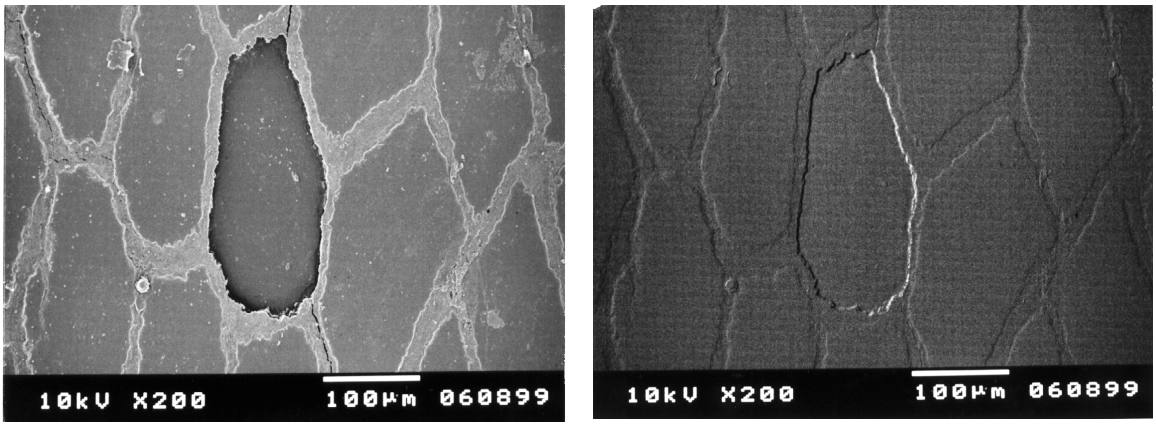

(a) (b)

Fig. 83. SEM photomicrograph of Si_3N_4/BN FM showing pushed-out cell in (a) secondary electron mode and (b) back-scattered-electron mode.

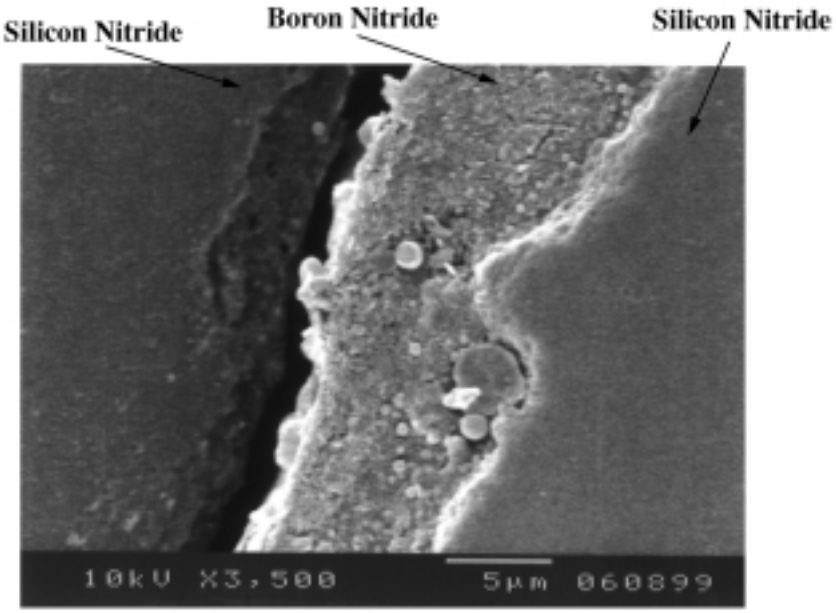

Fig. 84. High-magnification SEM photomicrograph of Si_3N_4/BN FM, showing sliding of cell at interface.

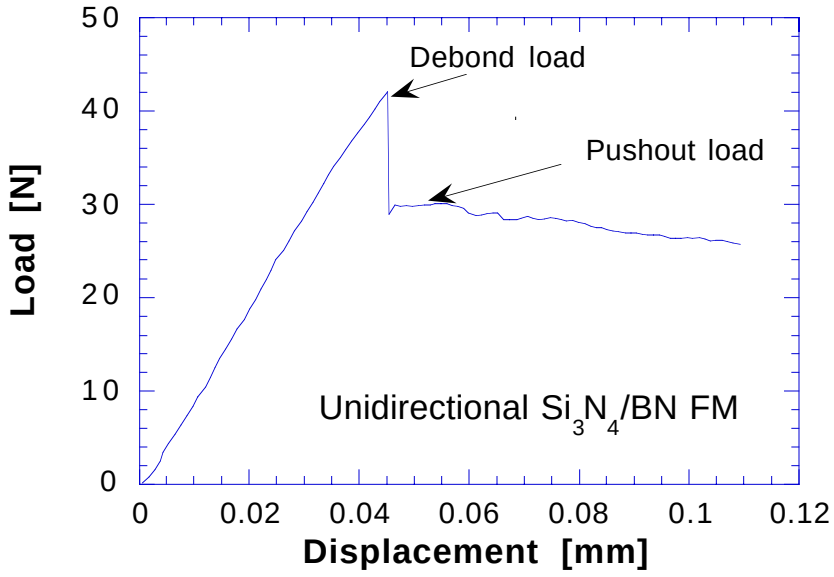

Fig. 85. Typical load-displacement plot for cell push-out in Si_3N_4/BN FM.

$$\tau_{d,s} = P_{d,s} / w t , \quad (4.1)$$

where w is the perimeter of the cell and t is the sample thickness. Based on >15 pushed-out cells, the average debonding stress was 45 ± 8 MPa and the average sliding stress was 25 ± 7 MPa.

4.2.4 Fracture of Si_3N_4/BN Fibrous Monoliths

The fracture strengths of specimens from the Si_3N_4 and BN plates and several Si_3N_4/BN FMs were measured in four-point flexure. The Si_3N_4/BN FMs were also tested in biaxial flexure.

Four-Point Flexure Tests

The strengths of the Si_3N_4 and BN materials and several Si_3N_4/BN FMs were obtained from samples ≈2.5 x 5 x 45 mm. The tensile surfaces were polished and beveled by standard techniques. The support and loading spans were 40 and 20 mm, respectively. The tests were conducted at a constant displacement rate of 1.27 mm/min in an Instron Model 1125 universal tester. In addition, a strain gauge was mounted on the tensile surface of some of the samples to obtain the stress-strain response accurately. For each specimen type, at least three samples were tested.

Typical load-displacement plots for monolithic Si_3N_4 and Si_3N_4/BN FM samples are shown in Fig. 86. Work-of-fracture of the FMs was determined from the area under the load-displacement plots. After the peak load was attained, the load-carrying ability of all the FMs was significantly greater than that of monolithic Si_3N_4. The peak stresses were highest for the uniaxial samples and lowest for the ±45° FMs (Table 15).

Laminate theory was used to predict values of E for the investigated architectures. For the uniaxial architecture, we used the well-known Voight rule-of-mixtures,

$$E_1 = E_{BN}V_{BN} + E_{SN}(1 - V_{BN}) , \quad (4.2)$$

where E_{BN} and E_{SN} are the Young's moduli of BN and Si_3N_4, respectively, obtained in mechanical testing; and V_{BN}, the volume fraction of BN phase, was taken to be 0.15. For the multiaxial architectures, the E values were calculated on the basis of the results for the unidirectional FMs as per laminate theory. The values agreed well with the predictions from laminate theory for uniaxial and 0°/90° architectures; however, a large discrepancy was noted between the predicted and measured values of E for the ±45 architecture. This may be due to the increased role of the weak BN phase in stress distribution in specimens with such cell orientation.

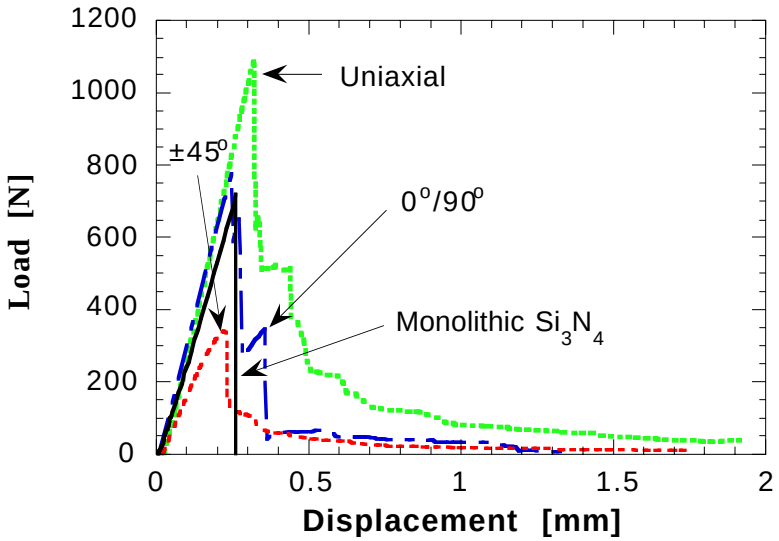

Fig. 86. Typical load-displacement data for specimens tested in four-point flexure.

Table 15. Mechanical properties of BN, Si_3N_4, and Si_3N_4/BN FMs

Sample type	Measured E (GPa)	Predicted E (GPa)	Strength (MPa)	Work-of-fracture (kJ/m^2)
Si_3N_4	242 ± 5	-	677 ± 127	-
BN	21	-	38 ± 3	-
Si_3N_4/BN (0°)	216 ± 2	209	476 ± 30	12.6 ± 1.9
Si_3N_4/BN (0/90°)	158 ± 34	167	379 ± 86	4.9 ± 2.2
Si_3N_4/BN (±45°)	92 ± 15	150	175 ± 13	2.7 ± 1.7

Measured WOF values for the three Si_3N_4/BN FM sets ranged from 12.6 kJ/m^2 for unidirectional FMs to as low as 2.7 kJ/m^2 for ±45° FMs. These values are comparable to those of many continuous-fiber-reinforced ceramic matrix composites. The dependence of WOF on cell orientation in FMs was related

qualitatively to the failure modes. Failure in unidirectional FMs was associated with toughening mechanisms such as extensive delamination and crack deflection. This propensity for delamination and crack deflection was significantly reduced in the multidirectional FMs with 0/90° and ±45° orientations.

Biaxial Flexure

To investigate the flaw sensitivity and failure mechanisms of FMs under generalized loading, Si_3N_4/BN FMs were also tested biaxially. In this method, a disk-shaped specimen was placed on a ring support on one side and loaded from the other side by oil pressure. The samples were separated from an oil reservoir by a thin metallic diaphragm and supported by a ring made of ball bearings that ran along the circumference of the disk. Ball-bearing support was used to minimize friction at the loading points (Fig. 87).

The distributions of radial (σ_r) and tangential (σ_t) stresses as a function of the distance from the center of the disk were determined from plate theory. Stresses in the 31.75-mm-diameter x 3.2-mm-thick disk with an applied pressure of 10 MPa are shown in Fig. 88. Maximum stresses are at the center of the disk and are equibiaxial.

For initial trials, stainless steel and Al_2O_3 disks 31.75 mm in diameter and 3 mm thick were used. The disks were first characterized for elastic moduli by ultrasonic methods. The average values for Young's modulus determined for stainless steel and Al_2O_3 ceramic were 198 and 368 GPa, respectively, in agreement with literature values.

Strain gauges were attached at the center of the tensile faces of the disks, which were then loaded. The applied transverse pressure on the disk and the corresponding strain were monitored. Theoretical lines of the peak strain (ε_b) as a function of maximum stress at the disk center σ_b, elastic modulus, and Poisson's ratio ν of the material were plotted per

$$\varepsilon_b t^2 = [\sigma_b (1 - \nu) t^2] / E \ . \qquad (4.3)$$

The correlation between the calculations and experimental data was excellent for both samples. The biaxial test system worked well and was deemed suitable for testing the Si_3N_4/BN FMs.

The FMs were tested until failure (Fig. 89). For all samples tested, failure strains were 1000–2000 με (Fig. 90). In addition, all samples exhibited an initial linear stress-strain relationship, followed by deviation from linearity, which appeared to indicate accumulation of damage in the FMs.

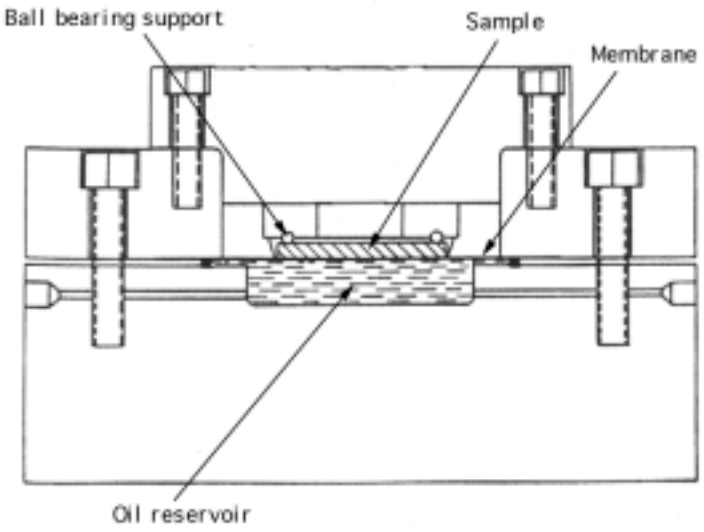

(a)

(b)

Fig. 87. (a) Schematic diagram of biaxial flexure test cell; (b) experimental setup for biaxial test system.

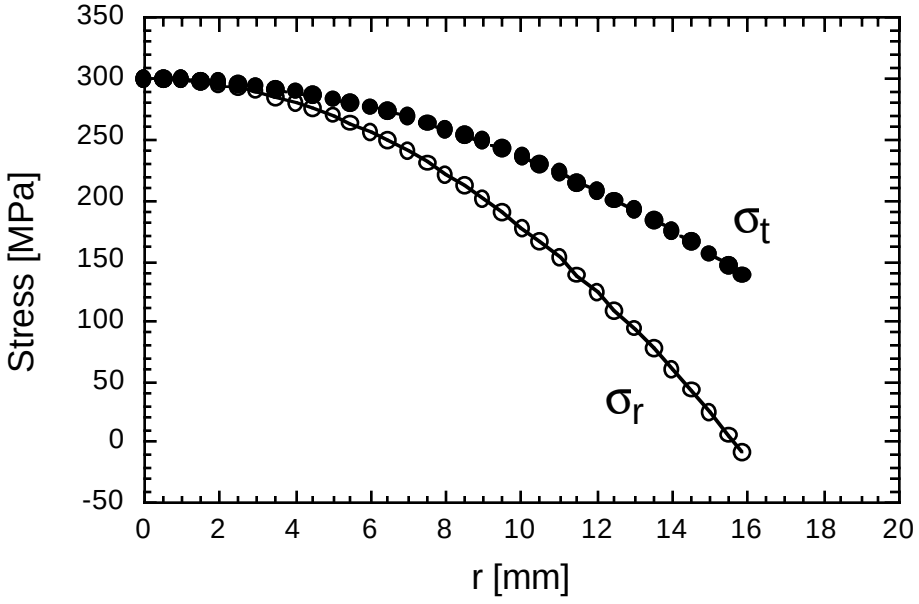

Fig. 88. Radial and tangential stresses developed in a 31.75-mm disk specimen subjected to biaxial loading.

A summary of the data collected at ANL is shown in Table 16. We are concerned that batch-to-batch billet variability in the FMs may significantly affect our interpretation.

Table 16. Properties of Si_3N_4 and Si_3N_4/BN FMs tested uniaxially and biaxially

Sample and test type	Measured E (GPa)	Predicted E (GPa)	Strength (MPa)
Si_3N_4/BN (0/90°, uniaxial)	158 ± 34	167	379 ± 86
Si_3N_4/BN (0/90°, biaxial)	200	—	283
Si_3N_4/BN (±45°, uniaxial)	—	150	175 ± 13
Si_3N_4/BN (±45°, biaxial)	224	—	167

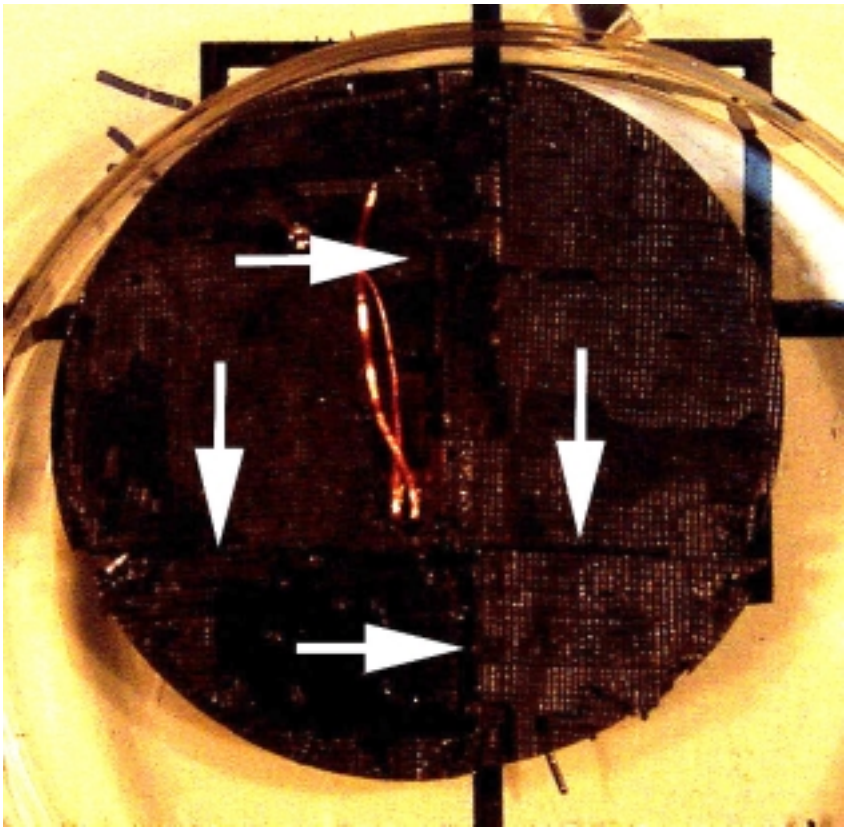

Fig. 89. 0/90° Si_3N_4/BN FM tested in biaxial flexure; complex fracturing, noted by white arrows, was observed.

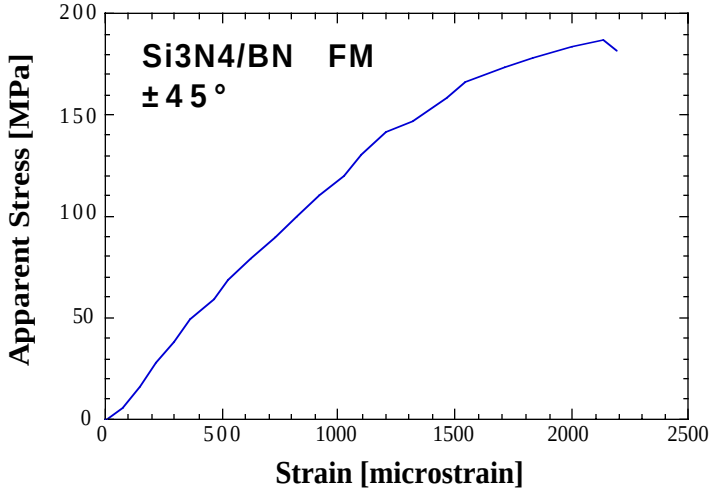

Fig. 90. Typical stress-strain curve for Si_3N_4/BN FM tested in biaxial flexure.

4.2.5 Thermal Expansion and Strains in Si_3N_4/BN Fibrous Monoliths

Residual stresses in ceramic composites, such as FMs, are determined primarily by the differences in CTE among the various components of the composite. To support the FM modeling work, CTEs and residual strains were measured for the BN and Si_3N_4 components and a few FMs.

Thermal Expansion in Si_3N_4/BN Fibrous Monoliths

CTEs were measured with a Theta Industries dilatometer (Port Washington, NY). Specimens were prepared by cutting 30-mm-long pieces from billets supplied by ACR. Measurements were made in N_2 to 1200°C. The CTEs of the BN and Si_3N_4 specimens are anisotropic because of preferred orientation of grains. Our CTE measurements were made perpendicular to the hot-pressing direction.

The expansion of BN specimen was nearly linear to 1200°C (Fig. 91). The CTE values of BN ranged from 1 x 10^{-6} °C^{-1} to 2 x 10^{-6} °C^{-1} at 400–1200°C. These values fall between the values of 7.5 x 10^{-6} °C^{-1} and 0.8 x 10^{-6} °C^{-1} reported in the literature for BN along parallel and perpendicular directions, respectively.

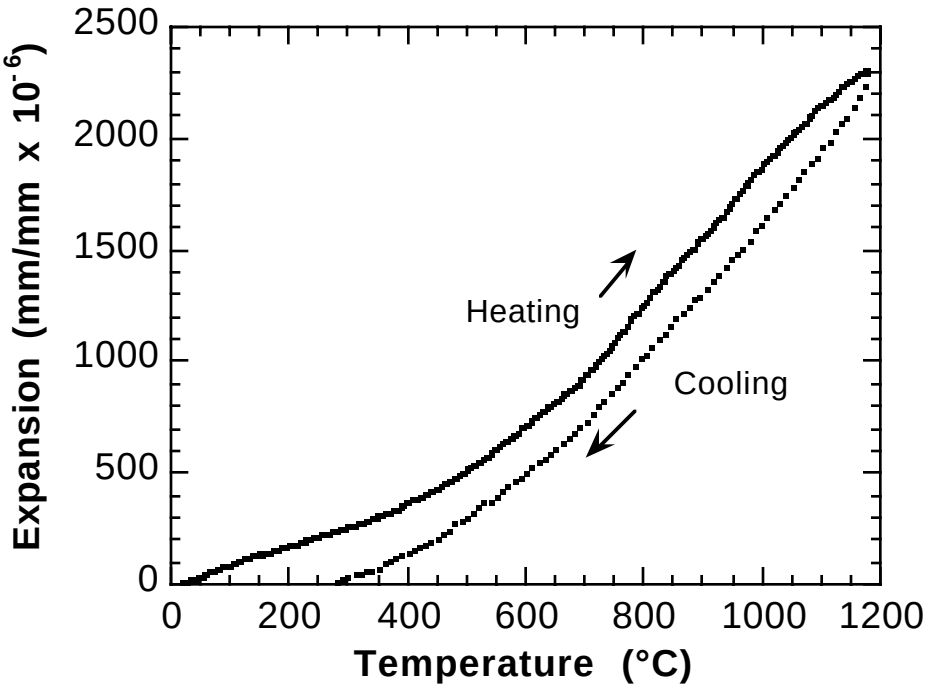

Fig. 91. Thermal-expansion data for monolithic BN in N_2.

The expansion of Si_3N_4 was also roughly linear to 1200°C (Fig. 92). In-plane CTE values were ≈2 x 10^{-6} $°C^{-1}$ at 200–1200°C. Out-of-plane values were 2.5–3.5 x 10^{-6} $°C^{-1}$. The reported values for hot-pressed Si_3N_4 in the literature are 3.0–3.9 x 10^{-6} $°C^{-1}$.

Thermal expansion of unidirectional FMs was also measured. Because these samples were hot-pressed, anisotropy was expected. Therefore, CTEs were obtained to 1200°C in three directions: in-plane parallel to the long axis of the cells, in-plane perpendicular to the long axis of the cell, and out-of plane, i.e., parallel to the hot-pressing direction (Fig. 93).

Results indicated roughly linear expansion to 1200°C. Although some hysteresis was observed, it was believed to be an experimental artifact. In-plane CTEs were quite similar, 2.5–4 x 10^{-6} $°C^{-1}$, whereas out-of-plane values were higher, 4–6 x 10^{-6} $°C^{-1}$.

Residual Strains in Si_3N_4/BN Fibrous Monoliths

At ANL's Intense Pulsed Neutron Source (IPNS), time-of-flight neutron powder diffraction was used to estimate residual strains in Si_3N_4/BN FMs supplied by ACR. The FM samples were placed in a diffractometer, as illustrated in Fig. 94. With time-of-flight diffraction, entire diffraction patterns were accumulated at all scattering angles. Thus, when an FM is oriented as shown, with the cell axis horizontal, strains in the longitudinal and transverse directions were measured simultaneously. To calculate strains, data from strain-free standards, prepared in an identical fashion as the FM, were required. We used monolithic pressed plates as strain-free standards.

Selected portions of longitudinal and transverse patterns from unidirectional Si_3N_4/BN are shown in Fig. 95. These patterns clearly illustrate the anticipated BN texture generated during hot-pressing, namely enhancement of BN(00l) intensity in the transverse direction and enhanced BN(l00) intensity in the longitudinal direction. In addition, these patterns show the β Si_3N_4 peaks.

Residual strains have been calculated for the Si_3N_4 phase by relating peak positions (i.e., lattice spacings) for individual reflections in the FM to those of the corresponding monolithic sample. Transverse scattering was the result of reflection geometry, whereas the longitudinal measurement was via transmission. Because BN is a good absorber of neutrons, a systematic offset of apparent lattice spacings for transmission geometry relative to reflection geometry was needed. Some uncertainty in values for the longitudinal strain therefore remained.

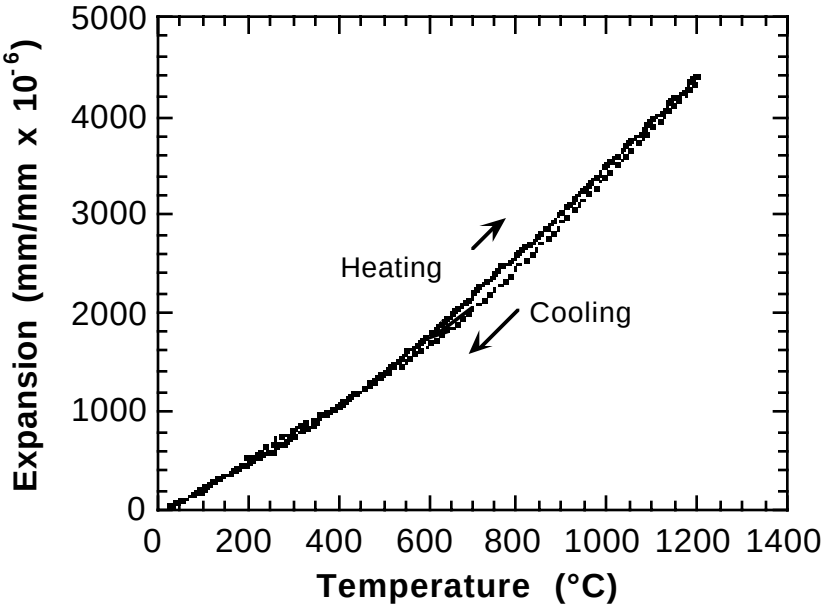

Fig. 92. Thermal expansion of hot-pressed Si_3N_4 in N_2.

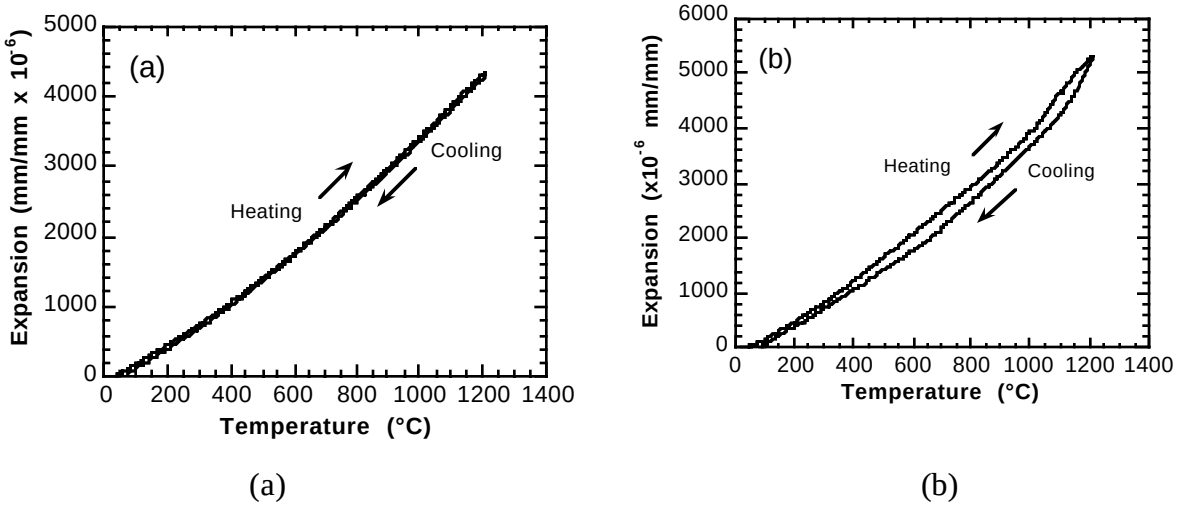

(a) (b)

Fig. 93. Representative thermal expansion data of unidirectional Si_3N_4/BN FMs: (a) in-plane parallel to cell length and (b) in-plane perpendicular to cell length.

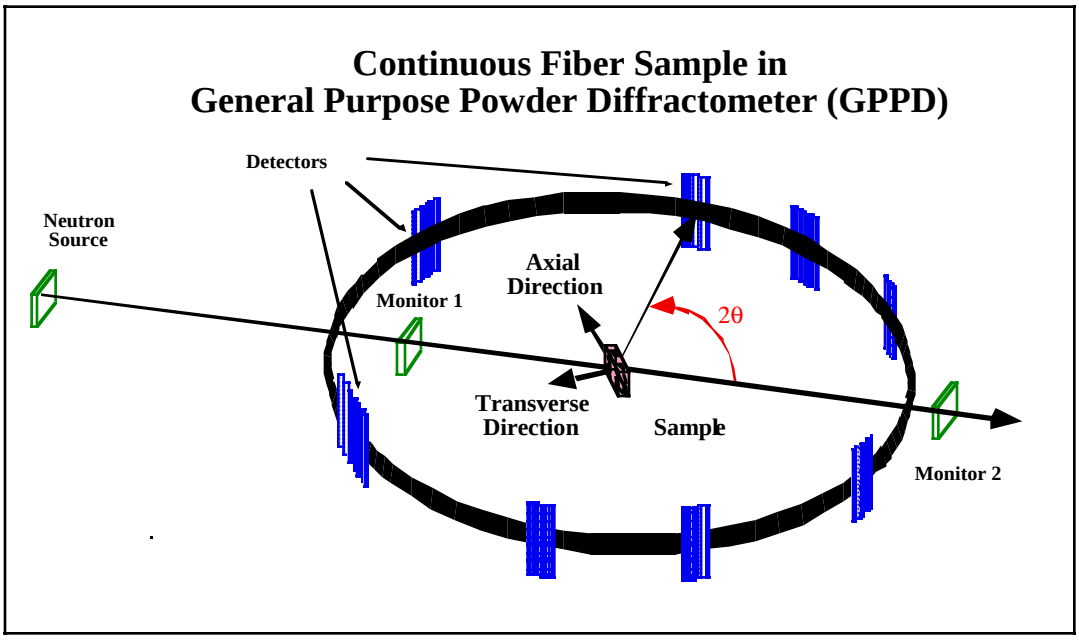

Fig. 94. Schematic layout of typical FM sample in the general purpose powder diffractometer at IPNS.

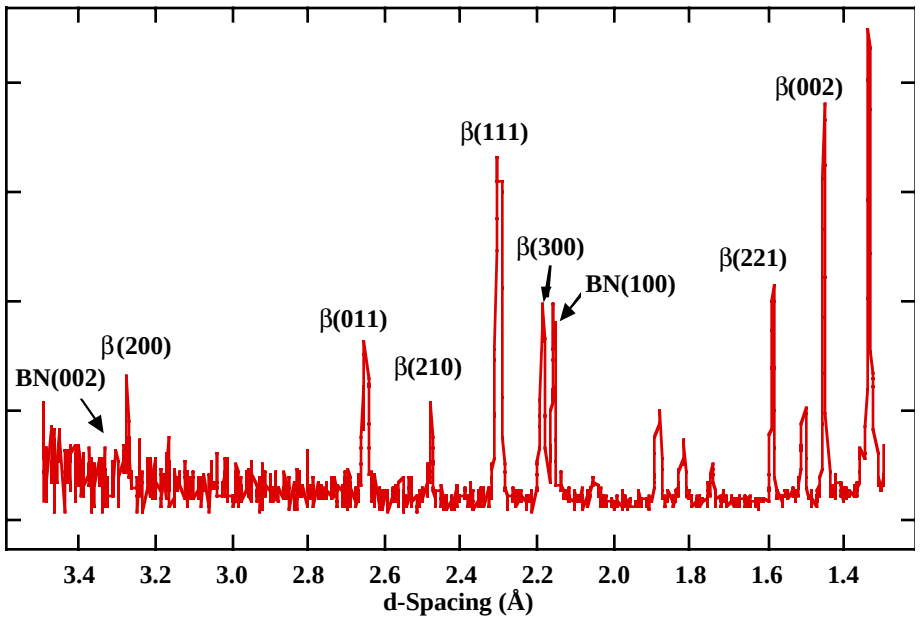

Fig. 95. Portion of diffraction data for unidirectional Si_3N_4/BN FM; longitudinal direction.

Our best estimates for transverse (normal to hot-pressing direction) residual strains in Si_3N_4 were: average ε (hk0) = $-6(1) \times 10^{-4}$, ε (002) = -8×10^{-4}, and average ε (hkl) = $-7(2) \times 10^{-4}$. The estimated errors given in parentheses are standard

deviations from averaging multiple values. These data were supplied to the UCSB team for the modeling efforts.

4.2.6 Creep of Si_3N_4/BN Fibrous Monoliths

To use Si_3N_4/BN FMs in most applications, it is essential that their high-temperature mechanical properties be known. Work at WPAFB has focused on tensile testing. Although elevated-temperature creep failures of ceramic composites often occur by shear, Si_3N_4/BN FMs had not been tested in compressive or shear loading. We therefore conducted two sets of studies to examine the response of these FMs to compressive loading in an inert atmosphere.

Right parallelepiped specimens ≈3 x 3 x 5 mm were cut from FM and Si_3N_4 billets with a slow-speed diamond-blade saw. The compression surfaces were polished to be flat and parallel.

In the first study, five types of specimens were prepared (Fig. 96). Each specimen was compressed at constant velocity between Si_3N_4 platens in an Instron Model 1125 universal tester. The atmosphere was stagnant N_2, the temperature was 1200–1400°C, and the engineering strain rates ($\dot{\varepsilon}$) were ≈1 x 10^{-6} to 5 x 10^{-6} s^{-1}.

The maximum strain (ε) was <0.04, but some specimens fractured during testing. Fracture surfaces and polished sections were examined by SEM.

The Si_3N_4 grains in both types of specimens were generally elongated, with a maximum length of ≈5 μm. The BN cell-boundary layer was thin and nearly continuous.

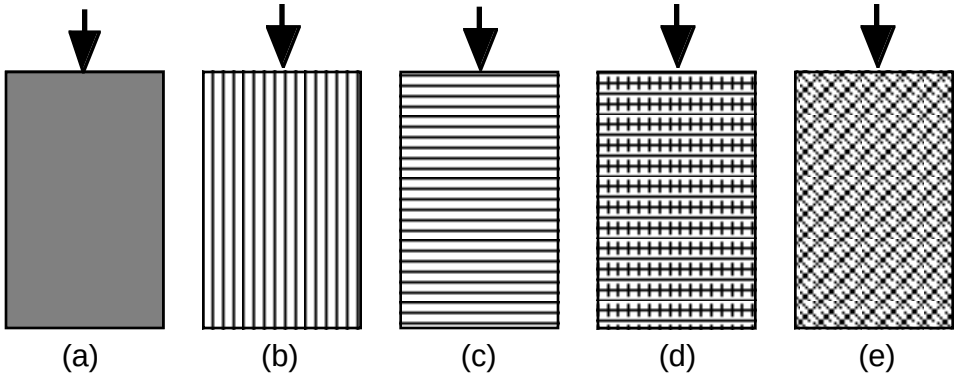

Fig. 96. Schematic diagram of specimens that were compressed: (a) Si_3N_4, (b) 0° laminate, (c) 0° laminate compressed at 90°, (d) 0/90° laminate, and (e) ± 45° laminate; arrows indicate compression direction.

The selected range of $\dot{\varepsilon}$ proved to be too fast to allow appreciable plastic deformation at 1200°C. The Si_3N_4/BN specimens that were compressed in a direction perpendicular to the long cell were relatively weak.

At 1300°C, the Si_3N_4 specimen appeared to achieve steady-state stresses; i.e., the stress saturated. The Si_3N_4/BN that was tested parallel to the long-cell direction also appeared to achieve steady state, but at a stress σ that was ≈20% lower than that for the Si_3N_4. As was the case at 1200°C, the 90° specimen fractured at $\sigma \approx 50$ MPa. The cross-ply laminates exhibited vastly differing responses, with the ±45° laminate fracturing at low stress. The 0/90° laminate appeared to achieve steady-state creep at $\dot{\varepsilon} \approx 2 \times 10^{-6}\ s^{-1}$; its maximum strength was approximately half that of the Si_3N_4 or the unidirectional FM that was compressed parallel to the long-cell direction. The ±45° laminates were weak and fractured between layers, through the BN boundary phase (Fig. 97).

The results of the first study revealed a need to compress at slower rates. In a followup study, in collaboration with the University of Seville, we compressed BN, Si_3N_4, and Si_3N_4/BN FMs under lower stresses and at higher temperatures. Specimen preparation was identical, but cross-ply laminates were not tested.

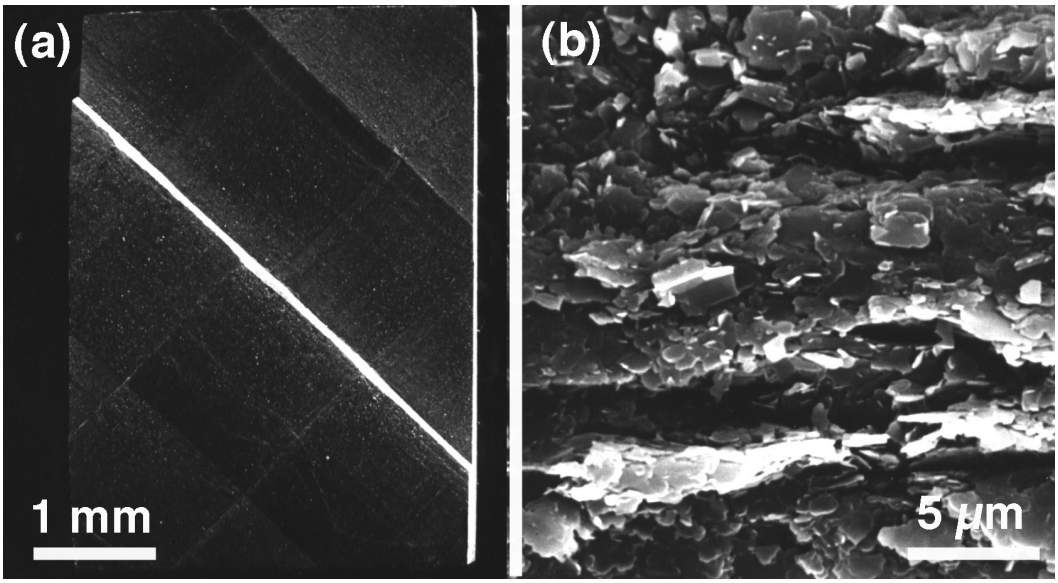

Fig. 97. SEM photomicrographs of fracture surface of ±45° Si_3N_4/BN laminate compressed at 1300°C: (a) low-magnification view and (b) higher magnification view that shows platelike BN grains on fracture surface.

Specimens from the BN were cut parallel (BNpara) and perpendicular (BNperp) to the cell extrusion direction. FMs were also cut parallel (FMpara) and perpendicular (FMperp) to the axis of the cells. The Si_3N_4 was tested in one orientation only. Both constant-strain-rate (CSR) and constant-load (CL) tests were conducted. The atmosphere was static N_2, the temperature was 1300–1500°C, and the engineering strain rates ($\dot{\varepsilon}$) were ≈1 x 10^{-6} to 5 x 10^{-6} s^{-1}. All compressive tests were completed within 10 h. For most tests, the specimens were unloaded and reloaded and at least two data points were taken for apparent steady-state stress (σ). Microstructures were analyzed by optical microscopy and SEM. Morphological changes of the cells were studied with an image analyzer (Zeiss Videoplan, Göttingen, Germany).

CSR tests were performed on BNpara and BNperp samples. Apparent steady-state stresses were higher for the BNpara samples than for the BNperp samples. These stresses were, however, essentially independent of temperature and strain rate. SEM revealed that the deformation of the BN samples was dominated by sequential fracture rather than true plasticity.

A summary of all of the creep tests that were performed on the FM and Si_3N_4 samples is shown in Fig. 98. The data points in this figure correspond to the range in which apparent steady states were measured. Below the minimum stress for each material, no deformation was recorded; above the maximum values, the high stresses led to accelerating deformation (i.e., tertiary creep). Over the experimental temperature range, BN was substantially softer than the Si_3N_4 and FM samples and did not deform in the steady state, as noted above.

The FMperp samples did not undergo significant plastic deformation under the test conditions. At 1400°C, only two data points were recorded in CL tests, at 12 and 40 MPa, before fracture occurred at only 0.7% strain. This orientation proved to be brittle. The cracked BN cell boundary could not prevent sliding of the Si_3N_4 cells, and fracture occurred, primarily by propagation of a single intercell crack, along a diagonal of the section perpendicular to the cells (Fig. 99). On the other hand, the FMpara and Si_3N_4 samples deformed ≈10% without fracture.

The FMpara samples did not deform in the steady state under lower stresses. For those stresses, the only significant feature was cracking within the BN matrix, until the load was fully transferred to the Si_3N_4 cells. At 1400°C, the first apparent steady state was measured at 75 MPa; at 1500°C, the lowest stress that yielded a steady state was 57 MPa. Once a critical stress was surpassed and the load could be transferred to the cells, the cells deformed plastically and controlled the deformation.

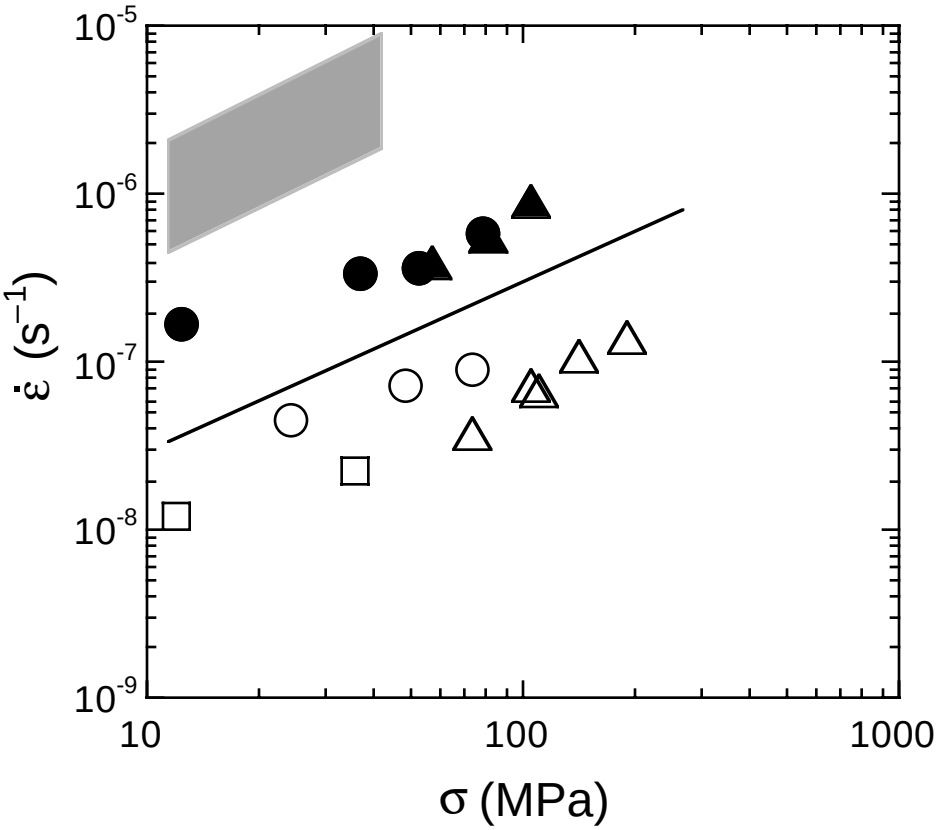

Fig. 98. CL tests on Si_3N_4 monoliths and FMs: open circles, Si_3N_4 – 1400°C; closed circles, Si_3N_4 – 1500°C; open triangles, FMpara – 1400°C; closed triangles, FMpara – 1500°C; and open squares, FMperp – 1400°C. Slope of the line is 1; shaded region indicates range of BN response.

The monolithic Si_3N_4 deformed in steady state at 1500°C at stresses as low as 13 MPa. At higher stresses, the agreement between the absolute creep rates of the FMpara and Si_3N_4 monolith was outstanding, because for both types of samples, the creep rate was controlled by the deformation of the polycrystalline Si_3N_4.

This conclusion was confirmed by studying the evolution of the sections of the cells of the FMpara samples during creep. The equivalent diameter of the undeformed cells was 103.0 ± 2.3 µm. A 3940-µm-long sample was compressed to a final length of ≈3500 µm (Fig. 100).

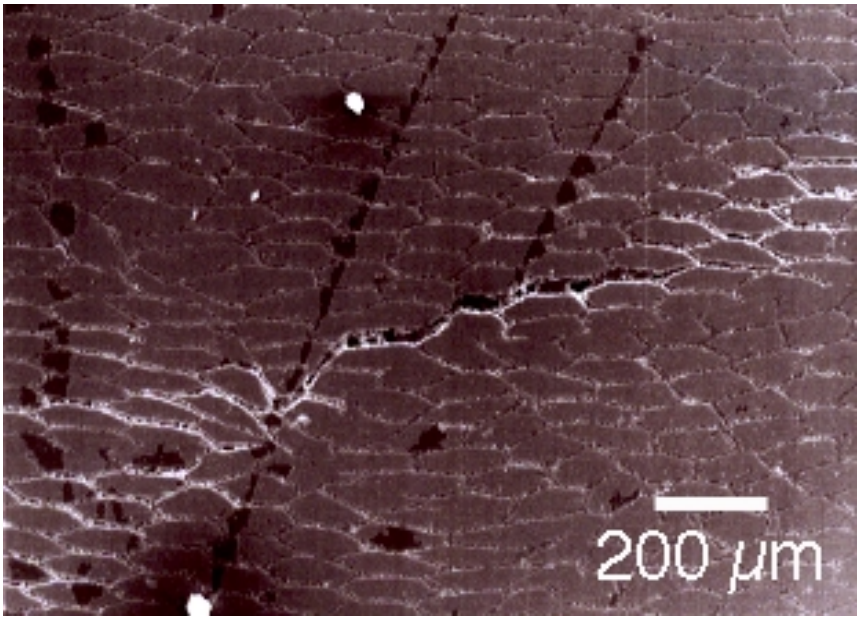

Fig. 99. SEM photomicrograph of deformed FMperp sample, showing formation of damage that led to failure; in the figure, compression axis was horizontal.

If one assumes a constant cell volume,

$$S_f = S_o(l_o/l_f) \text{ and } D_f = D_o\sqrt{l_o/l_f} \ , \tag{4.4}$$

where D, S, and l refer to the diameter, area, and length of a cell, and the subscripts o and f refer to the initial and final dimensions, respectively. Based on constant cell volume, the final average diameter of the cells was calculated to be 109.2 μm. The measured value was 110.0 ± 1.7 μm, in excellent agreement with the calculated value.

For analysis of the creep data, we used a classical semiphenomenological equation,

$$\dot{\varepsilon} = A\sigma^n e^{-Q/RT} \ , \tag{4.5}$$

where $\dot{\varepsilon}$ is the strain rate, σ is stress, T is absolute temperature, n and Q are adjustable parameters, A is a constant, and R is the gas constant.

The dependence of strain rate on stress was approximately linear (n ≈ 1); thus, a more-detailed understanding could be achieved by plotting the data on a linear-linear graph (Fig. 101). Linear regression lines were reasonable; both were selected to

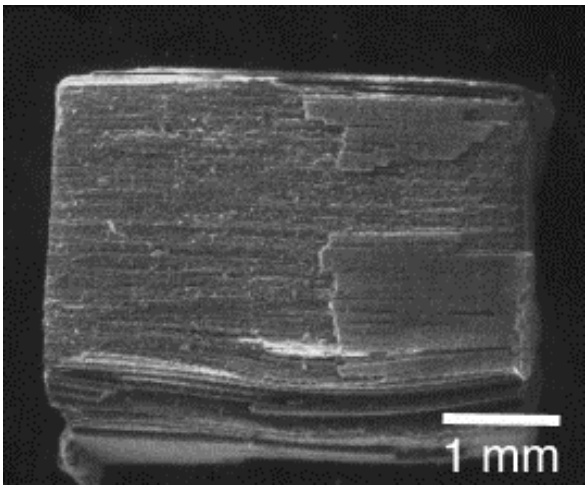

Fig. 100. SEM photomicrograph of deformed FMpara sample in which buckling of cells that were near the surface is observed.

intersect the origin. The slopes of the regression lines at T_1 = 1400ºC (B_1 = 7.6710 x 10^{-10} $MPa^{-1}s^{-1}$) and T_2 = 1500°C (B_2 = 7.7903 x 10^{-9} $MPa^{-1}s^{-1}$) were used to obtain an estimate of the activation energy as follows:

$$\frac{e^{-Q/RT_1}}{e^{-Q/RT_2}} = \frac{B_1}{B_2} \quad \Rightarrow \; Q = \frac{RT_1T_2}{T_1 - T_2}\ln\left(\frac{B_1}{B_2}\right). \tag{4.6}$$

Equation 4.6 yielded Q = 570 ± 150 kJ/mole. A specific experiment to determine Q directly was performed by temperature jumps between 1400 and 1500°C on an FMpara sample, under a constant stress of 105 MPa. The result was Q = 625 ± 40 kJ/mol, which is in reasonable agreement with the Q value calculated when all of the data points were considered.

These values for n and Q were in excellent agreement with previous work on Si_3N_4 that contains a grain-boundary phase. The data and observations indicated that the compressive creep occurred by grain-boundary sliding, probably accommodated by solution/reprecipitation of the Si_3N_4 phase and viscous flow of the boundary phase.

The creep studies of the Si_3N_4/BN FMs revealed that the Si_3N_4 cells controlled the creep rates. For orientations and test conditions in which the cells carried the load, the FMs were approximately as creep-resistant as monolithic, hot-pressed Si_3N_4.

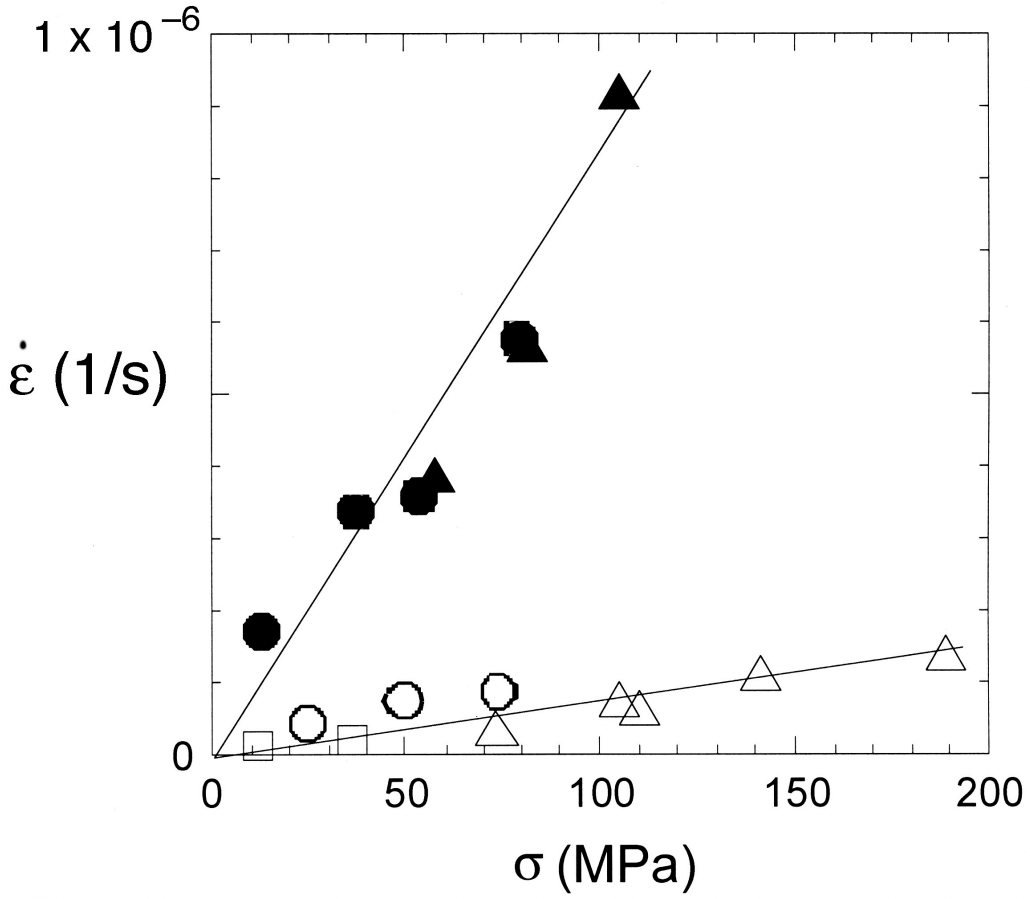

Fig. 101. CL creep results on a linear-linear graph; open and filled symbols as defined in Fig. 98.

5 Micromechanical Modeling of Fibrous Monolith Properties

The response of FMs to out-of-plane flexural loading was studied and modeled at the University of Michigan (c.f., e.g., D. Kovar et al., J. Am. Ceram. Soc. 80 (1997) 2471). The goals of this program were to extend those studies to in-plane fracture of cross-ply laminates and to model thermal residual stresses. In-plane fracture, which is the more likely occurrence in most service environments, is expected to differ from out-of-plane fracture in two ways: (1) following cracking of the cells that are aligned parallel to the loading direction, delamination will be resisted by the cells in the transverse direction; (2) the response will be anisotropic, varying with the direction of load with respect to the cell orientation. Thermal residual stresses are expected to be large and to have a profound effect on overall mechanical performance.

5.1 Fracture of Laminated Fibrous Monoliths

FMs are unique composites that share many attributes with conventional continuous-fiber structural ceramic composites and with laminates. To model FM fracture reliably, extensive microstructural characterization and mechanical testing were required to provide insight into the nature of these composites.

5.1.1 Preliminary Studies

At UCSB, two panels of Si_3N_4/BN FMs with 0˚/90˚ and ±45˚ fiber architectures were received from ACR. The volume fraction of BN was ≈17.5%.

A series of unnotched and notched in-plane bend tests was performed on the FMs in both orientations. The results were used to guide the activity of modeling the deformation and fracture characteristics of FMs. The test specimen geometries are shown in Fig. 102. The unnotched specimens were instrumented with two strain gauges on each of the compressive and tensile faces within the constant-moment region. The notched specimens were instrumented with a crack mouth opening displacement (CMOD) gauge. In addition, for both notched and unnotched specimens, the load-point displacement was measured with a deflection gauge placed in contact with the specimen. The tests on the notched specimens were periodically interrupted and unloading/reloading excursions were performed. The latter measurements were used to infer the effective crack length and assess the degree of hysteresis associated with nonlinear deformation.

The unnotched specimens in the 0/90˚ orientation exhibited small amounts of inelastic straining, which was initiated at a stress of ≈60 MPa (Fig. 103). The nonlinearity is believed to be associated with the development of cracks between the 90˚ fibers. At the stress maximum, the inelastic tensile strain was ≈0.03%. Fracture occurred catastrophically, with a precipitous load drop from the load maximum. Nevertheless, the specimens remained intact because of the interlocking of the broken cells, as shown below. The measured strength was 240 MPa.

Nonlinearity was also obtained in the ±45° orientation although the stress at the onset (≈115 MPa) was higher than that of the 0/90˚ specimens. In addition, the amount of inelastic strain was somewhat higher (≈0.05%). A particularly notable difference was the stable development of damage past the load maximum in the ±45˚ specimen (Fig. 104). Despite these differences, the bending strengths in the two orientations were essentially the same.

In both orientations, fracture occurred along a jagged path, the effect being more pronounced in the ±45˚ specimens (Figs. 105 and 106). These observations attest to the efficacy of the BN cell boundary in deflecting cracks. In addition,

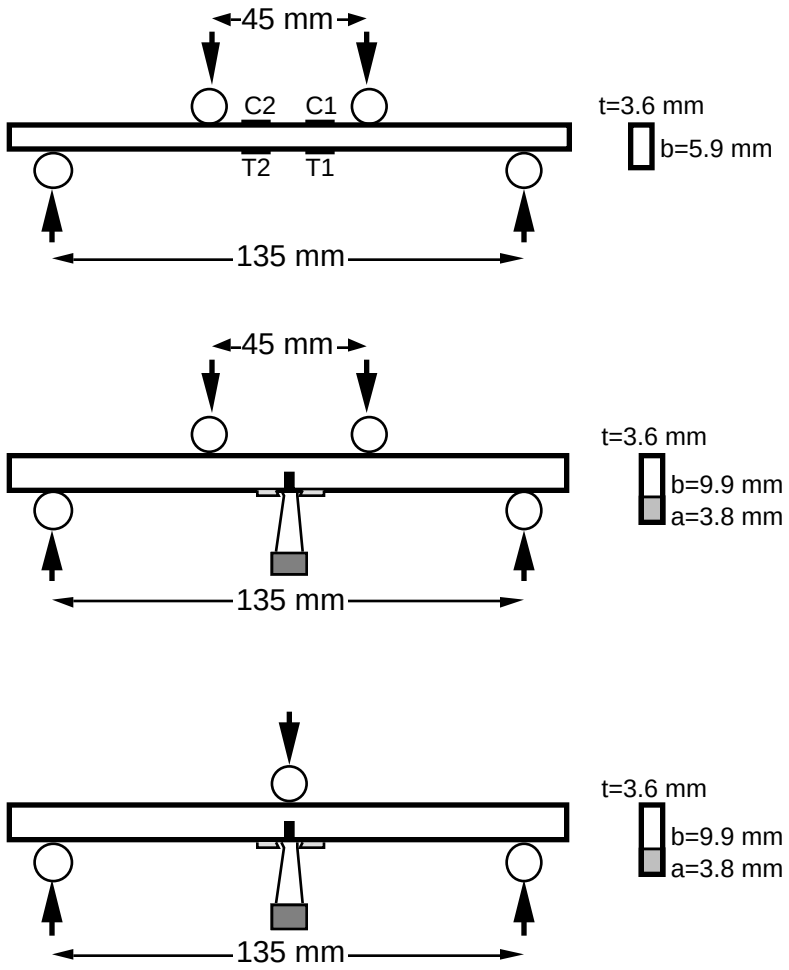

Fig. 102. Schematic diagrams, showing test geometries and dimensions (t is the specimen thickness, a is the notch length, and b is the full height).

observations on the tensile face of the ±45˚ specimens revealed regions in which substantial sliding had occurred between neighboring cells in adjoining layers (i.e. +45˚ and -45˚).

Notched three- and four-point specimens exhibited essentially identical properties. In both orientations, crack growth occurred stably past the load maximum. The unloading/reloading loops revealed significant amounts of hysteresis (Fig. 107), presumably because of the interlocking and frictional sliding between broken cells in the crack wake. The effects of this crack-wake friction were also reflected in the remarkably small changes in specimen compliance with increasing crack growth. The WOF values obtained from the notched tests were 2.15 and 5.71 kJ/m^2 for the 0/90˚ and ±45˚ orientations, respectively. The corresponding values of steady-state fracture resistance are 21.4 and 32.7 MPa(m)$^{0.5}$, which are much higher than the values typical of the toughest monolithic Si_3N_4 (≈8 MPa(m)$^{0.5}$).

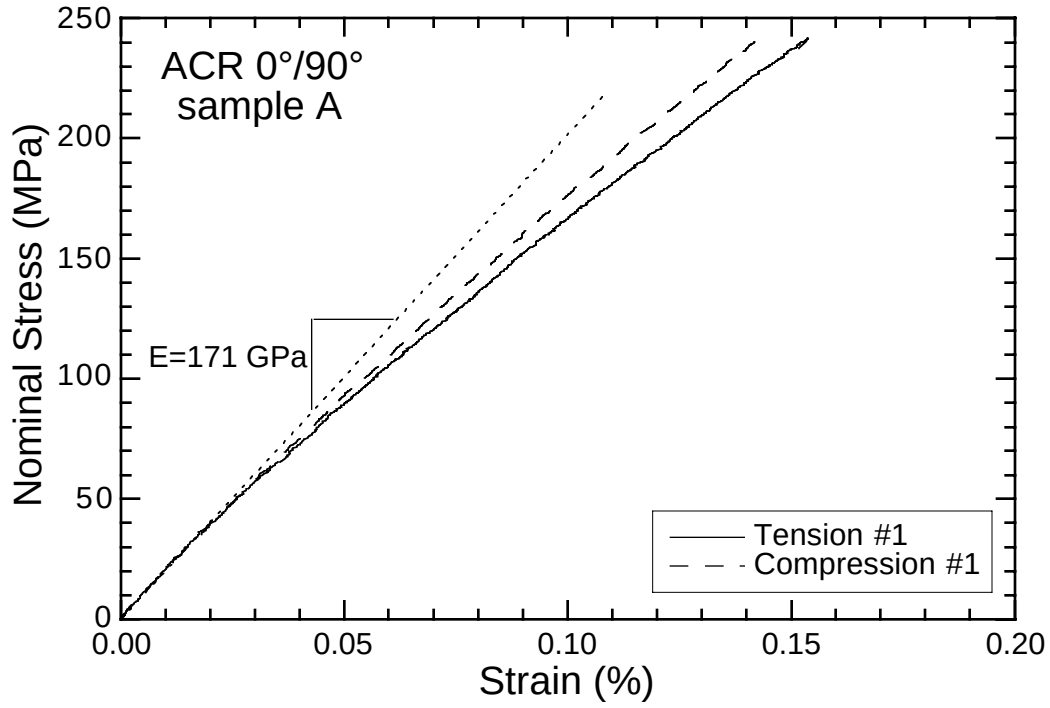

(a)

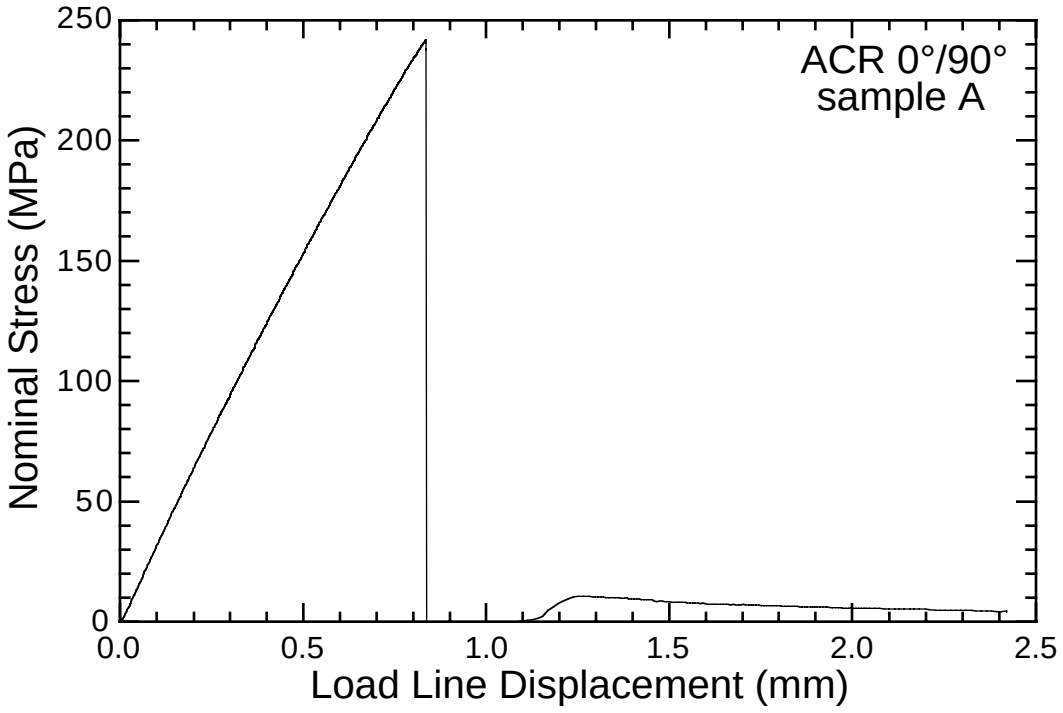

(b)

Fig. 103. Unnotched bending response in the 0/90° orientation in terms of (a) nominal stress vs. surface strain and (b) nominal stress vs. load-point displacement.

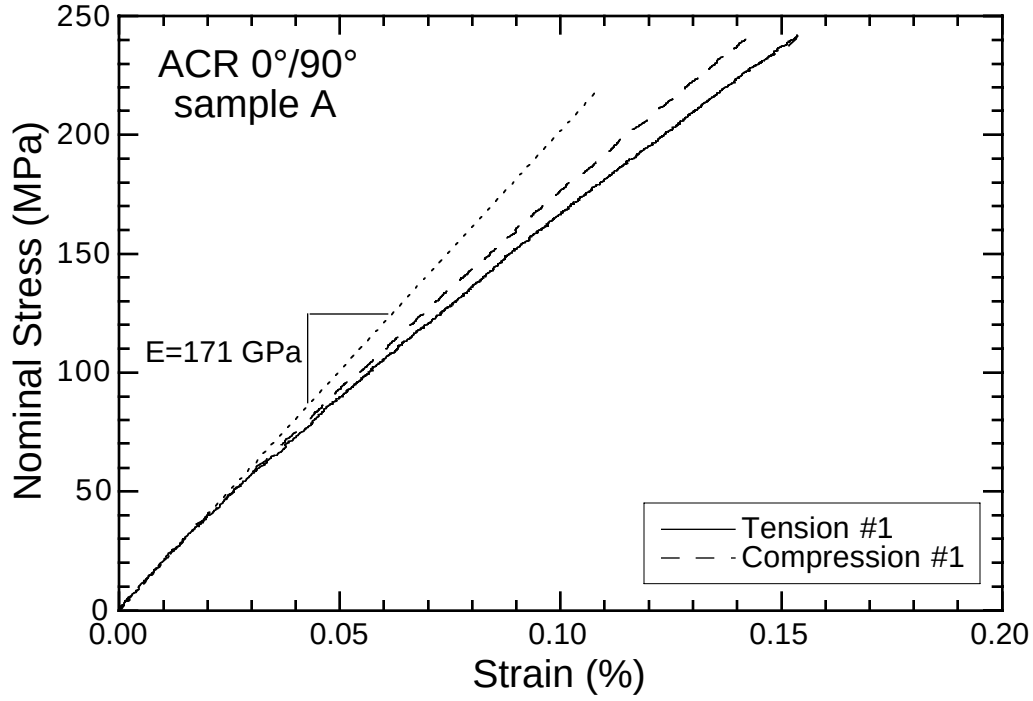

(a)

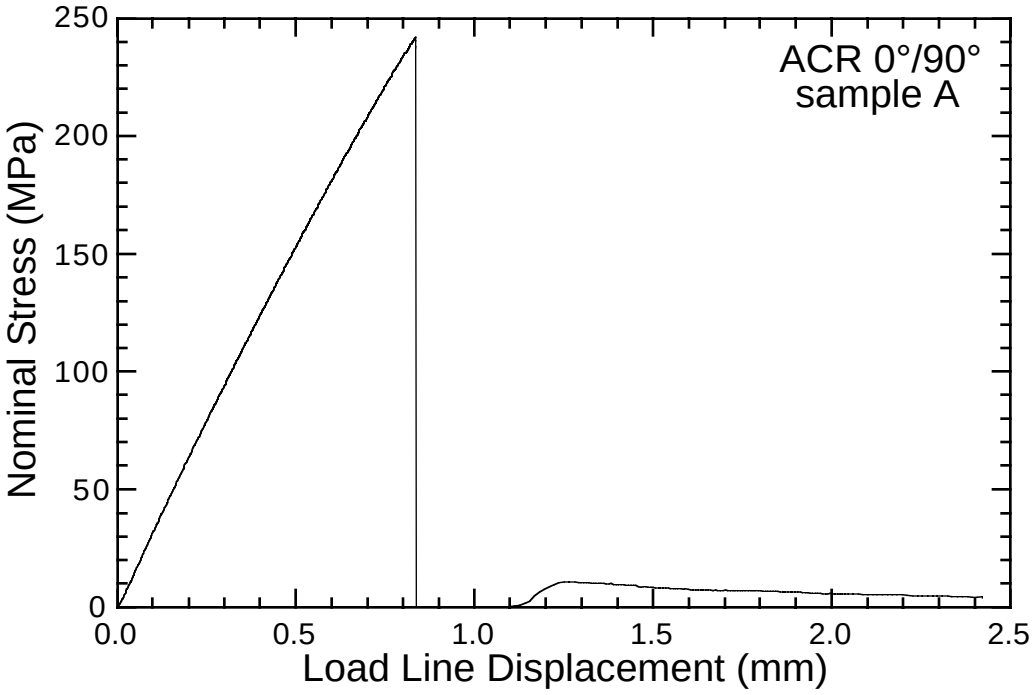

(b)

Fig. 104. Unnotched bending response in the 0/90° orientation in terms of (a) nominal stress vs. surface strain and (b) nominal stress vs. load-point displacement.

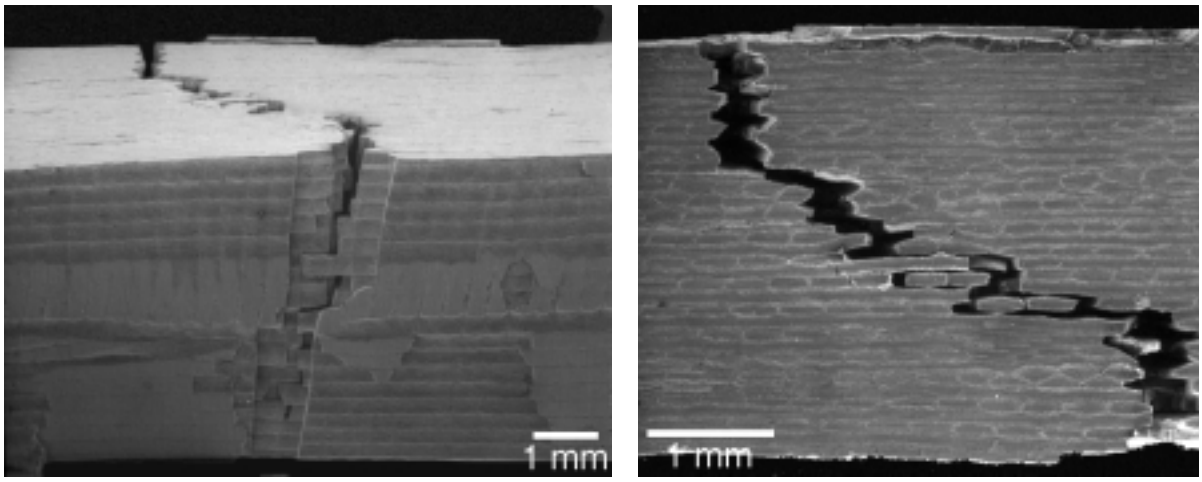

(a) (b)

Fig. 105. (a) SEM photomicrograph of a 0/90° unnotched bend specimen and (b) tensile surface of the same specimen.

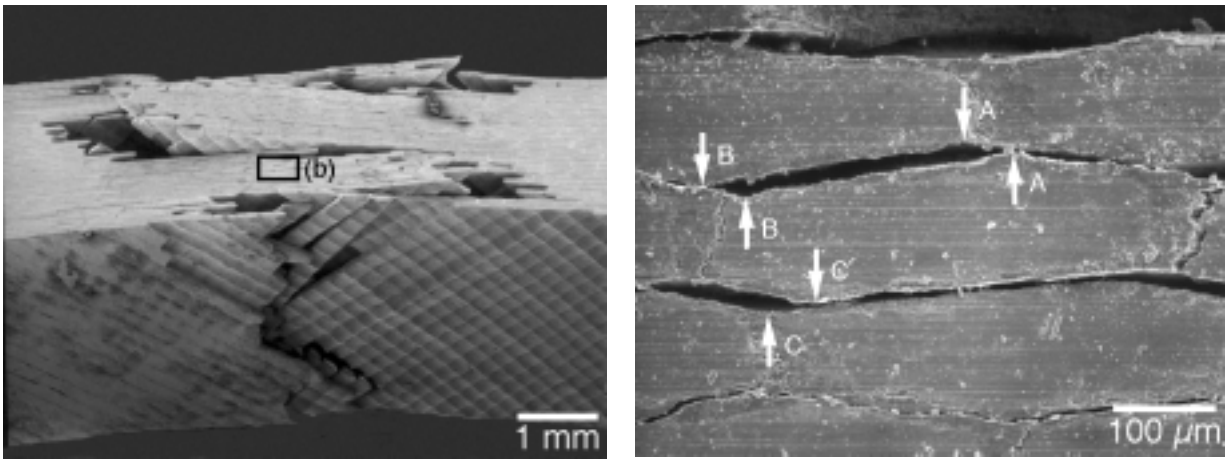

(a) (b)

Fig. 106. SEM photomicrographs of ±45° unnotched bend specimen and (b) tensile surface of same specimen, in which displacements are marked by letters A-C.

Examinations of the fracture surfaces revealed a more tortuous crack path and greater amounts of cell pullout in the ±45˚ specimens than in the 0/90° specimens (Fig. 108). Such effects are likely to be responsible for the higher values WOF and the enhanced stability of the cracks in the ±45˚ orientation.

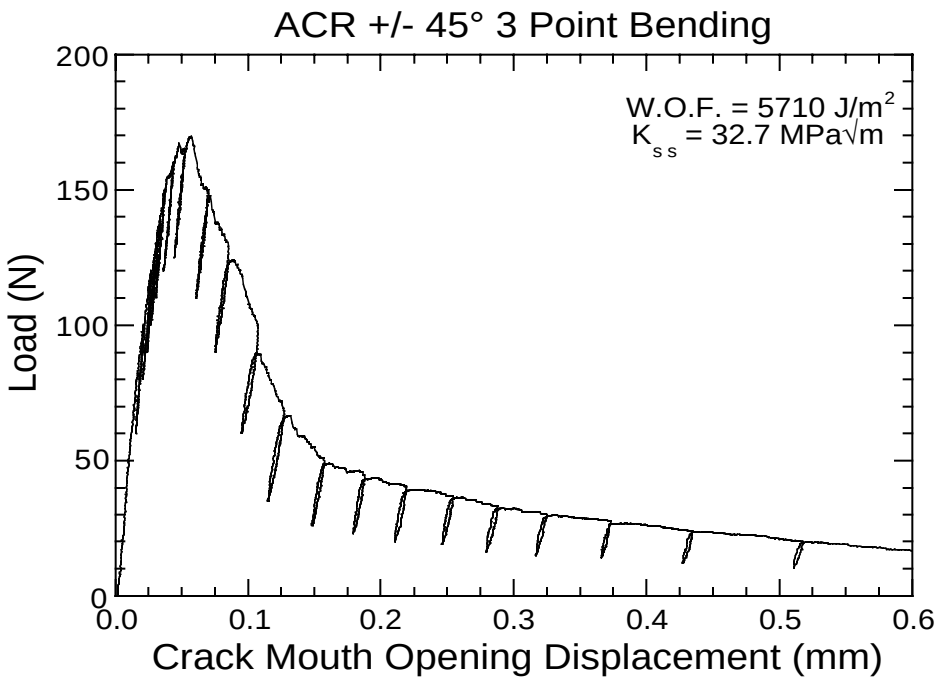

Fig. 107. Notched bending response of a ±45° specimen.

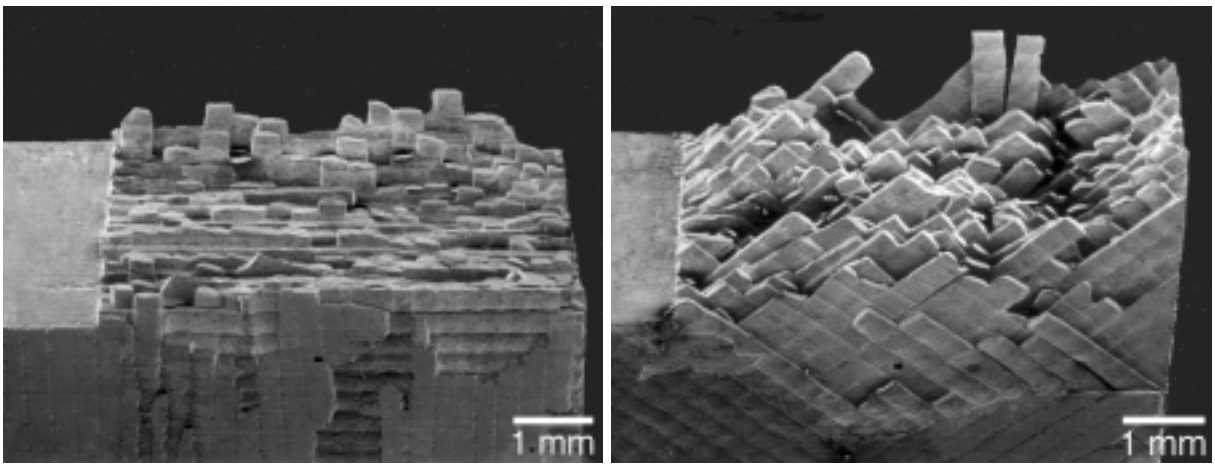

(a) (b)

Fig. 108. SEM photomicrographs of fracture surfaces of (a) 0/90° and (b) ±45° notched specimens, showing a more tortuous crack path and significant amounts of cell pullout after fracture.

These preliminary results allowed us to formulate plans to conduct a combined experimental and theoretical approach to understand fracture in FMs. The initial effort focused on assessing the utility of linear-elastic fracture mechanics in simulating both the load-CMOD and the compliance-CMOD curves for the notched

specimens. That effort was used as a starting point for the incorporation of nonlinear effects in the description of crack growth and fracture resistance.

5.1.2 Evaluation of Candidate Models for Fracture

The results of the notched bend test revealed significant levels of steady-state fracture energy in the cross-ply FMs: $\approx 2.2\ kJm^{-2}$ in the 0/90° orientation and $\approx 5.7\ kJm^{-2}$ in the ±45° orientation. Most of this energy appeared to be associated with frictional sliding between broken cells; the remainder came from fracture of the cells and crack deflection along the BN layers, the latter two processes occurring essentially at the crack tip. The implication was that the fracture resistance was not characterized by a unique fracture toughness, but rather by an R-curve, wherein the resistance increases with crack extension up to a limiting (steady-state) value at large crack extensions.

We then focused on assessing the utility and deficiencies of linear-elastic fracture mechanics (LEFM) in describing crack growth, measuring crack-growth resistance through J-integral testing, modeling crack-growth resistance with bridging concepts, and comparing experiments and simulations for the purpose of inferring the intrinsic material parameters that dictate fracture resistance. The following sections present highlights of the results.

Linear-Elastic Fracture Mechanics

The utility of LEFM was assessed by calculating the expected load-displacement response of notched bend beams for several assumed values of fracture toughness and comparing the results with experimental measurements (Fig. 109). The lack of agreement between the shapes of predicted and measured curves clearly demonstrates the deficiencies of LEFM in describing crack growth in FMs and provides the motivation for the subsequent work, i.e., incorporating the large-scale nonlinearity associated with crack growth.

Crack-Growth-Resistance Measurements

Crack-growth-resistance measurements were performed in accordance with ASTM Standard E1152, "Standard Test Method for Determining J-R Curves." The test specimen was an edge-notched three-point bend beam with a normalized notch length of $a_o / W = 0.5$, and a loading span of $S = 4W$. Both load-line displacement (δ) and CMOD were measured with appropriate gauges; the former for the purpose of calculating J and the latter for inferring crack length through a compliance technique. Also, polished side-surfaces of the test specimens were monitored in-situ through an optical microscope. The observations were recorded on a video

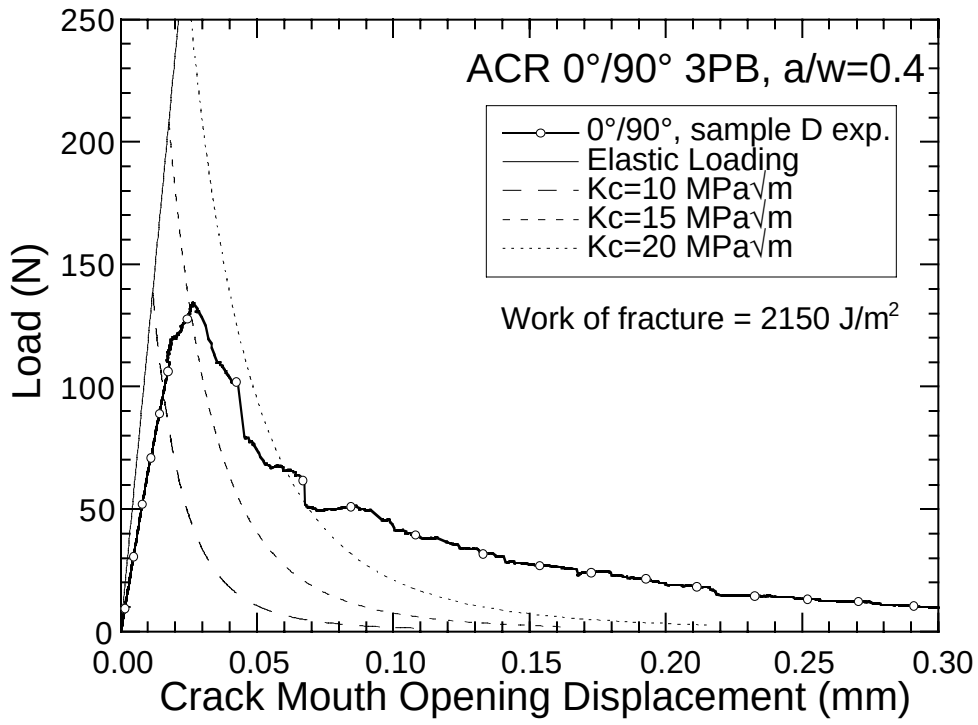

(a)

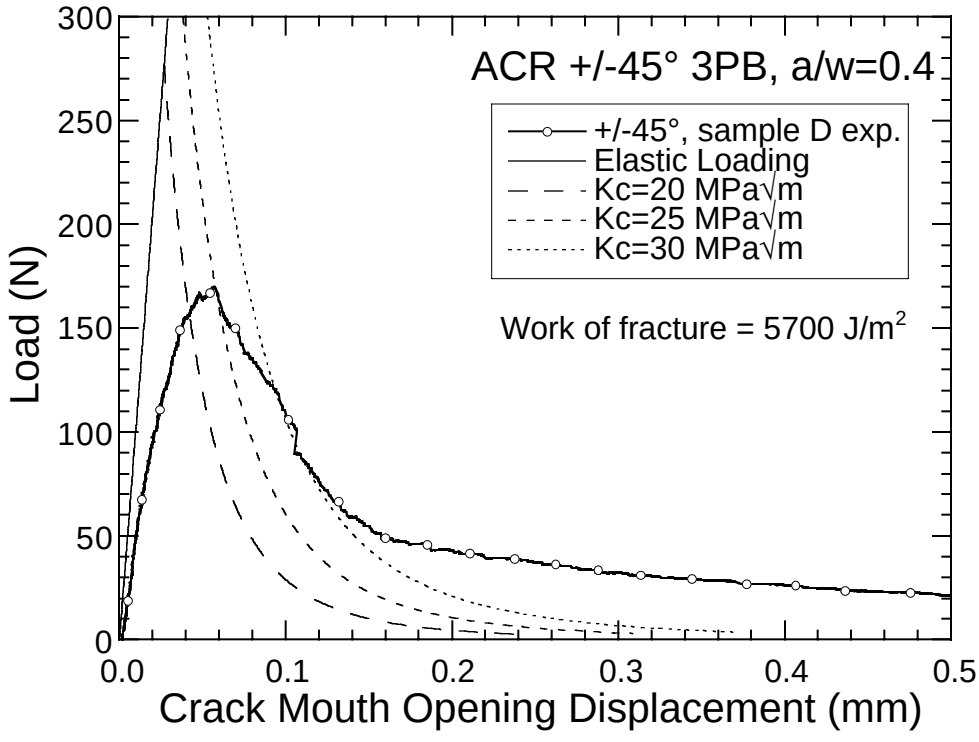

(b)

Fig. 109. Comparisons between measured (exp.) and predicted load-displacement response for notched FM bend specimens in (a) 0/90° and (b) ±45° orientations.

recorder, and used to determine the physical crack length and, subsequently, to assess the accuracy of measurements inferred from the compliance technique.

Figures 110-113 show the key results for a test performed on a 0/90° bend specimen. Cracking occurs sequentially through each of the cells on the polished surface, with each crack location being offset somewhat with respect to the neighboring ones, and each causing some deflection through the BN (Fig. 111). Indeed, the noncoplanar fracture sequence and the sliding that occurs subsequently between adjacent cells is responsible for a large portion of the fracture energy. The crack length increases with CMOD, up to a CMOD of ≈200 μm, at which point the entire specimen is cracked, i.e., $a/W = 1$. Subsequently, substantial additional CMOD is accommodated without fracture (Fig. 110), because of the interlocking and friction between the broken cells.

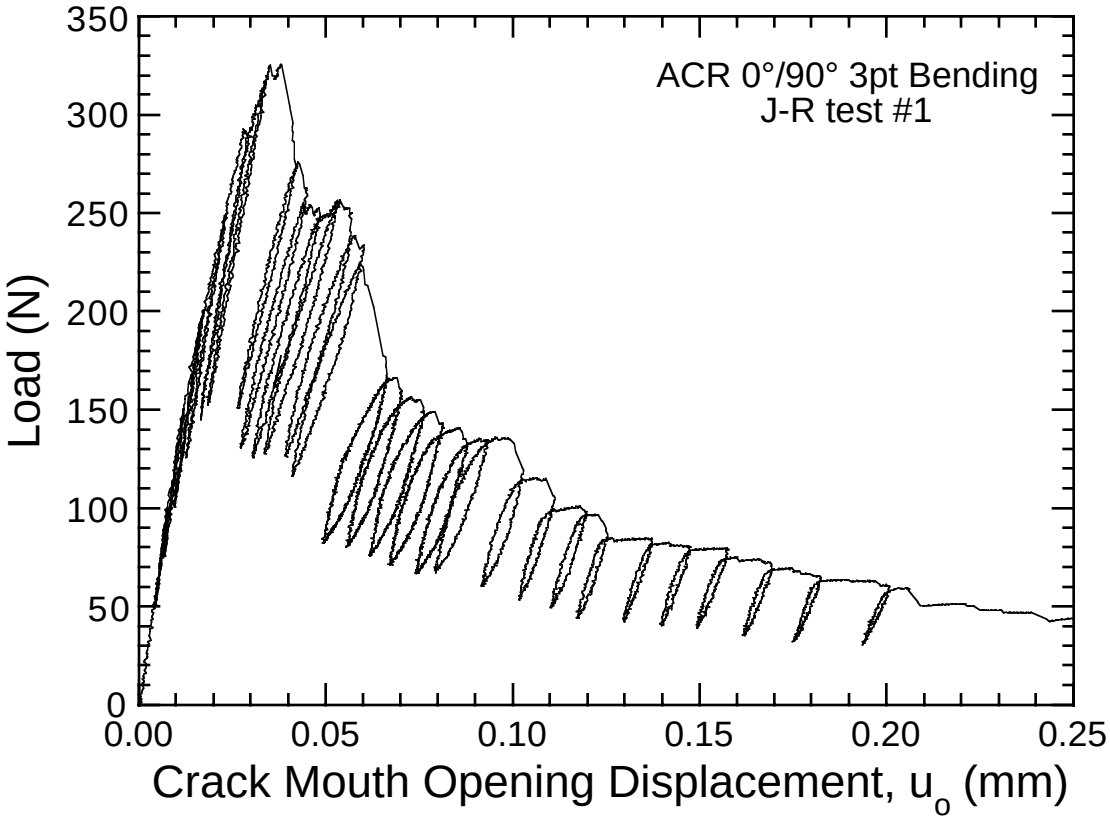

Fig. 110. Load-CMOD response measured for a 0/90° specimen.

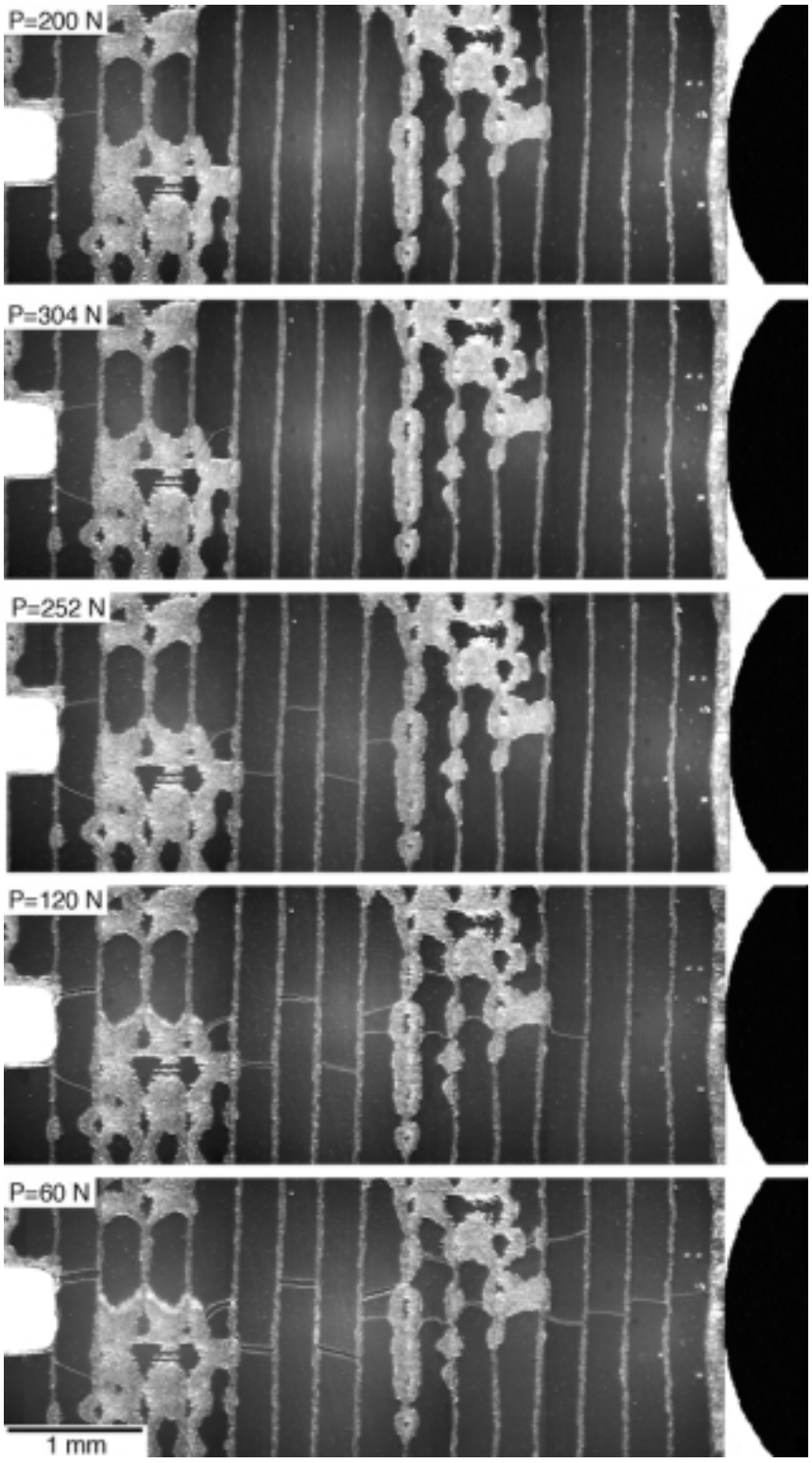

Fig. 111. A series of optical photomicrographs, taken in-situ, showing sequence of cracking events at increasing CMOD.

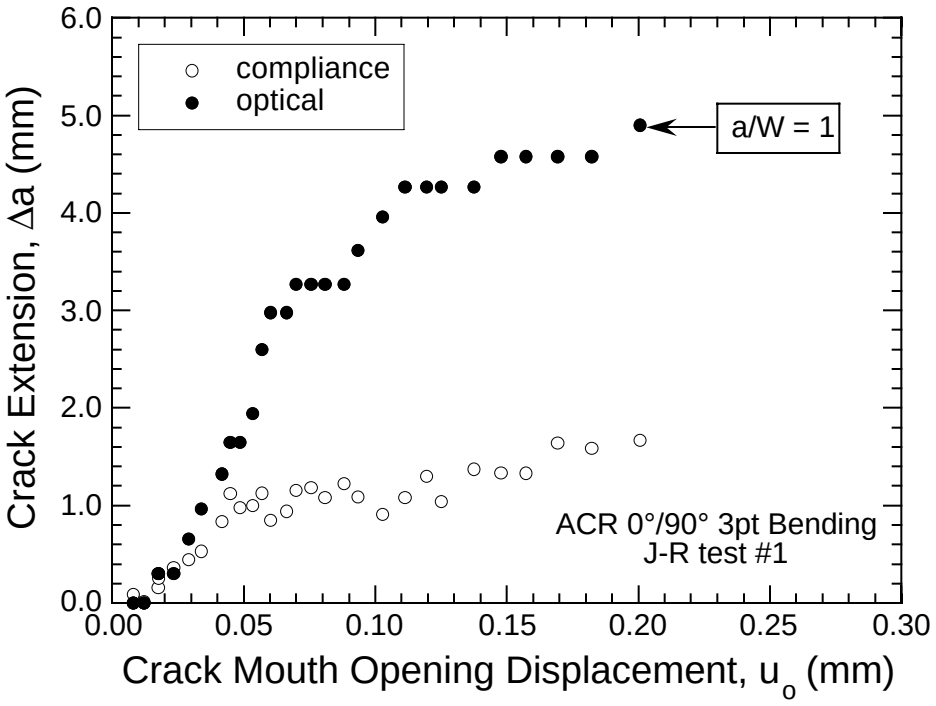

Fig. 112. Crack lengths measured optically and those inferred from the compliance technique.

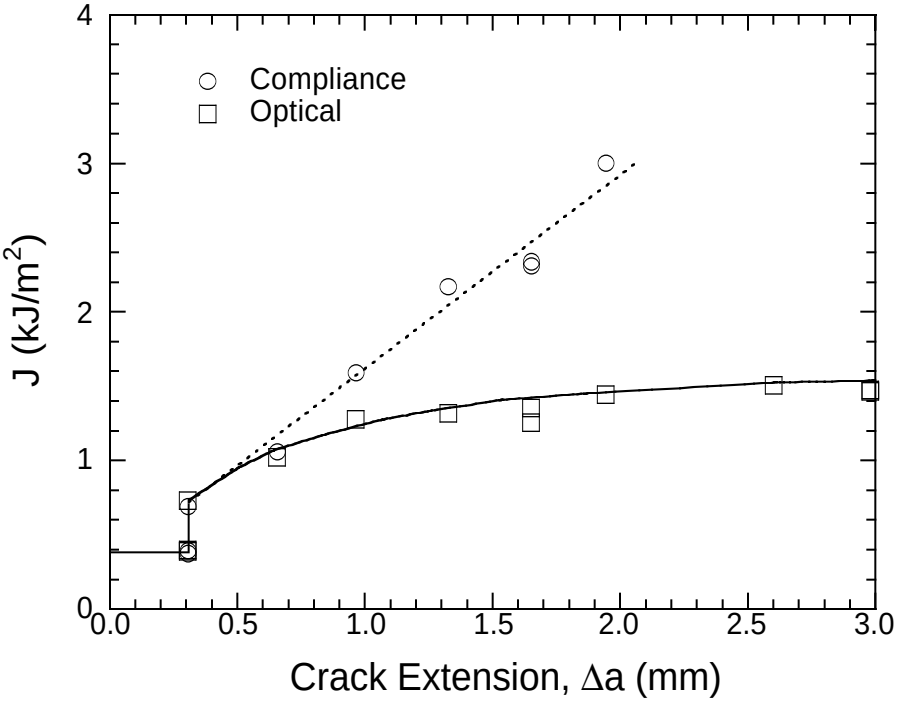

Fig. 113. J-R curve for 0/90° specimen.

Comparison between the crack length measured optically and inferred from the compliance technique shows close agreement for small crack extensions ($\Delta a < 1$ mm), but with significant discrepancies at higher values (Fig. 112). For instance, at CMOD = 150 μm, the actual crack extension is ≈4.5 mm ($a/W = 0.96$) and the one inferred from the compliance is only ≈1.4 mm.

The J-R curve for the 0/90° specimen is shown in Fig. 113. In calculating the plastic displacements associated with the plastic component of the J-integral, two approaches were used. The first was based on the actual specimen compliance, the second was based on the compliance calculated from the optically measured crack length. Both sets of results are plotted against the actual crack extension (measured optically). The curves exhibit several distinct regimes. The first is associated with a critical J needed to crack the first cell, occurring at $J \approx 400$ Jm^{-2} ($K \approx 8$ MPa $m^{1/2}$). Additional cracking is not observed until a significantly higher level: $J \approx 700$ Jm^{-2} ($K \approx 11$ MPa $m^{1/2}$). This increase in fracture resistance is believed to be associated with crack deflection into the BN ahead of the first crack, thus mitigating the stress concentration on the next cell and elevating the energy release rate needed for further cracking. Indeed, the latter value of J is likely the most appropriate to describe the intrinsic crack-tip toughness needed for continued crack growth, with any further elevations arising from friction in the crack wake.

Significant discrepancies exist in the J values obtained from the two techniques at large crack lengths.

Bridging Model

Descriptions of crack-growth resistance were developed by using concepts of crack bridging. The problem was cast in a continuum mechanics framework, wherein crack-wake friction was modeled by a continuous distribution of tractions acting across the opposing faces of the matrix crack.

The key parameter that characterizes the bridging elements is the bridging traction law, i.e., the relationship between the effective crack opening u and the closure (or bridging) stress σ_b that arises from friction. The results are in the form of integral equations that relate the bridging traction profile, the applied stress, the crack-tip stress-intensity factor K_{tip} and the dimensions of the crack and the specimen. Upon invoking the criterion for crack growth, that $K_{tip} = K_o$, where K_o is the intrinsic crack-tip toughness, the load-displacement response can be simulated, through to complete cracking ($a/W = 1$). Subsequent to the point of complete cracking, an alternative approach is used to simulate the load-deflection response, as described later.

Experience with fiber-pullout in conventional fiber-reinforced ceramic composites indicates that the bridging law can be adequately described by an exponential of the form

$$\sigma_b = \sigma_o \exp - u / h^* , \tag{5.1}$$

where σ_o and h^* are characteristic values of stress and crack-opening displacement. This law has been rationalized on the basis of a micromechanical analysis of pullout of an individual fiber, assumed to be coupled to the matrix through a constant friction stress τ_o, along with an exponential distribution of pullout lengths. In this context, h^* becomes the mean pullout length. Furthermore, the total (steady-state) energy dissipated through friction is

$$\Gamma_b = \int_o^\infty \sigma_b \, du = \sigma_o h^* . \tag{5.2}$$

The bridging analysis was implemented in collaboration with Prof. Matt Begley of the University of Connecticut. The main task involved development of numerical techniques to solve the governing integral equations. The goal was to develop a capability to simulate the load-displacement response in the region $a_o / W \le a / W < 1$ for arbitrary values of the intrinsic toughness and the bridging parameters.

Once the entire specimen is cracked ($a / W = 1$), an alternate approach is used. For this regime, a simple beam bending analysis is proposed to model the load-CMOD behavior. The analysis is based on the assumptions that the bridged crack acts as a plastic hinge, with no stress-concentrating effect coming from the notch; the neutral axis is essentially at the bottom (compressive) face of the specimen; and the crack-opening displacement profile u(x) is linear with distance x from the compressive face, in accordance with

$$u (x) = u_o \; x/W , \tag{5.3}$$

where u_o is the CMOD. By combining Eqs. 5.1 and 5.3, the spatial distribution of bridging tractions is obtained:

$$\sigma_b = \sigma_o \exp - \left[\left(\frac{x}{W} \right) \left(\frac{u_o}{h^*} \right) \right] . \tag{5.4}$$

The bending moment M that is supported by the tractions is

$$M = B \int_o^{W-a} x \, \sigma_b (x) \, dx , \tag{5.5}$$

where B is the specimen thickness. The corresponding nominal bending stress, from Eqs. 5.4 and 5.5, is

$$\sigma_{nom} = 6M/BW^2 = 6\sigma_o \left(\frac{h^*}{u_o}\right)^2 \left[1-\left(1+\frac{u_o}{2h^*}\right)\exp\frac{-u_o}{2h^*}\right]. \qquad (5.6)$$

Preliminary simulations of the stress-CMOD response in the fully cracked regime were performed by using Eq. 5.6, with σ_o and h^* being used as fitting parameters to match the experimental measurements. Typical results are shown in Fig. 114. Good correlations were obtained between experiment and theory for the parameter values shown on the figure, notably $\sigma_o \approx$ 20-30 MPa and $h^* \approx$ 70-90 μm. For these combinations, the steady-state toughness $\Gamma = \sigma_o h^* \approx 2$ kJm^{-2}, in accordance with the measured WOF (Γ = 2.2 kJm^{-2}), and the expectation that most of this work is done by crack-wake friction.

We assessed the inferred value of h^* by measuring the pullout lengths of essentially all of the cells on both halves of the fracture surface. This was accomplished through a series of SEM photomicrographs of the fracture surfaces,

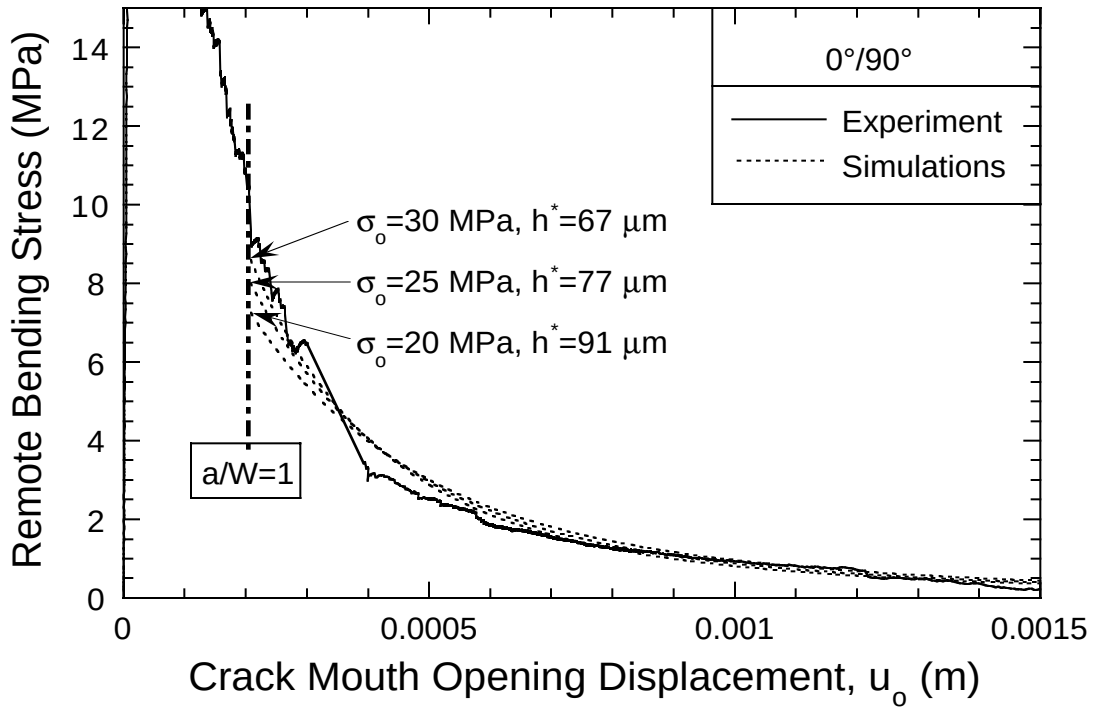

Fig. 114. Measured and predicted stress/CMOD response in the regime following complete specimen cracking (a/W = 1).

taken at a prescribed magnification and tilt angle such that the lengths could be directly converted to pullout lengths. Two measurements were made for each cell, one on each of the two broad faces (a total of >400 measurements). Pullout lengths were also determined from SEM photomicrographs of cross sections (Fig. 115). The resultant pullout distribution is plotted in Fig. 116. The mean pullout length is $h^* \approx$ 110 μm, in broad agreement with the range inferred from the bridging model and the bending analysis, through Eq. 5.6: $h^* \approx$ 70-90 μm.

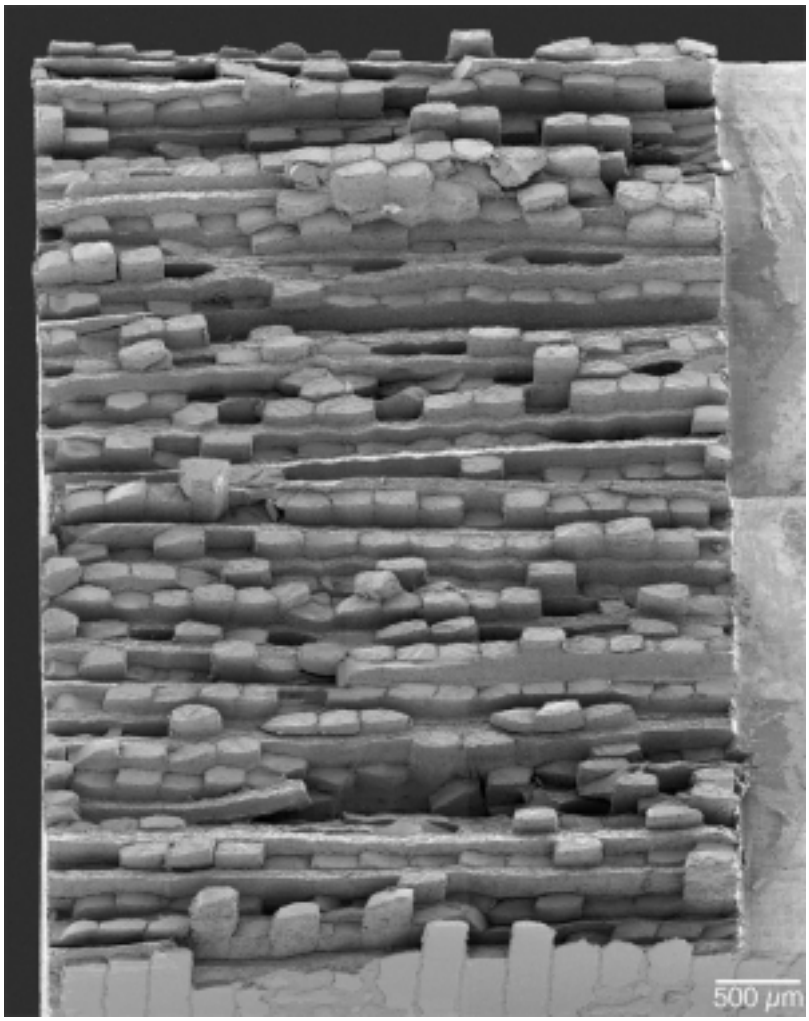

(a)

Fig. 115. (a) Fracture surfaces on which pullout measurements were made (two matching halves of the fractured test specimen are shown, the boundary between them is faint horizontal line in the notched region) and (b) transverse cross sections of 0/90° FM (top) and ±45° FM (bottom), showing more tortuous path and longer pullout length in ±45° FM

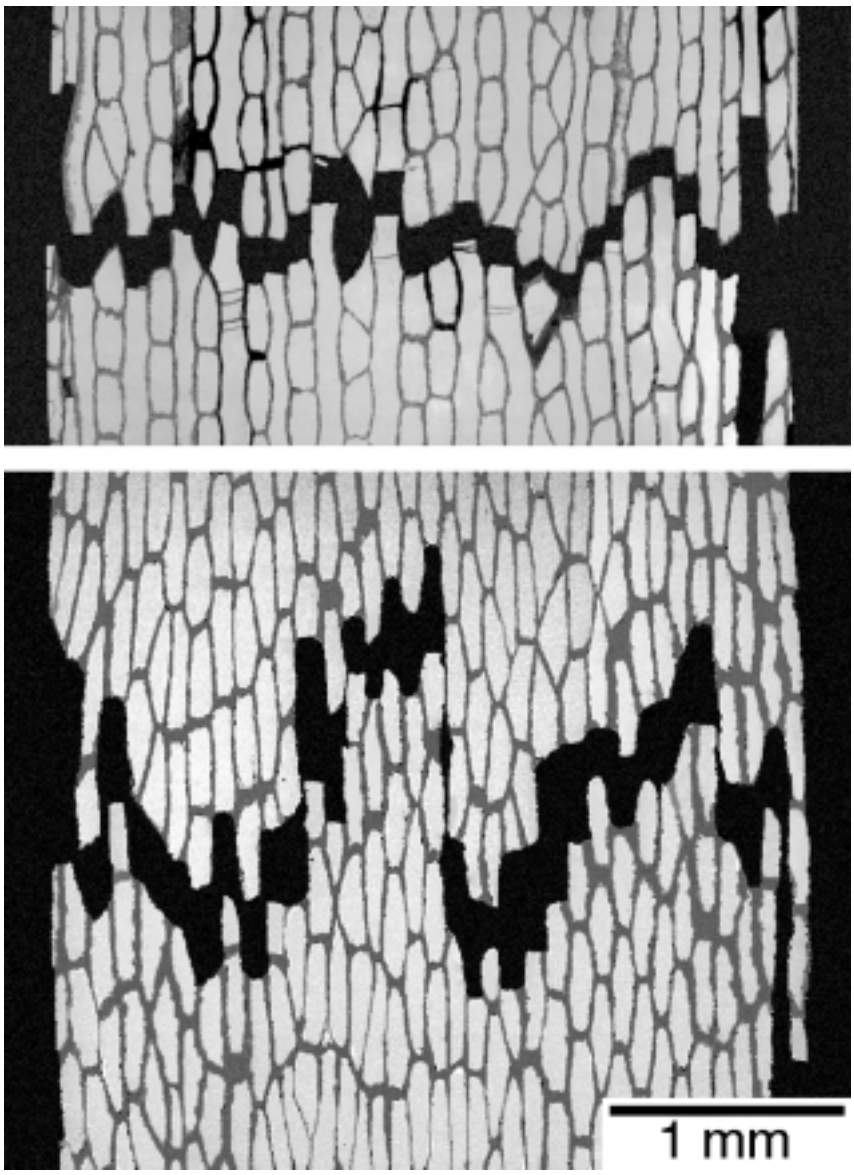

(b)

Fig. 115. (Contd.)

These results indicated a need to further analyze the pullout-length distribution and develop micromechanical models appropriate to the pullout process in FMs, and allowed us to further assess the proposed approach to simulating crack-growth resistance, as well as establish connections between the bridging parameters inferred from the macroscopic measurements and the intrinsic material parameters, including the friction stress τ_o and the pullout-length distribution. The results also formed the basis for fracture-mechanics-based simulations of the load-CMOD response in the regime $a_o/W < a/W < 1$.

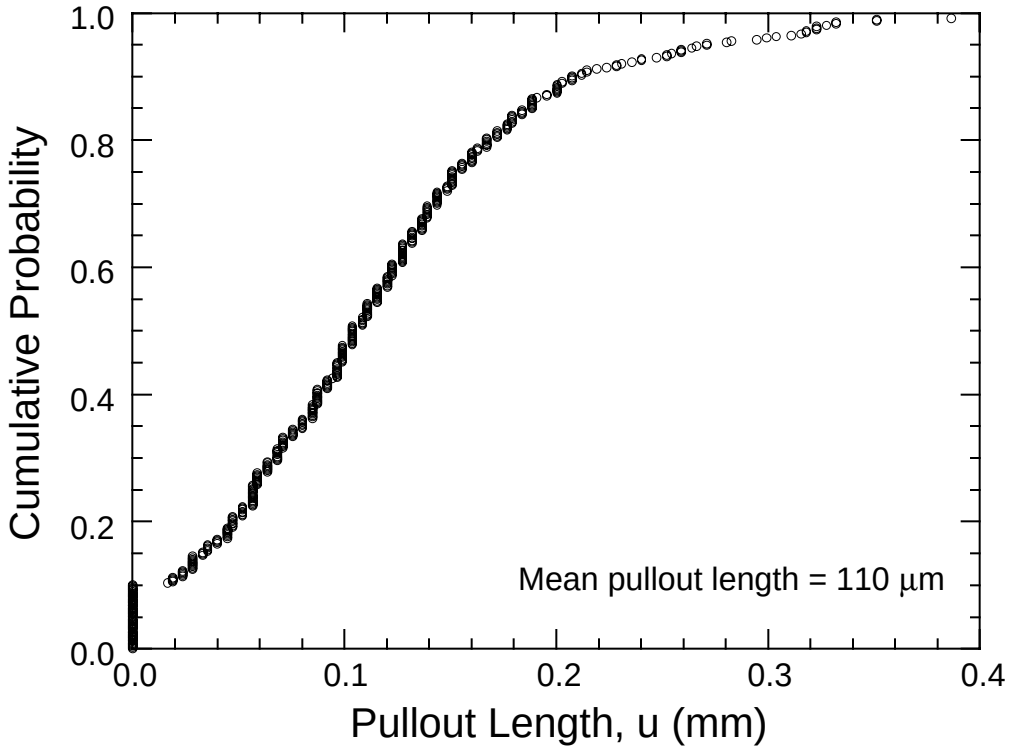

Fig. 116. Measured pullout-length distribution.

5.1.3 Bridging Model for Fracture of Fibrous Monoliths

Study of the in-plane fracture resistance of a cross-ply Si_3N_4/BN FM was undertaken after additional observations and analyses of crack bridging. Key results are summarized below. The study included experimental measurements of the fracture resistance of notched flexure specimens of the FM in both 0/90˚ and ±45˚ orientations, as well as simulations based on a crack-bridging fracture model.

The fracture resistance is characterized by a high intrinsic toughness ($K_o \approx$ 10–13 MPa$(m)^{0.5}$ for the two architectures) and a subsequent increase in fracture resistance with increasing crack growth. The intrinsic toughness is approximately three to four times that of the monolithic Si_3N_4, also measured in this study on a material made by the same extrusion method as that used for the FM. The latter difference is due to the deflection of cracks from the cells into the surrounding BN and the resultant reduction in the crack-tip stress field. The rising fracture resistance curve is attributable largely to pullout of broken cells in the crack wake, although there is some evidence that other dissipative mechanisms operate at the crack tip and further increase fracture resistance. The parameter that characterizes the effects of pullout is the bridging traction law $\sigma_b(u)$, where σ_b is the bridging stress and u is the crack opening displacement.

Two complementary approaches to determining the bridging law were developed: one based on a micromechanical model of cell pullout coupled with measurements of pullout lengths, the other, based on the load-displacement response of the flexure specimens following fracture of all cells. Both approaches indicate that the traction law follows an exponential form, characterized by a bridging strength and an effective pullout length. Using the former approach, combined with the measured WOF, we inferred that the interface sliding stress associated with pullout was ≈5–7 MPa. By comparison, the values obtained from push-out measurements on a similar unidirectional FM were $\tau = 25 \pm 7$ MPa.

The discrepancy between these values is believed to be associated mainly with variations in cross section along the cell length, the result of the indentation of adjacent transverse cells during pressing in the green state. The indentation also leads to the formation of cusps at many of the triple junctions between longitudinal and transverse cells. These features allow premature disengagement of the cells during pullout, and lead to an overestimation in the contact area when the measured pullout lengths are used. The result is an anomalously low inferred sliding stress. Further evidence of this effect was obtained by use of the latter approach to determine the bridging law (based on the response following complete cell fracture). From this approach, the inferred sliding stress is ≈23–33 MPa: comparable to the one measured by push-out on the unidirectional material (25 MPa). This correlation indicates that the latter approach to determining the bridging parameters is more reliable than the one based on pullout measurements alone. Nevertheless, the two approaches provide corroborating and complementary information about the form of the bridging law.

When used together, the two approaches to determine the bridging law also provide valuable insights into the factors that control the efficacy of the bridging, especially those related to the geometry of the cells. That is, the periodic variations in cell cross section and the cusps that occur at the triple points between the longitudinal and transverse cells limit the extent of debonding and sliding through the BN, to a distance comparable to the cell width. We surmised that the extent of this debonding and the efficacy of the bridging could be increased substantially by modifying the process.

An assessment of the crack-bridging model was made mainly by comparing simulations of the load vs. CMOD with those that were measured experimentally. The simulations in the regime before complete cell fracture show broad agreement with the measurements, with two exceptions. First, the measured curves exhibit slight nonlinearity before the load maximum, likely a result of fracture of the cells that had been cut in the notching operation and the ensuing debonding through the BN ahead of the fractured cells. This nonlinearity is not captured by the simulations because of the assumption that crack growth initiates at a crack-tip stress intensity

associated with the crack renucleation in the second row of cells. Second, beyond the load maximum, the measured curves fall off somewhat more gradually than the simulated ones for values of bridging strength and effective pullout length that are consistent with the pullout-dominated regime. This discrepancy is believed to be due to the debonding that occurs ahead of the crack tip before cell fracture, a feature not incorporated explicitly in the bridging model.

It is notable that in both the $\pm 45^{\circ}$ and $0/90^{\circ}$ orientations, the characteristic bridging strength is about an order of magnitude smaller than the unnotched strength. One implication is that the pullout process (after cell cracking) does not contribute substantially to the ultimate strength of the FM, except perhaps in the presence of very long cracks or notches. Nevertheless, it contributes substantially to the fracture energy because of the relatively large characteristic length. Furthermore, it is expected to impart a high level of damage tolerance under localized loading conditions, such as that associated with impact by foreign objects.

5.1.4 Refinement of Bridging Model for Fracture of Fibrous Monoliths

When the crack-bridging model was used to describe fracture resistance, predictions of the load-CMOD response were found to agree well with the measurements. Notwithstanding these correlations, the peak stresses in the notched specimens of both the 0/90° and ±45° architectures were found to be comparable to those of the corresponding unnotched specimens. This result raised concerns about the validity of a stress-intensity approach to modeling fracture behavior, especially in the region around the stress maximum. This issue was addressed through experiments on specimens of larger size.

To assess the effects of size scale on the notch sensitivity of the FMs, samples with differing notch-size-to-width ratios were machined from both the 0/90° and ±45° Si_3N_4/BN FMs and tested in flexure. The notched FM samples used in the previous study were 10 mm wide x 50 mm long x 3.4 mm thick, with 5-mm-long notches ($a_o/W = 0.5$) and a loading span of 40 mm. New samples were machined with the same thickness and notch length, but with a width of 25 mm, yielding $a_o/W = 0.2$. The loading span was increased commensurately to 100 mm to maintain the same span/width ratio. The latter geometry was selected because it yields a higher stress intensity at the same level of net-section stress, thus promoting K-dominated behavior. The results of the flexure tests are shown on Fig. 117 in terms of the net-section stress vs. the load-line displacement.

For the 0/90° FM, the net-section strength decreased appreciably with increasing sample width, from ≈240 MPa for W = 10 mm to 153 MPa for W = 25 mm. However, the parameters associated with toughness remained essentially unchanged. The initiation toughnesses (obtained from the load maxima) were $K_i \approx$

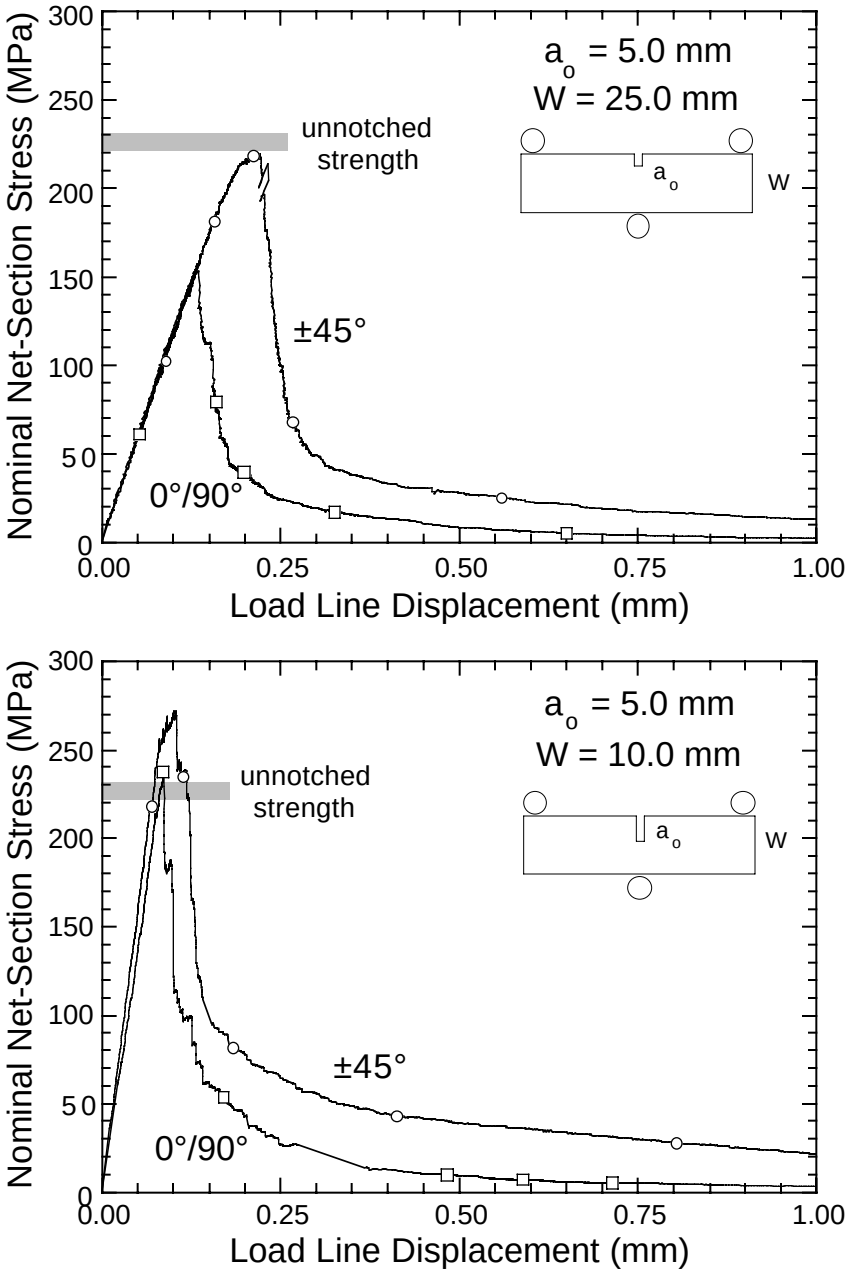

Fig. 117. Data from flexural tests of Si_3N_4/BN FMs, showing effects of a_o/W ratio.

12.2 and 10.6 MPa(m)$^{0.5}$ for W = 25 and W = 10 mm, respectively; the corresponding steady-state fracture toughnesses (obtained from the work of fracture) were $K_{ss} \approx 24.5$ MPa(m)$^{0.5}$ and 23.0 MPa(m)$^{0.5}$ for W = 25 and W =10 mm, respectively.

For the ±45° FM, the net-section strength decreased only slightly with increasing width (the effects of size being much less pronounced than in the 0/90° FM). Furthermore, for both sizes of ±45° samples, the strengths were comparable to or greater than the unnotched strength. In addition, the initiation and steady-state toughnesses increased substantially with width: $K_i \approx 12.3$ and 17.5 MPa(m)$^{0.5}$ for W = 10 and 25 mm; and $K_{ss} \approx 31.0$ and 40.6 MPa(m)$^{0.5}$ for W = 10 and 25 mm, respectively (Fig. 118).

The results indicate that the specimen geometries used to characterize the notched properties of the ±45° FMs in these studies are insufficient to produce K-dominated behavior. In contrast, the specimens are deemed adequate for achieving K-dominance in the 0/90° FMs.

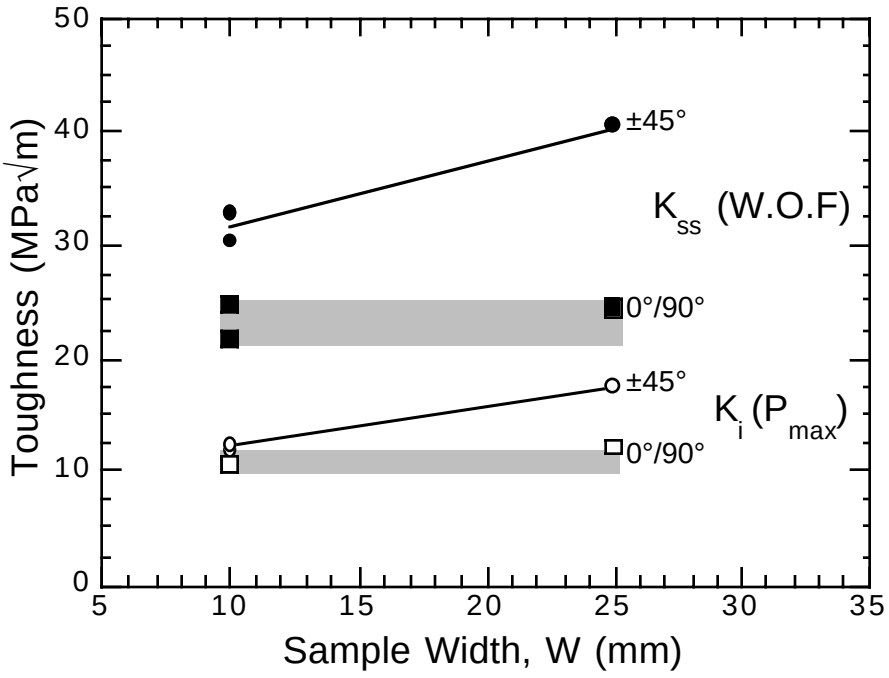

Fig. 118. Variations in the initiation and steady-state toughnesses with sample width for 0/90° and ±45° FMs.

Previously, the strengths of the FMs were rationalized by the stress to initiate a crack, assuming K-dominated response. The nominal net-section bending stress that corresponds to a prescribed initiation toughness K_i is:

$$\sigma_{nom} = \frac{K_i\left(1+\frac{2a_o}{W}\right)\left(1-\frac{a_o}{W}\right)^{3/2}}{\sqrt{a_o}\left(1.99-\frac{a_o}{W}\left(1-\frac{a_o}{W}\right)\left(2.15-3.93\frac{a_o}{W}+2.7\left(\frac{a_o}{W}\right)^2\right)\right)} \tag{5.7}$$

for a span-to-width ratio of 4 (see, e.g., Tada et al., "Stress Intensity Handbook," Del Research Corp., 1985). Conversely, if the strength of the material is notch-insensitive, the net-section strength is expected to follow

$$\sigma_{nom} = \sigma_{NS}\left(1-\frac{a_o}{W}\right)^2, \tag{5.8}$$

where σ_{NS} is the unnotched net-section strength. The predictions from the two criteria are compared with the experimental measurements in Fig. 119. The results provide corroborating evidence that K-dominated behavior is obtained (approximately) in the 0/90° FMs, but not in the ±45° FMs. In the latter FMs, the strength appears to follow a simple net-section strength prediction, indicating highly notch-insensitive behavior.

5.1.5 Enhanced Pullout in Fibrous Monoliths

We determined from the first set of Si_3N_4/BN FMs that cell pullout in the 0/90° FM was inhibited by nonuniformities in the cell cross sections. These nonuniformities were a result of indentation of the longitudinal cells into the adjacent transverse cells during green-state pressing. The indentation also led to the formation of cusps at many of the triple junctions between longitudinal and transverse cells. Examples of such cusps are highlighted in Fig. 120. It was anticipated that eliminating these nonuniformities would increase the pullout lengths and hence the fracture resistance of the FM.

To eliminate the nonuniformities in the cell cross section, it was suggested that ACR warm-roll unidirectional tapes before layup. In principle, this would produce cells of uniform cross section, ideally in the shape of rectangular prisms. These tapes would then be stacked in a 0/90° configuration; the binder burnout and hot-pressing steps would remain the same as for the previously examined FMs.

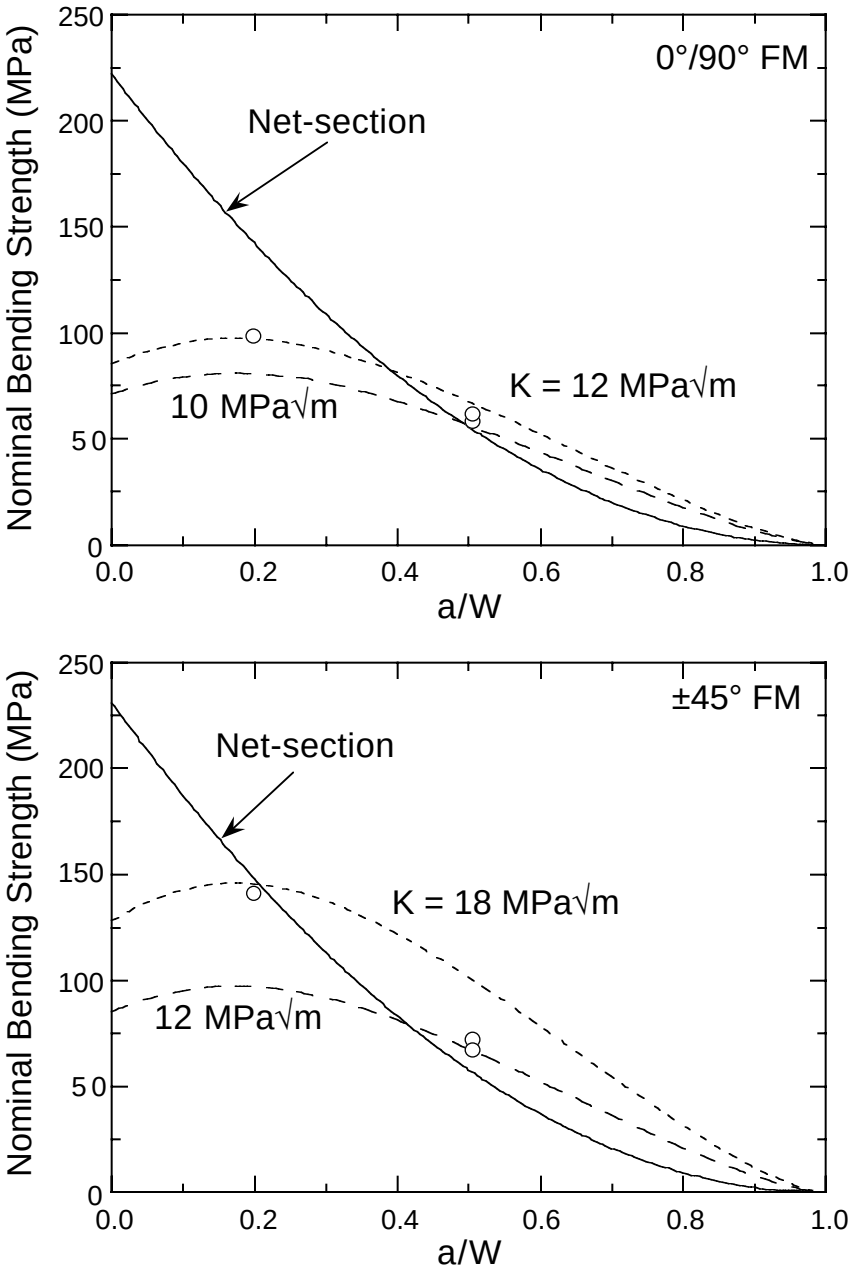

Fig. 119. Experimental and predicted measurements for 0/90° and ±45° FMs, based on initiation-controlled fracture criterion (Eq. 5.7) and the net-section strength criterion (Eq. 5.8) for a_o = 5.0 mm.

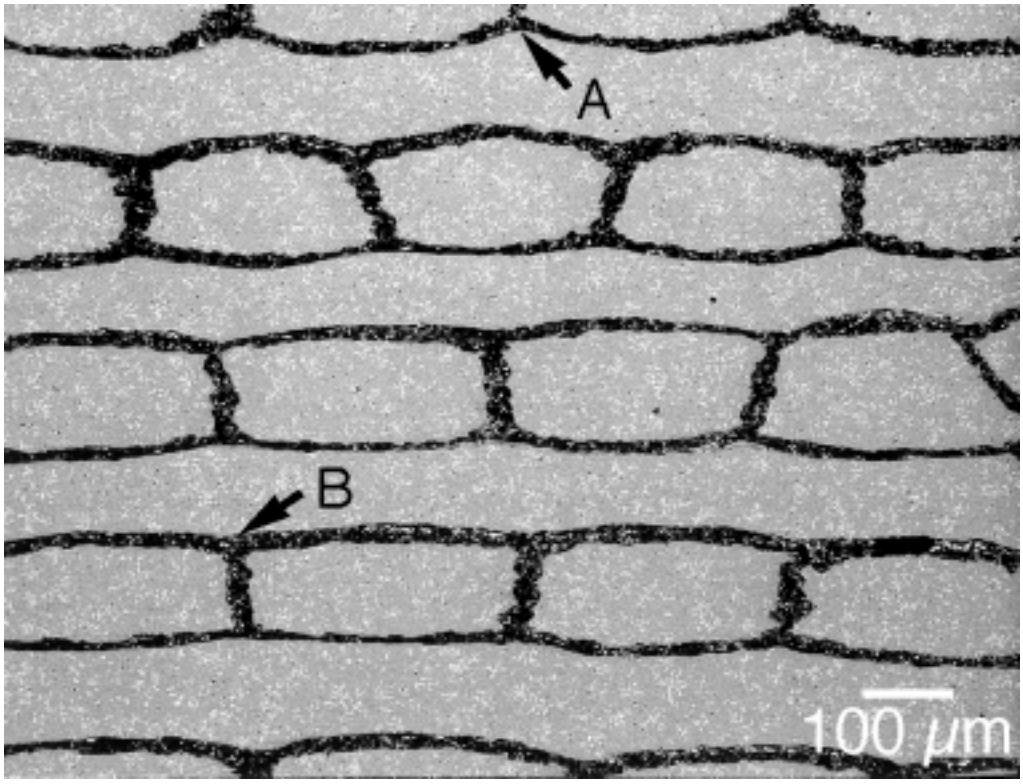

Fig. 120. SEM photomicrograph of Si_3N_4/BN FM; Arrow A shows example of cusps formed at triple junctions between longitudinal and transverse cells, and Arrow B shows a triple point at which a cusp did not form.

ACR produced one small plate (2.6 x 33 x 25 mm) of 0/90° Si_3N_4/BN FM, by the new process, and sent it to UCSB for testing. Small samples were cut from the plate for microstructural characterization by SEM (Fig. 121). Several features are noteworthy: the layup was different from that of the previous 0/90° plates; the new material was of the form $[0_2/90°_2]$, whereas the previous plates were [0/90°]. Apparently, the uniformity of the cell cross section was slightly improved. Although the cusps shown in Fig. 120 were largely eliminated, the cross-sectional shape exhibited large variations, and the cells appeared to undulate within each lamina (Fig. 122). There were distinct variations in the compositions of the cells and cell boundaries, as revealed by the contrast in images obtained in back-scattered electron imaging mode. Approximately half of the cells exhibited white spots (consistent with the presence of Y_2O_3 and/or Al_2O_3), whereas the remaining cells appeared to be devoid of such spots (Fig. 122c). The cell boundary contained elongated fibrous features, which were absent in previous FM materials (Fig. 122d).

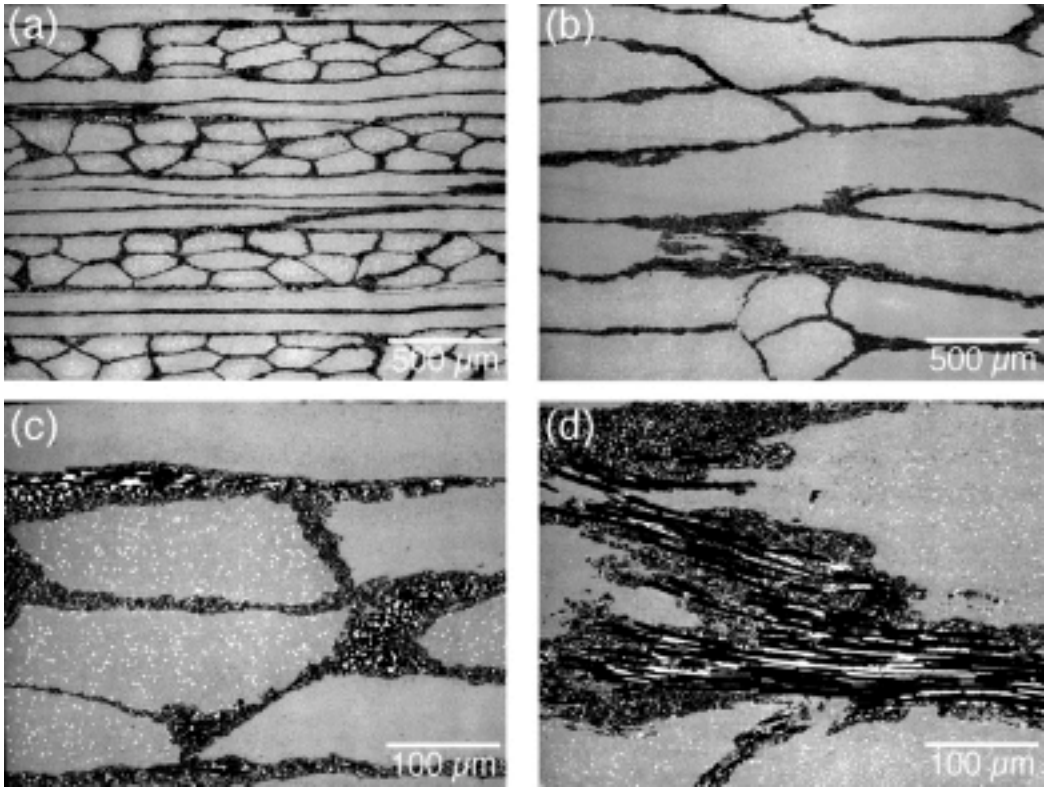

Fig. 121. Back-scattered electron photomicrographs of new 0/90° FM: low-magnification taken (a) parallel and (b) perpendicular to hot-pressing direction; (c) intermediate-magnification image, showing variations in composition of cells, as manifested by the presence or absence of white spots; and (d) higher-magnification image, showing thin, fiber-like features within BN phase.

Despite the presence of some of these unexpected microstructural features, notched flexure tests were performed to characterize the contribution of pullout to fracture resistance. For this purpose, the plate was surface ground and polished on each face to facilitate observation, and then machined to produce two notched bars; the pertinent dimensions were: thickness, B = 2.3 mm; width, W = 6.6 mm; and notch length, a_o = 3.4 mm. The samples were loaded in three-point flexure, with a span of 30 mm.

The load-displacement response is shown in Fig. 123. The initiation and steady-state fracture toughness values were calculated from the load maximum and the WOF, respectively. The initiation toughness K_i was 5.2-5.6 MPa $(m)^{0.5}$; the

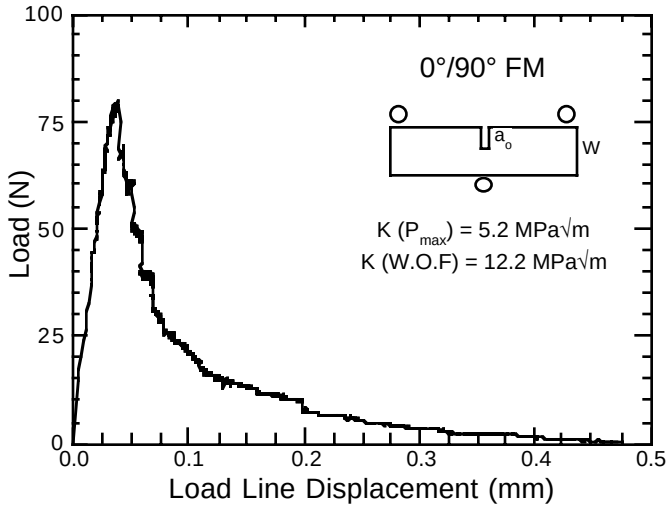

Fig. 122. Load-displacement response of new 0/90° FM in notched three-point flexure.

steady-state toughness K_{ss} was 11.6-12.2 MPa $(m)^{0.5}$ (with the WOF being 760-850 J/m^2). Although these values were higher than those of the monolithic Si_3N_4, they were approximately one-half of those obtained on the previous 0/90° plate: K_i = 10.5-10.7 MPa $(m)^{0.5}$, K_{ss} = 21.7-24.8 MPa $(m)^{0.5}$.

The reduction in toughness is associated with diminished cell pullout. A representative fracture surface is presented in Fig. 124, along with a fracture surface of a sample from the previous plate for comparison. The 0 and 90° cells tended to fracture on the same plane, leading to very little frictional sliding as the surfaces separate. The previous material exhibited more extensive pullout, with sliding occurring between 0 and 90° plies, as well as between adjacent 0° cells.

It is clear that the properties of the new FM were inferior to the previous material. Remedies are being sought.

5.2 Thermal Stresses in Fibrous Monoliths

The difference in CTE between the cell and cell boundaries of FMs can be expected to introduce significant residual stresses. The stresses were modeled numerically and analytically. Modeled results were compared with measured values, and as will be shown, the agreement was quite good.

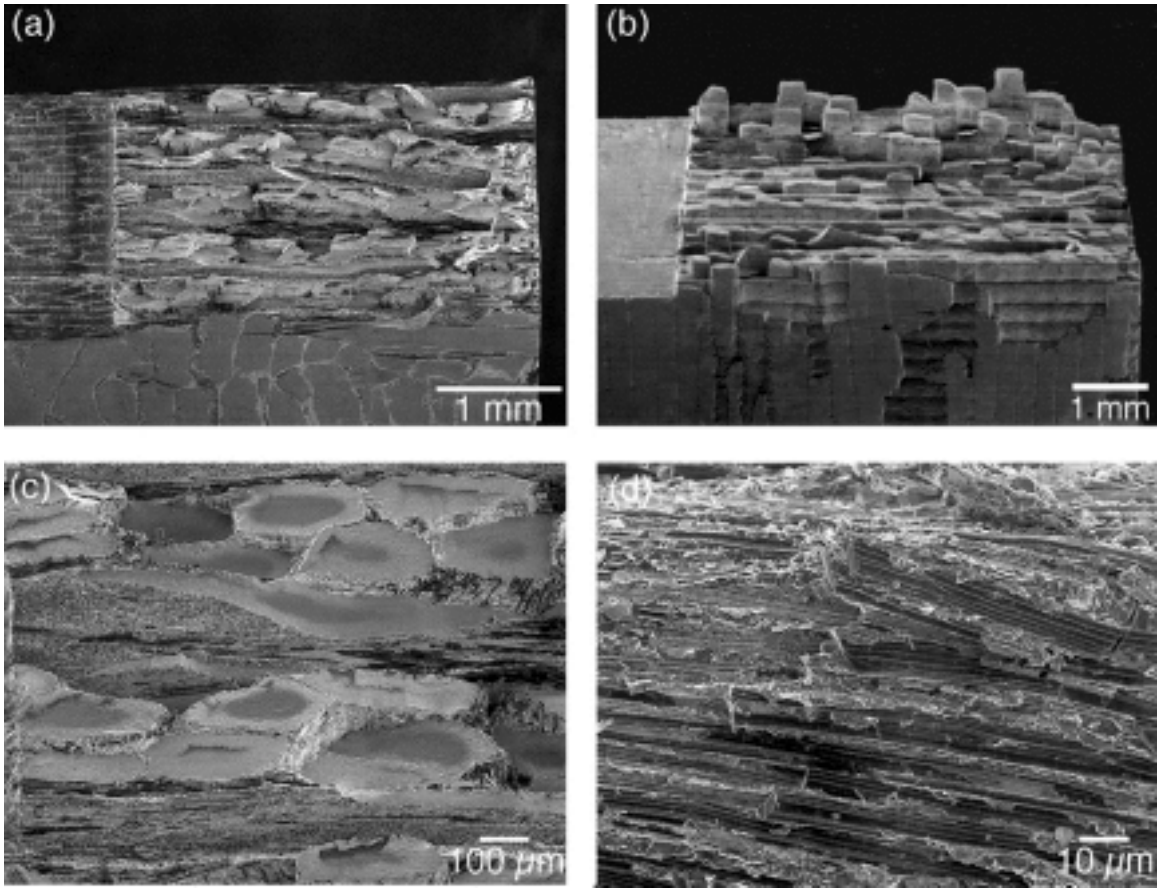

Fig. 123. SEM photomicrographs of fracture surfaces for (a) new, and (b) old 0/90° FMs, illustrating the differences in cell fracture and pullout; and are higher-magnification images of fracture surface of the new material, showing (c) nearly coplanar fracture and (d) fiber-like features in the BN interphase.

5.2.1 Unidirectional Fibrous Monoliths

The models for unidirectional FMs are based on stress analyses of representative unit cells, selected to match the key features in real FM microstructures. In unidirectional materials, the cells will be called fibroids to distinguish them from the unit cells of our analysis. The fibroids adopt a shape that resembles a flattened hexagon and the BN forms an essentially uniform coating around each fibroid (Fig. 124). A schematic diagram of the idealized fibroid shape used in the model is shown in Fig. 125. The shape is defined by a regular hexagon that has been re-scaled in the y direction by a factor $k < 1$. The re-scaling reduces the length of the short sides (parallel to the y direction) from 2ℓ to $2\ell k$, and the long sides from 2ℓ to $\sqrt{3 + k^2}\ \ell$. The long and short axes of the hexagonal become $a = 2\sqrt{3}\ \ell$ and $b = 4k\ell$, with a corresponding aspect ratio $a/b = \sqrt{3}/2k$.

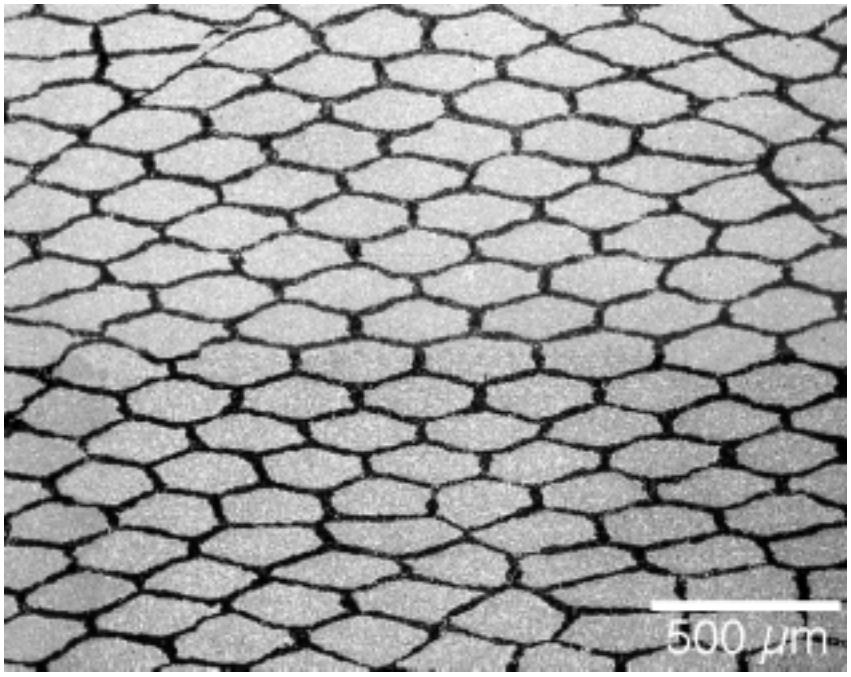

Fig. 124. SEM photomicrograph of cross section of unidirectional Si_3N_4/BN FM.

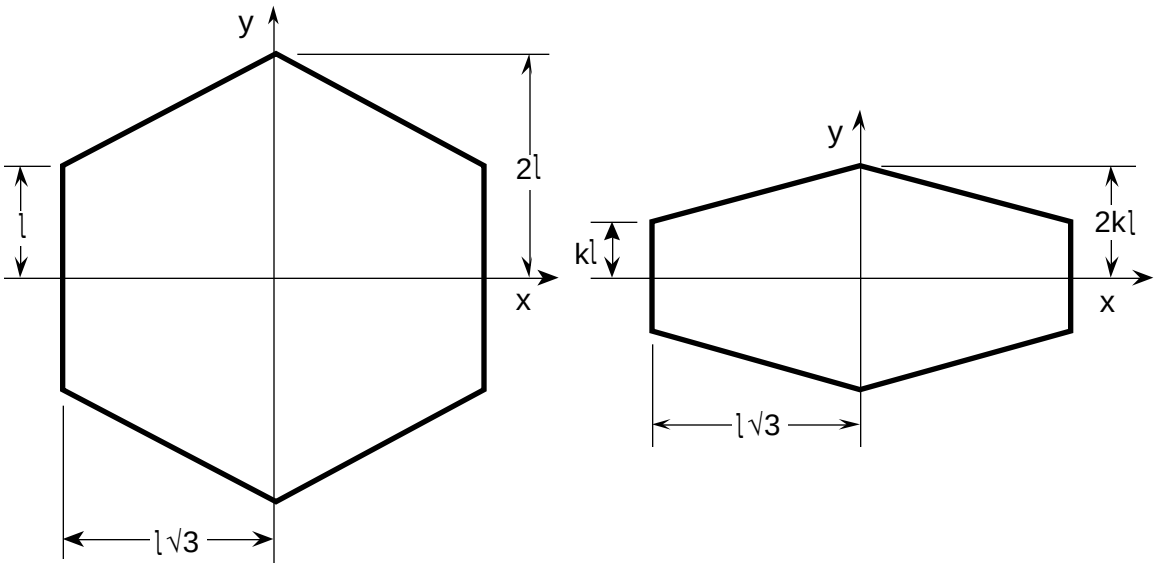

Fig. 125. Re-scaling of a regular hexagon to produce a flattened hexagon that resembles the cross section of the Si_3N_4 fibroids.

The value of k that gives the best fit of the flattened hexagon idealization to the actual fibroid shape was taken to be that which produces the combination of enclosed area A and perimeter P that correlates best with the real fibroids. For this purpose, the areas and perimeters of the fibroids were measured by quantitative metallography of a cross section that contained >300 fibroids. The resultant distributions are plotted in Fig. 126. The predicted values of these parameters, from the flattened hexagon idealization, are

$$P = 4k\ell\left[1+\sqrt{1+3/k^2}\right] \tag{5.9}$$

and

$$A = 6\sqrt{3}\,k\ell^2. \tag{5.10}$$

The relevant nondimensional ratio of these parameters is

$$\frac{P}{\sqrt{A}} = 4\sqrt{\frac{k}{6\sqrt{3}}}\left[1+\sqrt{1+3/k^2}\right]. \tag{5.11}$$

The distribution in the measured ratio $P/\sqrt{A}$ is plotted in Fig. 126c; its average value is $P/\sqrt{A} = 4.44$. From Eq. 5.11, the scaling factor that yields the same ratio of $P/\sqrt{A}$ is $k = 0.35$. To further demonstrate the correlation, several flattened hexagons for which $k = 0.35$ have been superimposed on a photomicrograph of the real fibroids in Fig. 127.

The unit-cell geometry and finite-element mesh used for calculating the thermal stresses are shown in Figs. 128 and 129. The relative amounts of Si_3N_4 and BN were selected to be consistent with the respective volume fractions $f = 0.8$ and $1 - f = 0.2$. Both phases were assumed to be elastic, with Young's moduli $E_f = 242$ GPa for the Si_3N_4 and $E_i = 20.7$ GPa for the BN. The Poisson's ratio for both phases was taken to be $\nu = 0.2$.

Finite-element calculations were performed with the ABAQUS code to determine the residual stresses due to an arbitrary thermal strain $\Delta\alpha\,\Delta T$, wherein $\Delta\alpha = \alpha_f - \alpha_i$ (f and i denoting fibroid and interphase, respectively) and ΔT is the temperature change after processing. The stress distributions in both phases are plotted in Figs. 130 and 131. The results are presented in nondimensional form, with the normalizing stress being $E_i\,\Delta\alpha\,\Delta T$.

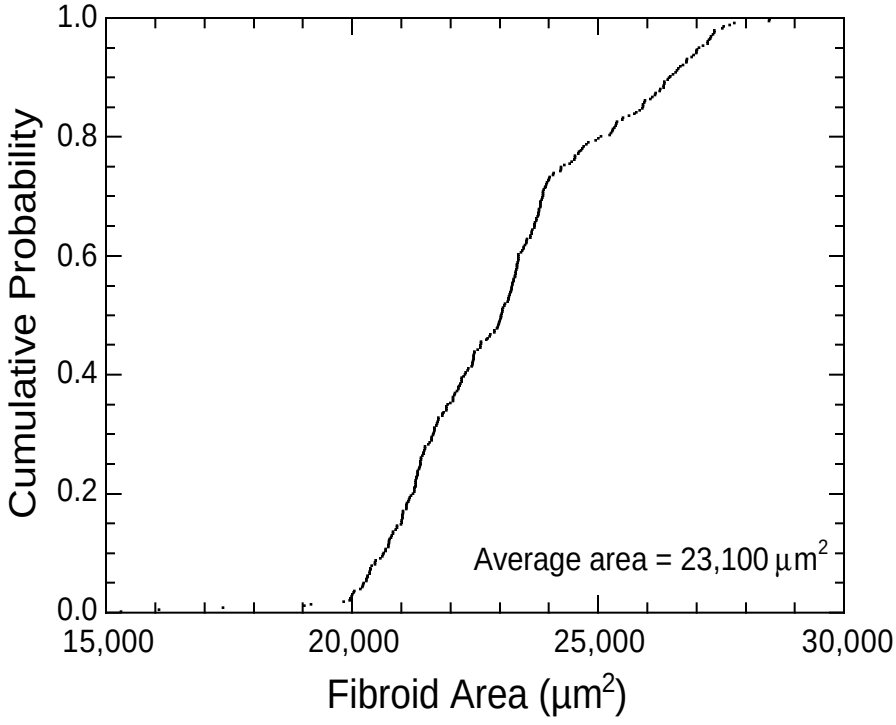

(a)

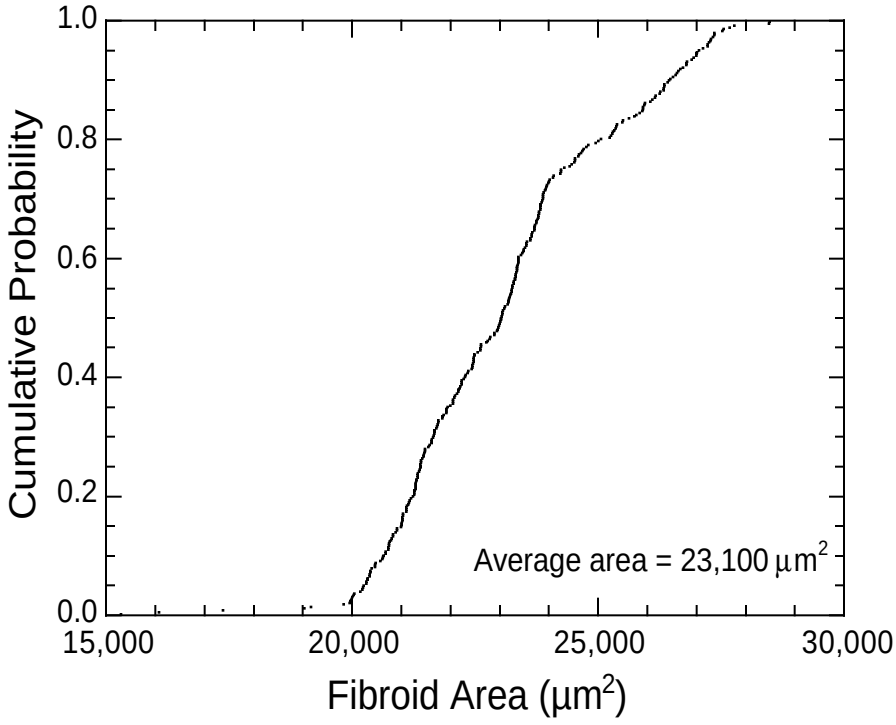

(b)

Fig. 126. Measured distributions of (a) perimeter P, (b) area A, and (c) ratio $P/\sqrt{A}$.

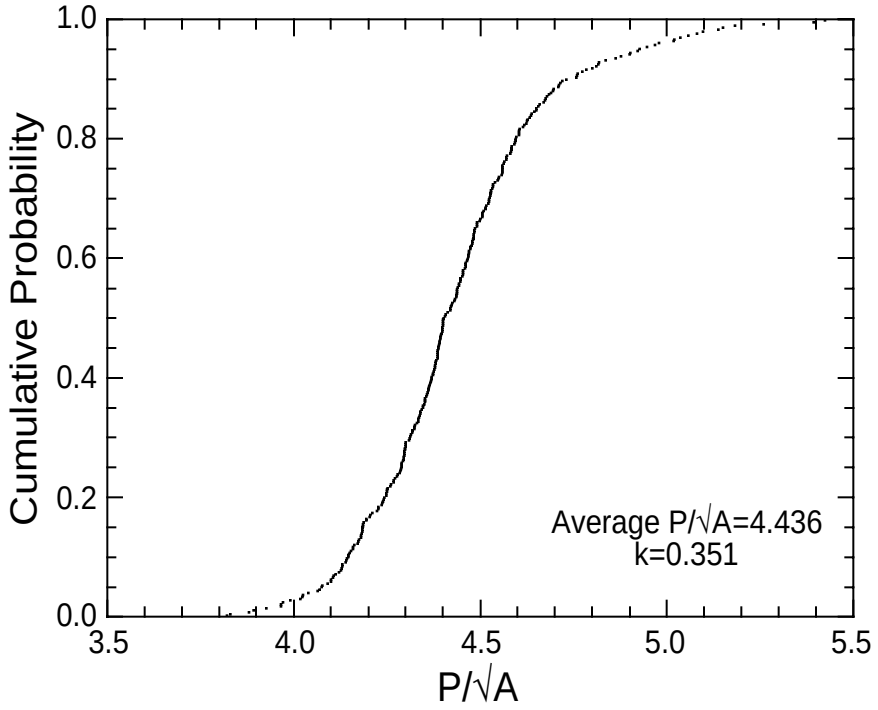

(c)

Fig. 126. (Contd.)

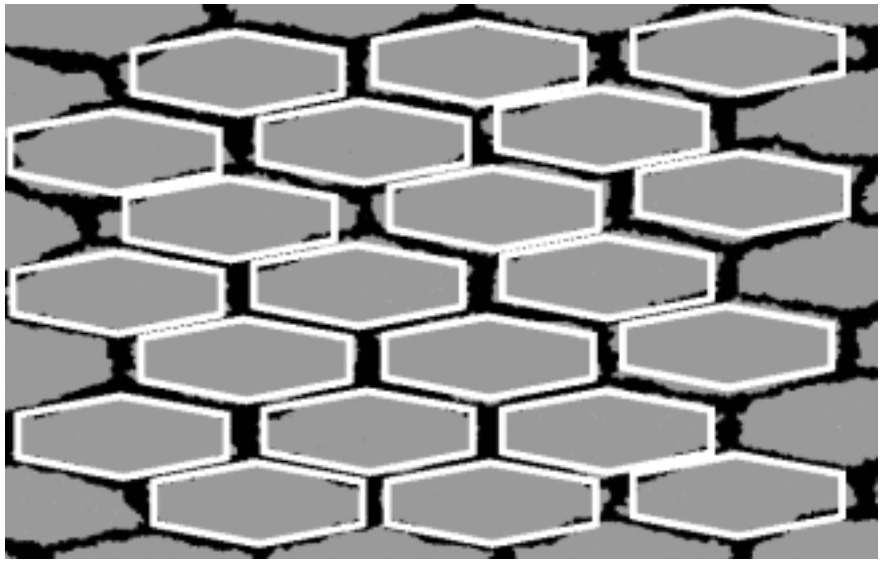

Fig. 127. Superposition of the best-fit flattened hexagon (k = 0.35) on actual fibroids.

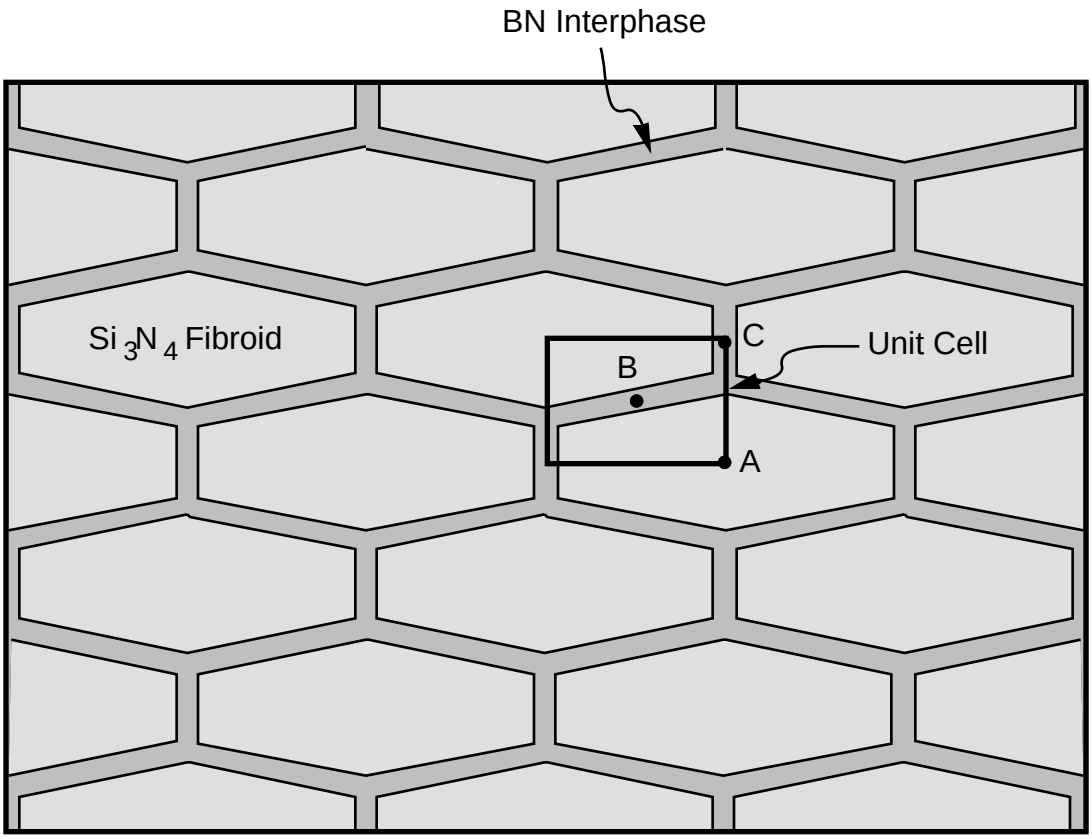

Fig. 128. Schematic diagram of the assumed periodic array of fibroids and associated unit cell.

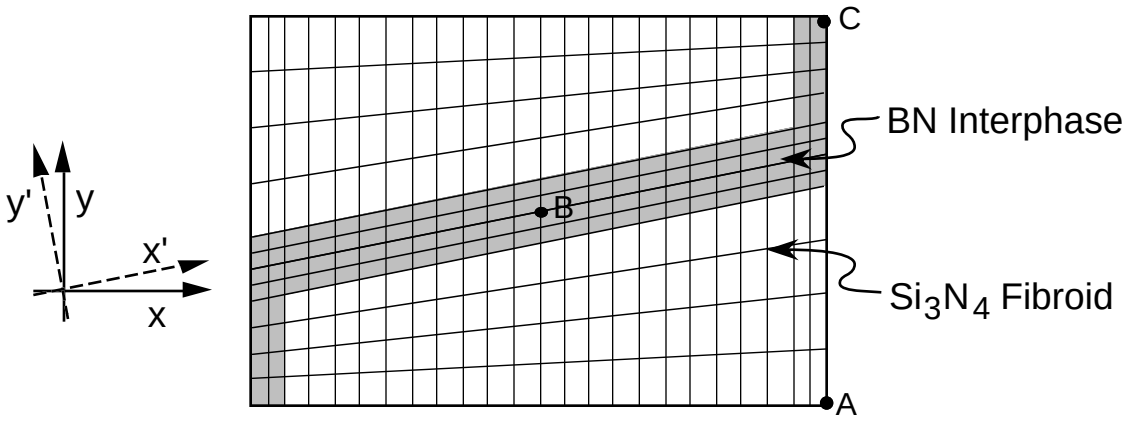

Fig. 129. Finite-element mesh of unit cell used to calculate thermal residual stresses. z-axis is orthogonal to x and y, x' is parallel to the interface along the long segment of BN interphase, and y' is orthogonal to x'.

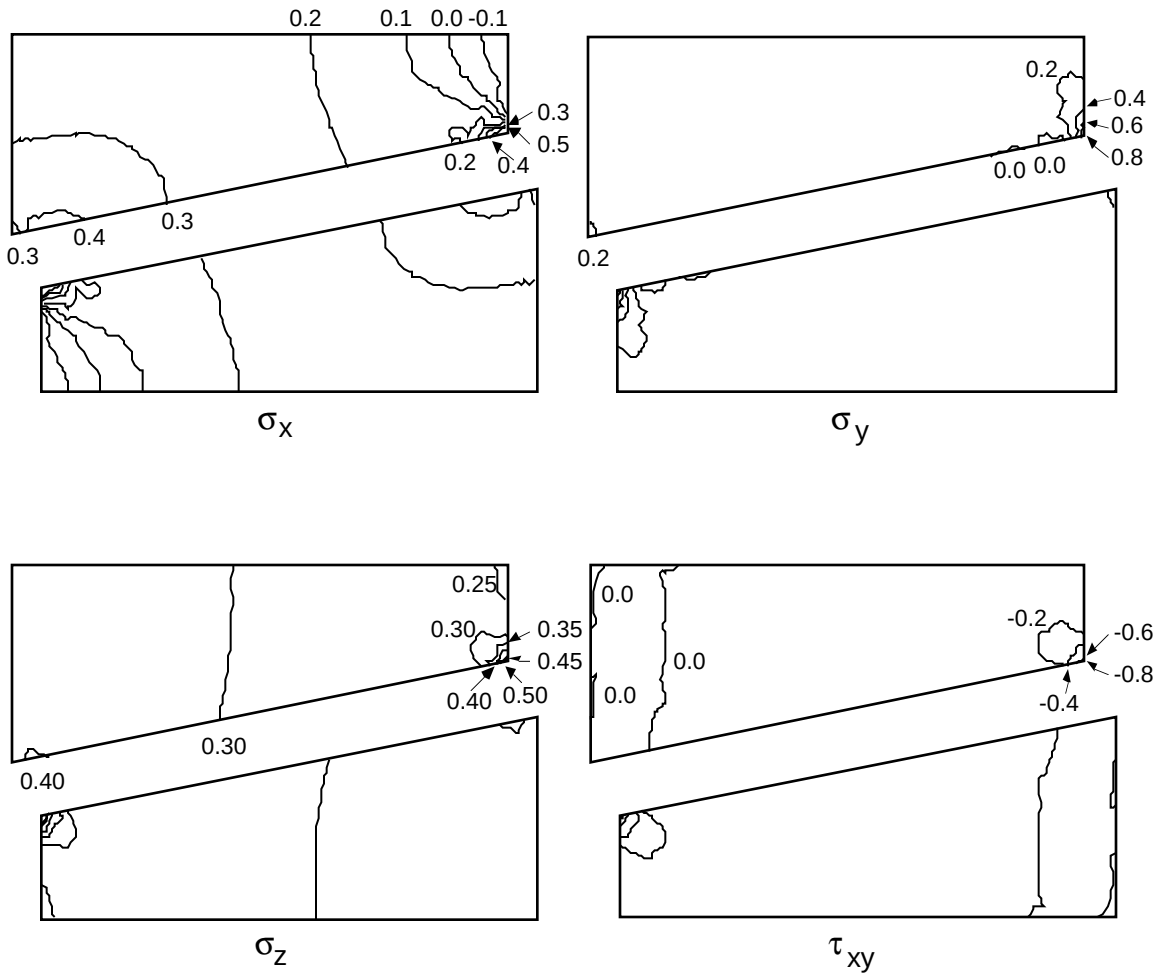

Fig. 130. Contour plots showing the stress distributions in Si_3N_4 fibroids; stresses are normalized by $E_i \Delta\alpha \Delta T$.

The results demonstrate that the axial stress in the fibroid is relatively uniform. At the fibroid center (designated point A in Fig. 129) and over most of its volume, the axial stress is $\sigma_z^f / E_i \Delta\alpha \Delta T \approx 0.30–0.32$. Very near the corners, it rises to values in the range 0.35–0.5. However, such sharp corners do not exist in the real fibroids, and consequently the stress concentrations in these regions are expected to be small. Similarly, uniform axial stresses are predicted for the BN interphase. At the center of the long segment of the interphase (designated point B in Fig. 129), the stress is $\sigma_z^i / E_i \Delta\alpha \Delta T = -1.21$. Small deviations from this value occur near the corners, but again these are not expected to occur in real FMs because of the absence of such sharp corners.

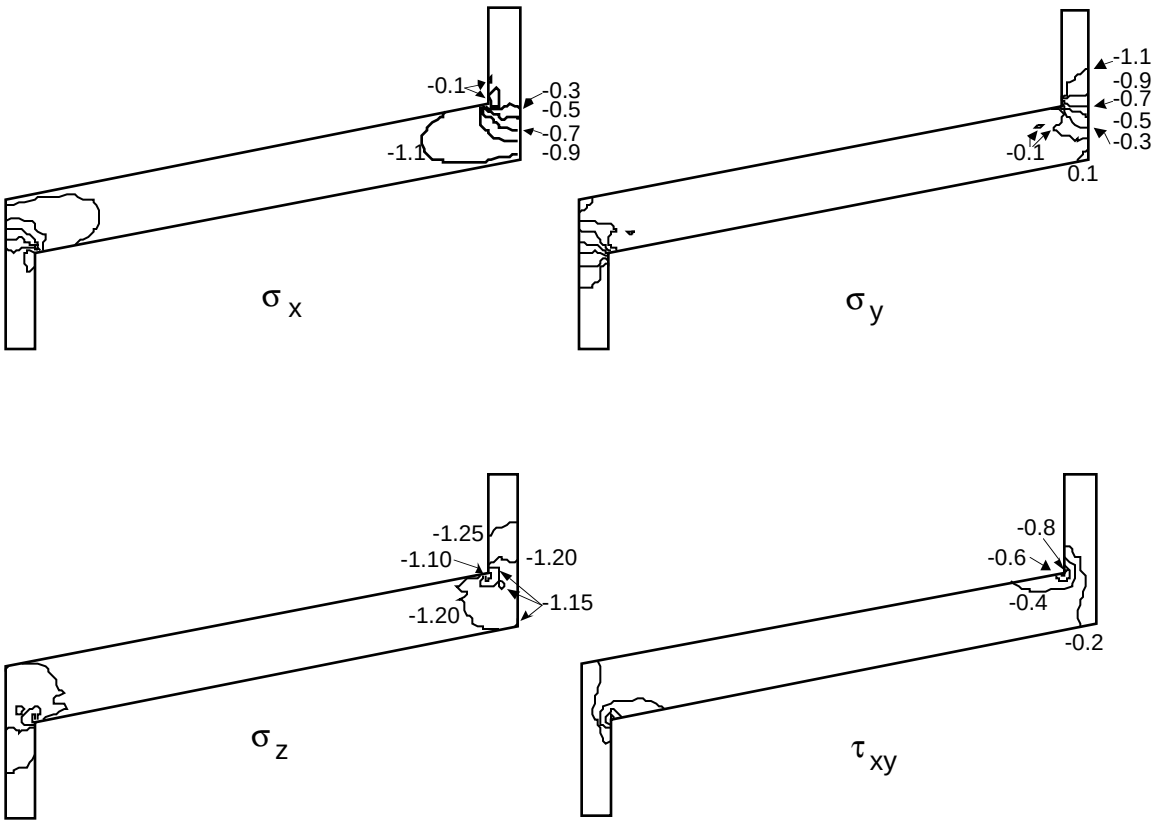

Fig. 131. Contour plots showing stress distributions in BN interphase; stresses are normalized by $E_i \Delta\alpha \Delta T$.

The normal stresses in the y direction in the fibroids (parallel to the short dimension) are considerably smaller. Over most of the fibroid, $\sigma_y^f / E_i \Delta\alpha \Delta T < 0.2$. Higher values are predicted only near the corners. Along the x direction, the normal stress develops progressively from the thin end of the fibroid, from $\sigma_x^f / E_i \Delta\alpha \Delta T \approx -0.15$ at the end, to ≈ 0.3 at the center, with only minor variations along the y direction. Qualitatively, this development of stress can be viewed as analogous to the shear-lag process that occurs at the end of a fiber or plate, owing to a mismatch of either the elastic moduli or the thermal expansion coefficients of the phases. Furthermore, it is noteworthy that the maximum value of this stress is comparable to the maximum axial stress.

The transverse stresses σ_x^i and σ_y^i in the BN interphase exhibit differing features. Notably, σ_x^i is relatively uniform along the long segment of the interphase, at $\sigma_z^i / E_i \Delta\alpha \Delta T \approx -1.1$, and diminishes in magnitude at the corners and along the short sections. The maximum value of σ_x^i is comparable to the maximum axial stress σ_z^i. In essence, the BN interphase exists as a thin constrained layer between adjacent fibroids, such that approximately uniform biaxial stressing is expected in the y-z plane. Indeed, this result is confirmed by calculations based on a

two-dimensional plate model, described below. In contrast, the stress component σ_y^i is negligible along the long segment of the interphase ($|\sigma_y^i / E_i \Delta\alpha \Delta T| < 0.1$), and builds up to high levels along the short segments, to $\sigma_y^i / E_i \Delta\alpha \Delta T \approx -1.2$, again comparable to the maximum values of σ_x^f and σ_z^i. This result also can be rationalized on the basis that approximately uniform biaxial stressing occurs along the short sections, in this case in the y-z plane. Quantitative comparisons with the plate model predictions are presented below.

The shear stresses τ_{xy} in both phases are relatively small. In the fibroid, $|\tau_{xy}^f / E_i \Delta\alpha \Delta T| \approx 0$–$0.2$, and in the BN interphase, $|\tau_{xy}^i / E_i \Delta\alpha \Delta T| \approx 0.2$–$0.4$.

To assess the sensitivity of the predicted thermal stresses to the unit-cell shape, additional finite-element calculations were performed; the fibroids were assumed to be either regular hexagons, characterized by k = 1, or more severely flattened hexagons, with k = 0.21 (Fig. 132). Furthermore, comparisons were made with the predictions of two other models, one based on concentric cylinders of the two phases, the other, based on parallel plates. Both of the latter models have well-established analytical solutions, which are presented below.

In the concentric-cylinder model, the axial stresses in the interphase and the fibroid are predicted to be uniform and are given by the following equations (B. Budiansky et al., J. Mech. Phys. Solids 34 (1986) 167):

$$\frac{\sigma_z^i}{E_i \Delta\alpha \Delta T} = \frac{\lambda f E_f}{E(1-\nu)} \tag{5.12}$$

and

$$\frac{\sigma_z^f}{E_i \Delta\alpha \Delta T} = \frac{-\lambda(1-f)E_m}{E(1-\nu)}, \tag{5.13}$$

where E is the longitudinal composite modulus, defined by

$$E = f E_f + (1-f) E_i \tag{5.14}$$

and λ is a nondimensional parameter:

$$\lambda = \frac{(1/2)(1+E/E_f)}{1-\frac{1}{2}\left(\frac{1-2\nu}{1-\nu}\right)(1-E/E_f)}. \tag{5.15}$$

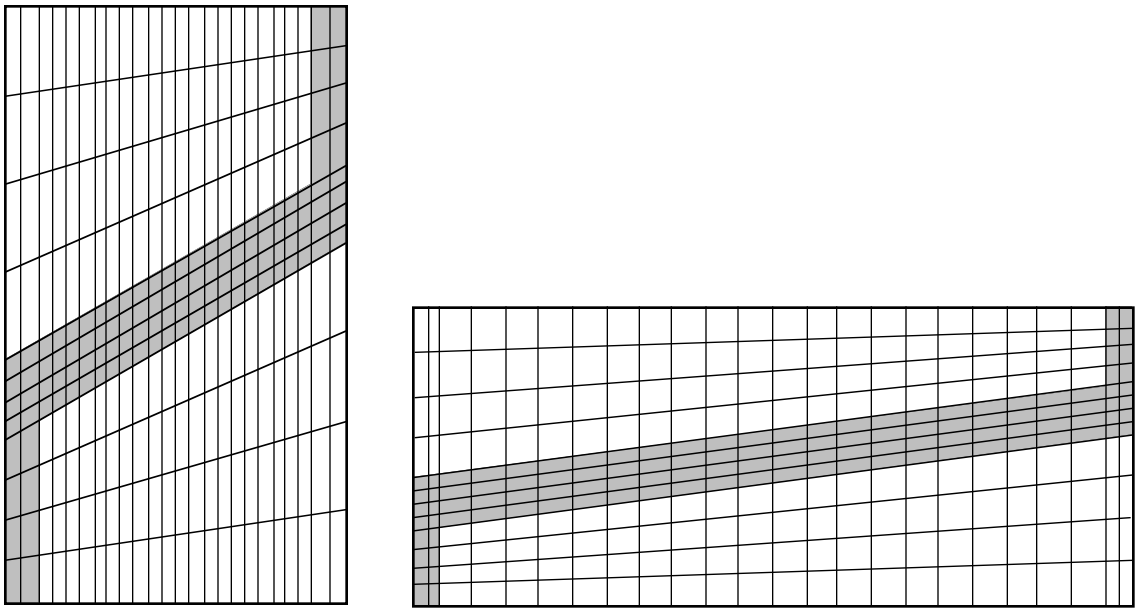

(a) k=1 (b) k=0.21

Fig. 132. Finite-element meshes of unit cells for cross sections that are (a) regular hexagons (k = 1) and (b) severely flattened hexagons (k = 0.21). The shaded regions represent BN.

From the appropriate elastic constants for Si_3N_4 and BN and the relevant volume fraction, the predicted residual stresses are $\sigma_z^i / E_i \Delta\alpha \Delta T = -1.194$ and $\sigma_z^f / E_i \Delta\alpha \Delta T = 0.299$.

The plate model also yields uniform in-plane stresses, given by

$$\frac{\sigma_z^i}{E_i \Delta\alpha \Delta T} = \frac{f E_f}{E(1-\nu)} \tag{5.16a}$$

and

$$\frac{\sigma_z^f}{E_i \Delta\alpha \Delta T} = \frac{-(1-f)E_f}{E(1-\nu)} . \tag{5.16b}$$

These results are identical to those of the concentric cylinder model (Eq. 5.15) when $\lambda = 1$. The latter condition is satisfied exactly when either $\nu = 0$ or $E/E_i = 0$. The predicted stresses for the Si_3N_4/BN system from the plate model are $\sigma_z^i / E_i \Delta\alpha \Delta T = -1.224$ and $\sigma_z^f / E_i \Delta\alpha \Delta T = 0.306$. These values are within 2.6% of those obtained from the concentric-cylinder model. The similarities arise because $\lambda \approx 0.974$, very near the value of unity needed for the two models to yield identical results.

Figure 133 shows predictions of the axial stresses from the concentric cylinder and plate models, and from finite-element calculations for the various hexagonal unit cells. For the latter geometries, the fibroid stress was taken at the fibroid center and the interphase stress was taken at the center of a long segment. Evidently, the axial stresses are insensitive to the selection of cell shape. For example, the fibroid stresses from the finite-element calculations for the three hexagonal cell geometries are within 7% of the value obtained from the concentric-cylinder model. Similarly, all of the predicted stresses for the BN from both the finite-element calculations and the analytical models fall within 2% of each other. The key conclusion is that either of the two approximate analytical models (Eqs. 5.12, 5.13, and 5.16) is adequate for estimating the average values of the axial stresses; finite-element calculations are needed only in cases where sharp corners exist and hence stress concentrations arise. In Si_3N_4/BN FMs of the type shown in Fig. 124, such concentrations are expected to be small because of the absence of sharp corners.

The plate model can be utilized also to rationalize the normal stresses in the interphase perpendicular to the fibroid axis. As noted earlier, the interphase exists essentially as a thin layer between adjacent fibroids; consequently, it is expected to be subject to uniform biaxial stressing in the plane parallel to the fibroid surfaces. For example, in the short segments of the interphase, biaxial stressing is expected in the y-z plane. By the plate model, these stresses are predicted to be $\sigma_z^i = \sigma_y^i = -1.22\, E_i \Delta\alpha\, \Delta T$. Similar values are obtained from the finite calculations at the center of the short segment of the interphase (point C in Figs. 128 and 129): $\sigma_z^i / E_i \Delta\alpha\, \Delta T \Delta T = -1.24$ and $\sigma_y^i / E_i\, \Delta\alpha\, \Delta T = -1.26$. The same arguments can be applied to the long segments of the interphase, i.e., the stresses parallel to the fibroid surface, defined as the x' – z plane in Fig. 129, are again predicted to be $\sigma_z^i = \sigma_{x'}^i = -1.22\, E_i\, \Delta\alpha\, \Delta T$. From the results in Fig. 131, and following standard procedures in the transformation of stresses, the finite-element calculations yield $\sigma_z^i / E_i\, \Delta\alpha\, \Delta T = -1.21$ and $\sigma_{x'}^i / E_i\, \Delta\alpha\, \Delta T = -1.22$ at the center of the long segment of the interphase (point B); again essentially identical to the predictions of the plate model.

The plate model also predicts zero normal stress perpendicular to the thin direction of the interphase. For example, along the short segments of the interphase, σ_x^i is expected to be zero, a result which is broadly consistent with the finite-element results (Fig. 131). Similarly, along the long segments, $\sigma_{y'}^i$ is expected to be zero. If the results in Fig. 130 are used, the value of this stress component at the center of the long segment is $\sigma_{y'}^i / E_i\, \Delta\alpha\, \Delta T = 0.097$; more than an order of magnitude smaller than the in-plane stresses $\sigma_{x'}^i$ and σ_z^i. These correlations further demonstrate the utility of the two-dimensional plate model, especially for predicting the principal stresses in the BN interphase.

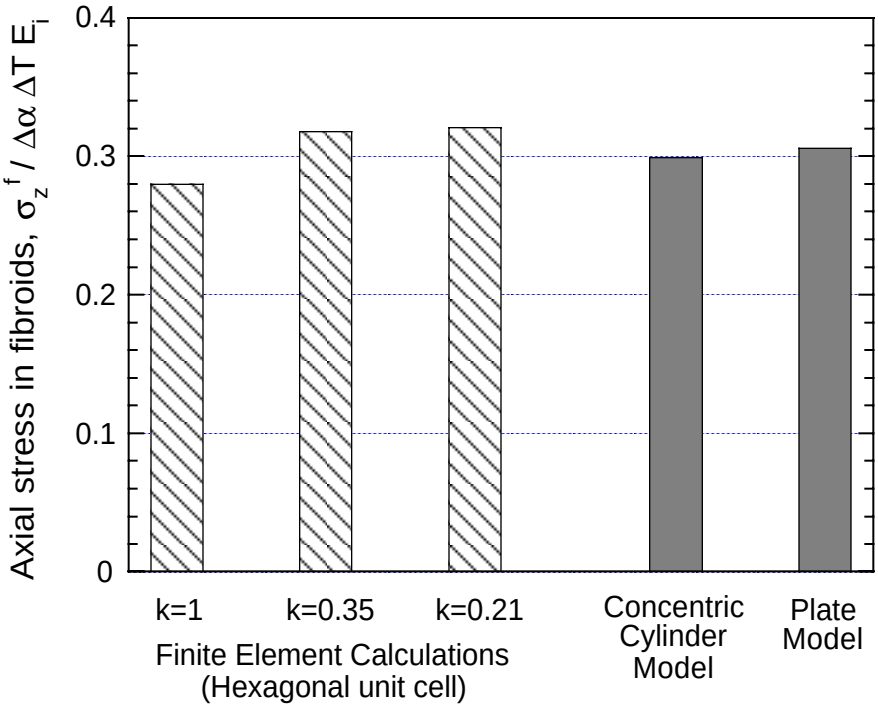

(a)

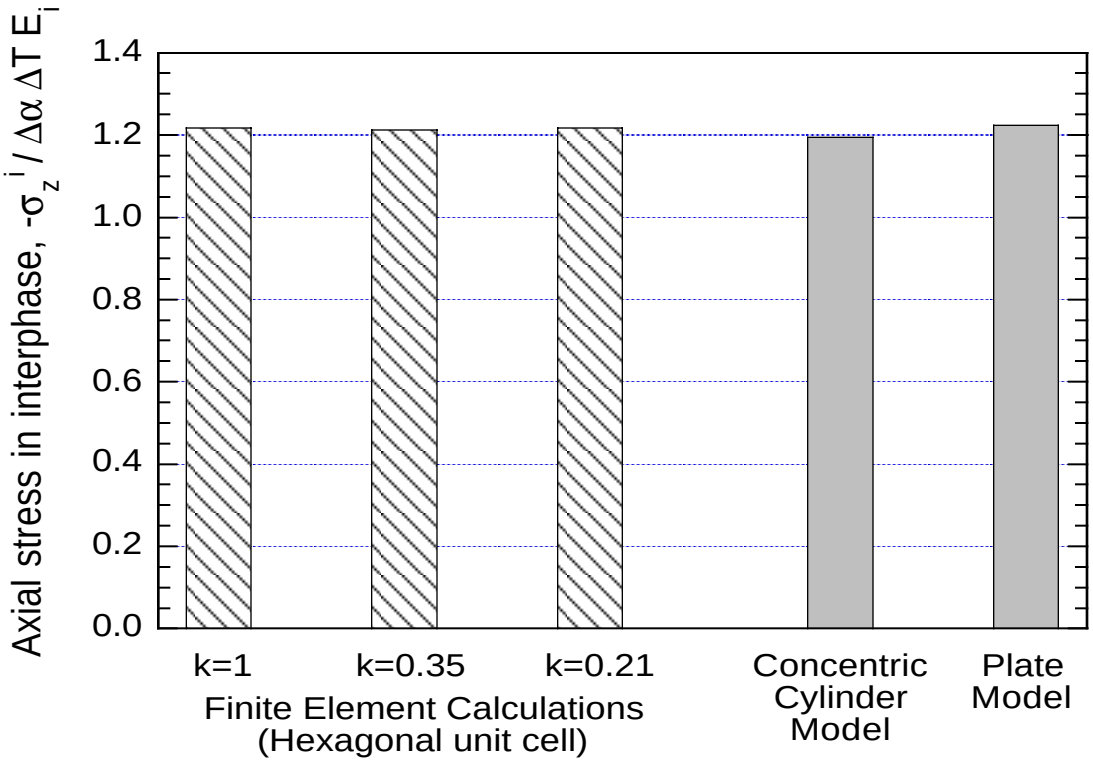

(b)

Fig. 133. Predicted axial stresses in (a) Si_3N_4 fibroids and (b) BN phase.

5.2.2 Cross-Ply Fibrous Monoliths

In the initial phase, models were developed for unidirectional FMs on the basis of stress analyses of representative unit cells, selected to match the key features in real FM microstructures. The analyses were based on both finite-element calculations and analytical models. The former were used to develop essentially exact results for a cell geometry that closely mimics the actual morphologies of the cells and the interphase in the FMs of current interest; the latter were based on simpler cell representations, including concentric cylinders and parallel plates. The utility of the approximate analytical models to describe the principal residual stresses was demonstrated.

In the second phase of this study, we focused on cross-ply FMs. As for the unidirectional materials, the models are based on the analysis of unit-cell models; both finite-element methods and approximate analytical models are used. For this purpose, the cells in the cross-ply materials are idealized as rectangular prisms, with a width-to-thickness ratio of ≈3.4. A typical photomicrograph showing the cell shape and the corresponding three-dimensional finite-element mesh are presented in Figs. 134 and 135.

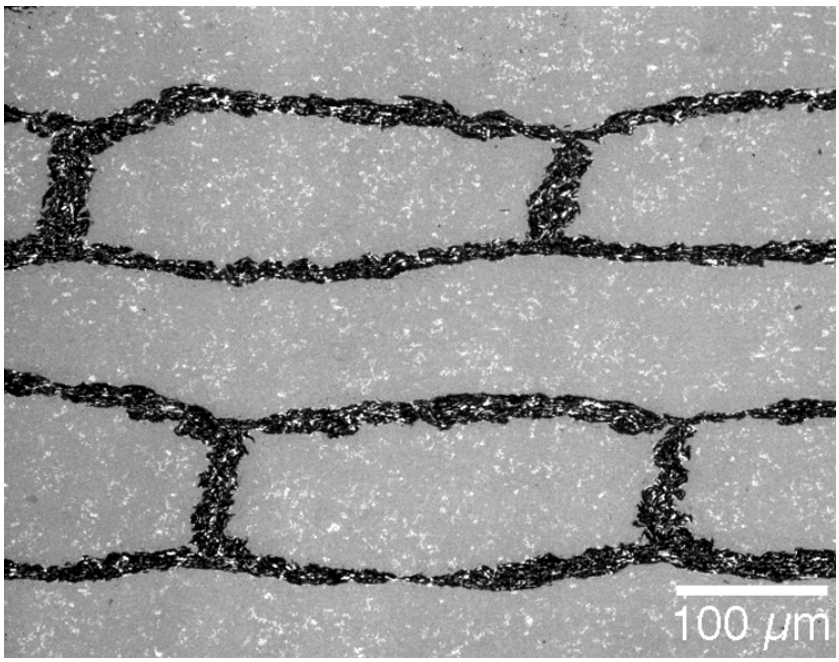

Fig. 134. SEM photomicrograph of cross section through a cross-ply Si_3N_4/BN FM.

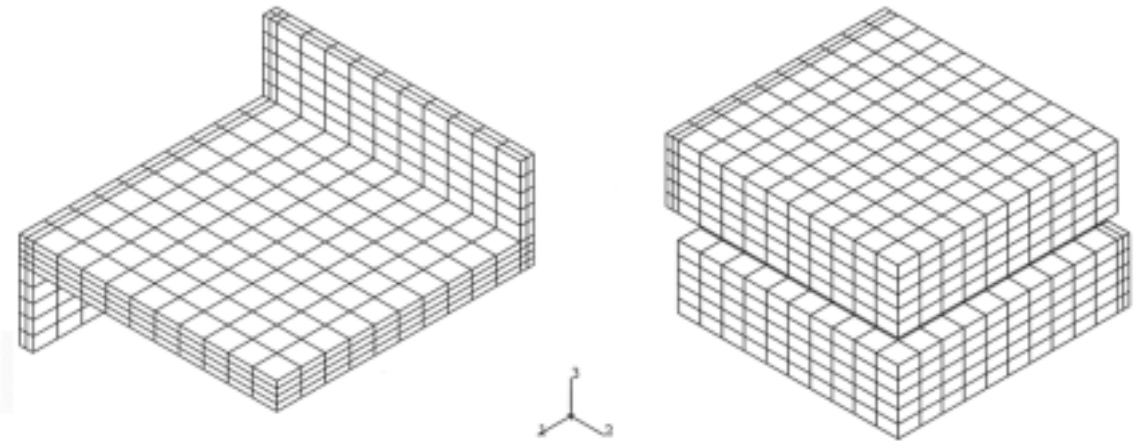

Fig. 135. Finite-element mesh of interphase (left) and cells (right) in idealized cell geometry.

Figures 136 and 137 show some representative numerical results for the stress distributions for an arbitrary thermal strain $\Delta\alpha\Delta T$. The volume fractions of Si_3N_4 and BN were taken to be, $f = 0.8$ and $1 - f = 0.2$, consistent with measured values. Both phases were assumed to be elastic, with Young's moduli $E_f = 242$ GPa for the Si_3N_4 and $E_i = 20.7$ GPa for the BN. The Poisson's ratio for both phases was taken to be $\nu = 0.2$.

In parallel with the numerical studies, approximate analytical models of the thermoelastic behavior of the cross-ply FMs were also developed. This was done in two steps.

In the first step, the individual (unidirectional) laminae were homogenized, and assigned properties that are consistent with the properties and morphology of the constituents. The properties of the laminae were calculated by using variations on existing composite models, utilizing upper- and lower-bound solutions, as appropriate. In the second step, the properties of the cross-ply laminate were calculated from the properties of the individual laminae by using classical lamination theory. The main results that were obtained were (1) the thermal residual stresses, with contributions arising from the thermal misfit between the constituents within an individual lamina and the misfit between adjacent laminae; (2) the CTEs. Although secondary in importance, the model also yielded approximate analytical solutions for the engineering elastic constants.

Finite-element calculations have been performed to determine the relevant properties of the individual laminae, through the use of a two-dimensional rectangular cell. Some typical results for the residual stresses are plotted in Figs. 138 and 139. A noteworthy feature of these results is that the average values of the

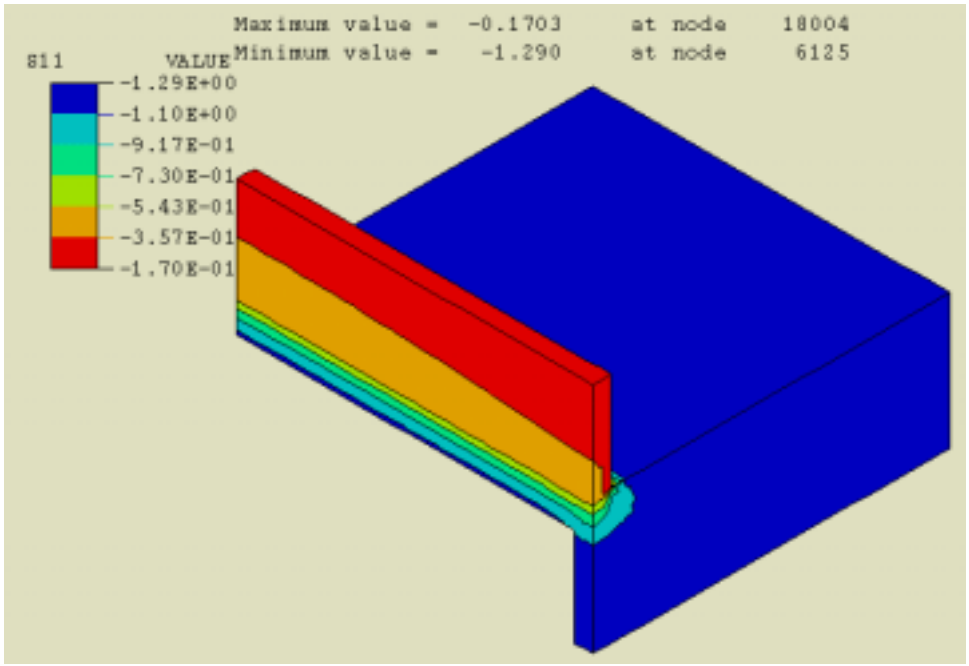

(a)

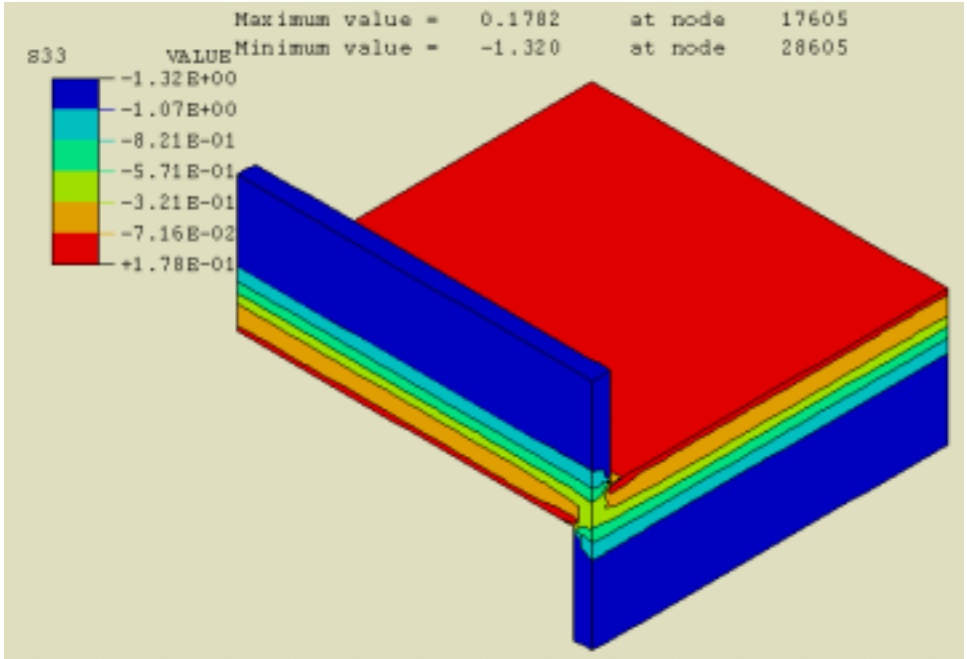

(b)

Fig. 136. Distributions of stress in (a) interphase, (b) cross-ply FMs; values normalized by $E\Delta\alpha\Delta T$. Cell for shear stress is inverted to show the stress concentration along the inner corner.

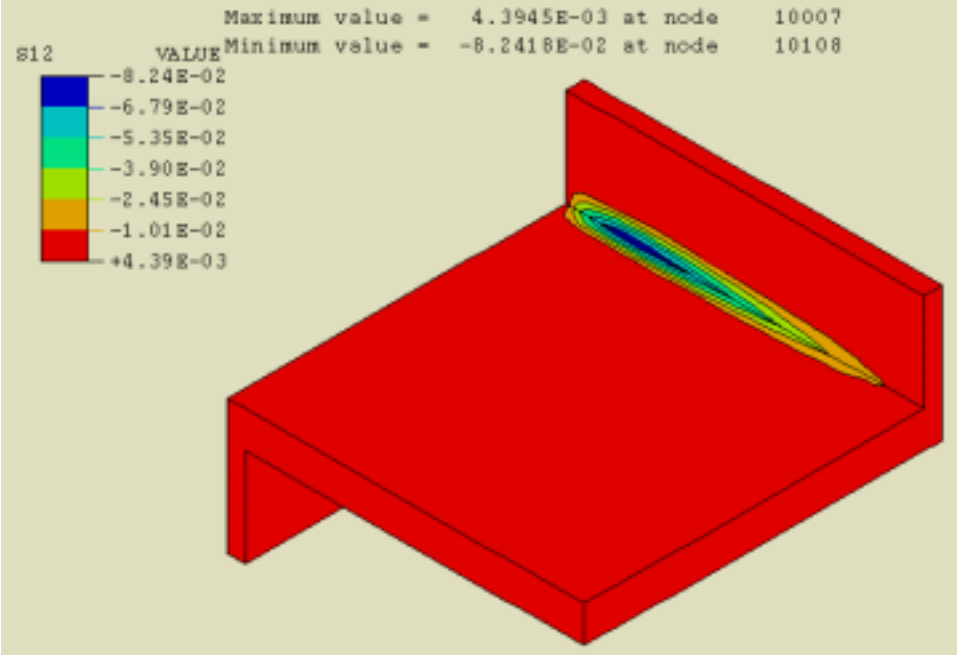

(c)

Fig. 136. (Contd.)

various stress components are essentially the same as those obtained from the flattened-hexagon geometry used for modeling the unidirectional FMs. For example, the axial stress at the cell center is $\sigma_z^f / E_i \Delta\alpha\Delta T \approx 0.30$, virtually identical to the values obtained for the hexagonal cell. Similar correlations are obtained in the interphase stresses in the two cell geometries.

The thermoelastic properties, including Young's moduli and thermal expansion coefficients, of the unidirectional laminae have been estimated in the following manner. The axial modulus E_z and CTE α_z are obtained from a straightforward two-bar model and yield the results:

$$\frac{E_z}{E_f} = f(1-\beta)+\beta \tag{5.17}$$

and

$$\alpha_z = \frac{\alpha_i(1-f)+\alpha_f f}{f+(1-f)\beta}\ , \tag{5.18}$$

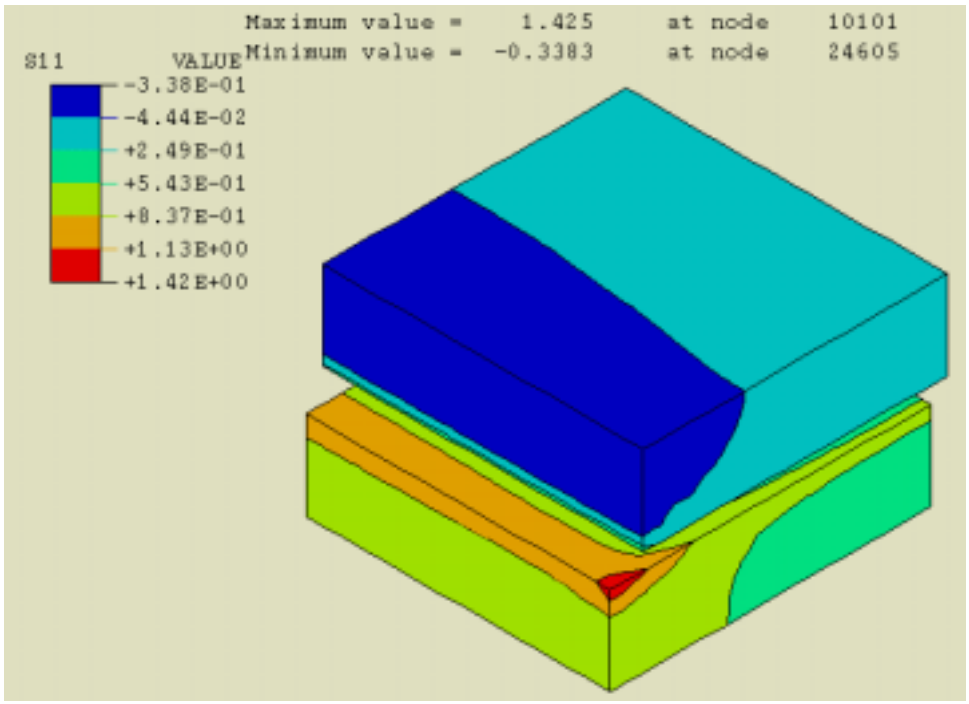

(a)

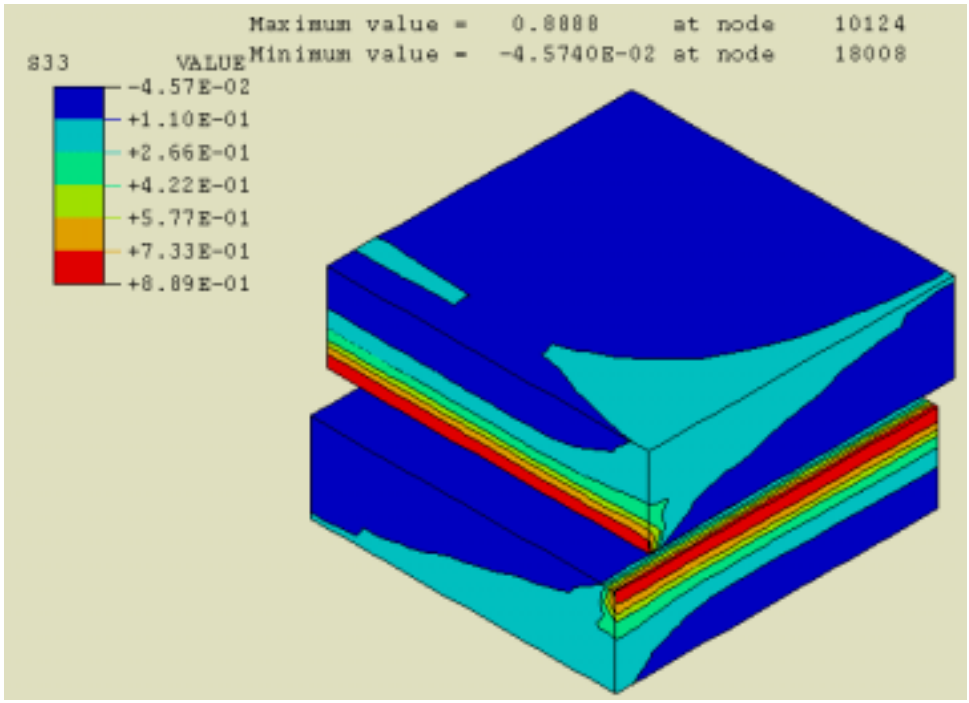

(b)

Fig. 137. Distributions of stress in cells in cross-ply FMs; values normalized by $E_i \Delta\alpha\Delta T$.

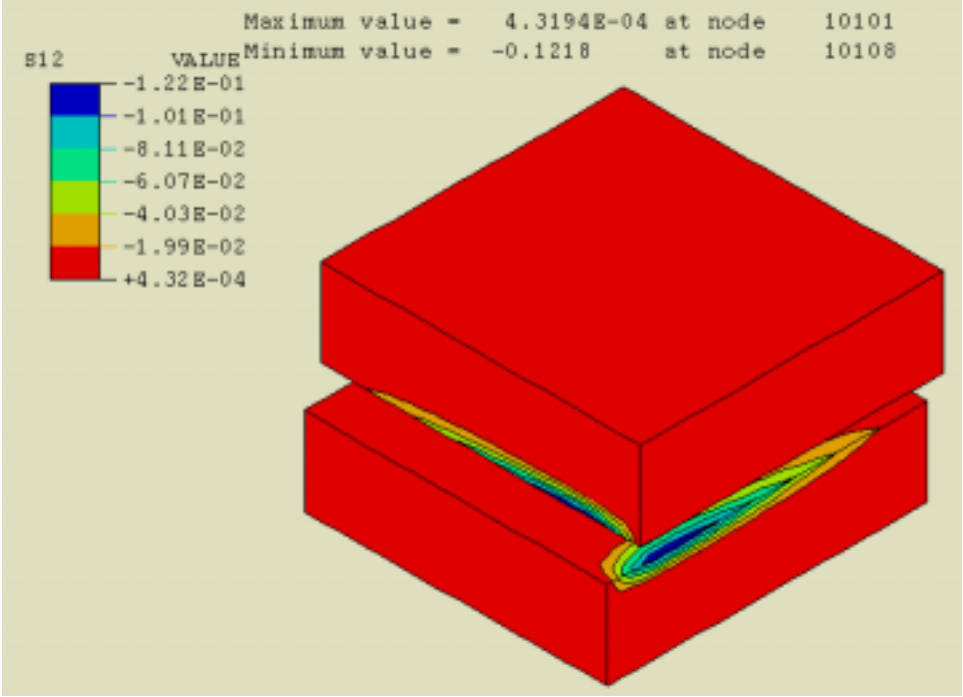

(c)

Fig. 137. (Contd.)

where $\beta \equiv E_i/E_f$, and α_i and α_f are the thermal expansion coefficients of the interphase and cell, respectively. Comparisons with finite-element calculations indicate that Eqs. 5.17 and 5.18 are essentially exact, with errors <<1%.

Transverse properties are obtained by first evaluating the properties of select portions of the unit cell, as illustrated in Fig. 140. For example, in Fig. 140b, the interphase is partitioned into two parts, denoted I_3 and I_4. The cell F is first combined with I_4. The elastic constants of this part of the cell in the x- and y-directions are evaluated by use of the upper and lower bounds, respectively, yielding

$$\frac{E_x^B}{E_f} = \frac{t}{1+t}\beta + \frac{1}{1+t} = \frac{1+\beta t}{1+t} \tag{5.19}$$

and

$$\frac{E_y^B}{E_f} = \frac{\beta(1+t)}{\beta+t}, \tag{5.20}$$

where λ and t are normalized dimensions, defined in Fig. 140a, and related to the cell volume fraction through

$$f = \frac{\lambda}{(1+t)(\lambda+t)} = \frac{\lambda}{\lambda+(1+\lambda)t+t^2}. \tag{5.21}$$

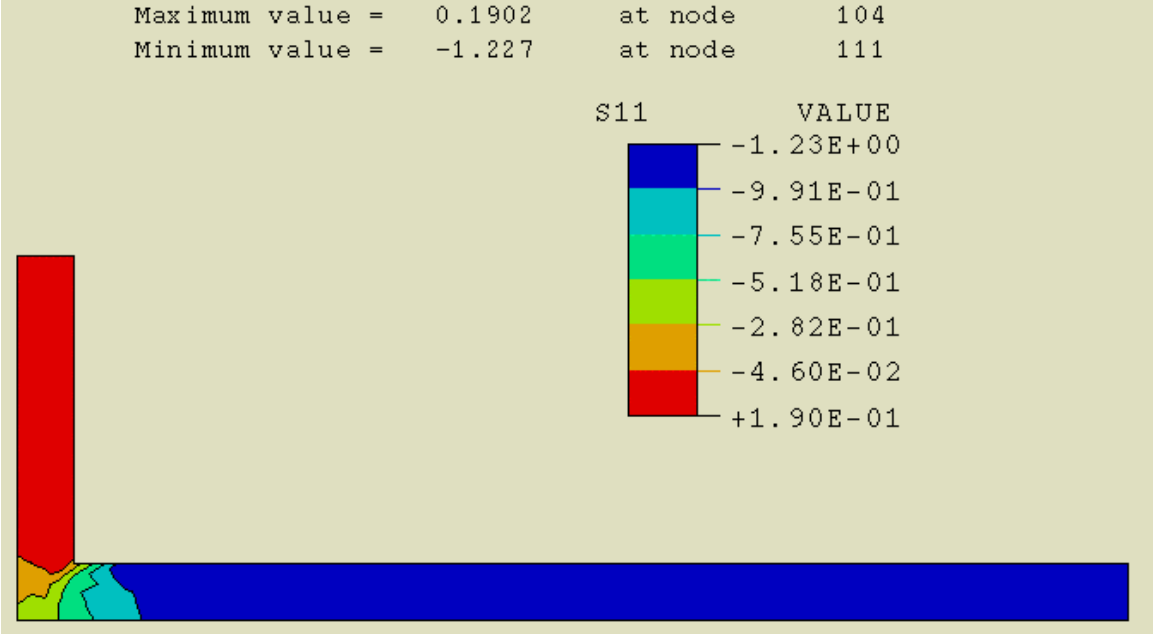

(a)

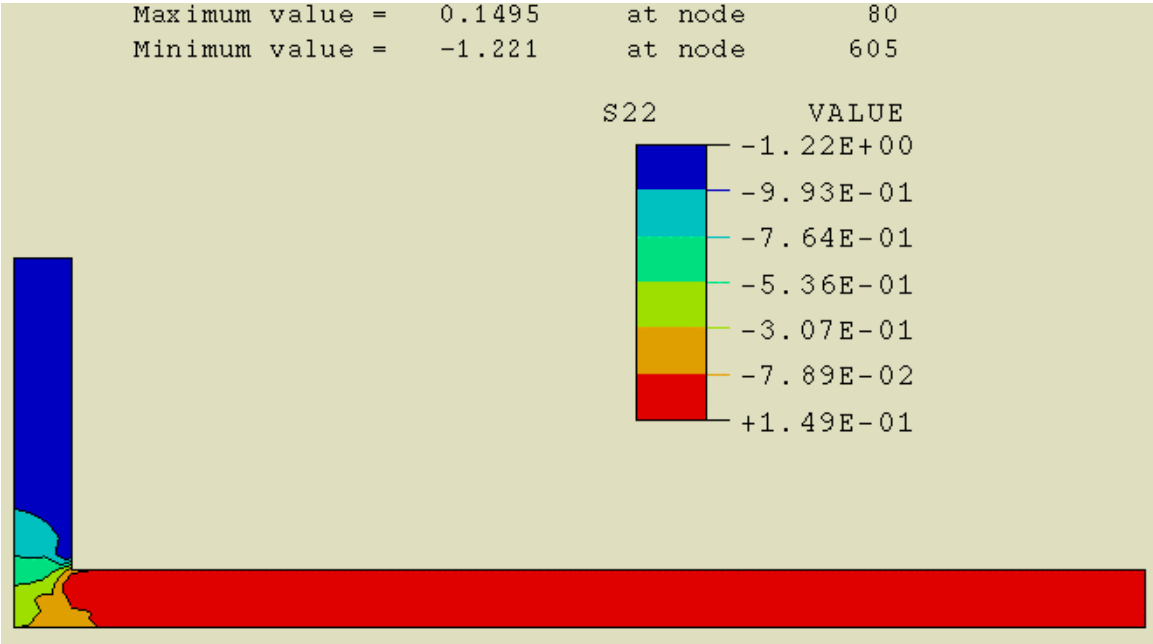

(b)

Fig. 138. Distributions of residual stress in interphase for a unidirectional lamina with rectangular cells. Values are normalized by $E_i\Delta\alpha\Delta T$.

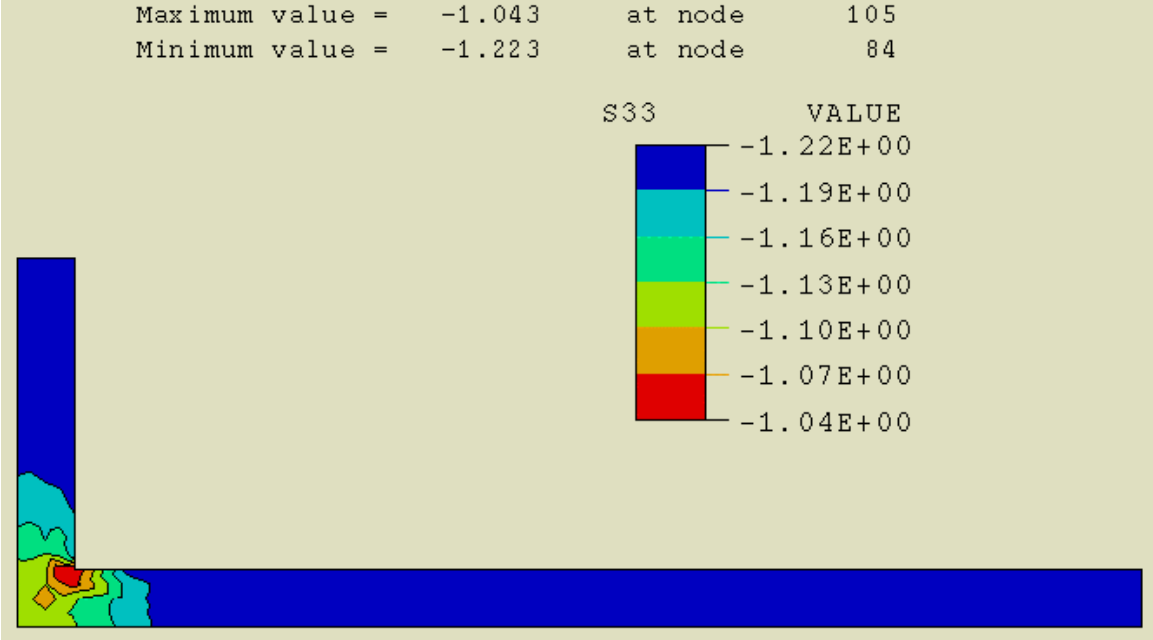

(c)

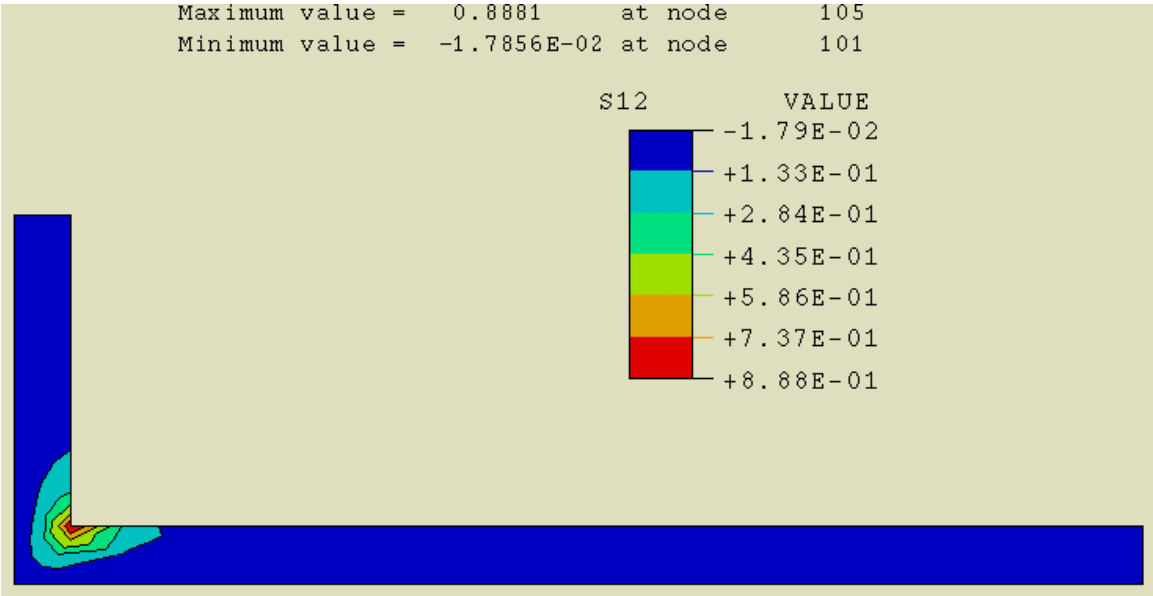

(d)

Fig. 138. (Contd.)

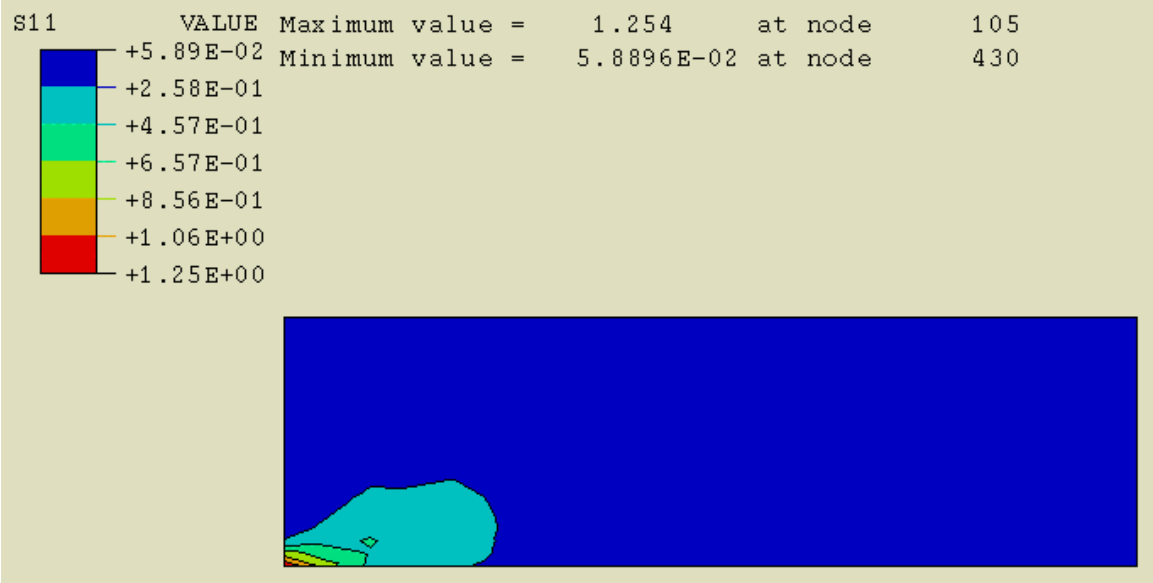

(a)

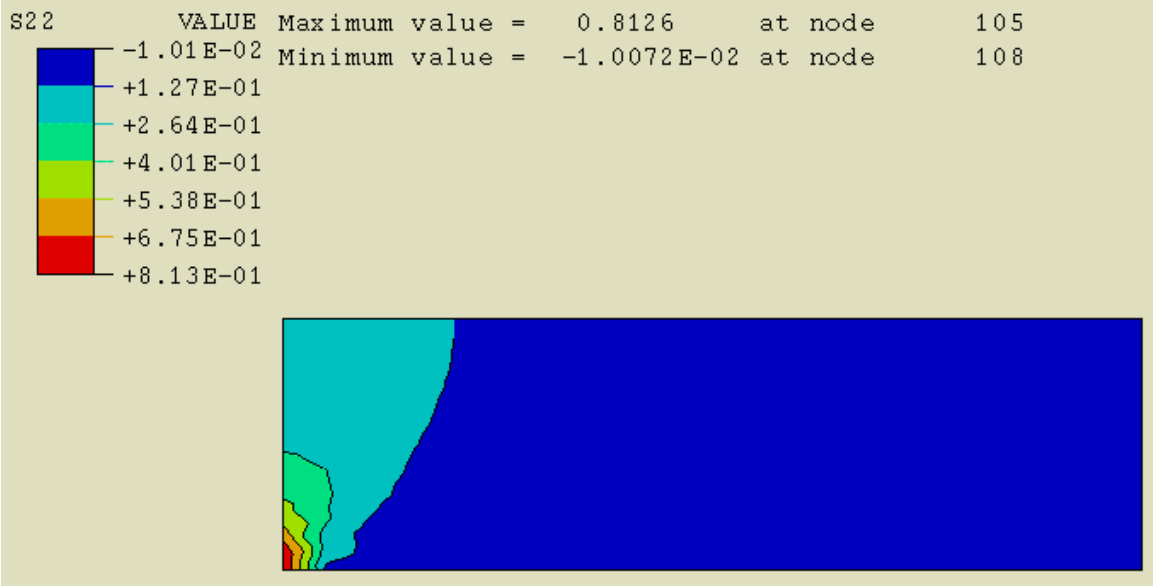

(b)

Fig. 139. Distributions of residual stress in cells for unidirectional lamina with rectangular cells; values normalized by $E_i \Delta\alpha\Delta T$.

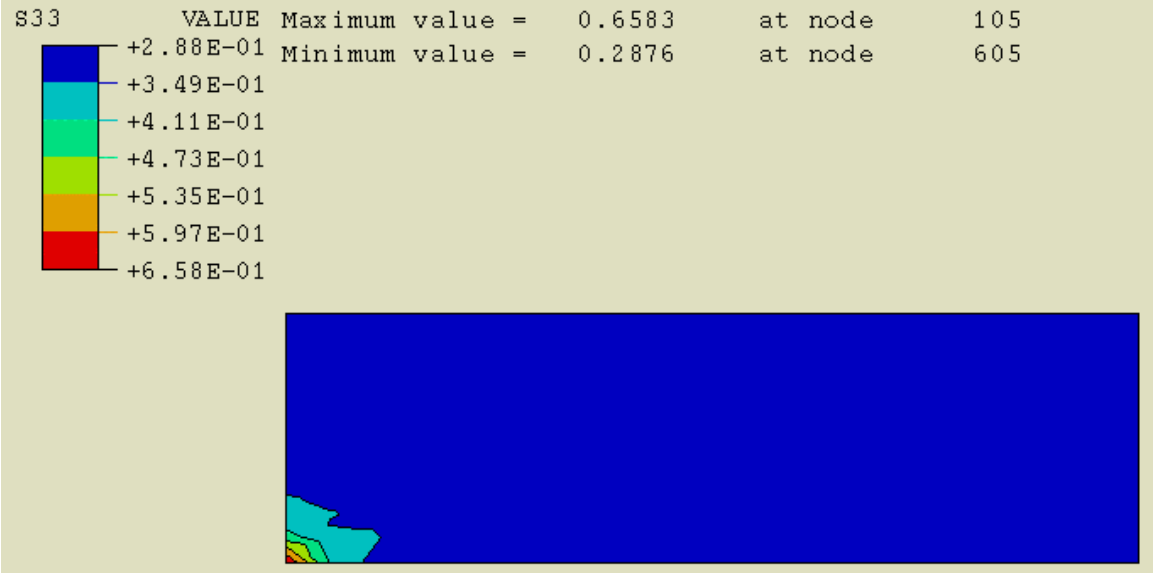

(c)

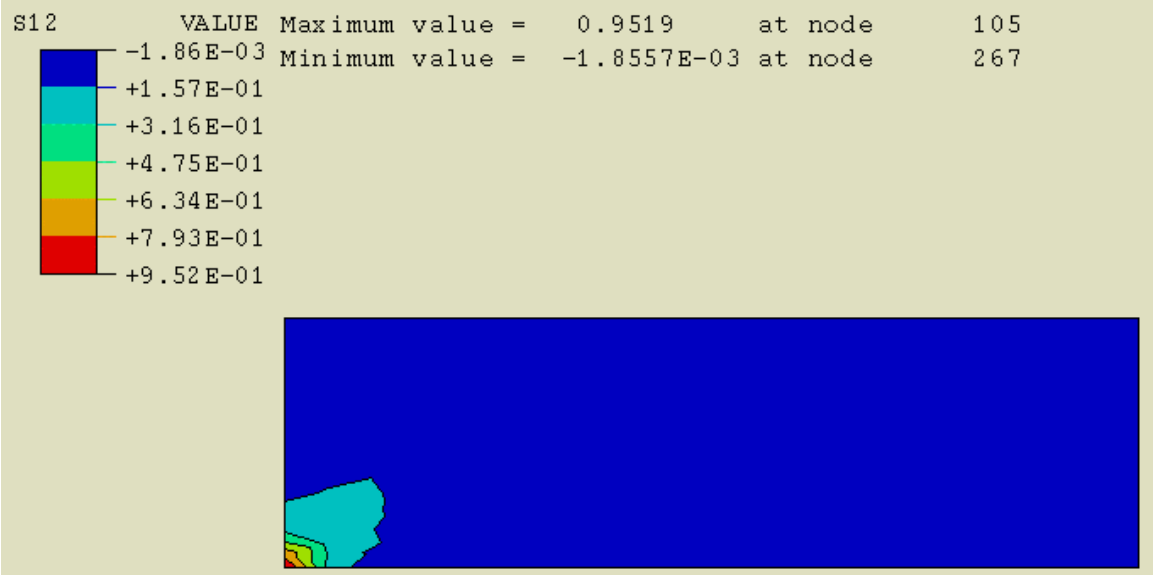

(d)

Fig. 139. (Contd.)

The properties of this part of the cell are then combined with the remaining interphase, I_3, yielding the results:

$$\frac{E_x}{E_f} = \frac{\beta(\lambda+t)(1+\beta t)}{t(1+\beta t)+\beta\lambda(1+t)} \tag{5.22}$$

and

$$\frac{E_y}{E_f} = \frac{\beta t(\beta+t)+\lambda\beta(1+t)}{(\lambda+t)(\beta+t)} \ . \tag{5.23}$$

Because of the way in which this averaging has been performed, it is expected that the results in Eqs. 5.22 and 5.23 will represent lower bounds to the actual values.

An alternative way to partition the interphase is shown in Fig. 140c. In this case, the cell F is first combined with the part of the interphase denoted I_1, to yield

$$\frac{E_x^c}{E_f} = \frac{\beta(\lambda+t)}{t+\beta\lambda} \tag{5.24}$$

and

$$\frac{E_y^c}{E_f} = \frac{\beta t}{\lambda+t} + \frac{\lambda}{\lambda+t} = \frac{\beta t+\lambda}{(\lambda+t)} \ . \tag{5.25}$$

Combing these properties with the remaining part of the interphase I_1 we obtain

$$\frac{E_x}{E_f} = \frac{\beta t}{1+t} + \frac{\beta(\lambda+t)}{(t+\beta\lambda)(1+t)} = \frac{\beta t(t+\beta\lambda)+\beta(\lambda+t)}{(t+\beta\lambda)(1+t)} \tag{5.26}$$

and

$$\frac{E_y}{E_f} = \frac{\beta(1+t)(\beta t+\lambda)}{t(\beta t+\lambda)+\beta(\lambda+t)} \ . \tag{5.27}$$

Again, Eqs. 5.26 and 5.27 are expected to be lower bounds.

Figure 141 shows the analytical solutions for the two transverse moduli and the results obtained from the finite-element calculations. Very good agreement is obtained for the property values relevant to the Si_3N_4/BN FMs. Furthermore, the analytical results lie slightly below the exact results, consistent with the expectation that the former should yield lower-bound estimates.

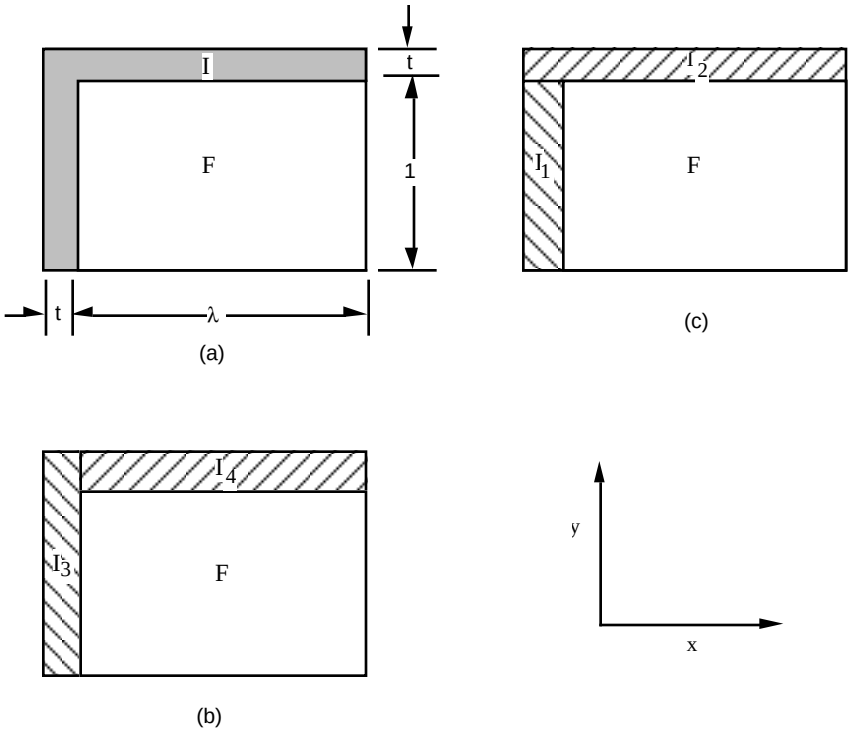

Fig. 140. Schematic diagram showing partitioning of unit cell into slabs.

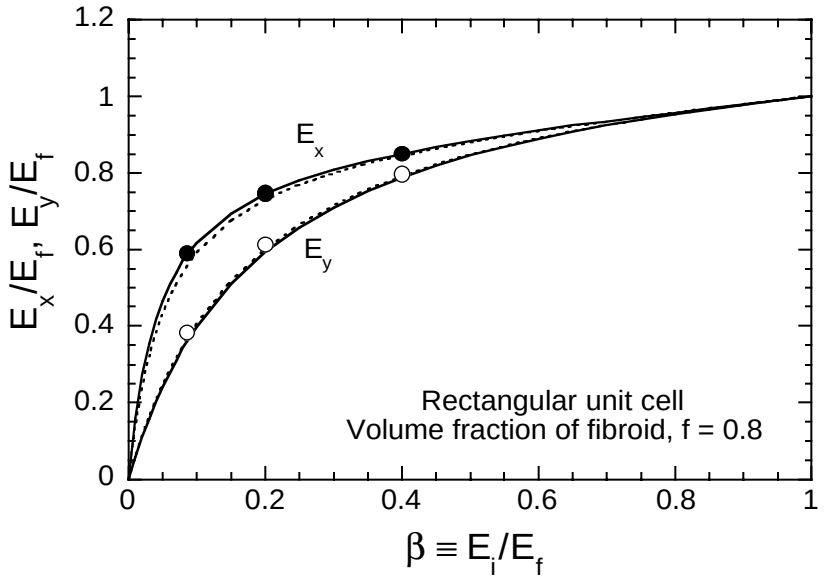

Fig. 141. Analytical solutions for elastic moduli (lines) and those obtained from finite-element calculations (symbols); solid lines are from Eqs. 5.22 and 5.23; dashed lines, from Eqs. 5.26 and 5.27.

A similar approach is used to determine the CTE values. Following the partitioning scheme shown in Fig. 140b, the coefficients in the x- and y-directions are

$$\alpha_x = \left(\frac{t}{\lambda + t} + \frac{\lambda \beta t}{(\lambda + t)(1 + \beta t)} \right) \alpha_i + \left(\frac{\lambda}{(\lambda + t)(1 + \beta t)} \right) \alpha_f \tag{5.28}$$

and

$$\alpha_y = \frac{1}{t(\beta + t) + \lambda(1 + t)} \left[t(\beta + t + \lambda)\ \alpha_i + \lambda \alpha_f \right] . \tag{5.29}$$

Similarly, following the partitioning scheme shown in Fig. 140c, they are

$$\alpha_x = \frac{1}{t(t + \beta\lambda) + (\lambda + t)} \left[\left(t(t + \beta\lambda) + t \right)\ \alpha_i + \lambda\, \alpha_f \right] \tag{5.30}$$

and

$$\alpha_y = \frac{t(\beta t + \lambda) + \beta t}{(1 + t)(\beta t + \lambda)}\ \alpha_i + \frac{\lambda}{(1 + t)(\beta t + \lambda)}\ \alpha_f \quad . \tag{5.31}$$

For the purpose of comparing the analytical solutions with the CTEs with those from the finite-element calculations, it is convenient to write the coefficients in the generic form

$$\alpha_x = C_{ix}\ \alpha_i + C_{fx}\ \alpha_f \tag{5.32}$$

and

$$\alpha_y = C_{iy}\ \alpha_i + C_{fy}\ \alpha_f \quad , \tag{5.33}$$

where the coefficients C_{iy} and C_{fy} represent the respective contributions from the interphase and cell to the CTE in the y-direction, and C_{ix} and C_{fx} are the corresponding values for the CTEs in the x-direction, which are obtained readily from Eqs. 5.28–5.31.

Comparisons of the analytical solutions for the latter coefficients and the finite-element results are plotted in Figs. 142 and 143. Acceptable agreement is obtained, providing confidence in the analytical approach.

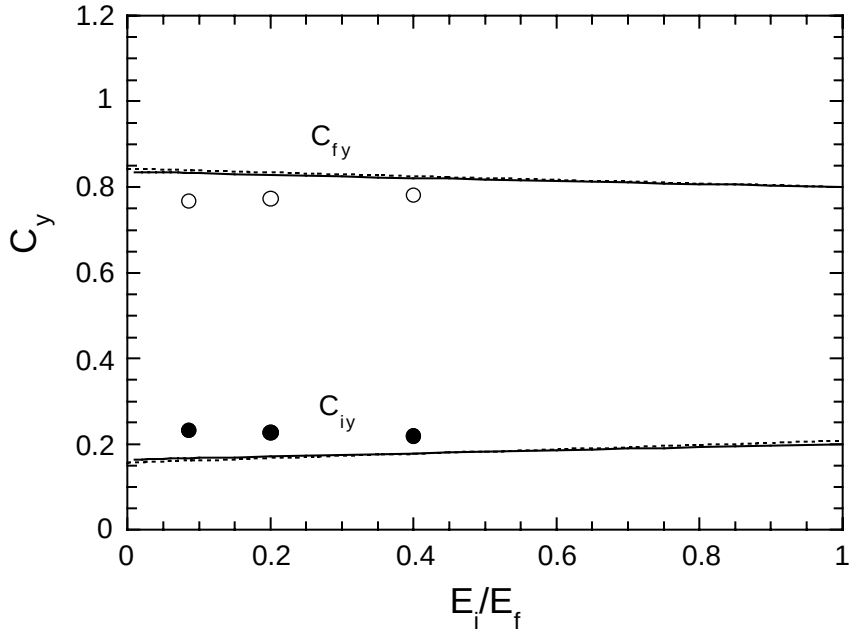

Fig. 142. Analytical solutions for CTE values in the y direction (lines) and those obtained from finite-element calculations (symbols); solid lines are from Eqs. 5.28 and 5.29; dashed lines, from Eqs. 5.30 and 5.31.

5.2.3 Comparisons between Theory and Experiment

The CTE values of the FMs and the monolithic constituents were measured directly with a differential dilatometer (Model Dilatronic, Theta Industries, Port Washington, NY). The technique involves measurement of the difference of expansion between the test sample and a standard material for which the expansion is known, thereby eliminating the expansion of the system. In these measurements, the standard was dense polycrystalline Al_2O_3. The displacements were monitored and the temperature profiles were measured by thermocouples; both were monitored and recorded by a computer.

Measurements of thermal expansion were made in either two or three orthogonal directions, depending on material symmetry. For the BN and Si_3N_4 specimens, the plane perpendicular to the hot pressing direction is thermally isotropic, with a value that, in general, differs from the through-thickness value. Similar symmetry exists in the 0/90° FM, because of the balanced cross-ply layup. By contrast, the 0° FM exhibits orthotropic symmetry; the three principal directions are: parallel to the fiber direction (denoted in-plane longitudinal), transverse to the fibers and aligned with the plane of hot pressing (denoted in-plane transverse), and parallel to the hot pressing direction (denoted through-thickness).

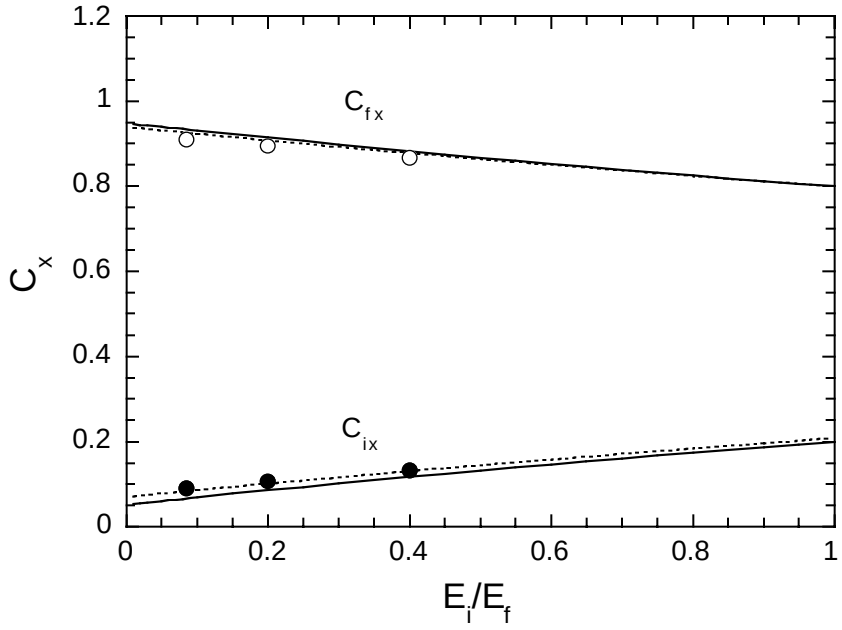

Fig. 143. Analytical solutions for CTE values in the x-direction (lines) and those obtained from finite-element calculations (symbols); solid lines are from Eqs. 5.28 and 5.29; dashed lines, from Eqs. 5.30 and 5.31.

The in-plane measurements were made with rectangular bars, ≈3 x 4 mm in cross-section and 30 mm long (the long axis corresponding to the principal direction of interest). The through-thickness measurements were made on a series of several stacked specimens, each ≈3 mm thick and each polished carefully to ensure flat and parallel faces. The use of several such specimens in a stack rather than a single thin specimen increases the total displacement associated with thermal expansion and hence increases the precision of the measurements. To verify the stacking technique, some measurements were made on stacked specimens cut from the in-plane orientation and the results were then compared with the ones obtained from the long (contiguous) rectangular bars. The two sets of measurements were found to be essentially equal to one another. The measurements were made in a N_2 atmosphere during both heating and cooling over the temperature range 20–1200°C. The heating and cooling rates were 2.5°C / min. The results are presented in the form of a secant value of α relative to ambient temperature, defined by

$$\alpha = [\varepsilon(T) - \varepsilon(T_a)] / (T - T_a) , \tag{5.34}$$

where $\varepsilon(T)$ is the thermal strain at temperature T, and $\varepsilon(T_a)$ is the thermal strain at ambient temperature T_a = 20°C.

The CTE measurements on the constituents and the FMs are summarized in Fig. 144. In the Si_3N_4, the in-plane CTE was almost independent of temperature. Its average value (2.0×10^{-6} K^{-1}) is comparable to those reported previously for a wide range of Si_3N_4 ceramics. The average through-thickness value was slightly higher, 2.7×10^{-6} K^{-1}. This anisotropy is likely due to slight texturing of the hexagonal β grains, with the basal plane oriented preferentially in the plane of hot pressing. The BN exhibited a similarly low in-plane α ($\approx 1.8 \times 10^{-6}$ K^{-1}), but a much higher through-thickness CTE ($\approx 13.5 \times 10^{-6}$ K^{-1}). Here, again, the anisotropy can be attributed to texturing of the hexagonal grains, coupled with the intrinsic anisotropy of the BN crystal. The FMs also exhibited some anisotropy in CTE, somewhat greater in magnitude than that of the Si_3N_4 but substantially less than that of the BN. This correlation can be rationalized qualitatively on the basis that the major constituent of the FM is Si_3N_4, and thus the behavior of the FMs should mimic that of the neat Si_3N_4. The models and analysis validated this assertion in a quantitative manner.

The relevant elastic properties are summarized in Table 17. These results are used in subsequent modeling, especially to establish connections between the α values of the constituents and those of the 0 and 0/90° FMs.

Table 17. Measured elastic moduli of Si_3N_4/BN FMs

Material	E (GPa)
BN	21 ± 2
Si_3N_4	242 ± 4
0° FM	216 ± 2
0/90° FM	181 ± 6
± 45° FM	174 ± 5

The key points of comparison between theory and measurements are plotted in Fig. 144. For the in-plane properties, the relevant constituent properties (α and E) were those measured on the neat Si_3N_4 and BN in the in-plane orientation. Very good agreement is obtained between the calculated and measured values. For the through-thickness properties, calculations are presented for two limiting cases: (1) with use of the in-plane properties of both constituents (lower line in Fig. 144c);

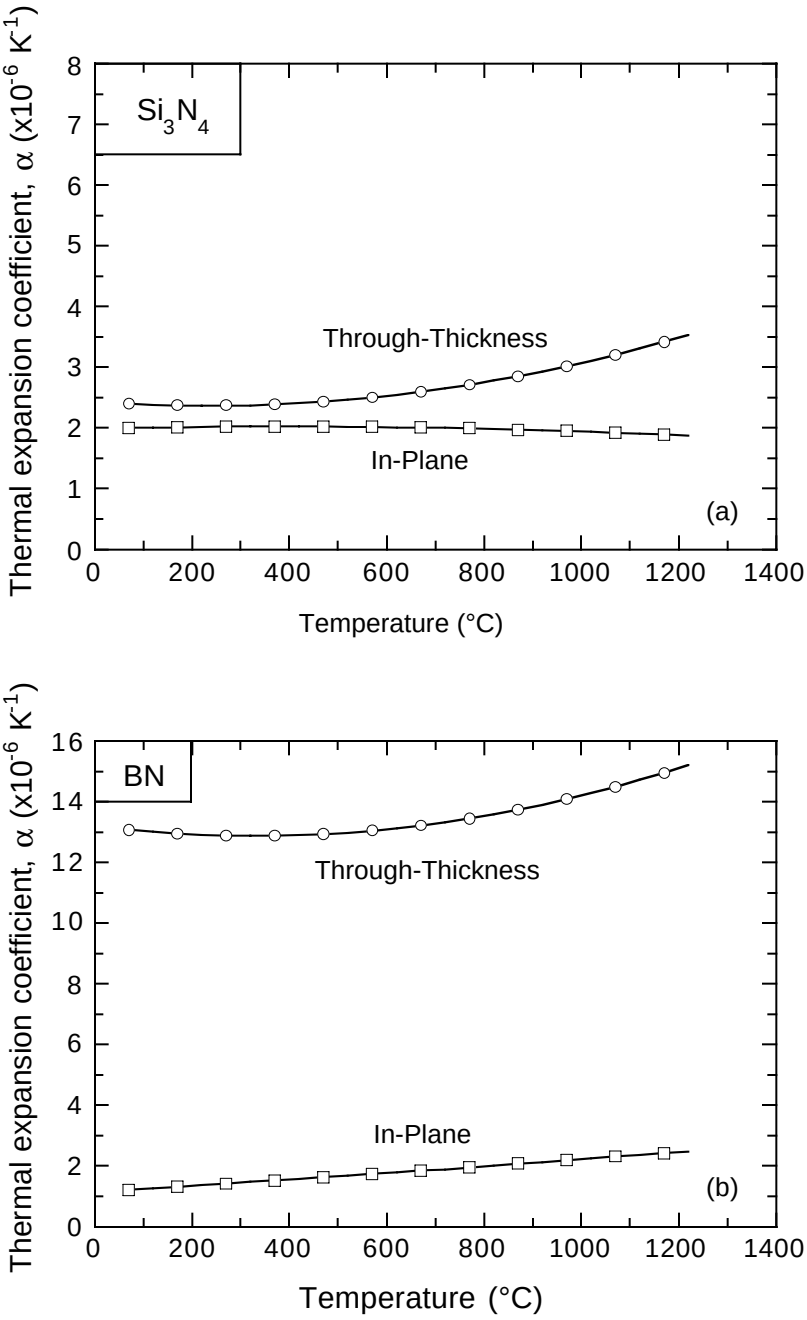

Fig. 144. Summary of α measurements on specimens as labeled.

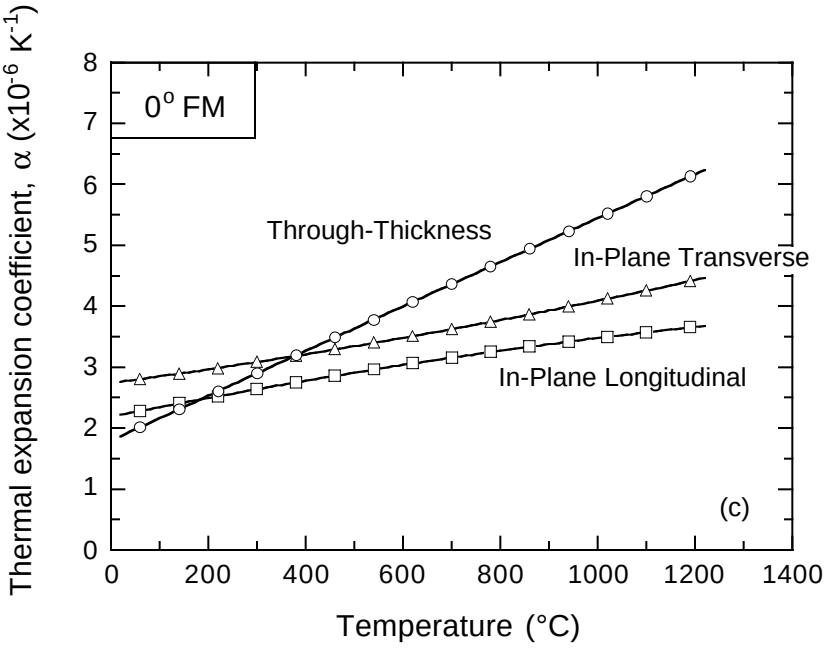

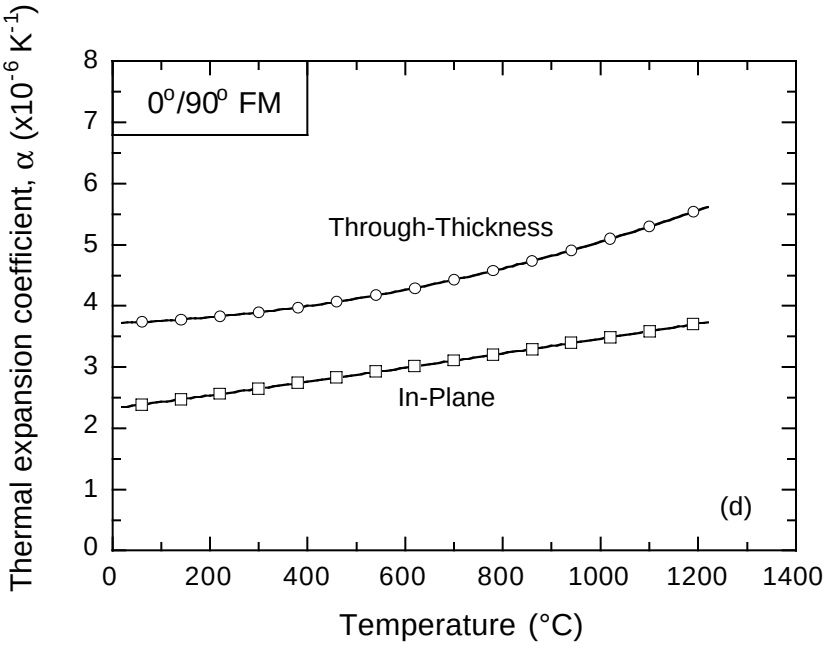

Fig. 144. (Contd.)

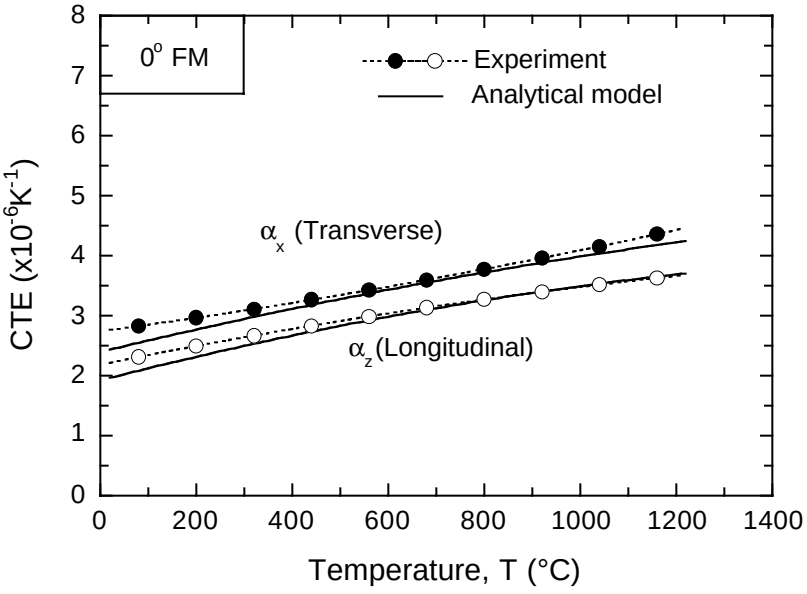

(a)

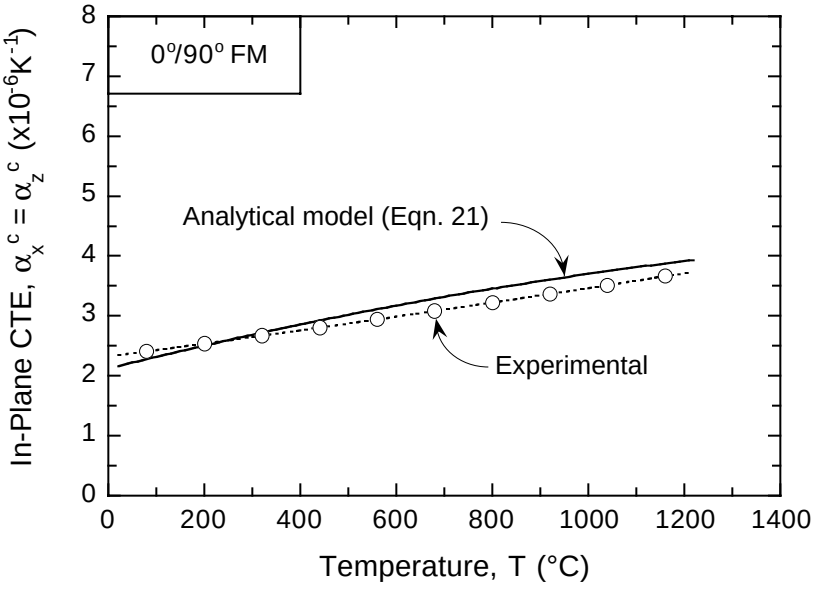

(b)

Fig. 145. Measured and predicted coefficients of thermal expansion (CTEs): (a, b) in-plane and (c) through-thickness.

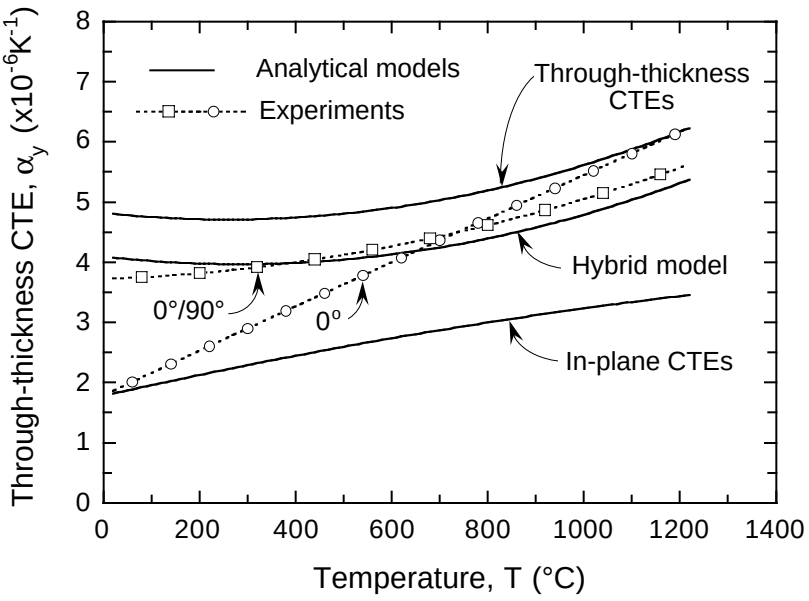

(c)

Fig. 145. (Contd.)

and (2) with use of the through-thickness properties of both constituents (upper line in Fig. 144c). These two sets of results appear to bound the experimental data. The results from a hybrid model that accounts for the anisotropy of the constituents in a rudimentary way is also shown in Fig. 144c (middle line). The latter model is based on the unit-cell subdivision scheme shown in Fig. 140b. In this case, the α values for the fibroid and the interphase subcell I_2 are taken to be those measured in the through-thickness orientation, whereas the α of the interphase subcell I_1 is taken to be that measured in-plane (assuming that the c-axis of the BN crystals is aligned circumferentially around the Si_3N_4 fibroid). This approach yields a predicted α that agrees somewhat better with the experimental data than do either of the two preceding limiting cases, especially when compared with the 0/90° FM.

5.2.4 Closing Remarks on Thermal Stresses

Analytical models for the CTE values of FMs have been developed, taking into account the fiber shape and architecture. The models have been validated through the use of finite-element-analysis calculations. Further validation of the models has been facilitated by comparisons between model predictions and experimental measurements. The correlations between theory and experiment appear to be good. Some uncertainty remains with regard to the degree of texturing (especially of the BN) and its effect on the properties of the FMs. This texturing does not appear to have a large influence on the in-plane thermal expansion of either the 0 or 0/90°

FMs, provided that in-plane CTEs of the constituents are used in the models. In contrast, the through-thickness thermal expansion is sensitive to the selection of the CTE of the BN, because the BN is the continuous phase in this orientation, and thus plays a more significant role in the thermal expansion of the FM. A rudimentary modification of the model to account for texturing and anisotropy of the BN appears to yield adequate results, although further work is needed to ascertain the extent of texturing and its effect on various thermomechanical properties of FMs.

6 Summary

6.1 Conclusions

The FM program encompassed several materials and approaches. It could be roughly divided into projects focused on producing new FMs and projects focused on improving our understanding of commercial FMs. Oxide FMs were produced and characterized, but the principal characterization and modeling efforts made use of commercially produced Si_3N_4/BN FMs that were obtained from Advanced Ceramics Research (ACR), Tucson, AZ.

The fabrication efforts were slanted toward materials systems that lend themselves to sintering at atmospheric pressure. Among the systems that were investigated were $ZrSiO_4$/$ZrSiO_4$, mullite/Al_2O_3, YAG/Al_2O_3, Al_2O_3/$AlPO_4$, and Al_2O_3/leucite. Duplex filaments for FM production were produced by conventional ram extrusion, by a new coextrusion process, and by solid-freeform fabrication. Tough FMs that exhibited graceful failure in flexural testing were produced. All of the FMs, however, exhibited a strength that was, in essence, determined by the fraction and perfection of the cell phase.

Attempts to overcome a rule-of-mixtures strength limitation through tailoring of residual stresses met with only partial success. Calculations supported the approaches that were taken, and prototypes were fabricated from suitable oxide systems based on mullite and Al_2O_3. The program, however, ran its course before FM test pieces could be produced and thoroughly studied.

The oxide FM fabrication effort was supported by a host of synthesis and sintering studies, many of which are reported on here. In addition, microstructures were characterized extensively and key mechanical properties, including creep, were studied in detail. A comprehensive understanding of the performance and performance-limiting features of these FMs emerged.

The ACR-supplied Si_3N_4/BN FMs proved to be essential to the modeling work. ACR was capable of supplying high-quality materials upon request. Cross-ply

0/90 and ±45° FMs were the most thoroughly studied. Previous studies of Si_3N_4/BN FMs had answered many of the questions related to flexure. The work in this program focused on in-plane properties. Fracture was modeled and fabrication procedures to improve performance were identified. Substantial testing of FMs and their constituents was required for this work.

Thermal properties of Si_3N_4/BN FMs were also studied and modeled. Thermal expansion coefficients and residual strains were measured. Data were assimilated into a model that can predict residual strains and strains in unidirectional and cross-ply laminates. These stresses can be large and have a strong effect on overall mechanical performance.

Work was begun to examine indentation and erosion of Si_3N_4/BN FMs. The erosion work will be completed in 2001 under new funding. We believe that FMs will prove to be resistant to strength degradation introduced by indentation or erosive damage. Determination of the tolerance of FMs to such damage may help to open new markets for these composites.

6.2 Future Work

Although the DARPA funding for FM research and development has been exhausted, we have continued to work under the auspices of new funding. Projects and possibilities are summarized briefly below.

1. ACR has been awarded a large, multiyear program by DOE to develop FM-based cutting tools for the mining industry. Subcontracts are expected to be signed with Prof. Zok for modeling and mechanical testing, Dr. Ellingson for NDE, and Dr. Goretta for general characterization.

2. Drs. Routbort and Goretta are working on a multiyear contract from DOE to study the joining of high-temperature materials by use of superplastic flow. Much of the multiphase sintering work and results of the FM creep studies have been incorporated into this project. To date, for example, ZTA has been shown to be a remarkably versatile material for joining other ceramics. Plans are in place, also, to join composites such as FMs.

3. Prof. B. I. Smirnov (St. Petersburg, Russia), Prof. A. R. de Arellano-López (Seville, Spain), and Dr. Goretta have a small, approximately two-year, contract from the North Atlantic Treaty Organization to examine new mechanical properties of FMs. Included in this work will be direct measurements of solid-particle erosion resistance.

4. Other proposals are pending. We will continue to search for new funds to continue our FM work.

We believe that vast improvements in FM fabrication can be effected and that the costs of FM manufacture can be reduced substantially. Technologies such as pressureless sintering and SFF are key to these advances. Our current understanding of the mechanical properties of FMs is quite good. It reinforces our belief that FMs offer promise in many current and future applications.

7 Administrative Details

Several publications and patent applications emerged from this program. In addition, many students and postdoctoral appointees were supported. A brief summary follows.

7.1 Publications and Inventions

7.1.1 Publications

Published

Damage characterization of a Si_3N_4-BN fibrous monolith using NDE techniques
J. L. Finch, J. M. Staehler, L. P. Zawada, W. A. Ellingson, J. G. Sun, and C. M. Deemer
Ceram. Eng. Sci. Proc. 20 [3] (1999) 341-351.

High-temperature compressive deformation of Si_3N_4/BN fibrous monoliths
J. L. Routbort, K. C. Goretta, E. T. Park, D. Singh, J. Finch, J. Staehler, L. Zawada, and G. E. Hilmas
Ceram. Eng. Sci. Proc. 20 [3] (1999) 427-434.

The preparation and characterization of alumina-leucite composites
D.-K. Kim, J. L. Schull, and W. M. Kriven
Ceram. Trans. 103 (2000) 63-73.

Fabrication and characterization of oxide fibrous monoliths produced by coextrusion
B. J. Polzin, T. A. Cruse, R. L. Houston, J. J. Picciolo, D. Singh, and K. C. Goretta
Ceram. Trans. 103 (2000) 237-244.

Mechanical-property characterization of multidirectional Si_3N_4/BN fibrous monoliths
M. Tlustochowitz, D. Singh, W. A. Ellingson, K. C. Goretta, M. Rigali, and M. Sutaria
Ceram. Trans. 103 (2000) 245-254.

Controlled densification of mullite for composite applications
T. A. Cruse, B. J. Polzin, P. J. Phelan, D. Singh, K. C. Goretta, and
A. R. de Arellano-López
Ceram. Trans. 108 (2000) 463-472.

Mechanical response of cross-ply Si_3N_4/BN fibrous monoliths under uniaxial and biaxial loading
D. Singh, T. A. Cruse, D. J. Hermanson, K. C. Goretta, F. W. Zok, and J. C. McNulty
Ceram. Eng. Sci. Proc. 21 [3] (2000) 597-604.

A comparison study of the processing methods and properties for zirconium silicate fibrous monoliths
A. J. Mercer, G. E. Hilmas, T. A. Cruse, B. J. Polzin, and K. C. Goretta
Ceram. Eng. Sci. Proc. 21 [3] (2000) 605-612.

Development of oxide fibrous monoliths
K. C. Goretta, D. Singh, W. A. Ellingson, W. R. Kriven, J. C. McNulty, and F. W. Zok
Proceedings of 23rd Annual Conference on Ceramic, Metal and Carbon Composites, Materials and Structures (AMPTIAC, Rome, NY, 2000), Paper CB-0140.

Fabrication and characterization of a porous-matrix oxide fibrous monolith
B. J. Polzin, T. A. Cruse, D. Singh, J. J. Picciolo, M. Tlustochowicz, J. T. Dusek, and
K. C. Goretta
Proceedings of 23rd Annual Conference on Ceramic, Metal and Carbon Composites, Materials and Structures (AMPTIAC, Rome, NY, 2000), Paper CB-0142.

Plastic deformation of silicon nitride/boron nitride fibrous monoliths
A. R. de Arellano-López, S. López-Pombero, A. Domínguez-Rodríguez,
J. L. Routbort, D. Singh, and K. C. Goretta
J. Euro. Ceram. Soc. 21 (2001) 245-250.

In-plane fracture resistance of a cross-ply fibrous monolith
J. C. McNulty, F. W. Zok, and M. R. Begley
J. Am. Ceram. Soc. 84 (2001) 367-375.

Elasticity and anelastisity of ceramic samples of boron nitride
B. K. Kardashev, Yu. A. Burenkov, B. I. Smirnov, V. V. Shpeizman, V. A. Stepanov,
V. M. Chernov, D. Singh, and K. C. Goretta
Phys. Sol. State 43 (2001) 1084-1088.
[Fiz. Tverd. Tela (St. Petersburg) 43 (2001) 1048-1052.]

In press

Toughened oxide composites based on porous, alumina platelet interphases
W. M. Kriven and S.-J. Lee
J. Am. Ceram. Soc. (in press, 2001).

Compressive creep of polycrystalline $ZrSiO_4$
K. C. Goretta, T. A. Cruse, R. E. Koritala, J. L. Routbort, J. J. Melendez-Martinez, and A. R. de Arellano-López
J. Euro. Ceram. Soc. (in press, 2001).

Development of fibrous monoliths from mullite, alumina, and zirconia powders
B. J. Polzin, T. A. Cruse, D. Singh, J. J. Picciolo, R. N. Tsaliagos, P. J. Phelan, and K. C. Goretta
Ceram. Trans. (in press, 2001).

Plastic deformation of mullite/oxide glass composites
A. R. de Arellano-López, J. J. Meléndez-Martinez, J. L. Routbort, T. A. Cruse, R. E. Koritala, and K. C. Goretta
Bull. Span. Soc. Ceram. Glass (in press, 2001).

Elasticity and anelasticity of silicon nitride/boron nitride fibrous monoliths
B. I. Smirnov, Yu. A. Burenkov, B. K. Kardashev, D. Singh, K. C. Goretta, and A. R. de Arellano-Lopez
Phys. Sol. State **43** (in press, 2001).

Thermal expansion of unidirectional and cross-ply fibrous monoliths
M. Y. He, D. Singh, J. C. McNulty, and F. W. Zok
J. Comp. Sci. Technol. (submitted, 2001).

In preparation

Several publications will be prepared in 2001. Papers will emerge from the Universities of Illinois at Urbana-Champaign, California at Santa Barbara, and Missouri at Rolla on work covered in this report, but not yet published. From ANL, we intend to write a paper on the biaxial-flexure work, a paper on the cell-pushout study, and one on synthesis of mullite by a sol-gel method. In concert with collaborators, we will be cowriting papers on creep of mullite, internal friction in Si_3N_4/BN FMs, and additional studies of toughening mechanisms in Si_3N_4/BN FMs.

7.1.2 Patent Applications

Improved process for fabricating low-cost ceramic composites
Kenneth C. Goretta, Dileep Singh, Bryant J. Polzin, Terry A. Cruse, and John J. Picciolo; U.S. Patent application filed.

Improved process for fabricating low-cost ceramic composites by extrusion
Kenneth C. Goretta, Dileep Singh, Bryant J. Polzin, Terry A. Cruse, and John J. Picciolo; U.S. Patent application filed.

Composite structures with alumina-platelet-based interphases
Waltraud M. Kriven et al.; U.S. Patent application filed.

7.2 Personnel Summary

In addition to providing support for several staff members at ANL, and supporting research efforts at three U.S. universities (California at Santa Barbara, Illinois at Urbana-Champaign, and Missouri at Rolla), funds from the FM program supported several undergraduate and graduate co-op students, three postdoctoral researchers, and four graduate thesis students. This funding led to the following degrees:

Bryant J. Polzin, M.S., Illinois Institute of Technology, 1999 (major support).

Angela J. Mercer, M.S., University of Missouri–Rolla, expected 2001 (major support).

Dong Kyu Kim, Ph.D., University of Illinois at Urbana-Champaign, in progress (partial support).

Todd W. Spohnholz, M.S., Illinois Institute of Technology, 1999 (minor support).

7.3 Acknowledgments

This program was supported by the Defense Advanced Research Projects Agency, under the guidance of W. S. Coblenz. It was administered by the U.S. DOE, through an Interagency Agreement, under Contract W–31–109–Eng–38. It was managed by J. E. Jonkouski of the Chicago Operations Office of DOE.

Several colleagues contributed significantly to our efforts. We thank S. E. Dorris for assistance with thermal-expansion measurements, J. W. Richardson, Jr., for help with the residual-strain measurements, R. L. McDaniel for installation and maintenance of furnaces, U. Balachandran for advice and many helpful discussions, and several collaborators for measurements of elastic moduli.

7.4 Contact Information

Principal Investigator: Ken Goretta
ET–212
Argonne National Laboratory
Argonne, IL 60439–4838
Phone: 630–252–7761
FAX: 630–252–3604
goretta@anl.gov

NDE and SFF: Bill Ellingson
ET–212
Argonne National Laboratory
Argonne, IL 60439–4838
Phone: 630–252–5068
FAX: 630–252–4798
ellingson@anl.gov

Mechanical modeling: Frank Zok
Materials Department
University of California
Santa Barbara, CA 93106
Phone: 805–893–8699
FAX: 805–893–8486
zok@engineering.ucsb.edu

New oxides: Trudy Kriven
University of Illinois
Dept. of Materials Science and Engineering
1304 W. Green Street
Urbana, IL 61801
Phone: 217–333–5258
FAX: 217–333–2736
w-kriven@uiuc.edu

Extrusion development: Greg Hilmas
Ceramic Engineering Department
222 McNutt Hall, 1870 Miner Circle
University of Missouri–Rolla
Rolla, MO 65409–0330
Phone: 573–341–6102
FAX 573–341–6934
ghilmas@umr.edu